SANDIA REPORT

SAND96–2792 • UC–610
Unlimited Release
Printed November 1996

Development and Assessment of the CONTAIN Hybrid Flow Solver

K. K. Murata, D. W. Stamps

Prepared by
Sandia National Laboratories
Albuquerque, New Mexico 87185 and Livermore, California 94550
for the United States Department of Energy
under Contract DE-AC04-94AL85000

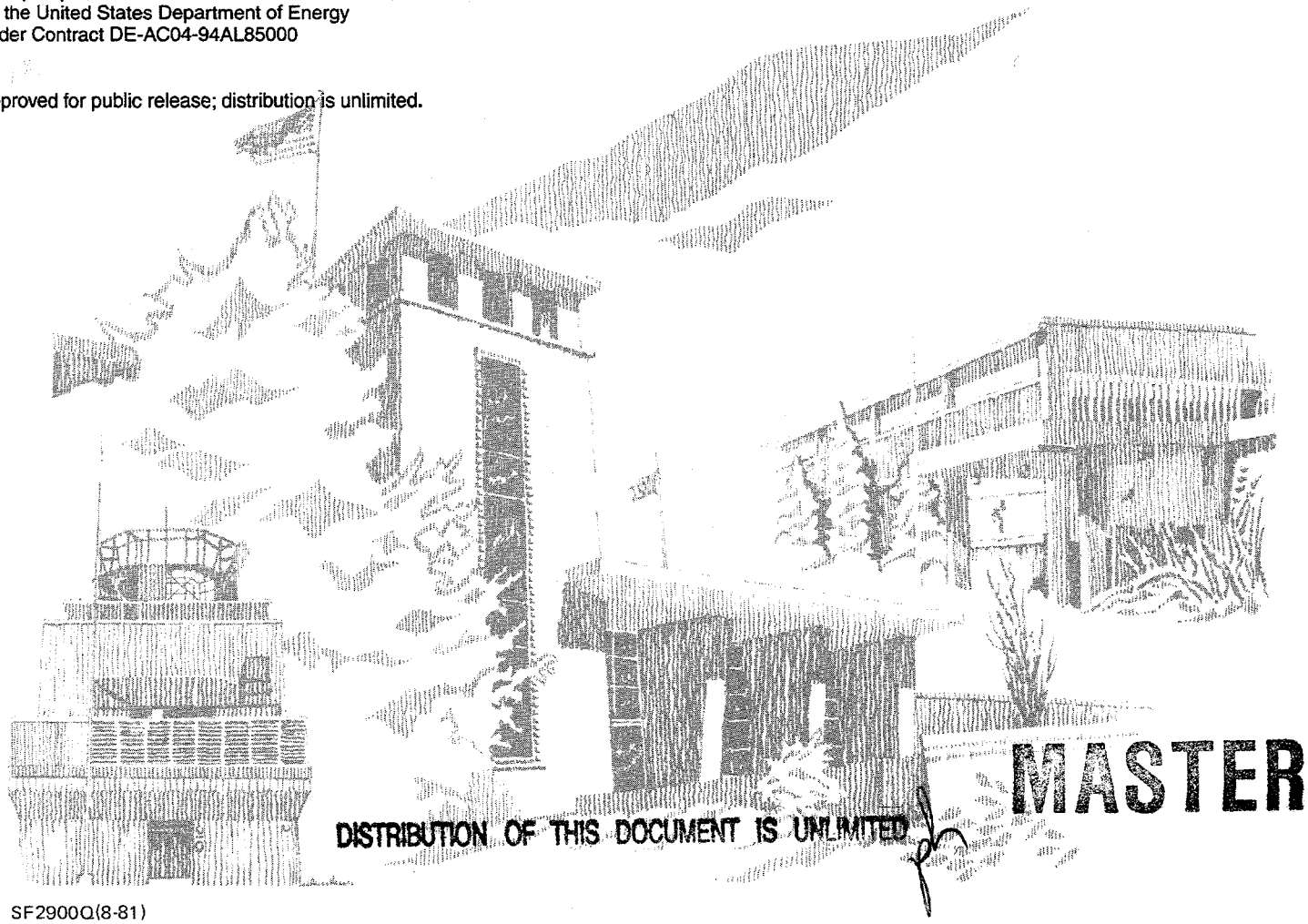

Issued by Sandia National Laboratories, operated for the United States Department of Energy by Sandia Corporation.

Available to DOE and DOE contractors from
Office of Scientific and Technical Information
PO Box 62
Oak Ridge, TN 37831

Prices available from (615) 576-8401, FTS 626-8401

Available to the public from
National Technical Information Service
US Department of Commerce
5285 Port Royal Rd
Springfield, VA 22161

NTIS price codes
Printed copy: A08
Microfiche copy: A01

SAND96-2792
Unlimited Release
Printed November 1996

Distribution
Category UC-610

Development and Assessment of the CONTAIN Hybrid Flow Solver*

K. K. Murata and D. W. Stamps**
Modeling and Analysis
Sandia National Laboratories
Albuquerque, NM 87185-0739

Abstract

A new gravitational head formulation for the treatment of stratified conditions has been developed for CONTAIN 1.2, a control volume code used primarily for the analyses of postulated accidents in nuclear power plants. The new CONTAIN formulation of gravitational heads, termed the hybrid formulation, is described. This method of calculating stratified conditions is compared with the old, average-density formulation used in code versions prior to CONTAIN 1.2. Both formulations are assessed in this report with experimental data from three large-scale experiments in which stratified conditions formed by injection of a buoyant gas were observed. In general, the hybrid formulation gives a substantially higher degree of stratification than the old formulation. For stable, fully developed stratifications, the hybrid formulation also gives much better agreement with the measured degree of stratification than the old formulation. In addition, the predicted degree of stratification is robust and not sensitive to nodalization, provided a set of nodalization guidelines are followed. However, for stratification behavior controlled by special physics not modeled in CONTAIN, such as momentum convection, plume entrainment, or bulk molecular diffusion, one should not expect good agreement with experiment unless special measures to accommodate the missing physics are taken.

---

*This work was supported by the U. S. Nuclear Regulatory Commission and performed at Sandia National Laboratories, which is operated for the U. S. Department of Energy under Contract No. DE-AC04-94AL85000.

**Presently at the Department of Mechanical and Civil Engineering, University of Evansville, Evansville, IN, 47722.

Table of Contents

List of Figures

List of Figures (continued)

List of Figures (continued)

List of Figures (continued)

List of Figures (continued)

List of Figures (continued)

List of Figures (continued)

List of Figures (continued)

List of Figures (concluded)

List of Tables

1. Introduction

Control volume codes are particularly well suited to analyze complex phenomena in complicated large-scale geometries because their numerical formulation allows many physical processes to be modeled. CONTAIN is a thermal hydraulics code that is based on a control volume formulation. Although it has general applicability, it has been used primarily to predict the physical, chemical, and radiological conditions inside the containment and connected buildings of a nuclear reactor in the event of an accident. A detailed description of all of the models in CONTAIN is beyond the scope of this report but can be found in Reference Mura96.

In the analysis of severe accidents in nuclear power plants, the ability to predict accurately the mixing behavior of injected hydrogen and steam into a containment from the reactor coolant system is an important capability for control volume codes. Containment pressure is determined in part from the distribution of steam within the containment. The potential combustion modes that may occur are determined by the distribution of hydrogen and steam in the containment. However, in the past, control volume codes, including CONTAIN, have shown a tendency to overpredict the rate and extent of mixing of such gases in a containment. This behavior was illustrated in the results of the International Standard Problem 29 (ISP-29), as reported in Reference Karw92. This Standard Problem was based on the HDR E11.2 experiment. In the first part of the experiment, steam and hydrogen were injected into the upper part of the HDR containment. The measured steam and hydrogen concentrations were generally underpredicted in the dome and overpredicted in the lower part of the containment by the participating control volume codes, including CONTAIN.

ISP-29 showed that a common problem with control volume codes is the inability to predict highly stratified conditions. To overcome this general deficiency, a new gravitational head formulation for the CONTAIN flow solver has been developed. This formulation, and the corresponding modifications to the CONTAIN flow solver, are referred to below as the "hybrid flow solver." The objectives of this report are to describe the formulation of the hybrid flow solver and assess the old and hybrid flow solvers against three experiments, including HDR E11.2, that had highly stratified conditions. Besides HDR E11.2, this assessment utilizes the NUPEC M-8-1 experiment[OECD94] and the Surtsey ST-3 test[Blan95].

It should be noted that the present comparisons form only a part of the assessment work that has been done. A preliminary version of the hybrid formulation was presented to the CONTAIN peer review[Boya95], along with preliminary supporting calculations of the NUPEC M-8-1[OECD94] and HDR E11.2[Karw92] experiments, two experiments with substantial stratification. Concurrent with the peer review process, the old and hybrid formulations were used[Stam95] to analyze a series of NUPEC experiments[OECD94] that were well-mixed as well as stratified. Recently, the old and

hybrid formulations were also used to analyze[Till96] transient and steady-state experiments with substantial stratification that were conducted in the Westinghouse Large Scale Test (LST) facility. Reference Stam95 demonstrated that the hybrid formulation gives essentially the same result as the old formulation when conditions are well-mixed. Thus, we will focus here only on stratified conditions.

The hybrid formulation is introduced in Section 2. In Section 2.1, background information on stratifications and the requirements imposed on the flow solver with respect to the proper treatment of stratifications are presented. In Section 2.2, the hybrid formulation is described in detail. In Section 2.3, the results of plume simulation calculations with the old and hybrid solvers are discussed. Finally, in Section 2.4 general considerations related to the applicability of the hybrid solver to stratified conditions are discussed.

In Section 3, the experiments used to assess the old and hybrid solvers are first introduced and then the results of each experiment comparison are presented in detail. User guidance on the hybrid flow solver is provided in Section 4. Finally, the summary and conclusions from this assessment are presented in Section 5.

2. Description of the Hybrid Flow Solver

The term "hybrid" flow solver refers to a revised treatment of gas gravitational heads, developed for the CONTAIN implicit flow solver, that has been developed to satisfy a minimum set of requirements to allow CONTAIN to model natural convection in a reasonable manner. These requirements are (1) consistency with the derivation of the CONTAIN momentum equation for flow paths; (2) the correct behavior in the well-mixed asymptotic limit; and (3) provisions for properly treating the stability of a stratification, when present. The requirements imposed on the flow solver with regard to the proper treatment of stratifications are first discussed in Section 2.1, and the hybrid formulation is discussed in Section 2.2. The performance of the old and hybrid solvers in plume simulation calculations is discussed in Section 2.3. Finally, general considerations related to the applicability of the hybrid solver to stratified conditions are discussed in Section 2.4.

2.1. Flow Solver Requirements

Prior to presenting the hybrid formulation, it may be useful to give some background information on stratifications and flow solver requirements. We start this section by discussing the requirements imposed on the gravitational head formulation by the momentum equation. We then discuss the requirements imposed by a proper treatment of the well-mixed asymptotic limit.

We begin by referring to the derivation of the CONTAIN momentum equation given in Appendix A. This derivation assumes that the time-derivative of the local density can be ignored along a streamline; that is, it is assumed that the density instantaneously reaches steady state. In this case, the effective gas density ρ_f to use for the gas gravitational head in the flow path is shown to be a mean density corresponding to a density occurring somewhere within the flow path. (It should be noted that a flow path in CONTAIN is only a model for transfer rates between mass and energy control volumes and not a repository, and consequently no actual inventory is considered to be "in" a flow path.) Since the two cells connected by the flow path may have considerably different densities, it is clear that the gravitational head density is closely related to the upstream, or donor, gas density ρ_u to within parameters that are small under typical containment conditions; that is,

$$\rho_f = \rho_u + O(\epsilon) + O(M^2) \qquad (2\text{-}1)$$

where $\epsilon = g\rho\Delta H/P$ and M is the Mach number. In the expression for ϵ, g is the acceleration due to gravity, ΔH is a characteristic height in the problem, and P is the local pressure. It should be noted that ϵ is typically a small parameter; for air, it is on the order of 10^{-4} per meter of characteristic height under ambient conditions. Equation (2-1) defines the gravitational head density as the donor density

to within small corrections. This definition is adequate except in the well-mixed asymptotic limit, where the corrections of order ϵ become important. We discuss the nature of these corrections below.

Prior to discussing the well-mixed asymptotic limit, it is useful to define the various types of stratifications first. These can be classified as either unstable, metastable, or stable. The metastable stratification is the dividing line between a stable stratification and unstable stratification. The nature of a stratification is determined by the composition and temperature gradients present, as well as the heat transfer conditions during gas flow. For an adiabatic atmosphere with homogeneous composition and without condensation, the metastable adiabatic stratification has a temperature gradient $dT/dz = - g/C_p$ and a density gradient $d\rho/dz = - g\rho^2/(\gamma P)$, where C_p is the gas specific heat (per unit mass) at constant pressure, z is the elevation, and γ is the specific heat ratio. For adiabatic atmospheres with more positive temperature and more negative density gradients than this, the stratification is locally stable, and with more negative temperature and positive density gradients the atmosphere is locally unstable. Stability in this case is defined in terms of whether a parcel of gas at a given elevation, and in equilibrium with its surroundings, accelerates or encounters a restoring force, when perturbed from its initial elevation. For an isothermal atmosphere, in intimate contact at all elevations with a heat sink at fixed temperature, the metastable stratification has a somewhat different density gradient of $d\rho/dz = - g\rho^2/P$. It will be assumed below that, in general, metastable stratifications will lie somewhere between adiabatic and isothermal behavior with respect to their density gradients.

It should be noted that metastable density gradients are typically associated with the well-mixed asymptotic limit attained after a period of convective mixing, although an atmosphere may also stably stratify at some point and not completely mix. The density gradients involved with such metastable stratifications are relatively small, with a relative variation in density of order ϵ. In a containment with appreciable heat or steam and hydrogen sources, the density gradients from composition and temperature effects are likely to be much larger. If achieved, such a metastable stratification is likely to be achieved only after a long period of time and only after any driving forces for convection have reached a low level. Thus, the well-mixed asymptotic regime in which the metastable stratification is approached is not likely to be an important regime for containment analysis -- this regime will presumably occur at a time when the need to continue the containment analysis is minimal. However, the requirement that well-mixed asymptotic behavior be properly reproduced is still important because a code that continues to mix in the absence of driving forces clearly cannot be trusted to mix properly in the presence of driving forces.

In a convection process, the atmosphere will either form a locally stable stratification or mix until a (locally) metastable stratification is achieved. If local pressure equilibrium has not yet been achieved,

a parcel of gas will continue to rise (like a thermal) or sink until it is in pressure equilibrium with its surroundings. In the following we assume that convective mixing has been induced by driving forces that have since been removed and assume that the momentum and residual density differences are such that a metastable stratification is formed.

We now return to the discussion of the correction terms to the gravitational head density. Consider a convection loop formed between two mass and energy control volumes *i* and *j* that are part of a metastable stratification, as in Figure 2.1. (Note that such control volumes are also called cells below.) We assume that the upward leg is modeled by one CONTAIN flow path, and the downward leg by another flow path, with equal mass flow rates. These legs are assumed to be terminated at the control volume centers. The pressure equilibrium condition for the path from *i* to *j* in the final stages of mixing is

$$P_i - P_j + \rho_{f,ij}\, g(H_i - H_j) = 0 \qquad (2\text{-}2)$$

where H_i and H_j are the elevations of the gas centers of volume of the control volumes, as indicated more clearly in Figure 2.2, and $\rho_{f,ij}$ is the gas density used in the path from *i* to *j*. The equation for the path from *j* to *i* is obtained by permuting the *i* and *j* indices in this equation. An energy balance under adiabatic conditions can also be performed on control volume *j* to obtain

$$C_p T_i + g(H_i - H_j) = C_p T_j \qquad (2\text{-}3)$$

with a similar equation for *i*. Equations (2-2) and (2-3) can be used to derive the standard expressions for the density and temperature variation in a metastable stratification in an ideal adiabatic atmosphere. In addition, Equation (2-2) and the one obtained by permuting its indices require that $\rho_{f,ij}$ and $\rho_{f,ji}$ be equal, and therefore $\rho_{f,ij}$ must be symmetric in the *i* and *j* indices. If one expands $\rho_{f,ij}$ in a Taylor series in $H_j - H_i$ about the average density $\rho_{av} = (\rho_i + \rho_j)/2$, the odd terms drop out, and one obtains

$$\rho_{f,ij} = \rho_{f,ji} = \rho_{av} + O(\epsilon^2) \qquad (2\text{-}4)$$

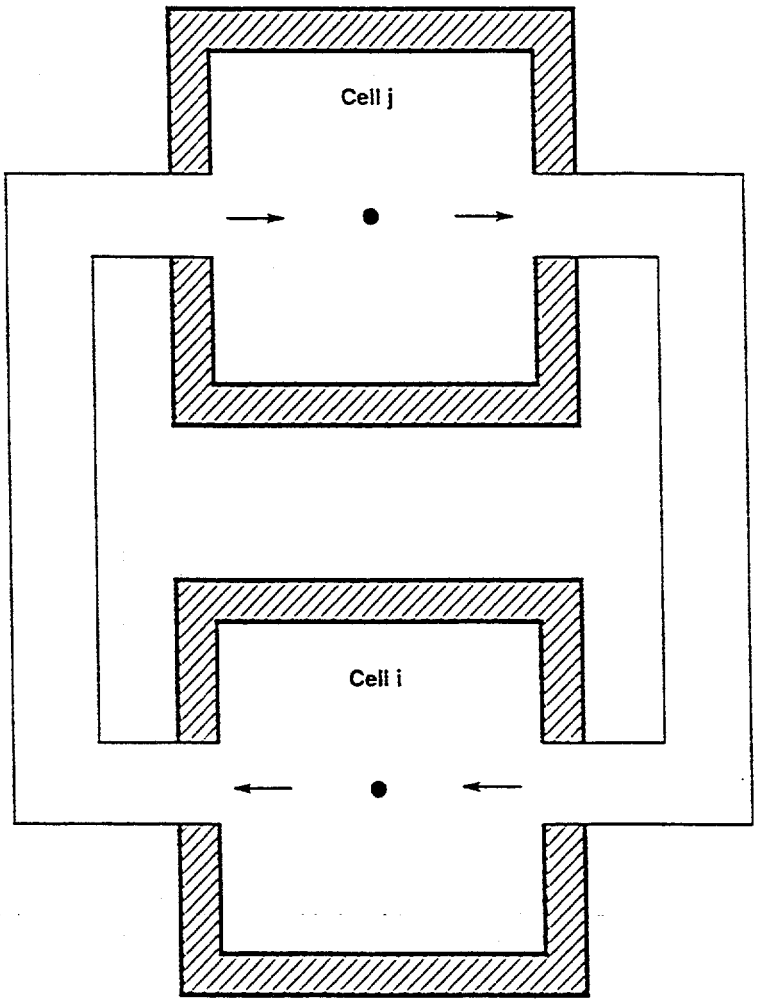

Figure 2.1. A convection loop formed between two CONTAIN control volumes, enclosing gas that is assumed to be part of a larger adiabatic metastable stratification.

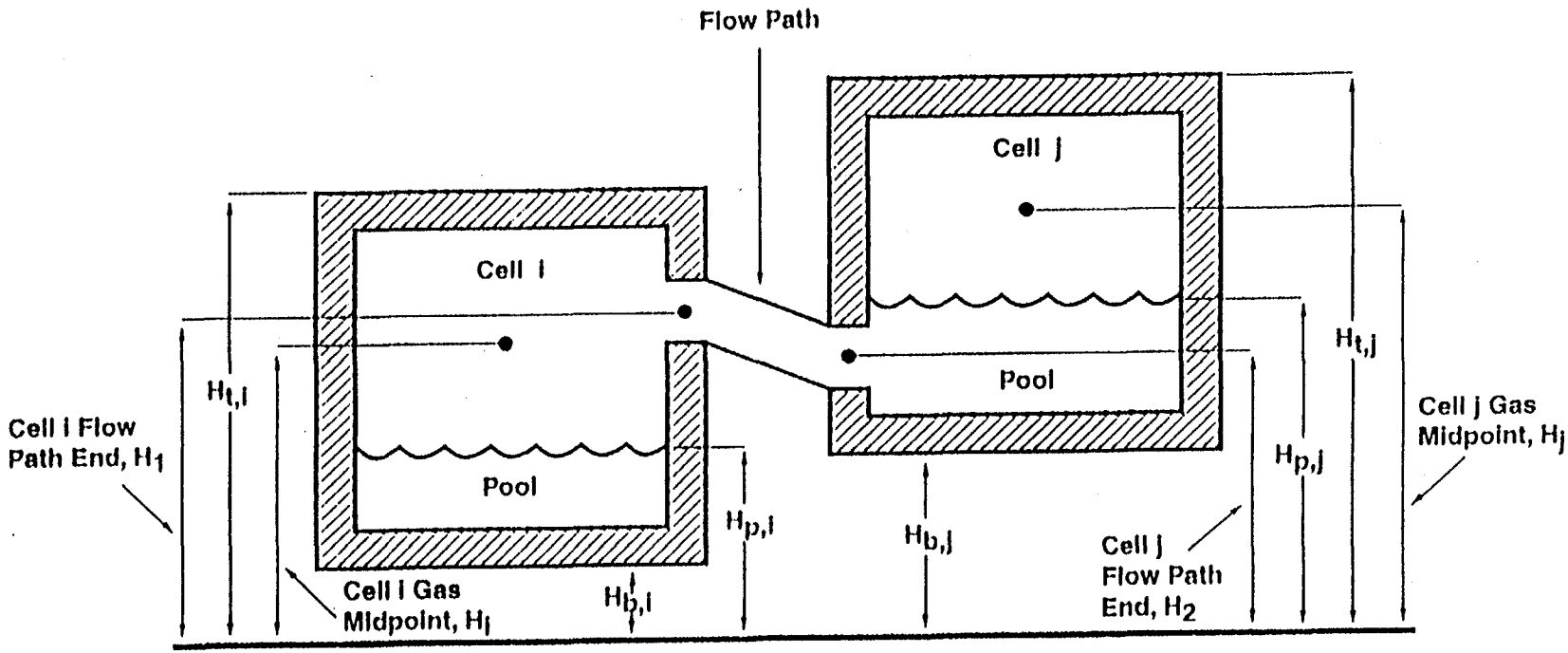

Figure 2.2. Definitions of the elevations used in conjunction with CONTAIN cells and flow paths.

One should note that Equation (2-4) would not be satisfied if donor densities were used for $\rho_{f,ij}$ and $\rho_{f,ji}$ since in this case they would not be equal to order ϵ^2 but would differ at order ϵ. From the momentum equations for the two paths, one can deduce that a spurious opposing driving force of order ϵ results from the donor formulation, and therefore in this case any mixing approaching the asymptotic limit would terminate within a finite time depending on the initial momentum in the flow. When this behavior is compared with the correct asymptotic behavior given in Equation (2-5) below, it is clear that excessively stable asymptotic behavior could be predicted with the use of donor densities.

Note that Equation (2-1) implies that the donor density is in general the appropriate density to use in the flow path, as long as corrections of order ϵ and M^2 can be neglected. Far from the asymptotic limit, when density differences are large, the donor density and not the average density is clearly appropriate. Equation (2-4) implies that in the well-mixed asymptotic limit, when density differences become small, the corrections of order ϵ to the donor density must be taken into account and, when they are, the corrections to the leading donor term produce the average density to first order.

The asymptotic decay of the flow rate under adiabatic conditions can be calculated under the assumption that the long term decay of flow in convection loops is momentum dominated. We consider for simplicity only the two-cell case illustrated in Figure 2.1, for which the flow paths are symmetric and terminated at the cell centers, and also assume that Equations (2-2) and (2-3) are satisfied exactly. Then, according to Equation (2-2), the gravitational head terms can be neglected in Equation (A-8). Integrating Equation (A-8) with this assumption results in the asymptotic behavior

$$W = \frac{W_0}{1+W_0\frac{A}{L}\frac{C_{FC}}{\rho_f A^2}(t-t_0)} \qquad (2\text{-}5)$$

in the notation of Equation (A-8), where W_0 is the flow rate at time t_0. The behavior in Equation (2-5) has been shown to be reproduced fairly well by CONTAIN in a test case with the input options set to select the average-density formulation and with the cells set up initially to satisfy Equations (2-2) and (2-3).

The above discussion indicates that a donor formulation is not always appropriate. For this reason, a hybrid formulation is proposed below. In this formulation, for most conditions, a donor formulation is used for the gravitational head density. However, an average-density formulation is used over a narrow range of density gradients spanning the isothermal and adiabatic metastable stratifications, so that excessive stability does not manifest itself in the well-mixed asymptotic limit. This hybrid

formulation is discussed in detail in the next section.

2.2. The Hybrid Formulation

In the hybrid formulation of gas gravitational heads, the formulation for the flow density ρ_f discussed in the preceding section depends on the densities and elevations of the two mass and energy control volumes connected by the flow path. The hybrid formulation interpolates between two methods. One method, correct in the well-mixed asymptotic limit, is based on the use of an average gas density $\rho_f = \rho_{av} = (\rho_i + \rho_j)/2$, where ρ_i and ρ_j are the gas densities of the two cells *i* and *j* connected by the flow path. The other method, used away from the asymptotic limit, reduces to the donor method discussed in the preceding section as a limiting case. For numerical reasons related to the efficiency of the flow solver, the latter method is actually based on what is called a virtual dynamic interface (VDI) within a flow path. The VDI method eliminates the discontinuity in the flow that would occur at flow reversal when a strictly donor method is used. The VDI eliminates the discontinuity by defining a continuum of possible locations within the flow path at which the density changes from that of one cell to that of the other. This density crossover location is used to calculate the flow path gravitational heads. Figure 2.3 shows some possible VDI locations for the flow paths in a four-cell problem, in response to a slight increase in the density of cell 1. The term "virtual" refers to the fact that this density crossover point is used only to calculate the gravitational head, since CONTAIN flow paths are not repositories and have no actual resident inventory associated with them. The VDI has its own dynamic equation (Equation (2-10) below) based on a flow path filling considerations. However, the motion of the interface is artificially accelerated (through the parameter κ in Equation (2-10)) so that the VDI method much of the time gives results corresponding closely to the donor treatment. Alternatives to this default flow path formulation, including a formulation similar to that used in code versions prior to CONTAIN 1.2, may be specified through user input (see the discussion of the MSTABLE and RESOLVHD keywords below). Regardless of the gravitational head modeling options invoked, the gravitational head formulation will always revert back to an asymptotically correct expression, based on the average density and gas center-of-volume elevations, in the well-mixed limit. Hence, the overall approach is a "hybrid" one.

To be more specific, the gravitational head $\Delta P_{g,ij}$ in the momentum Equation (A-8) between two cells *i* and *j* is taken to be a linear combination of the asymptotically correct expression for the gas head $\Delta P'_{g,ij}$ calculated using the average density and gas centers of volume and the VDI expression for the gas head $\Delta P''_{g,ij}$ used away from the asymptotic limit:

$$\Delta P_{g,ij} = y \Delta P'_{g,ij} + (1-y) \Delta P''_{g,ij} \qquad (2\text{-}6)$$

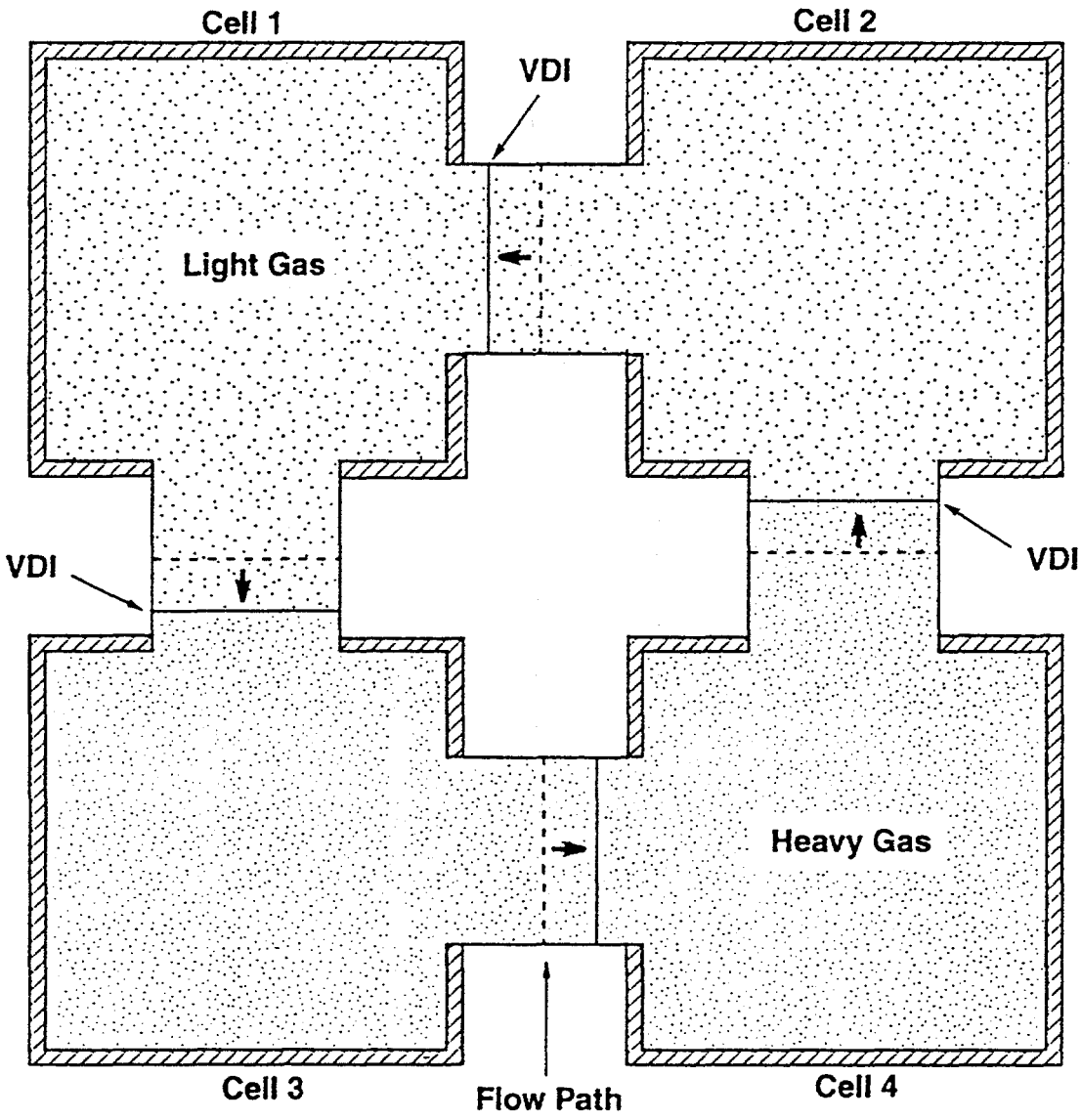

Figure 2.3. Position of the virtual dynamic interfaces (VDI) in the flow paths of a four-cell problem in response to a slight increase in density in cell 1.

where y is a crossover parameter and where we have neglected, for simplicity, the possible presence of pool liquid heads from submergence of a flow path connection below the pool surface. The crossover parameter y, $\Delta P'_{g,ij}$, and $\Delta P''_{g,ij}$ are defined in the order given in the following paragraphs.

The crossover parameter y determining the relative weighting of the $\Delta P'_{g,ij}$ and $\Delta P''_{g,ij}$ terms depends on the value of the typically small parameter ϵ introduced in the preceding section. Here, it is defined as $\epsilon = g\rho_{av}|H_i - H_j|/P_{av}$, where $P_{av} = (P_i + P_j)/2$ is the average pressure, g is the acceleration due to gravity, and H_i and H_j are the elevations of the gas centers of volume of the two cells i and j connected by the flow path, as shown in Figure 2.2. The reader may recall that the ϵ parameter corresponds to the absolute value of the first-order relative change in density in an isothermal metastable stratification between H_i and H_j. The crossover also depends on a second parameter δ, which is the actual cell relative density difference: $\delta = (\rho_i - \rho_j)/\rho_{av}$ if $H_i < H_j$; $\delta = (\rho_j - \rho_i)/\rho_{av}$ if $H_j < H_i$; $\delta=0$ otherwise. Note that $\delta< 0$ corresponds to an unstable configuration, whereas $\delta>0$ could correspond to either unstable, metastable, or stable cases.

The crossover parameter y is defined according to the relation between ρ and ϵ:

$$
\begin{aligned}
y &= 0 && \text{if } \delta \geq 2\epsilon \text{ or } \delta<0 && (\textit{VDI}) \\
&= 2(\epsilon - \delta/2)/\delta && \text{if } 2\epsilon > \delta \geq \epsilon && (\textit{interpolated}) \\
&= 1 && \text{if } \epsilon > \delta \geq 0. && (\textit{averaged})
\end{aligned}
\qquad (2\text{-}7)
$$

where the names of the three different hybrid solver regimes (VDI, interpolated, and average-density) are also indicated. Figure 2.4 illustrates these three different regimes for $H_i<H_j$ within the one-dimensional space relating the fractional cell densities $\rho_i/(\rho_i+\rho_j)$ and $\rho_j/(\rho_i+\rho_j)$, which are subject to the obvious constraint $\rho_i/(\rho_i+\rho_j) + \rho_j/(\rho_i+\rho_j) = 1$. This figure also gives the inherent isothermal stability regimes of the cells. Note that in a well-mixed adiabatic metastable stratification, as opposed to an isothermal one, the first-order relative density difference would be ϵ/γ, where γ is the specific heat ratio, instead of ϵ. In practice, metastable stratifications are neither exactly isothermal or adiabatic, and the density difference is likely to lie somewhere in between these two values. Note that the crossover parameter y is always equal to one over the range of δ's (i.e., $\epsilon \geq \delta \geq \epsilon/\gamma$) corresponding to the possible types of metastable stratifications.

Although the crossover values for δ in Equation (2-7) are selected so that the average density is used for possible metastable stratifications, there is no physical basis for selecting the particular crossover values shown in Equation (2-7). The assumption is that as long as the possible metastable stratifications are bracketed and the crossovers occur in the regime of small density differences, the particular values are not important or are moot. The reader should recall that $\epsilon \sim 10^{-4}\ |H_i - H_j|$, with

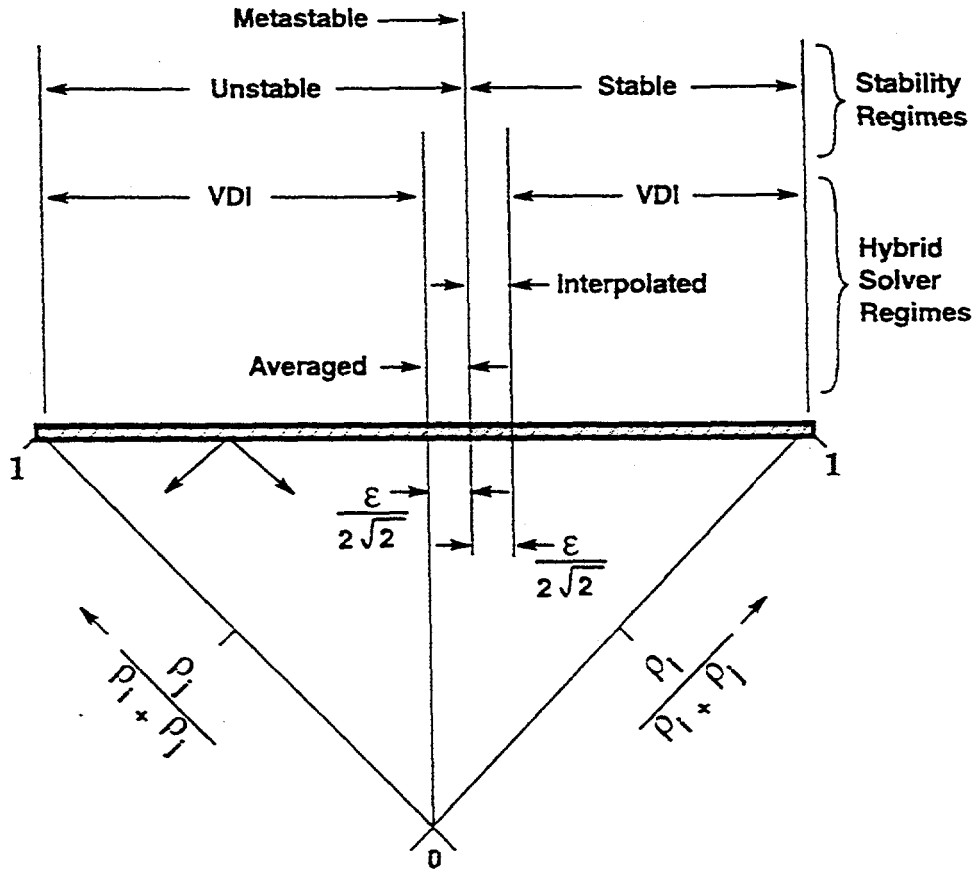

Figure 2.4. Illustration of the hybrid solver regimes, relative to the stability of the stratification.

H in meters, so that the crossover behavior is confined to the regime of very small density differences. In this regime either the mixing rate of such stratifications is not important to the calculated results or the uncertainties in the gravitational head modeling are moot because of the uncertainties in the modeling of the conditions within the stratification, including inhomogeneities, at the level of detail required to describe its mixing. The former is true in most cases for stratifications generated by weak sources, since the mixing rate of the stratification would have almost no impact on thermal-hydraulic conditions.[1] However, it is possible that very small density differences might be found between two cells with considerably different temperatures and compositions. The concern here is the excessive

[1]The mixing rate of the stratification could be important if the weak source had other implications beyond the usual thermal-hydraulic ones, such as radiological consequences.

mixing associated with the average-density formulation. There are two possibilities to consider. If the molar specific heats of the gas in the two cells are significantly (i.e., more than a few per cent) different, any mixing would cause the densities of the cells to diverge, and thus the densities would not remain in the average-density regime for long. On the other hand, if the molar specific heats are constant and identical, the ideal gas approximation is applicable, and heat transfer can be ignored, then it can be shown that the densities and pressures of the cells will be identical to that of the well-mixed gas, with an effective temperature determined by molecular weight scaling. Thus, under these conditions, the densities could remain in the average-density or crossover regime while mixing occurred. In such a case, accurate modeling of gravitational heads, as well as the detailed conditions within the stratification, may be required to describe its mixing. An example of the mixing of a stratification with large composition variation and small density variation is discussed in Section 3.3.3, in conjunction with the HDR E11.2 experiment.

The definition of the asymptotically correct head $\Delta P'_{g,ij}$ is

$$\Delta P'_{g,ij} = g(H_i - H_j)\rho_{av} \tag{2-8}$$

where again, for simplicity, we have neglected the possible presence of pool liquid heads. This asymptotically correct head cannot be modified through user input.

The definition of the VDI head $\Delta P''_{g,ij}$ used away from the well-mixed asymptotic limit is

$$\Delta P''_{g,ij} = g\rho_i(H_i - H_1') + g[f_{ij}\rho_i + (1-f_{ij})\rho_j](H_1' - H_2') + g\rho_j(H_2' - H_j) \tag{2-9}$$

The definitions of the VDI parameter f_{ij} and the elevations H_1' and H_2' depend on two user options, controlled by the MSTABLE and RESOLVHD keywords, as discussed below. The f_{ij} parameter gives the location of the VDI in the flow path in terms of a fraction of the effective length of the path in the direction from *i* to *j*. The default treatment is a dynamically calculated f_{ij}, as discussed below, in which the interface is assumed to span the entire elevation difference between the gas centers of volume. If MSTABLE is specified, then f_{ij} is simply set to ½, a value which corresponds to using the average density over the elevation span normally spanned by the VDI model. Specification of the RESOLVHD keyword invokes a treatment whereby the elevation difference normally spanned by the VDI is restricted to the elevation difference between the flow path ends, and the appropriate cell density is used within a cell to span the elevation change between the gas center of volume and the flow path end. In other words,

$H_1' = H_i$ if the RESOLVHD keyword has not been specified for the path
$= H_1$ if the RESOLVHD keyword has been specified for the path, and

$H_2' = H_j$ if the RESOLVHD keyword has not been specified for the path
$= H_2$ if the RESOLVHD keyword has been specified for the path,

where H_1 and H_2 are the elevations of the flow path connections to cells *i* and *j*, respectively, as shown in Figure 2.2. Note that RESOLVHD will have no effect if the flow paths are attached at the gas center of volume at each end.

The MSTABLE and RESOLVHD options have been made available to recover the old gravitational head modeling used in code versions prior to CONTAIN 1.2, and also to add flexibility to the hybrid solver modeling. Use of MSTABLE and RESOLVHD and specification of flow path elevations at the gas centers of volume will allow the user to recover the "old," average-density gravitational head formulation used in versions prior to CONTAIN 1.2 in most cases. This prescription will work provided the gas flow path connections are not submerged and significant displacement of the gas centers of volume by the pool does not occur.

In the VDI model, if MSTABLE is not specified, f_{ij} is determined dynamically, using an initial value $f_{0,ij} = ½$. The motion is governed by the rate at which one considers the flow path to become filled with material from the upstream cell:

$$\frac{df_{ij}}{dt} = \frac{\kappa W}{\rho_u A L'} \qquad (2\text{-}10)$$

where W is the mass flow rate in the path, as determined from the momentum equation, ρ_u is the upstream, or donor, density, κ is a dimensionless acceleration factor defined below, $L' = MAX(|H_i'-H_j'|, L)$ is the effective filling length of the flow path, and L is the inertial length. Equation (2-10) is coupled to the momentum equation through Equation (2-9) above and is solved with the constraint $0 \le f_{ij} \le 1$. Note the value $\kappa = 1$ when $L' = L$ would correspond to physically filling an area equal to the actual flow path area A over the inertial length L, and $\kappa = \infty$ corresponds to an instantaneous flow path filling, or donor, assumption. In practice, for reasons discussed below, large values of κ are used to accelerate the filling. Much of the time the VDI method gives essentially the same results as a straightforward donor-cell approach, which corresponds to setting $f_{ij} = 1$ if $W>0$ and $f_{ij} = 0$ if $W<0$, in Equation (2-9). This occurs whenever flow in one direction has persisted for a sufficient time to cause f_{ij} to be pinned at its maximum or minimum value. The time required for pinning to occur is clearly reduced as κ is increased.

It should be noted that in the derivation of CONTAIN flow or momentum equation, the changeover in density within the flow path to that based on the donor cell is assumed to be instantaneous. Thus, Equation (2-10) is not strictly consistent with the assumptions of the momentum equation unless κ is effectively infinite. In practice, the value used for κ is chosen sufficiently large to give results close to donor cell results but not so large that the discontinuities associated with the donor cell approach result in numerical problems. The value used is

$$\kappa = \mathrm{MAX}\left[10, \frac{L'}{g(\Delta t_f)^2}\right] \qquad (2\text{-}11)$$

where Δt_f is the flow timestep.

If f_{ij} were in fact solved using values of κ close to the "physical" value, in contradiction to the momentum equation assumption, gravity wave behavior would in general be observed with a stable stratification. If one views the density difference between cells as representing a stratified layer interface, then these gravity waves would cause unphysical mixing of inventories across the interface, since in CONTAIN material entering a flow path is instantaneously transported to and mixed with the downstream cell. (This unphysical mixing could be prevented through a code upgrade in which flow paths are modified to be repositories, but this upgrade is not feasible at present.)

Because of this unphysical mixing, the present numerical implementation of the VDI attempts to assure that any gravity waves are artificially and strongly damped. First of all, self-consistent end-of-timestep (implicit) values of f_{ij} are calculated and used in Equation (2-9) whenever the response of f_{ij} is in a direction to retard the flow; beginning-of-timestep values are used otherwise. The use of such implicit values, coupled with a large κ, should overdamp the gravity waves. (In the limit $\kappa=\infty$, the flow must be damped to zero with a stable stratification and weak perturbations since a "flow gap" in which no flow is possible occurs in the self-consistent donor method in such cases.) Thus, only quasi-static waves, formed in response to local perturbations, should remain. Note that for weak perturbations these waves are virtual in the sense that they are reflected in the VDI locations only, and not in flow or inventories. Only for large perturbations, sufficient to generate full wave heights greater than the vertical span of a flow path, will a significant change occur in cell inventories above and below the stratified layer interface because of the wave.

We close this section with an illustration of how stability is treated in the average-density treatment invoked with the MSTABLE keyword, compared to the VDI method. The average-density treatment in effect treats the interface between stratified layers as diffuse, i.e., as spanning more than one cell,

whereas the VDI method uses a virtual interface between cells. Take, for example, the configuration shown in Figure 2.3. We assume cells 1 and 2 are initially filled with gas of the same density, as are cells 3 and 4, but the density of the latter is greater than $1+2\epsilon$ times that of cells 1 and 2. All of the gas is assumed initially to be at the same temperature and pressure, and it is assumed that RESOLVHD has not been specified for any of the paths. This configuration is perturbed by slightly increasing the gas density in cell 1. If MSTABLE has been specified, convective flow will occur in the counterclockwise direction until the density changes of the cells rebalance the gravitational head. Again, if one views the interface between the upper cells and lower cells as sharp, as when they represent two different stratified layers, then this mixing is unphysical, because gas is mixed over a distance equal to the vertical cell separation, regardless of the magnitude of the perturbation. If MSTABLE is not specified and the VDI method is consequently used, this convective flow will occur only until the motion of the VDI's causes an opposing head to develop. At this point the flow will go to zero. Since the VDI motion is accelerated through the κ parameter in Equation (2-10), for small perturbations relatively little flow will occur before the gravitational heads rebalance. This is the "virtual" approach to the interface, which for weak perturbations essentially eliminates the effects of mixing between the two stratified layers represented by the four cells.

2.3. Simulation of a Plume Using CONTAIN

Buoyant steam/hydrogen plumes are of particular interest in containment analysis because they lead to a commonly postulated type of gas stratification within the containment. Prior to discussing the advantages and limitations of the hybrid solver, it is helpful to give results of CONTAIN calculations that simulate a buoyant plume in an enclosed volume, using both the hybrid and the old, average-density formulations. In this simulation, the plume is composed of a slightly buoyant, 0.1 kg/s source of nitrogen at 298 K into air at 298 K and one atmosphere. This source is injected into an initially stagnant volume containing 4620 m^3 of air. The 12-cell nodalization used is shown in Figure 2.5, with volumes and cell heights as defined in Table 2.1. Cells 1-5 in the figure are assumed to be cylindrical with flow paths defined at the top, side, and bottom of each cell. Cells 7-11 are assumed to be cylindrical annuli, with flow paths at common cell boundaries. The flow paths at those boundaries are taken to include the entire area of the boundary, with a loss coefficient $C_{FC} = 1$ and a nominal inertial length of 3 m for all paths. The flow paths are also assumed to be connected between cell centers, with respect to the gravitational heads generated within each flow path. The buoyant gas is assumed to be injected into cell 1. Since CONTAIN ignores the momentum convection associated with the source, the buoyant gas source should result in a buoyancy-driven plume, rather than a jet. As discussed in Reference Pete94, in such a case a stable stratification should form above the injection point.

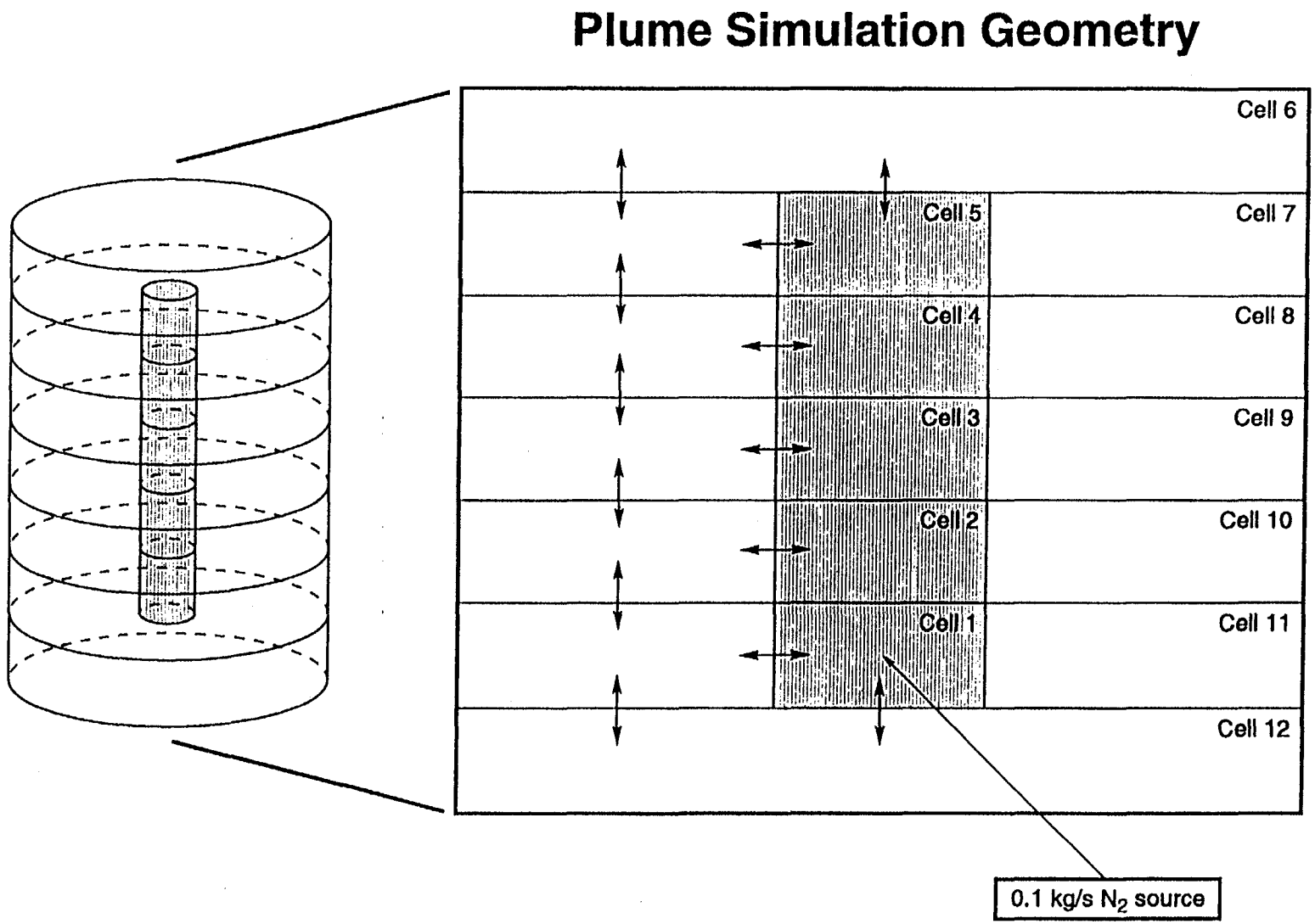

Figure 2.5. CONTAIN nodalization used in the simulation of a buoyant plume.

Table 2.1. Cell volumes and heights used in the plume simulation problem

Cell Number	Cell Volume (m^3)	Cell Height (m)
1	60	3
2	60	3
3	60	3
4	60	3
5	60	3
6	660	3
7	600	3
8	600	3
9	600	3
10	600	3
11	600	3
12	660	3

Initially, the flow patterns calculated within the hybrid and average-density formulations are similar and somewhat complex and reflect a redistribution of the gas to correspond to the adiabatic metastable density gradient. Figure 2.6 shows the quasi-steady flow rates resulting from the source buoyancy at 1500 seconds after the start of injection, when the average density is used for the flow density. (This option is invoked by the MSTABLE keyword discussed above, and gives results corresponding to the old flow solver.) Figure 2.7, on the other hand, shows the corresponding quasi-steady flow rates when the default hybrid solver is used. At this time, the hybrid solver is essentially using a donor-density formulation. The principal difference in these results is that the flow patterns with the average-density formulation involve a significant entrainment of gas from below the source,

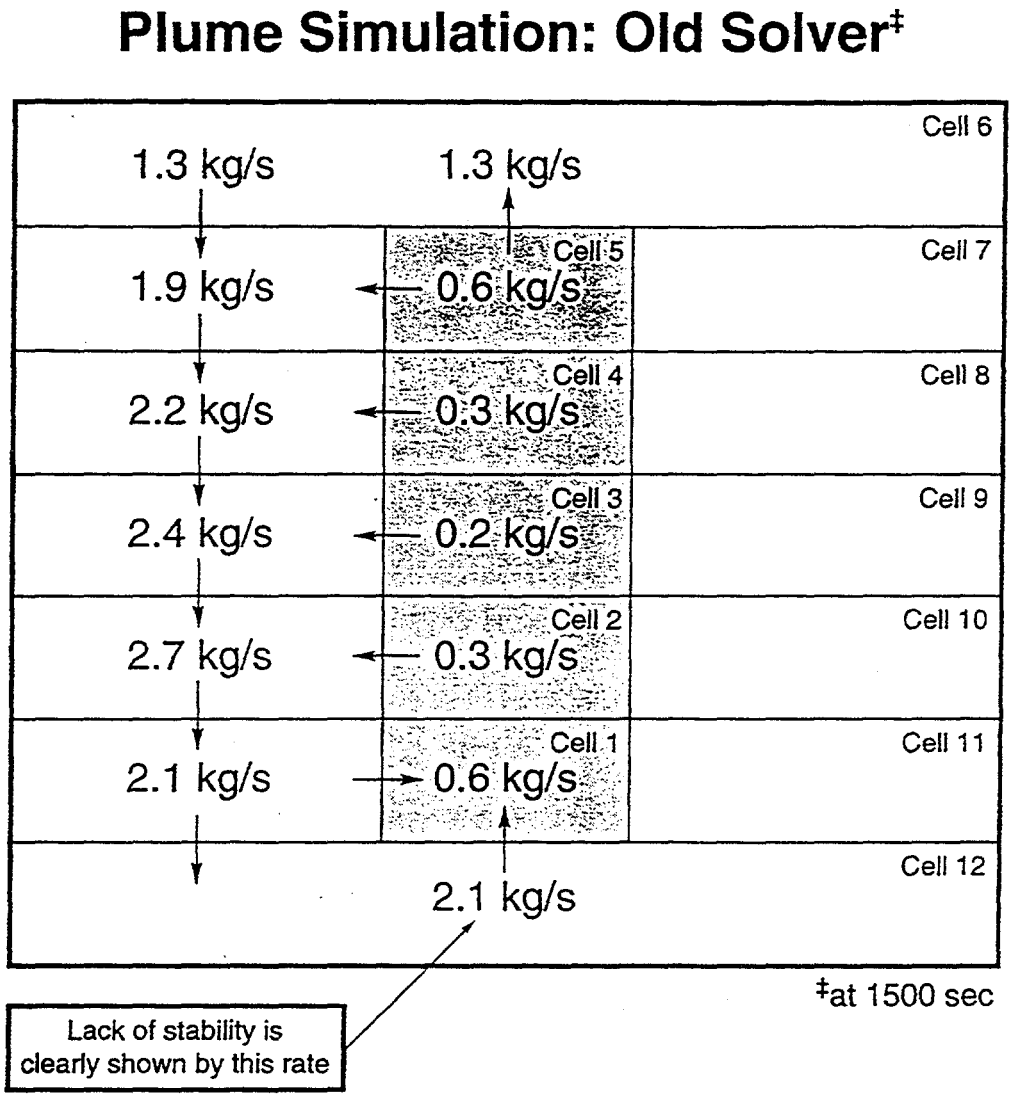

Figure 2.6. Flow patterns in the plume simulation resulting from the average-density formulation.

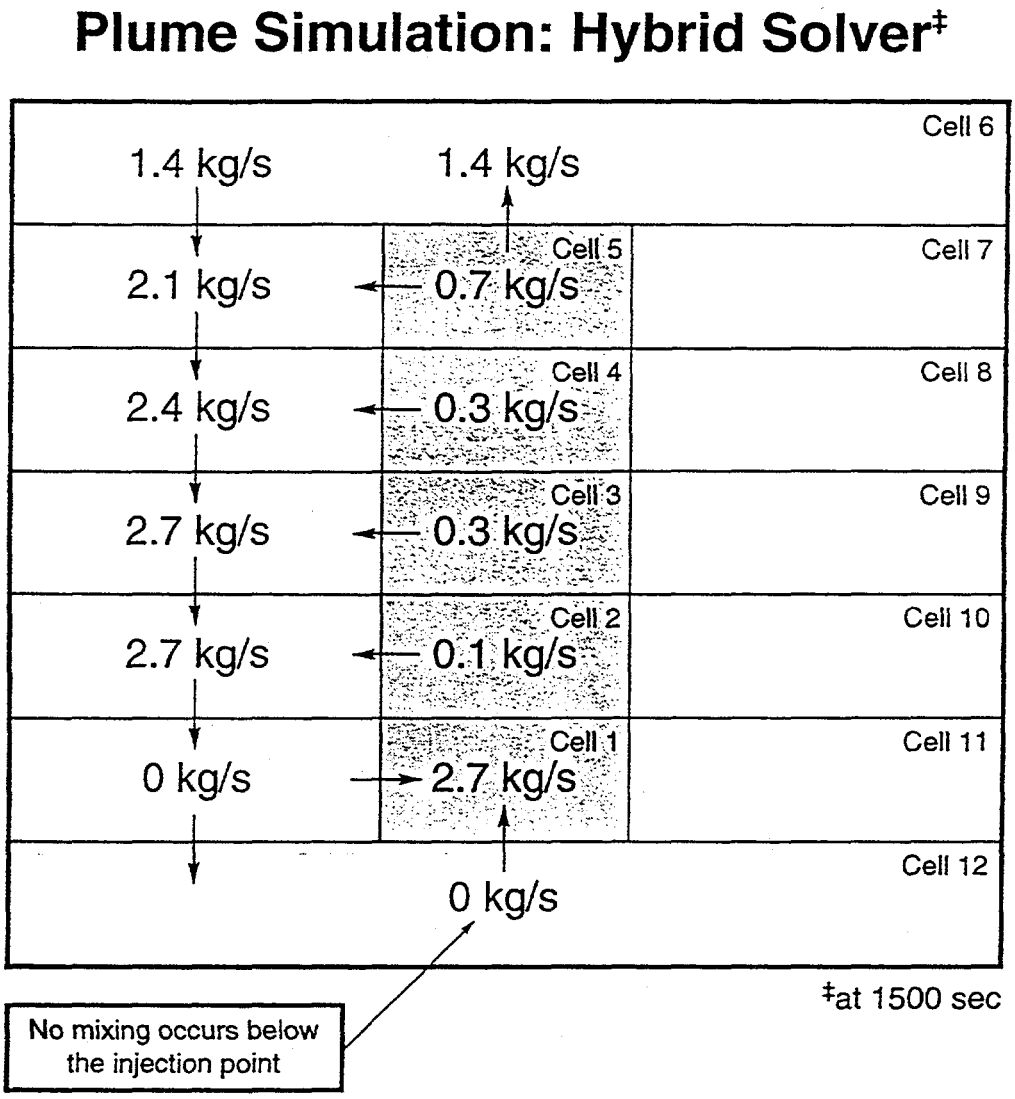

Figure 2.7. Flow patterns in the plume simulation resulting from the donor-density formulation.

whereas this entrainment is absent at the time shown with the hybrid formulation. The flow patterns in the hybrid solver case are consistent with the fact that nitrogen should accumulate above the injection point and form a stable stratification. (One should note that in the hybrid case at 1500 seconds the gas density at the source level in cell 11 is 1.19551 kg/m^3 and below the injection in cell 12 it is 1.19632 kg/m^3. Therefore, the density difference does not have to be large for the stability to manifest itself in the hybrid solver. Note, however, that the density difference is large enough at this time that one can neglect metastable density gradient effects.)

The correct flow patterns for a plume may be calculated from an asymptotic free plume correlation. The term "asymptotic" in this case refers to a plume which has evolved over a sufficient distance that entrance conditions no longer affect the plume behavior. The term "free" implies that there is sufficient distance from vertical confining boundaries, if any, so that the entrainment rate is not affected by those boundaries. The correlation, valid for round plumes that are only slightly less dense than the surrounding gas, has the form[Blev84]:

$$Q = 0.15B^{1/3}z^{5/3}$$
$$D = 0.22z \qquad (2\text{-}12)$$

where Q is the volumetric flow rate of the plume, D is its effective diameter, z is the vertical rise relative to an extrapolated zero, and B is the buoyancy factor, given by

$$B = Q_0 g(\rho_a - \rho_0)/\rho_a$$

where Q_0 is the volumetric flow rate of the injected material, ρ_a is the density of the ambient gas surrounding the plume, and ρ_0 is the density of the injected material. Equation (2-12) allows the calculation of mass flow rates, using a zeroeth-order constant density assumption for the surrounding gas and plume material.

An important aspect of plume behavior is the behavior of the entrainment flow, which is the flow of gas surrounding the plume to replace gas entrained into the plume. The classic picture of this entrainment is that it occurs into the sides of the plume, as a result of shear between the plume and the surrounding gas. For a round vertical plume, the entrainment velocity is therefore defined as the horizontal time-averaged velocity of the surrounding gas toward the plume, defined at the plume-gas interface. (Apparently, any surrounding gas acquiring a significant vertical time-averaged velocity as a result of shear with the plume can be considered to good approximation to be already

incorporated into the plume.) Presumably, this classic picture of entrainment into the sides of the plume neglects entrance effects, which might result in some entrainment flow from below. However, such effects are typically weak and will be ignored in discussions below of correct plume behavior.

The steady-state entrainment mass flow rates that should be present at the central column radial boundaries on the basis of the above asymptotic correlation are given in Figure 2.8, assuming that the entrainment velocities are horizontal. In calculating the flow rates, it has also been assumed that the plume is contained entirely within the central column. This assumption is consistent with the plume width, which goes approximately as 0.22z, and the rise height of the column. Note that the plume is not assumed to be well-mixed within the center column, since that assumption would be inconsistent with the correlation for plume width, but the plume is assumed to contribute all of the indicated upward flow. By comparing Figure 2.6 with Figure 2.7, we see that the average-density formulation incorrectly predicts substantial entrainment from below. Also, by comparing Figure 2.7 with Figure 2.8, one can see that the hybrid solver, while eliminating the entrainment from below, erroneously predicts the entrainment flow to be directed almost entirely into the source cell (cell 1). As seen in Figure 2.8, the entrainment flow should actually increase with plume elevation.

Thus, there are two distinct aspects to the problem of plume simulations with a control volume code: the spurious entrainment from below that is illustrated above with the average-density formulation, and the incorrect spatial distribution of the entrainment flow into the sides of the plume that is illustrated above with both gravitational head formulations. The effects of this incorrect spatial distribution are discussed in the next section.

2.4. Applicability of the Hybrid Solver Formulation to Stratifications

This section summarizes what can and can not be expected from the implementation of the hybrid solver. The hybrid solver addresses the treatment of gravitational heads developed within flow paths, with the intent of improving the treatment of stable stratifications created by plumes or low-velocity buoyant jets. However, other fundamental modeling limitations with respect to stratifications still exist in CONTAIN, and these may prevent the proper treatment of stratifications. The principal limitations are: (1) the assumption that momentum convection within a control volume can be neglected, (2) the lack of a proper entrainment or mixing model for plumes, jets, and shear layers, (3) the lack of thermal conduction or molecular diffusion modeling across gas-gas interfaces. The impact of these limitations is discussed below.

A standard assumption made in a control volume code like CONTAIN is that momentum convection within a control volume can be neglected. Thus, CONTAIN is limited to situations in which momentum convection does not play a dominant role. This clearly places constraints on the type of

Plume Simulation: Mixing Correlations

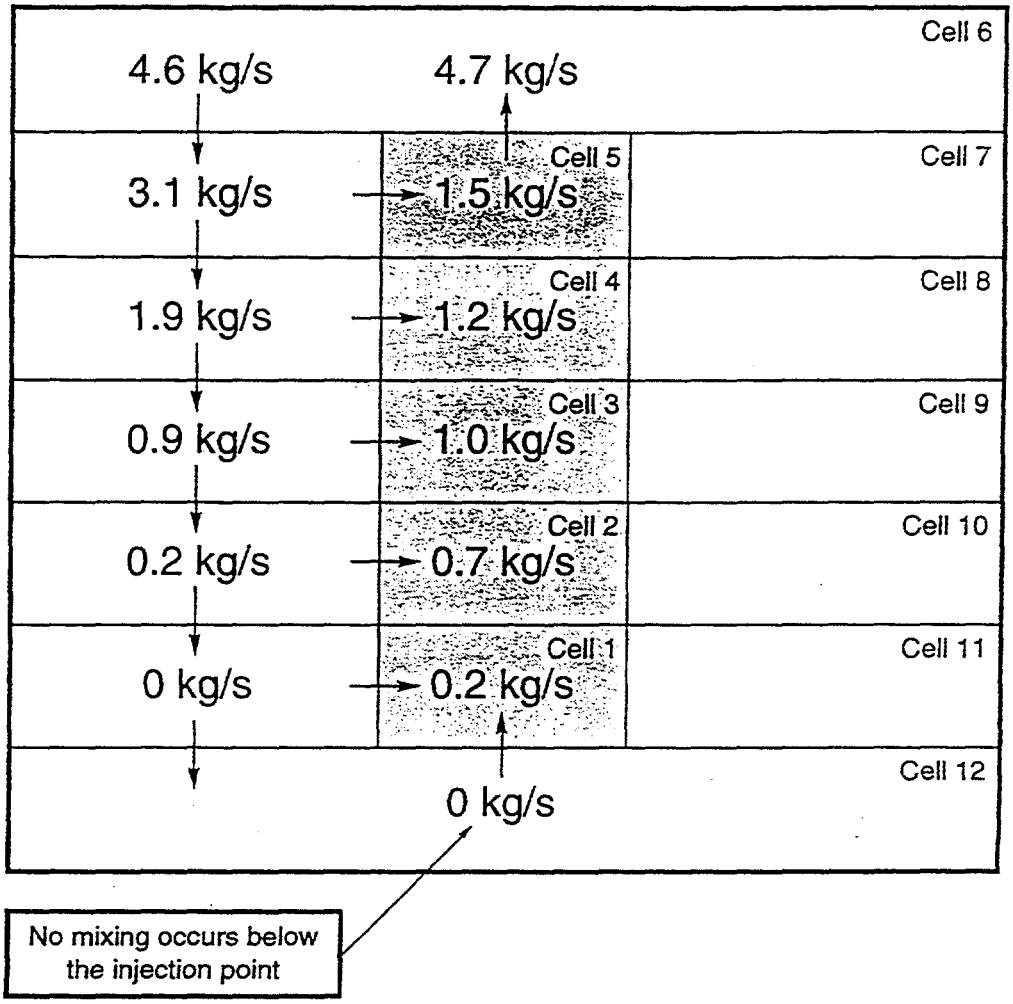

Figure 2.8. Flow patterns expected in the plume simulation on the basis of plume correlations.

stratification that can be modeled. In particular, stratifications created by buoyant high-velocity jets may be unstable with respect to the momentum convection carried by the jet[Pete94,Hiha95]. In the unstable case, recirculating flows become localized near the jet and the downflow carries the buoyant material below the injection point of the jet. Highly unstable behavior clearly cannot be modeled. To assess the hybrid solver with respect to marginally unstable stratifications, in Section 3.2 we give code comparisons to an experiment, Surtsey ST-3[Blan95], in which a marginally unstable stratification was created.

Of the many types of stratifications of interest in containment analysis, stratifications generated within enclosures by nearly free plumes or buoyant jets have been studied in detail[Pete94]. Nearly free plumes or jets by definition are those for which the entrainment of surrounding gas into the plume or jet is not significantly affected by the presence of vertical confining walls. This requires that the plume or jet occupy a small part of the cross-section of the containment[Hiha95]. Reference Pete94 discusses the formation of such stratifications in detail, including the conditions under which the stratification is stable with respect to momentum convection. Considerable simplification in the treatment of this type of stratification is possible provided it is stable and provided the residence time of the buoyant material within the plume or jet is short compared to the time scale of interest. In this case, the conditions of primary interest are not those in the plume or jet but are related to the buildup of buoyant material and/or temperature in the surrounding gas.

It can be shown[Pete94] for plumes or low-velocity buoyant jets of relatively small cross-section that the buildup can be treated as one-dimensional, accumulating at the penetration height of the plume or jet and working downward, and that it moreover can be predicted through integral entrainment correlations, without need for detailed modeling of the transport processes and conditions within the plume or jet. An example of such an integral correlation is provided by Equation (2-12). Additional simplifications occur for a stratification that satisfies the conditions described above, when the stratified layer has worked its way down to the injection elevation of the plume or jet. We call this a fully developed stratification. At this point the conditions between the penetration height and the injection point become essentially well-mixed. Thus, if the length of time required for the stratified layer to work down to the injection point is also short compared to the time scale of interest, a proper entrainment model may not be needed. Note that the resulting stratified layer can extend below the injection point if the pressurization effect of the plume or jet is sufficiently large. However, such an extension for a stable stratification arises from compression effects, i.e., a piston-like downward motion, rather than an extension below the injection point of the recirculating entrainment flow above the injection point. Code comparisons to an experiment, NUPEC M-8-1[OECD94], with a fully developed stratification are given in Section 3.1.

Proper entrainment rate modeling, as well as modeling for the other omitted phenomena listed above,

may be important when one does not have a stable, fully developed stratification. In cases in which the stratification is formed by a nearly free plume or jet and is stable but not yet fully developed, modeling the behavior of the stratification requires modeling of the rate and spatial distribution of the entrainment of surrounding gases by the plume or jet. Released versions of CONTAIN do not have such models for plume or jet entrainment. However, as described in Section 3.3.4, in one sensitivity calculation done for the HDR E11.2 experiment, we modified the code to treat a steam plume as a separate entity from the surrounding gas within a control volume and used a plume entrainment correlation to calculate the entrainment rate of the gas into the plume.

In the absence of such special code modifications, when a portion of a plume or jet is present within a control volume, it is simply assumed to be well-mixed with the surrounding gases in that control volume. The impact of the lack of a proper entrainment model for a nearly free plume can be examined by comparing Figures 2.7 and 2.8, which show the convection patterns set up in a CONTAIN simulation of a buoyant plume using the hybrid solver and those obtained from a plume correlation, respectively. The differences in the flow rates between these figures imply that significant distortions in the driving pressures and in the transient gas distributions are present in the CONTAIN simulation. As discussed below, the distortions in the driving pressures can also adversely affect the stability of the stratification.

We next consider the stability, within the framework of a control volume treatment, of a stratification that is in the process of being formed by a buoyant source. A useful criterion can be derived by considering the horizontal entrainment flow per unit area W/A into the source cell, as indicated in Figure 2.9. It is of interest to know when the gas just below the source cell is stable against participation in the recirculating entrainment flows occurring above the source elevation. This criterion can be derived by considering the conditions required to cause the recirculating flow to branch below the source cell, along the path indicated by a question mark in Figure 2.9. We assume that a light gas layer with density ρ_1 is present over a heavy gas layer with density ρ_2, as a result of source buoyancy and the recirculating flows above the source. Note that ρ_1 is the density present at the source cell level outside of the source cell. Within the well-mixed assumption, the source cell density itself would be somewhat less than ρ_1. The driving pressure difference causing the flow to branch is the same as that generating the entrainment mass flow per unit area, W/A, in Figure 2.9. For stability against recirculating flows below the source, this pressure difference must be less than the overall gravitational head ΔP_g required to move the lighter gas with density ρ_1 downward and the denser gas below the source with density ρ_2 upward. When this pressure difference is expressed in terms of flow rates and loss coefficients, the stability condition required to prevent recirculating flow below the source elevation can be expressed as:

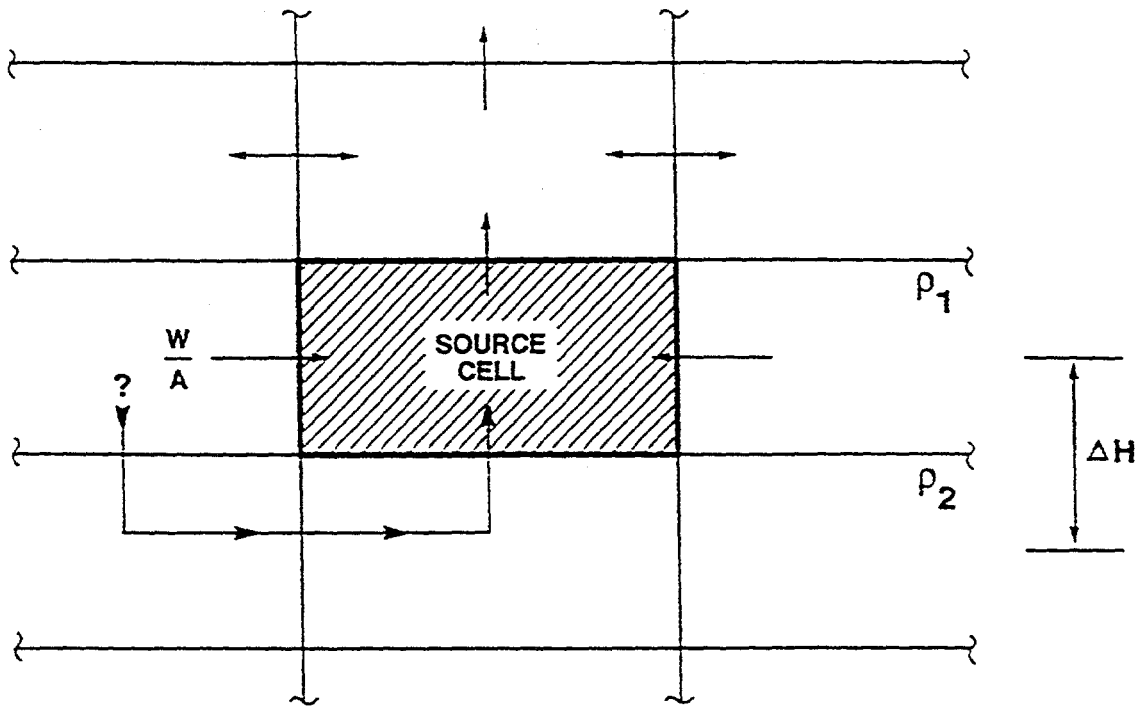

Figure 2.9. Identification of the quantities involved in the control volume stability criterion, under conditions of buoyant gas injection.

$$\left(\frac{W}{A}\right)^2 \frac{c_{FC}}{\rho_1} \leq \Delta P_g \tag{2-13}$$

where c_{FC} is the loss coefficient for the flow W shown in Figure 2.9. ΔH is the vertical separation (assumed to be uniform) of the cell centers between the source cell level and the level below. For sufficiently large density differences ($\delta > 2\epsilon$, as indicated in Equation (2-7)) and under quasi-steady-state conditions, the gravitational head within the default hybrid solver formulation may be evaluated using donor densities over a vertical span equal to the cell-center separation. This leads to the result

$$\left(\frac{W}{A}\right)^2 \frac{c_{FC}}{\rho_1} \leq 2g(\rho_2 - \rho_1)\Delta H \tag{2-14}$$

The right hand side of this equation is positive under the conditions described. In contrast, it should be noted that if the average-density treatment is invoked through the MSTABLE keyword, the right hand side of Equation (2-13) can be shown to be negative, because of the fact that the source cell density is less than ρ_1 with a buoyant source within a well-mixed assumption. Therefore, stability against recirculating flows below the source is never achieved. Note that the recirculating flow below the source can be eliminated in this case only by using a nodalization that eliminates the possibility of recirculating flows at the source level and above. Equation (2-14) will be referred to below as the control volume or *de facto* condition for stability with the hybrid solver, to distinguish it from the condition for stability of a stratification against the momentum convection carried by a high velocity buoyant jet[Pete94,Hiha95]. The *de facto* condition, of course, is derived within a control volume treatment neglecting momentum convection and therefore applies primarily to pressure or buoyancy-driven flow in compartmentalized or channeled geometries. For a nearly free plume, the physical significance of the loss coefficient in Equation (2-14) may not be obvious, but as we discuss below, Equation (2-14) is almost always satisfied in that geometry for any reasonable value of the loss coefficient. This is consistent with the well-known fact that a plume is almost always stable[Pete94].

It should be noted that the *de facto* stability criterion depends on the entrainment flow rate W at the source cell level. As discussed above, in situations involving nearly free jets or plumes, the well-mixed assumption causes considerable distortions in the distribution of the entrainment flow. Consequently, the *de facto* stability of a stratification may also be distorted. To see how much the stability criterion of Equation (2-14) could be affected by lack of an entrainment model, one should compare the mass flow rate W into the source cell in Figure 2.7 against the much smaller corresponding mass flow rate in Figure 2.8 from the asymptotic plume correlation. In the case of a nearly free plume, one would conclude that because of the lack of an appropriate plume entrainment model, the hybrid solver could have difficulty predicting a stable stratification.

Fortunately, even with the distortions introduced by the lack of an appropriate plume entrainment model, the *de facto* stability criterion appears to be easily satisfied, at least for configurations with the unrestricted entrainment flow areas consistent with nearly free plumes. For example, for the conditions shown in Figure 2.7, the left hand side of Equation (2-14) is equal to 2.7×10^{-3} Pa and the right hand side, with $\rho_1 = 1.19551$ kg/m^3 and $\rho_2 = 1.19632$ kg/m^3, is equal to 4.8×10^{-2} Pa. Thus, even for the small density differences present in this example, stability is in no danger of being violated. For typical gas stratifications of interest in containment analysis, the right side of Equation (2-14) is typically two to three orders of magnitude larger than the left, for unrestricted entrainment flow areas and flow loss coefficients of order unity.

Up to now, we have been discussing stable stratifications formed by nearly free plumes and buoyant jets. However, a nearly free plume or jet represents only one limiting case, in which confining vertical

walls do not significantly affect the entrainment rate of the surrounding gas into the plume or jet. The other limit, in which confining walls severely affect the entrainment rate, is also of interest in containment analysis. The simple case in which the confining walls correspond to the enclosure vertical boundaries has been discussed in Reference Hiha95. However, the confining walls could also be those of a subcompartment. The possible subcompartment geometries and effects on stratification depend on plant and primary system break geometry and are therefore highly varied. It should be obvious, however, that subcompartment effects could affect stratification behavior considerably through flow channeling, flow splitting, and momentum dissipation effects.

The initial preheat period of the HDR E11.2 experiment provides an example of a case in which "subcompartment" effects apparently affected the stratification behavior. As discussed in Section 3.3, in a calculation in which the stability associated with nearly free plume behavior was achieved during the preheat, the agreement with experiment with respect to pressures and steam concentrations worsened considerably. The absence of plume-like stability during the preheat is attributed to the fact that horizontal entrainment flow areas into the source cell were highly restricted in that experiment, a condition that forced entrainment flow from below and lead to an interesting buoyancy-driven loop-flow behavior.

To illustrate how this could happen, we consider what would happen when the behavior in Figure 2.8 is altered through imposition of a "subcompartment" effect: in this case, partial blockage of the flow areas between the central column and annulus in Figure 2.8, such as that between cells 1 and 11. We also assume that the central column is sufficiently tall so that the plume fills the central column cross-sectional area at the top of the column. As the degree of blockage is increased, one should see a change in behavior from plume-like to loop-flow behavior, which we define as recirculating flow through the central column cells, with uptake from below. Within a control volume treatment, this loop-flow behavior would begin at the point at which the stability criterion given by Equation (2-14) ceases to be satisfied. We can therefore consider such loop-flow behavior to be the "unstable" counterpart of plume-like behavior. Note that the amount of flow depends in general on the buoyancy generated in the central column cells, and this depends on the mixing length of the injected buoyant gas, defined as the rise height required for the injected gas to become well-mixed across the central column cross-sectional area.

The final point is that in some situations, particularly when a plume or jet is absent, the growth of a layer can be controlled by thermal conduction or molecular diffusion processes across the interface between two gas layers. For example, as discussed in Section 3.3, the slow downward growth of a cold, hydrogen-rich layer during the spray period in the HDR E11.2 experiment[Karw92] is believed to be the result of convectively enhanced molecular diffusion across the interface between the hydrogen-rich layer and the gas below. It is not clear how important this type of behavior is in

general. Since CONTAIN does not model gas-gas interfaces within a control volume, or thermal conduction or molecular diffusion across such interfaces between control volumes, such behavior cannot be modeled.

3. The Code Assessment Matrix

This section discusses code comparisons to three experiments that showed significant stratification. Results are given from both the hybrid formulation of gravitational heads, as implemented in CONTAIN 1.2, and the old, average-density formulation used in code versions prior to CONTAIN 1.2. In these comparisons, the results described as being from the "old solver" were obtained by using CONTAIN 1.2 with the MSTABLE option. The three experiments used in the present assessment are the NUPEC M-8-1 experiment[OECD94], the Surtsey ST-3 experiment[Blan95], and the HDR E11.2 experiment[Karw92]. The last experiment is perhaps best known as the basis of the ISP-29 international standard problem. The choice of experiments was dictated by the desire to demonstrate both the capabilities and limitations of the hybrid solver. The NUPEC M-8-1 experiment produced a classic stable, fully-developed stratification, for which, as explained in Section 2.4, the limitations of the hybrid solver are minimized. The last two experiments are less suitable for CONTAIN, in the sense that some key phenomena in the experiments are not modeled in CONTAIN. The Surtsey ST-3 experiment produced a highly stratified condition, but one that was marginally unstable against the momentum convection of the high velocity jet used to create the stratification. Since CONTAIN neglects momentum convection within a control volume, this instability is ignored, and the predicted behavior with the hybrid solver is expected to be too stable. In the HDR E11.2 experiment, the stratification behavior was extremely complex. During the early phases of the experiment, stratifications that could not be characterized as stable were created in the upper containment. The prediction of stratifications other than stable, fully developed ones generally requires an entrainment or mixing model, which is typically available only for idealized situations, such as a free plume. At late time, motion of a stratified layer interface thought to be controlled by a coupled convection/molecular-diffusion process was observed. This coupled process is also not modeled with respect to gas-gas interfaces in CONTAIN.

3.1. NUPEC Helium Mixing Test M-8-1

The NUPEC model containment is a 1/4 linearly scaled model of a 4-loop PWR containment as shown in Figure 3.1. A detailed discussion of the facility can be found in Reference OECD94. A series of tests were performed in the NUPEC 1/4-scale model containment to investigate the thermal hydraulics of co-injecting helium and steam into a containment with and without the operation of internal water sprays. The tests simulated severe accident conditions in a nuclear power plant under simplified conditions in which helium (as a nonflammable substitute for hydrogen) and steam were released into a containment. The purpose of conducting the test series was to determine the thermal-hydraulic response and the mixing behavior of helium injected into the containment and to provide data for code verification.

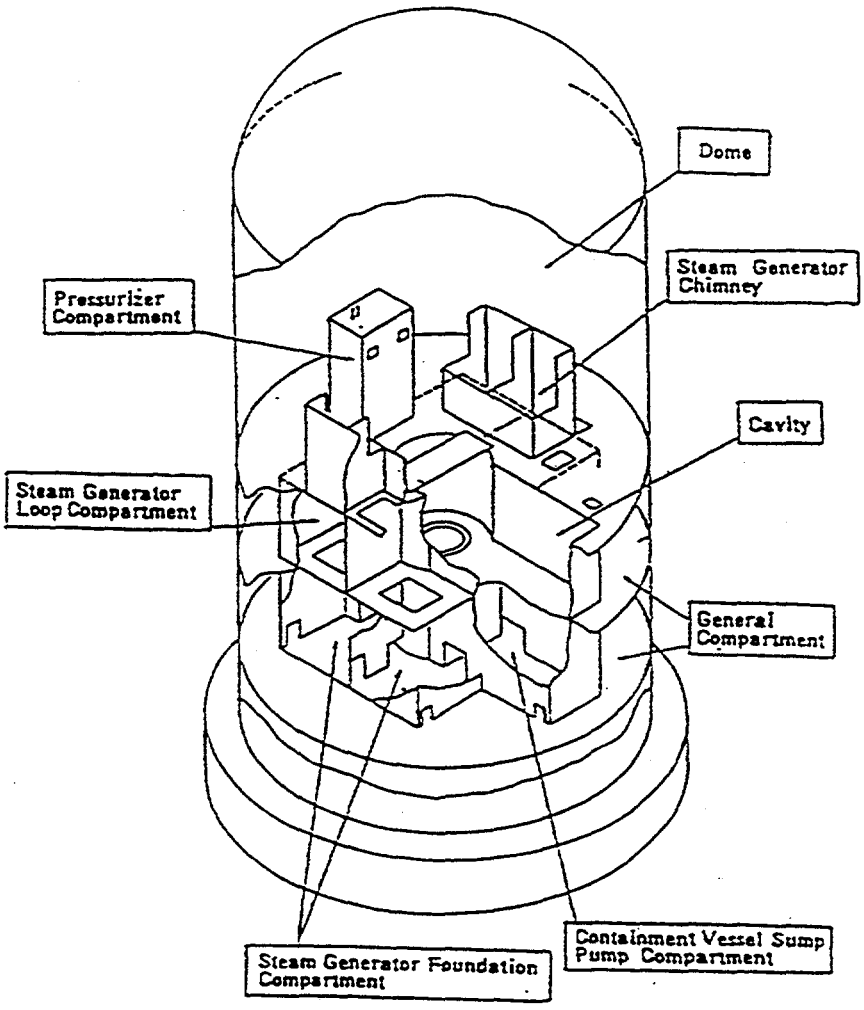

Figure 3.1. Schematic of the NUPEC 1/4-scale model containment[OECD94].

The NUPEC M-8-1 experiment was selected for the hybrid solver assessment because it was highly stratified and furthermore provided a classic example of a stable, fully developed stratification, as defined in Section 2.4. As discussed in that section, the limitations of the hybrid solver are minimized in the modeling of such stratifications.

The NUPEC facility is a domed cylinder, approximately 10.8 m in diameter, 17.4 m high, and 1310 m^3 in volume, as shown in Figure 3.1. The facility contains 28 compartments of which only 25 are interconnected. Of the 25 compartments that are interconnected, however, the dome compartment constitutes approximately 71% of the total containment volume. The containment is constructed entirely of steel. The containment shell and floors are 12 mm thick except for the first floor which is 16 mm thick. The compartment walls are 4.5 mm thick. The outside of the containment is covered with a layer of insulation which is itself covered by a thin metal sheet to protect the insulation from weather damage. The insulation around the cylinder and hemisphere are 125 mm and 150 mm thick, respectively. A water storage tank is located below the first floor of the containment so that condensate and spray water could drain. The water storage tank is separated from the rest of the containment by a 100 mm thick layer of insulation. The facility is equipped with a remote boiler to supply saturated steam to the facility, a helium supply at ambient temperature, and a mixing chamber in which the steam and helium are mixed before being co-injected into the facility.

Nine different series of experiments were performed. These experiments were performed to determine the convective mixing from gas density differences as well as from forced convection due to water sprays. The effect of different release locations was also investigated. Experiments were performed with the injection of helium and steam individually as well as together, with the injection of helium with water sprays, and with the injection of helium and steam with water sprays. The gases were injected in either a steam generator room or pressurizer relief tank room at the bottom of the containment or in the pressurizer room in the middle of the containment.

Test Series 1 through 7 included both integral and separate effects tests to investigate the factors contributing to the thermal-hydraulics with the source in the lower part of the containment. Test Series 8 repeated selected tests from Test Series 1 through 7 with the source in the pressurizer room, which is located just above the operating floor of the containment, as shown in Figure 3.1. In particular, test M-8-1 involved the release of helium and steam into the pressurizer room with the containment initially at ambient temperature and without actuation of the internal water sprays. This injection location lead to a stratification in the facility external to the pressurizer room, with the stratified layer interface located approximately at the openings at the top of the pressurizer room. It should be noted that the pressurizer room is closed at the bottom in the model, and therefore recirculation through the pressurizer room was not possible. Thus, the injection conditions with respect to the stratification external to the pressurizer room effectively were those at the top of the

pressurizer room.

The helium concentrations were sampled from the center of 24 rooms and at 5 locations in the dome. Samples were drawn through tubes, cooled, dried by passing through a desiccant, and analyzed by gas chromatography. Because of the gas sampling technique, the predicted results were normalized to the volume percentage of helium in dry air to compare to the data. Actual volume percentages of helium on a wet basis were reduced further by the presence of steam. The sample tubes were at the center of each room and the specific locations of each of the helium sample tubes are shown in Figure 3.2. The dome sample tube elevations were all above the source elevation.

The gas temperatures, wall temperatures, and stored water temperature were measured with approximately 200 Cr-Al thermocouples. Thermocouple locations are shown in Figure 3.3. The gas pressure was measured by a pressure gauge in the top of the dome. The steam and helium flow rates were measured by a differential pressure transducer across a venturi.

The gas pressure in the facility at the beginning of the experiment was approximately 101 kPa and the structure and gas temperatures were at room temperature (approximately 7 °C to 10 °C). At the beginning of the experiment, helium and steam were co-injected into the pressurizer room. The helium and steam mass flow rates were constant at 0.027 kg/s and 0.33 kg/s, respectively, during the 30 minute injection period. It was assumed that helium and saturated steam were injected into the containment at 10°C and 108°C, respectively. Because the pressurizer room is closed except for openings at the top, these openings determined the injection conditions into the rest of the containment. The Froude number $Fr = \rho_a U_0^2 / [g(\rho_a - \rho_0)D]$ of this injection was quite low. Based on the major flow path from the pressurizer room into the containment the Froude number is estimated to have been 0.08. Thus, plume-like behavior is expected, and the stratification in the containment is expected to have been quite stable against momentum convection.

A detailed description of the approach and models used in CONTAIN to analyze the M-8-1 experiment is given in Reference Stam95. A brief discussion of the 35-cell nodalization used in the current set of calculations is given here to facilitate interpretation of the results. A vertical cross-sectional view and two horizontal cross-sectional views of the 35-cell nodalization are shown in Figures 3.4 and 3.5. The interconnection of the cells is shown in Figure 3.6. The water storage tank, reactor vessel, and primary shield rooms (cells 26-28, respectively) are closed rooms and are not represented in Figure 3.6. The 35-cell nodalization basically uses one cell for each physical room except for the dome and the pressurizer room. To model gas circulation, the dome is subdivided into central and annular cells, and the pressurizer room is divided into 2 cells.

Calculations with the old and hybrid formulations have already been performed and reported in

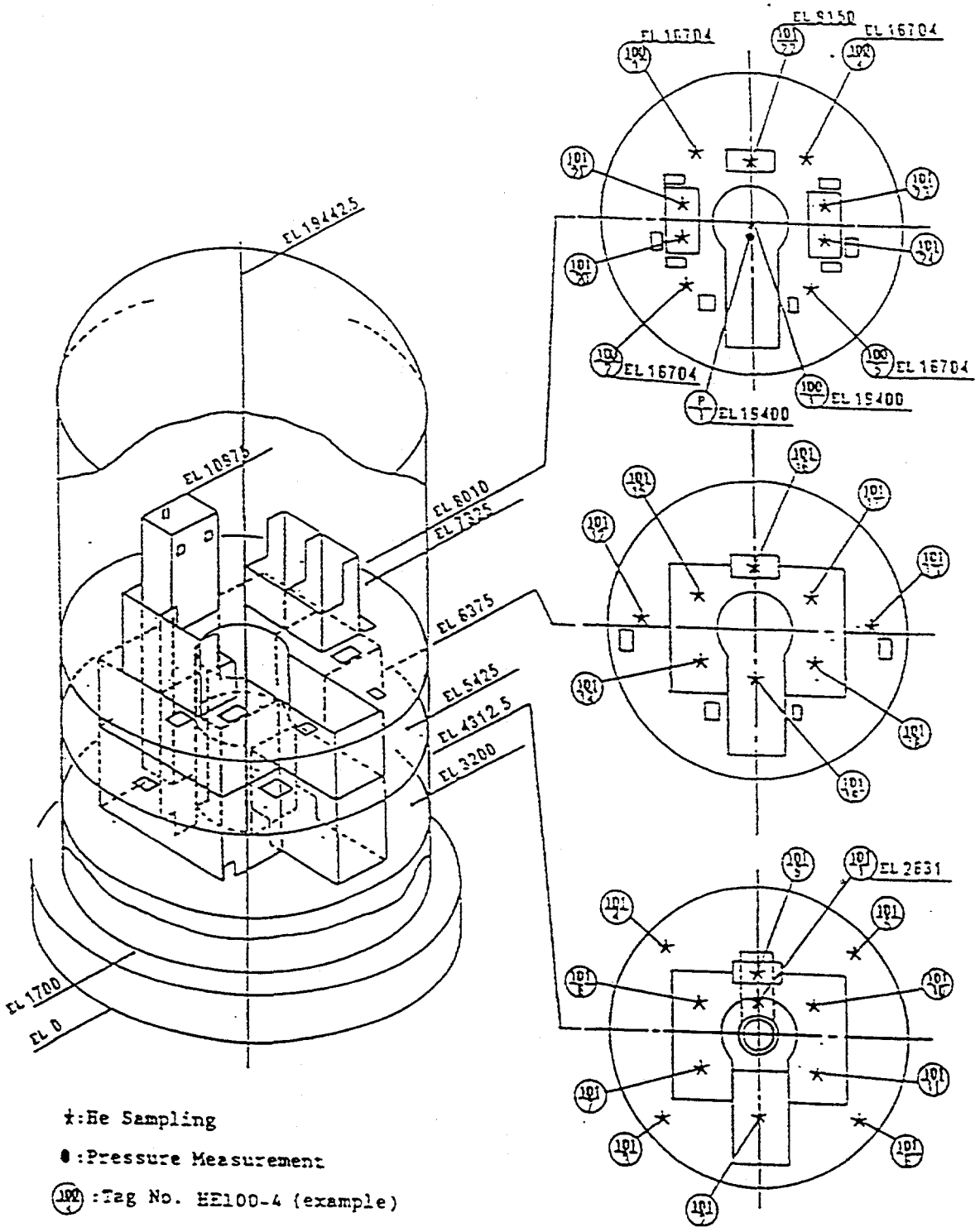

Figure 3.2. Location of the helium sampling locations and pressure measurement points in the NUPEC facility[OECD94].

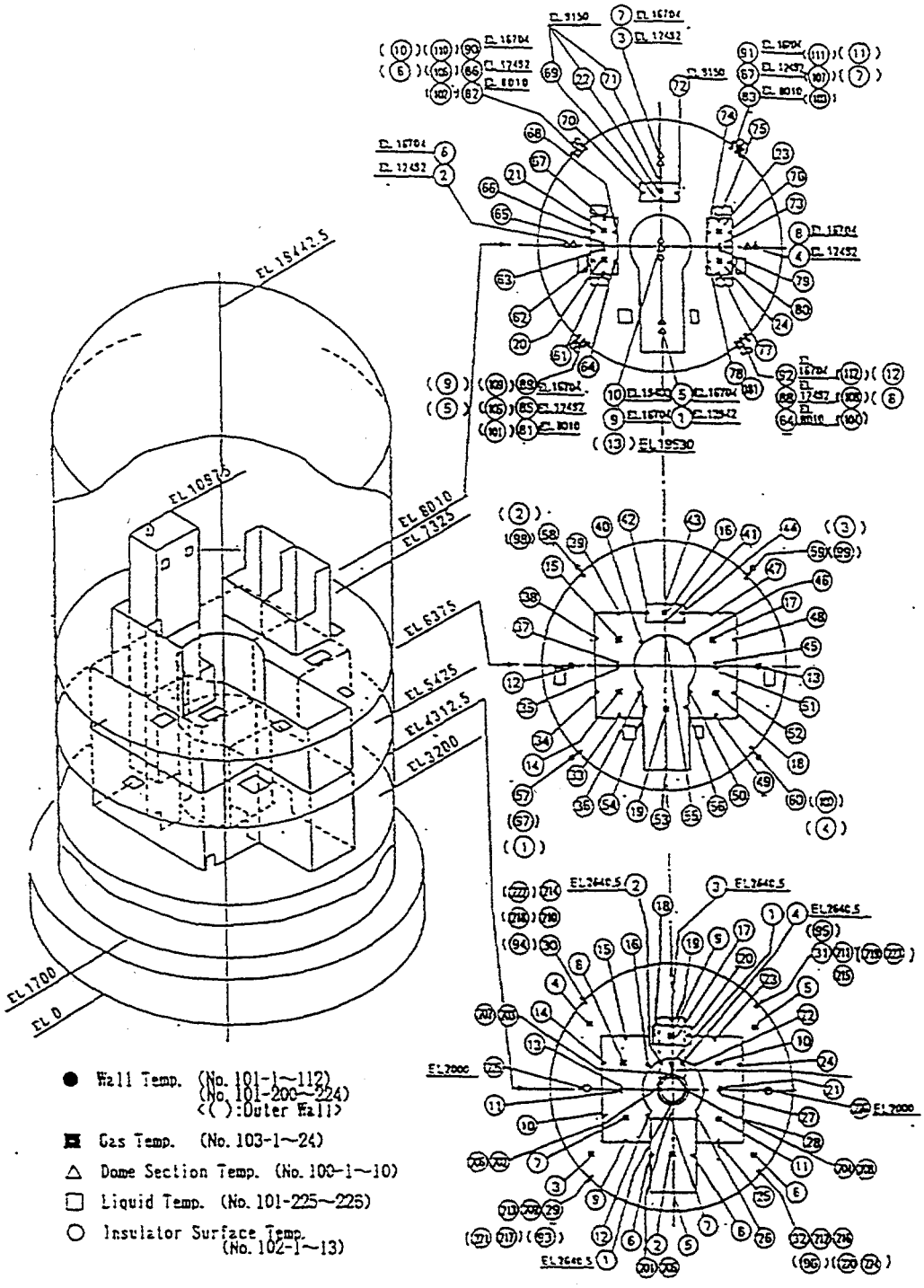

Figure 3.3. Location of the temperature measurement points in the NUPEC facility[OECD94].

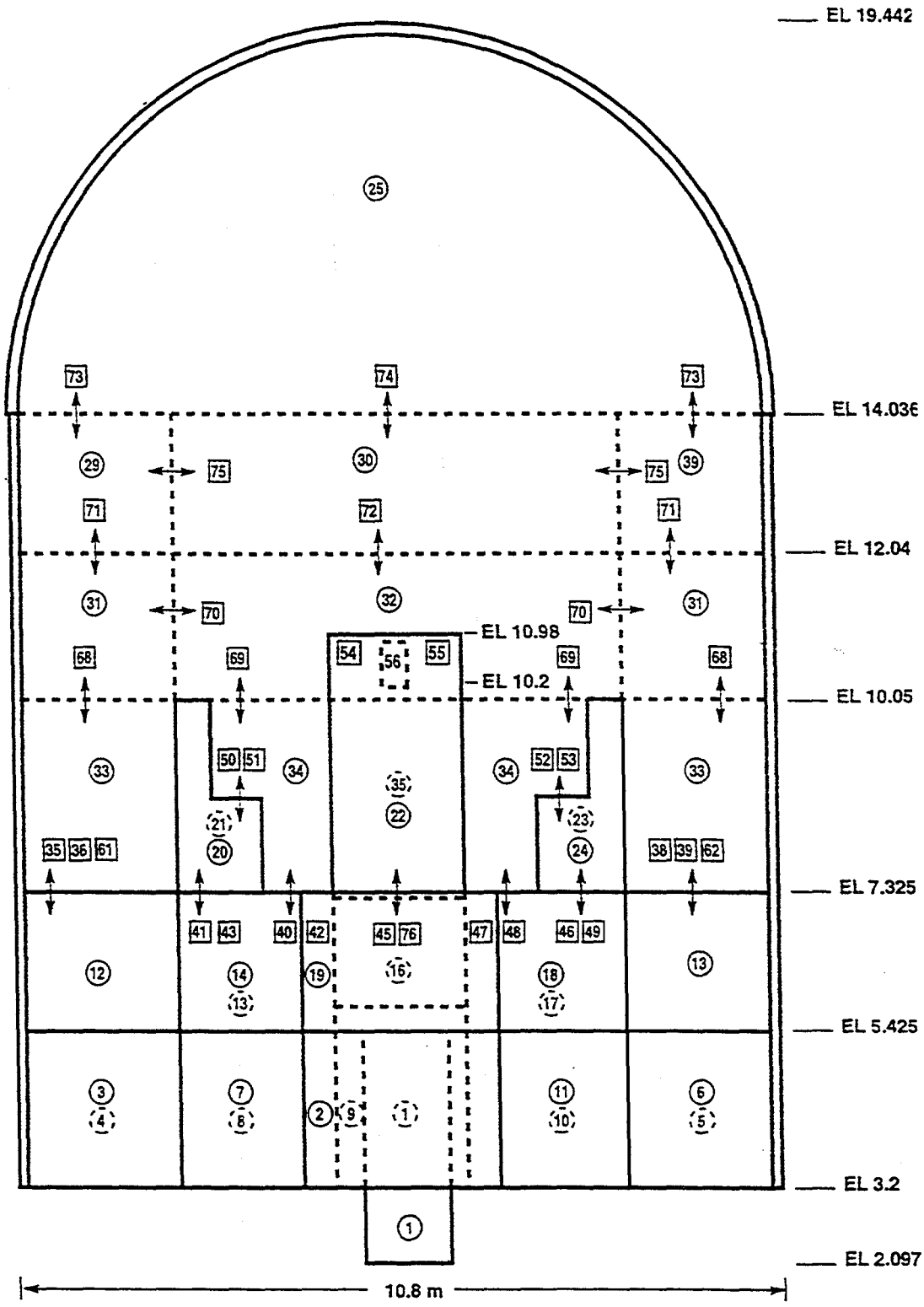

Figure 3.4. Vertical cross-sectional view of the CONTAIN 35-cell nodalization for the NUPEC facility.

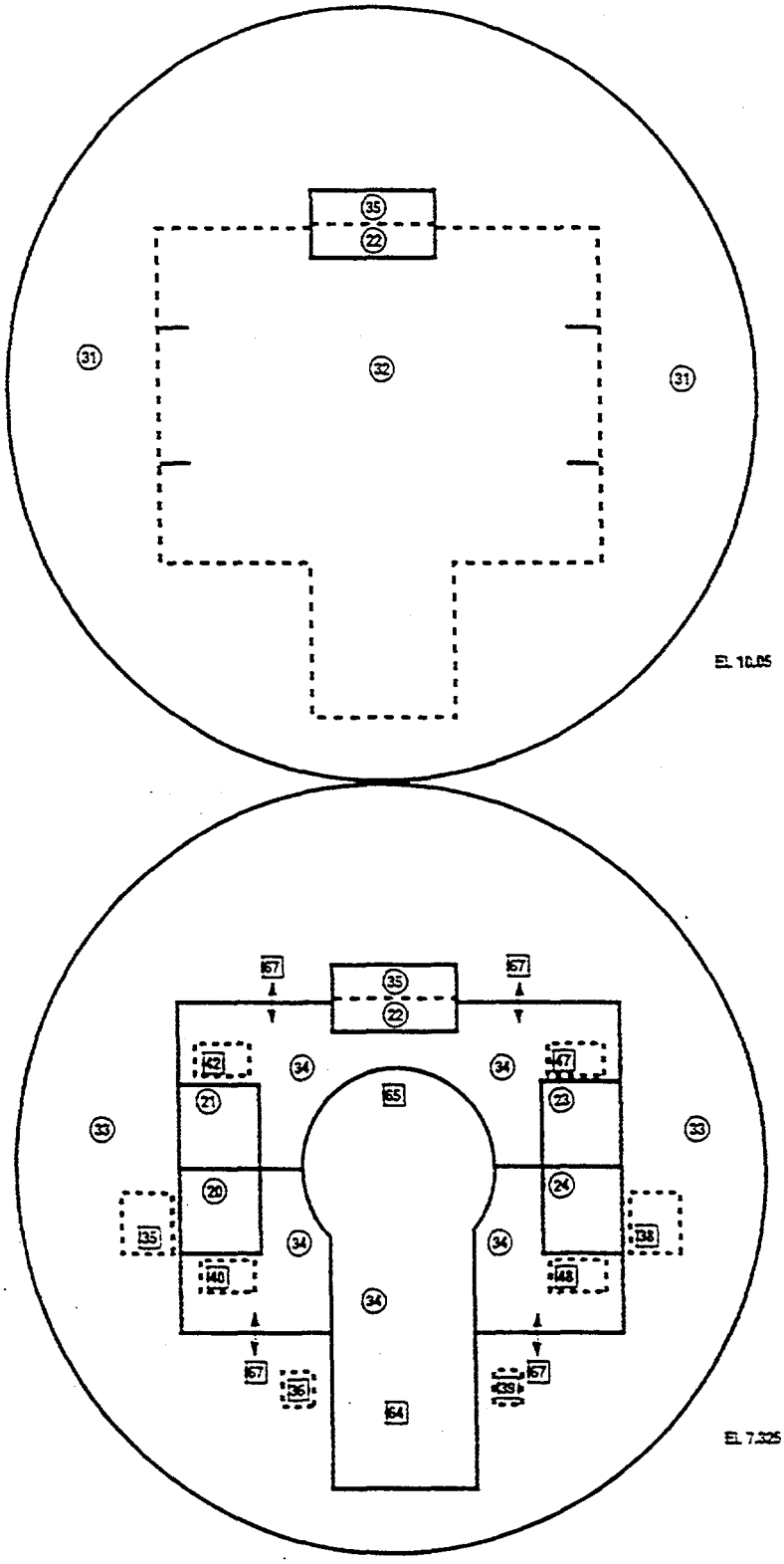

Figure 3.5. Horizontal cross-sectional view of the CONTAIN 35-cell nodalization for the NUPEC facility at (a) the 10.05 m elevation and (b) the 7.325 m elevation.

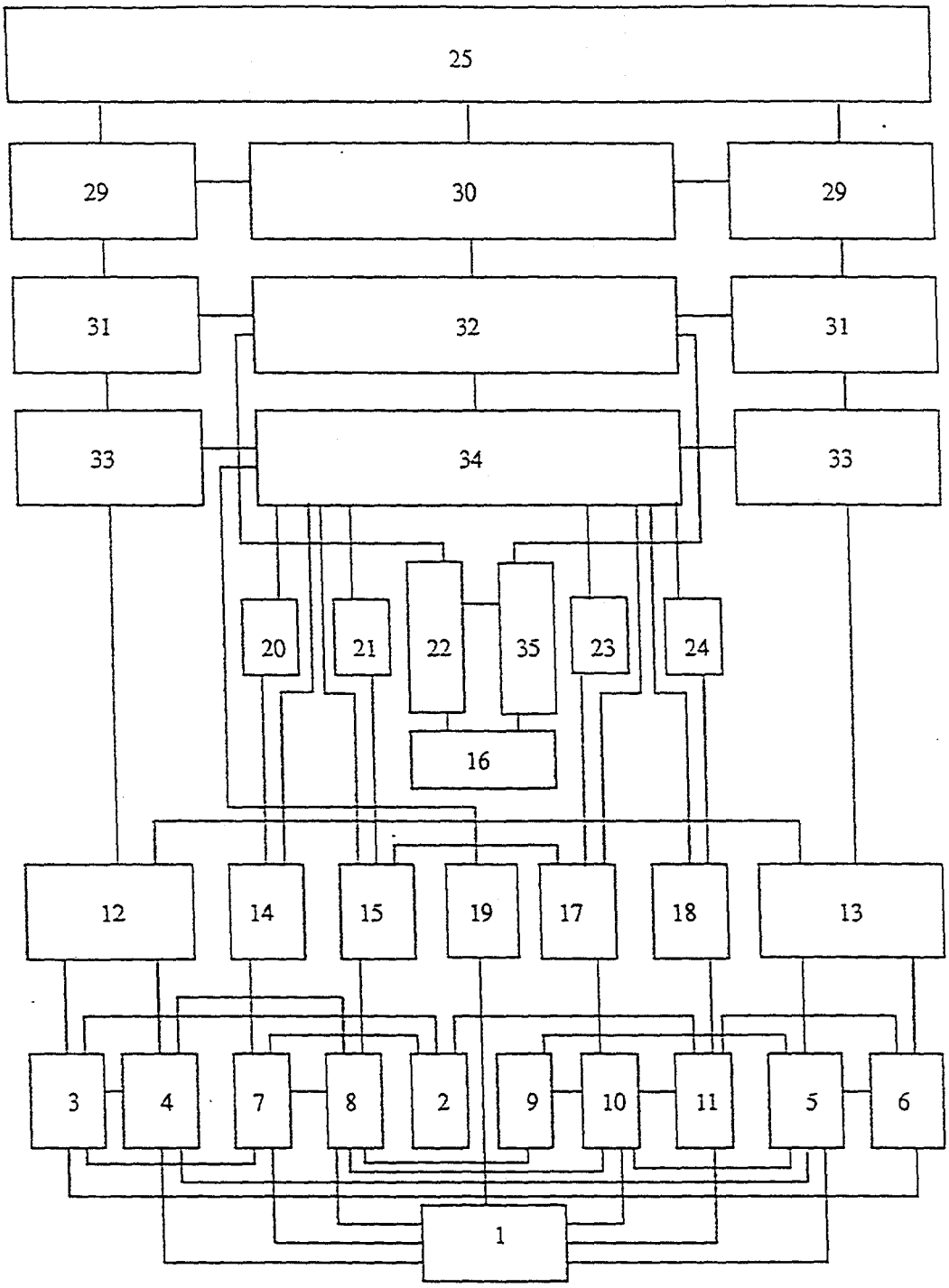

Figure 3.6. Block schematic of the 35-cell nodalization for the NUPEC facility showing cells and flow paths.

Stam95. These results have been recalculated with CONTAIN 1.2. Note that the predicted helium concentrations presented here are in a somewhat different format than that in Reference Stam95. The results in Reference Stam95 were reported according to the original ISP-35 specification[OECD94] for the helium concentrations, whereas the present concentrations are reported according to the conventional definition for dry concentrations. Apparently, the conventional dry definition is the more appropriate one to use.[2]

The M-8-1 experiment provides a classic example of a stable, fully developed stratification, for which, as discussed in Section 2.4, the limitations of the hybrid solver are minimized. There are at least two reasons for concern *a priori*. First of all, as shown by comparing Figures 2.7 and 2.8, the hybrid solver does not predict the spatial distribution or amount of entrainment into the plume correctly. At the start of injection, the plumes entering the containment dome region from the pressurizer room will tend to collect first at the top of the containment, with the resulting stratified layer interface working its way down to the injection elevation with time. In contrast, the differences between Figure 2.7 and 2.8 indicate that the hybrid solver will tend to mix the entire region above the pressurizer room openings from the beginning. It should be noted that the results show good agreement between the hybrid solver predictions and the measurements, particularly at early times. This indicates that the period of time required for attainment of a well-mixed condition above the source was relatively short. (In the CONTAIN calculation, this mixing time was about 30 seconds.) Secondly, on the basis of Equation (2-14), one might expect the stratifications predicted by the hybrid solver to be initially unstable, when density differences are small. In the above comparisons, there is no sign of initial instability in the hybrid solver predictions. As indicated by the discussion in Section 2.4, for a nodalization like that in Figure 3.6, with a source cell (effectively, cell 32) that is an open volume, one would expect stability to be present with any significant gas buildup.

With respect to the helium concentrations and gas temperatures, the results are organized according to distance from the center of the containment, using inner, middle, and outer vertical columns of rooms. The inner rooms are in the center of containment, the middle rooms are in line with one of the steam generator towers, and the outer rooms are adjacent to the containment shell.

The pressures calculated with both the old and hybrid formulations are presented and compared with the measured pressures in Figure 3.7. The predicted helium concentrations in the containment for a middle column of rooms are compared with the measurements in Figures 3.8 and 3.9 for the old and hybrid solvers, respectively. The predicted and measured gas temperatures similarly presented in Figures 3.10 and 3.11. The predicted pressures and temperatures are quite similar to those in Reference Stam95. The helium concentrations would also be quite similar if they had been reported

---

[2]H. Tezuka, Systems Safety Department, NUPEC, private communication, 1996.

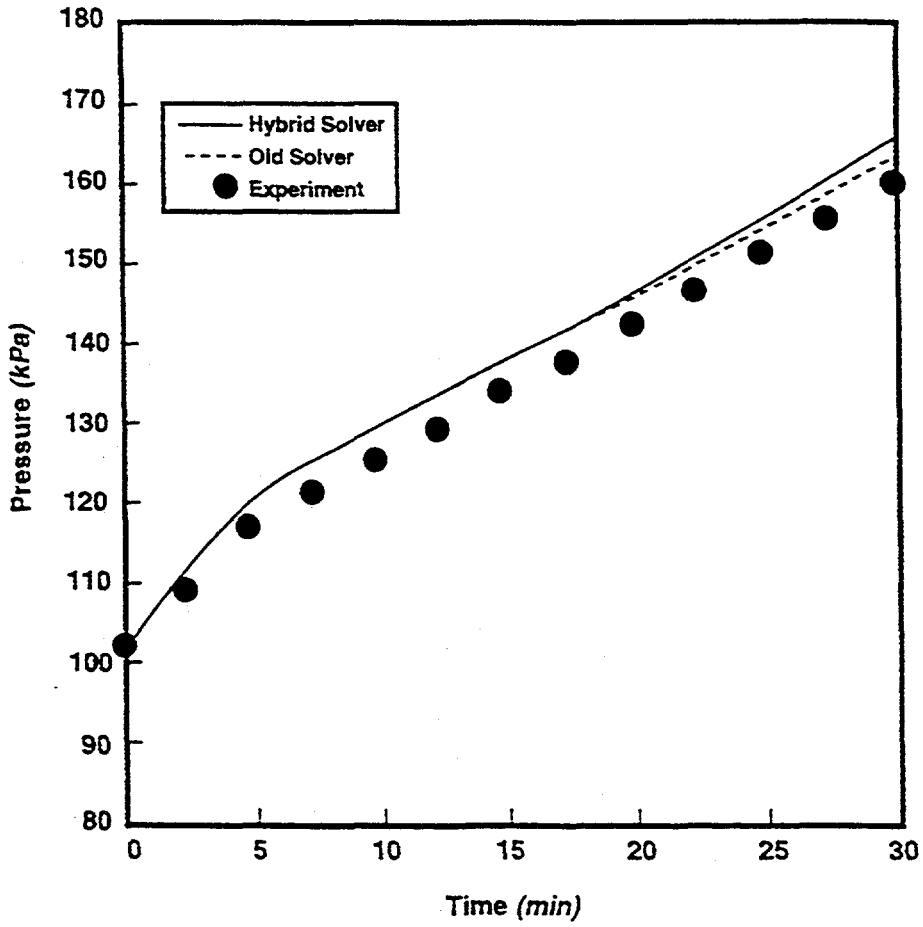

Figure 3.7. Comparison between the predicted pressures in the NUPEC facility for test M-8-1 and the experimental data[OECD94].

in the same format as that reference. Thus, we will present only a summary of the results.

With regard to the predicted stratification behavior, the differences between the old and hybrid solvers may be summarized through the helium concentration and temperature profiles at the end of the 30-minute source injection period. These are presented in Figures 3.12 through 3.17. The predicted concentrations and temperatures are displayed in a stepwise manner because each cell is assumed to be well-mixed. The vertical profile predicted by both of the formulations are compared to the data, which is represented by the open symbols. The symbols are plotted at the elevations where the data were taken.

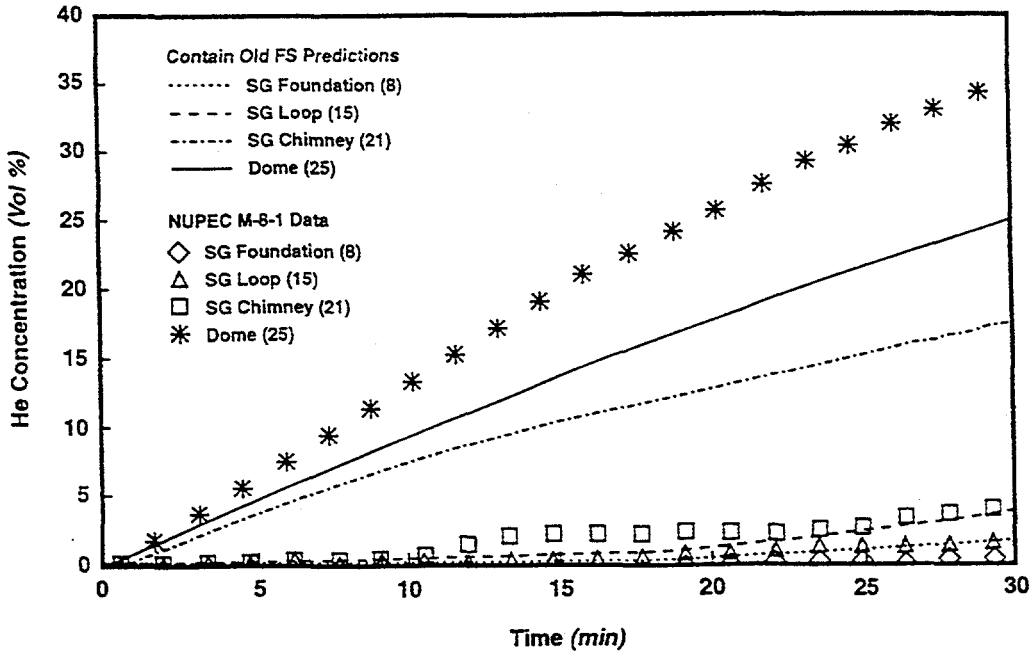

Figure 3.8. Comparison between the helium concentrations predicted by the old gravitational head formulation in a middle column of rooms in the NUPEC facility and the experimental data for test M-8-1[OECD94].

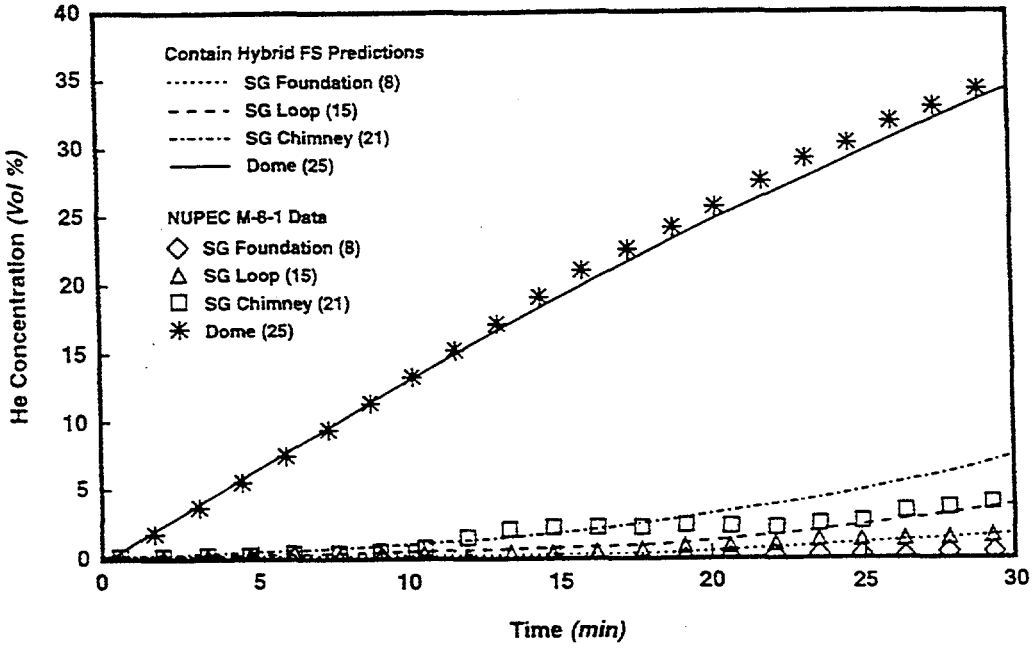

Figure 3.9. Comparison between the helium concentrations predicted by the hybrid gravitational head formulation in a middle column of rooms in the NUPEC facility and the experimental data for test M-8-1[OECD94].

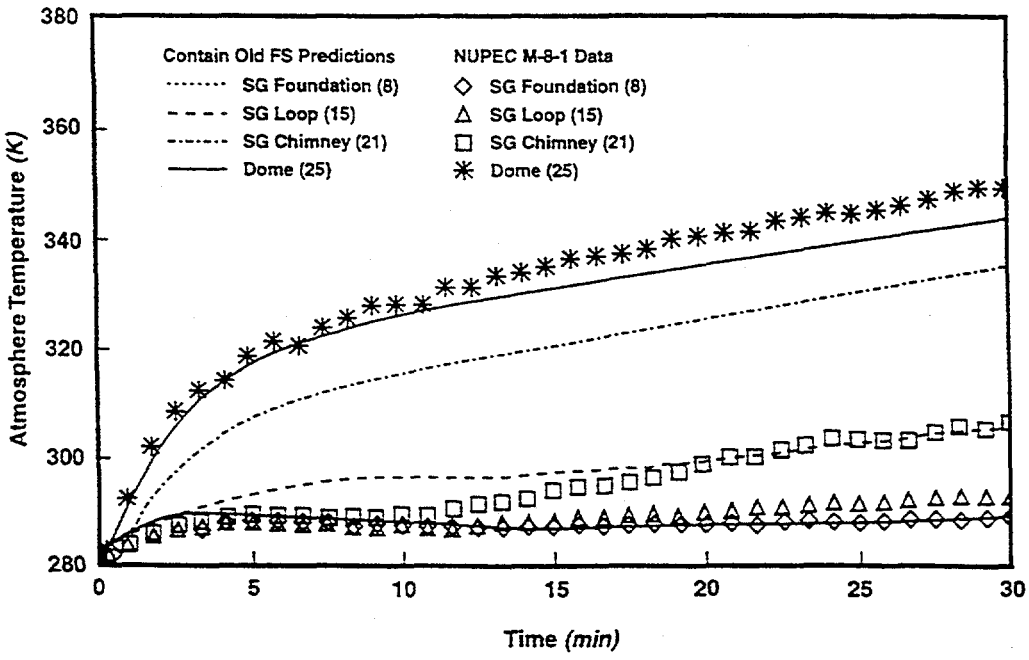

Figure 3.10. Comparison between the gas temperatures predicted by the old gravitational head formulation in a middle column of rooms in the NUPEC facility and the experimental data for test M-8-1[OECD94].

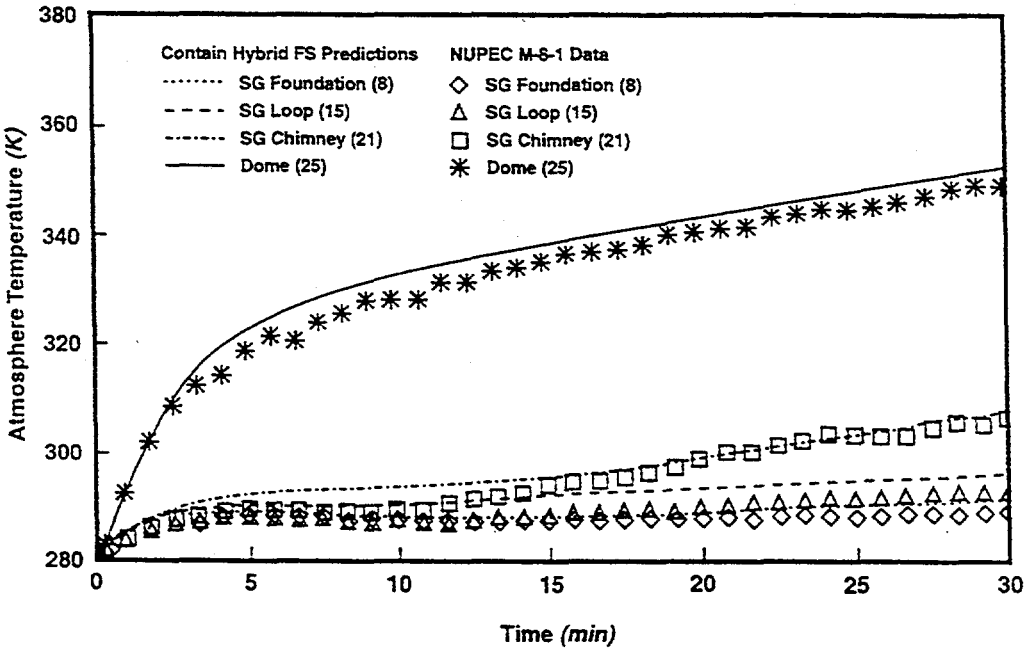

Figure 3.11. Comparison between the gas temperatures predicted by the hybrid gravitational head formulation in a middle column of rooms in the NUPEC facility and the experimental data for test M-8-1[OECD94].

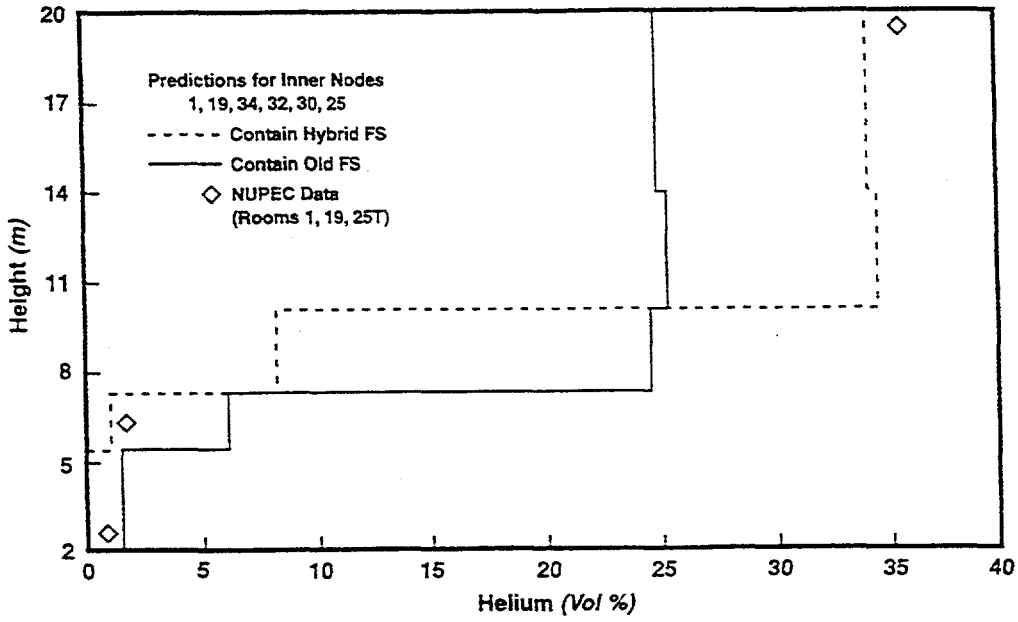

Figure 3.12. Comparison between the predicted helium distribution in an inner column of rooms in the NUPEC facility for test M-8-1 and the experimental data[OECD94].

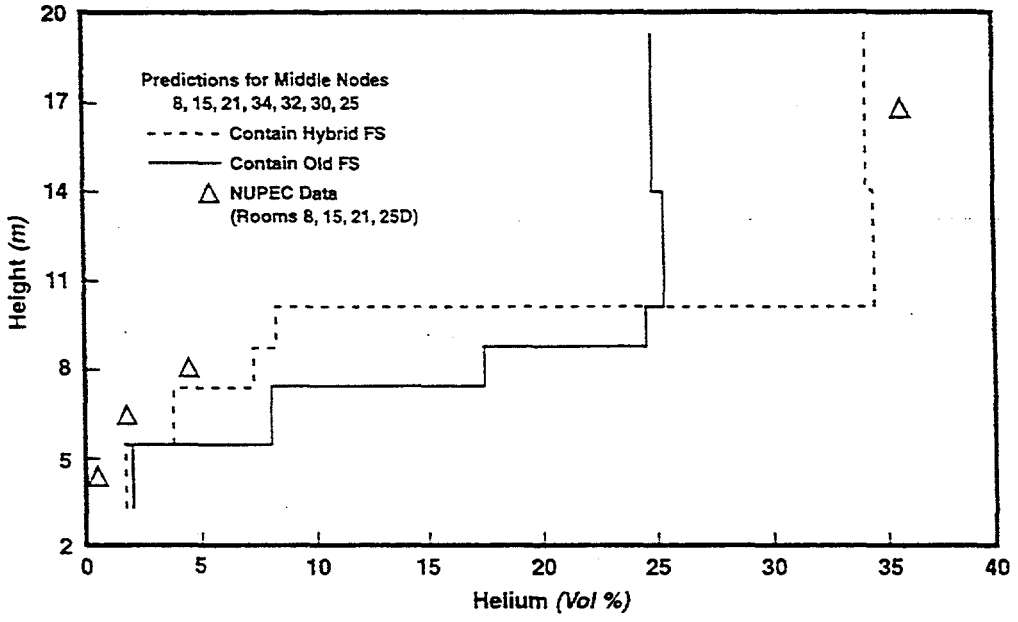

Figure 3.13. Comparison between the predicted helium distribution in a middle column of rooms in the NUPEC facility for test M-8-1 and the experimental data[OECD94].

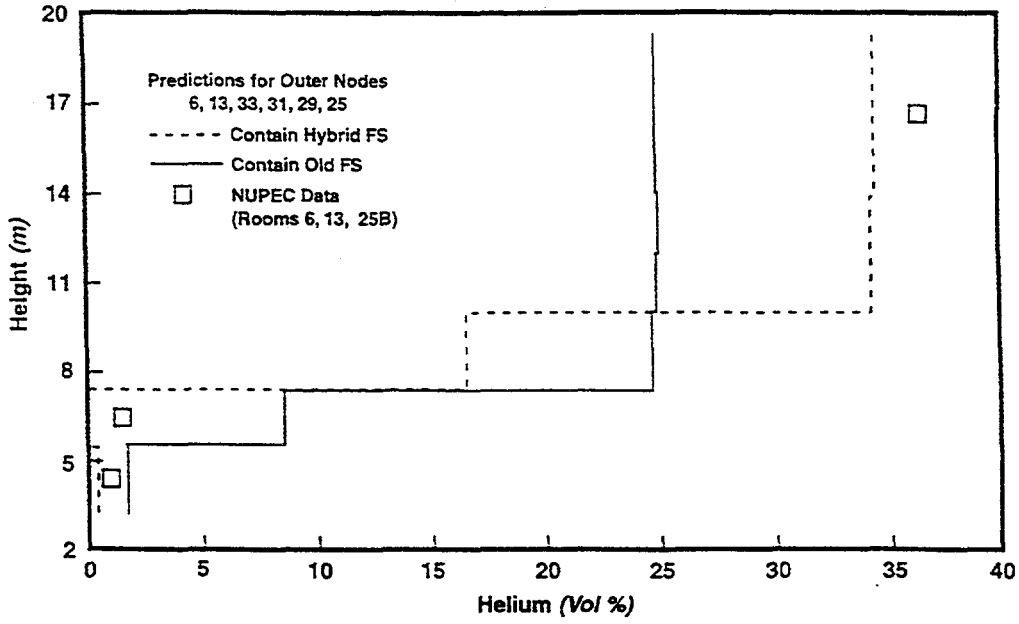

Figure 3.14. Comparison between the predicted helium distribution in an outer column of rooms in the NUPEC facility for test M-8-1 and the experimental data[OECD94].

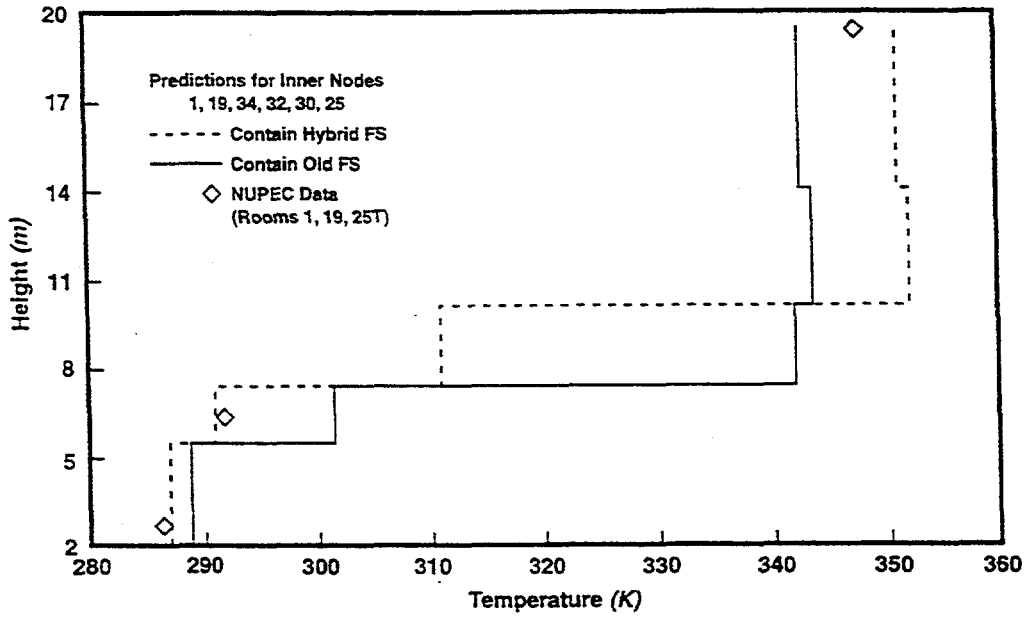

Figure 3.15. Comparison between the predicted gas temperature distribution in an inner column of rooms in the NUPEC facility for test M-8-1 and the experimental data[OECD94].

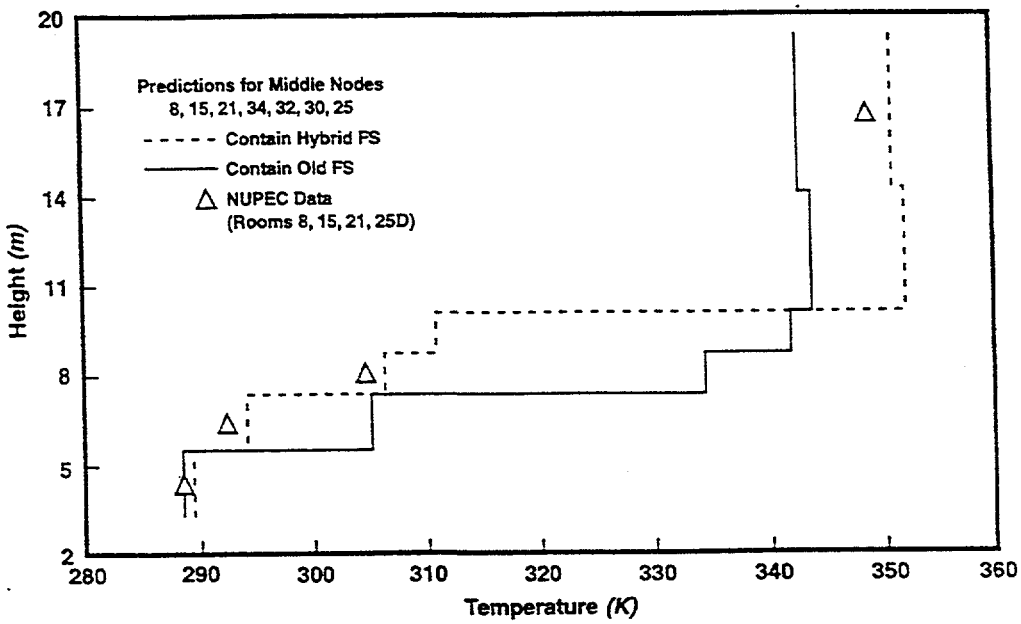

Figure 3.16. Comparison between the predicted gas temperature distribution in a middle column of rooms in the NUPEC facility for test M-8-1 and the experimental data[OECD94].

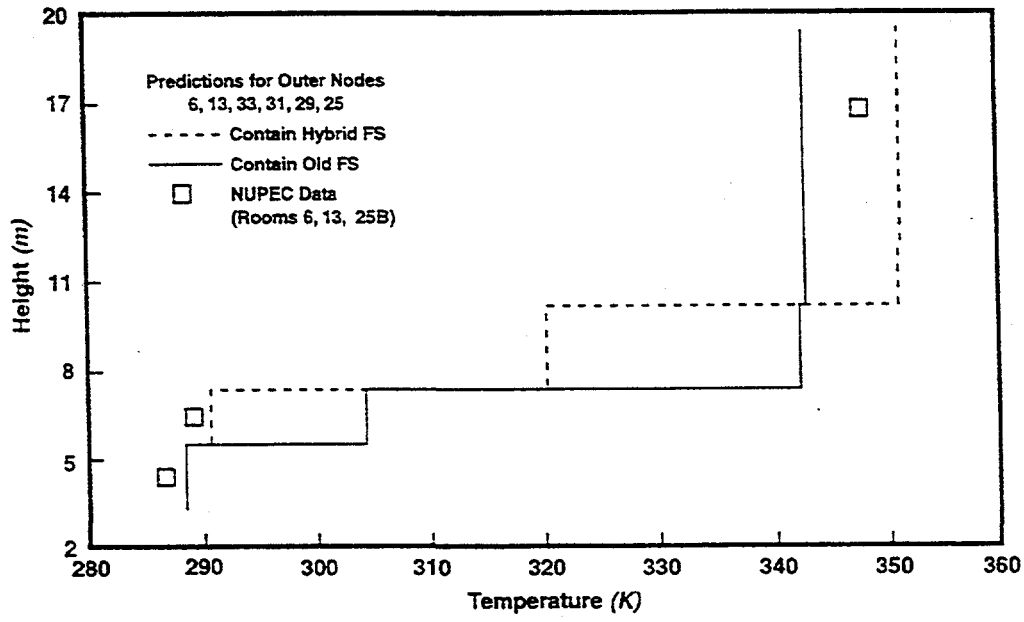

Figure 3.17. Comparison between the predicted gas temperature distribution in an outer column of rooms in the NUPEC facility for test M-8-1 and the experimental data[OECD94].

The helium concentration profiles in the inner, middle, and outer columns of rooms are shown in Figures 3.12 through 3.14, respectively, at the end of the thirty minute injection period. The following general observations can be made. The concentration profiles predicted by the hybrid formulation show a higher degree of stratification than those predicted by the old formulation and are in very good agreement with the data. For the results based on the old formulation, the predicted helium concentration in the cell just below the source is nearly equal to those in the cells above the source. As discussed in the next section, this behavior is also shown in the calculations for the Surtsey ST-3 test, for nodalizations that explicitly model recirculating flows at the source level and above.

The gas temperature profiles in the selected set of inner, middle, and outer columns of rooms are shown in Figures 3.15 through 3.17, respectively. Like the results for the helium concentrations, the predicted temperature profiles based on the hybrid formulation show a higher degree of stratification than the results based on the old formulation and are in very good agreement with the data.

3.2. Surtsey Hydrogen Mixing Test ST-3

The main objective of the hydrogen combustion tests performed in the Surtsey facility[Blan95] was to observe the combustion behavior of initially nonflammable hydrogen-air-steam mixtures that were rendered flammable by the action of water sprays. The combustion tests included both well-mixed and stratified mixtures. In order to determine how rapidly the water sprays could mix stratified hydrogen, a separate mixing test, called ST-3, was also performed. This assessment utilizes only the hydrogen injection period in ST-3, during which the sprays were not activated and the hydrogen remained highly stratified.

With respect to the hybrid solver assessment, the high jet velocity of the vertically injected hydrogen in the ST-3 test is of interest with respect to the effects of momentum convection on the formation of a stratified hydrogen layer. As discussed in Section 2.4, because CONTAIN does not model momentum convection within a control volume, the stability of the layer could be overpredicted, especially in the case of the hybrid solver, which will presumably treat the stratification as stable. The degree to which stability was overpredicted by the hybrid solver is illustrated below. Because of its approximately isothermal nature, the ST-3 test also provided an opportunity to conduct nodalization sensitivity studies without the complexities of having to modify heat sinks.

The Surtsey facility is a domed cylindrical tank. The steel vessel walls are 9.52 mm thick and are covered with at least 101.6 mm of fiberglass insulation or equivalent material. For the hydrogen tests, an uninsulated steel floor was installed to partition the facility into an upper and lower half. Only the upper half of the facility as shown in Figure 3.18 was utilized in the hydrogen tests. The upper part of the facility is 3.6 m in diameter, 5.5 m high, and 59.1 m^3 in volume.

For the tests discussed in this report, the upper region of the Surtsey facility did not have any internal compartments. It did contain a number of engineered systems and instrumentation. The engineered systems included water sprays, mixing fans, and hydrogen igniters which are shown in Figure 3.18. Hydrogen could be injected at three different elevations. The Surtsey facility was instrumented with pressure transducers, thermocouples, and hydrogen microsensors. The hydrogen microsensors provide a voltage output that is proportional to the partial pressure of hydrogen. They work on the principle that the sensor resistance changes with the adsorption of hydrogen. The array of hydrogen microsensors allowed for a real-time spatially resolved measurement of hydrogen concentrations in the facility. Gas grab samples were also taken and were analyzed using gas mass spectroscopy. The thermocouples and hydrogen microsensors were mounted on five instrumentation rakes that are shown in Figure 3.19. Rakes A, B, and C were 0.3 m from the wall and were spaced 120° apart. Rake D was spaced equally between the wall and the center rakes, labeled C and E, respectively.

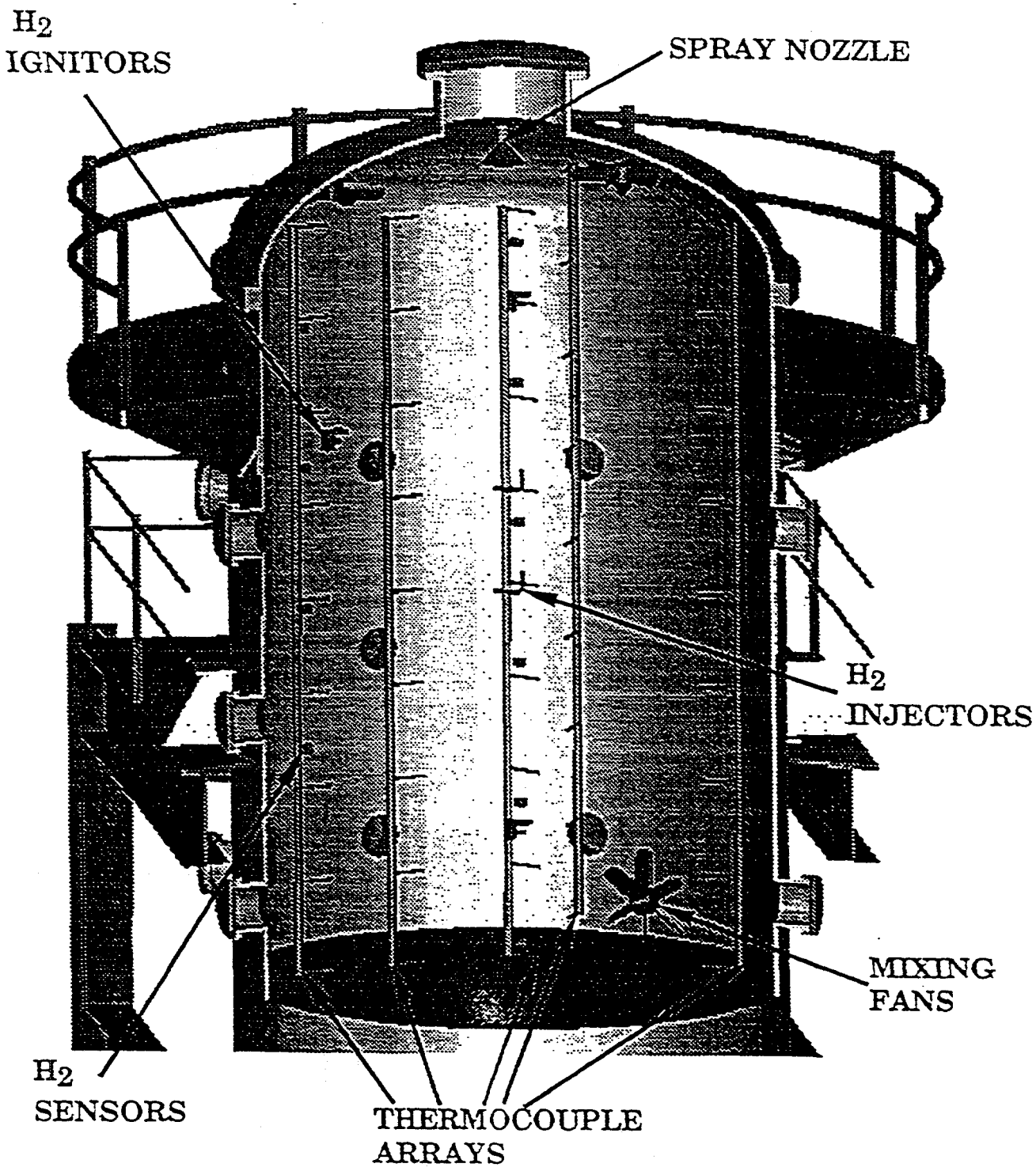

Figure 3.18. Cutaway view of upper part of the Surtsey facility[Blan95].

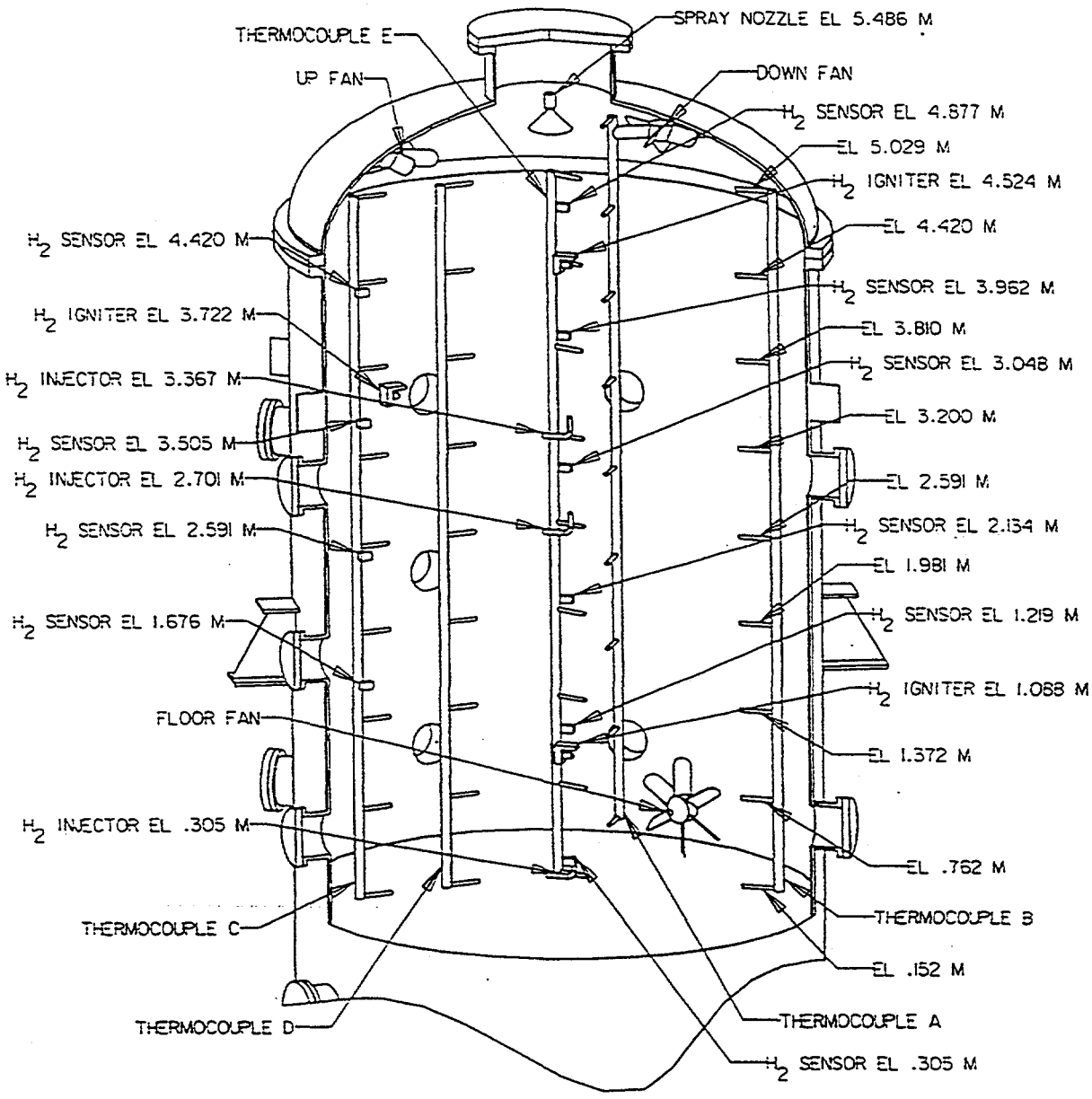

Figure 3.19. Schematic of the upper part of the Surtsey facility showing instrumentation, mixing fans, hydrogen injectors, and spray nozzle[Blan95].

Details of the test can be found in Reference Blan95, and the results of this test are shown in Figure 3.20. Initially the facility was filled with air at 82.7 kPa and 284 K. Hydrogen at 284 K was injected at a flow rate of 0.00225 kg/sec for 277 seconds through a 6.35 mm diameter tube pointed upward and located in the center of the facility at an elevation of 2.701 m above the floor. The data from the hydrogen microsensors appear as lines without symbols in Figure 3.20. It should be noted from this figure that the region above the injection point appears to become reasonably well-mixed after injecting for approximately 50 seconds. The additional mixing that appears to occur after about 1100 seconds was the result of inadvertent opening of valves. After approximately 15 minutes the water sprays were activated, and the hydrogen in the vessel was thoroughly mixed. The post-injection and spray periods of the test will not be addressed in this report.

The Froude number for the injection was a relatively high $Fr = 10^7$ and the ratio of rise height to jet diameter was 440. The jet momentum at this Froude number and height to diameter ratio is sufficient to cause the stratification to be either marginally stable or marginally unstable with respect to momentum convection, depending on the correlation used[Pete94]. Consequently, one might expect some mixing below the source elevation. As can be seen from Figure 3.20, there was some mixing below the source elevation during the injection. For example, the microsensor at the 2.59 m elevation, located just below the injector, showed the hydrogen concentration was nearly the same as locations above the source elevation after about 50 seconds. After the injection period but prior to the sprays, the microsensor at the 1.68 m elevation also indicated some hydrogen was present although the two lowest sensors did not record any hydrogen.

Gas grab samples were also taken during the test after the injection phase and after the sprays had mixed the hydrogen. These measurements appear as closed symbols in Figure 3.20. Above 2.59 m, the hydrogen concentration ranged from 17.8% - 19.7% with an average value of 19.1% based on the gas grab sample analysis. In the same region, the hydrogen concentration ranged from 20.8% - 22.2% with an average value of 21.5% based on the hydrogen microsensors. The gas grab sample value at 1.68 m agreed with the microsensor value, but the value at 1.22 m was higher the corresponding microsensor value. After the sprays stopped the hydrogen was fairly well-mixed. Based on the gas grab samples the hydrogen concentration ranged from 12.6% - 14.0% in the facility, with an average value of 13.3%. The hydrogen microsensors indicated a higher concentration, ranging from 11.0% - 15.5%, with an average value of approximately 14.5%. The well-mixed concentration of hydrogen based on the mass of hydrogen added and the pressure increase should have been approximately 13.0% hydrogen, which agrees reasonably well with the average gas grab sample measurement of 13.3%. The hydrogen microsensor measurements, therefore, were approximately 10% high.

Because the test was essentially an isothermal one during the injection, only the CONTAIN gas

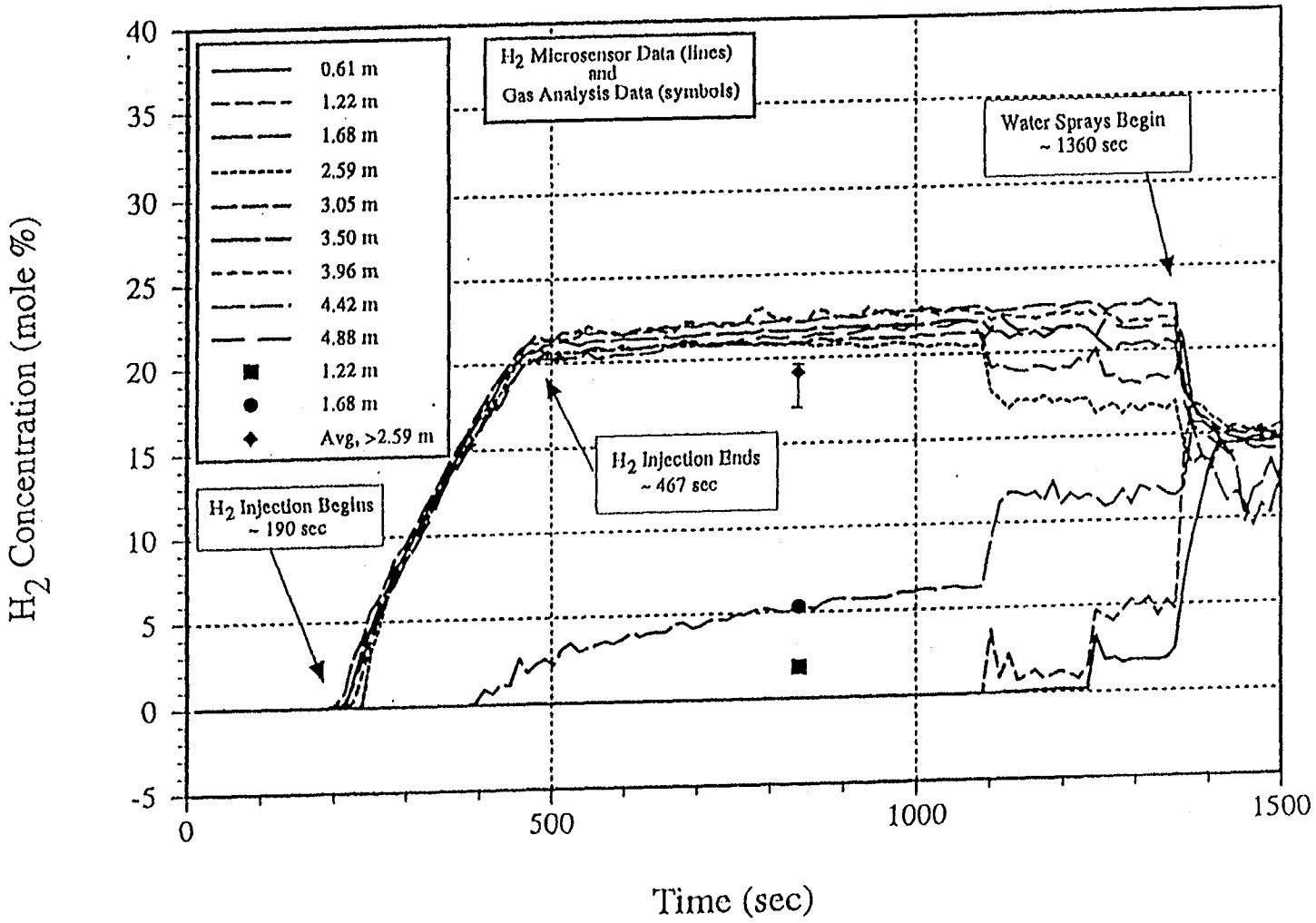

Figure 3.20. Hydrogen concentration measurements by microsensors and gas grab samples in Surtsey hydrogen mixing test ST-3[Blan95].

thermodynamic and flow models were invoked in the experiment comparison. Heat transfer structures were not explicitly modeled. The simplicity of the modeling allowed a number of different nodalizations to be constructed. The nodalizations ranged from one as simple as 3 cells (2 internal cells and an environment cell) to one with 16 cells (15 internal cells and an environment cell). In all nodalizations, a horizontal cell boundary was placed at the source elevation. Except for the 3-cell nodalization, all nodalizations were divided into central and annular cells to allow gas circulation patterns to be modeled. The flow areas were always taken to be the full face areas between cells, and the loss coefficient was assumed to be equal to one for all flow paths, as typically done in CONTAIN decks when modeling open volumes.

One of the 16-cell nodalizations is shown in Figure 3.21. The Surtsey volume was divided into 8 levels which allowed roughly a one-to-one comparison between a hydrogen microsensor and a node level. The cell boundary between the central and annular cells was specified at a radius that resulted in equal horizontal cross-sectional areas for the central and annular cells. All cells are approximately of equal height and, therefore, of approximately equal volume. An alternate 16-cell nodalization, shown in Figure 3.22, is the same as the one shown in Figure 3.21 except the horizontal cross-sectional areas are different. In this nodalization, the horizontal cross-sectional areas of the annular cells are 3 times larger than those of the central cells. The 10-cell and 9-cell nodalizations, shown in Figures 3.23 and 3.24 respectively, are limiting cases in which the region above or below the source elevation was collapsed to one cell, with the opposite region subdivided. The 3-cell nodalization, shown in Figure 3.25, has one cell both above and below the source elevation. This nodalization is qualitatively different from the other nodalizations in that no gas circulation is possible and all mixing occurs by compressive effects.

For each nodalization, calculations were performed with the old formulation and the hybrid formulation. Since the test was isothermal and involved only the injection of pure hydrogen into air, the only variable of interest is the hydrogen concentration. The results of each calculation are presented in two plots: the hydrogen mole fraction is first plotted as a function of time for all of the center cells and then the outer annular cells, if present. (The only exception is the 3-cell nodalization which does not have central and annular cells.) The predicted results are the lines without symbols that are identified by the cell number and the cell center elevation. The hydrogen microsensor output is represented by lines with open symbols. Where practical, predictions and data at similar elevations are plotted with similar line types to aid in the comparison.

Results from the 16-cell nodalization shown in Figure 3.21 are given for the old formulation in Figures 3.26 and 3.27 and for the hybrid formulation in Figures 3.28 and 3.29. The predicted hydrogen concentration profiles are also plotted against height in Figure 3.30 for the old and hybrid

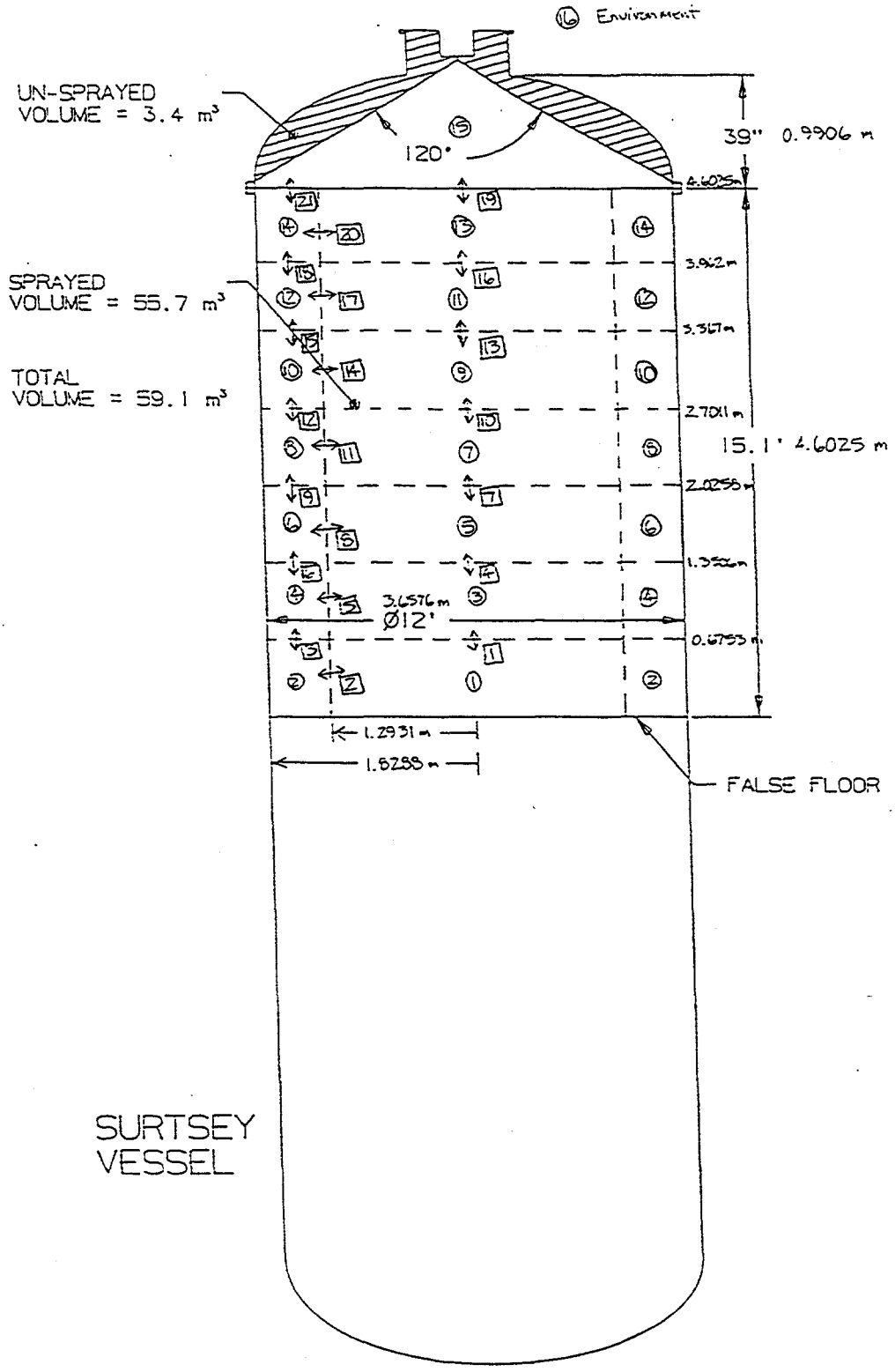

Figure 3.21. CONTAIN 16-cell nodalization for the Surtsey facility

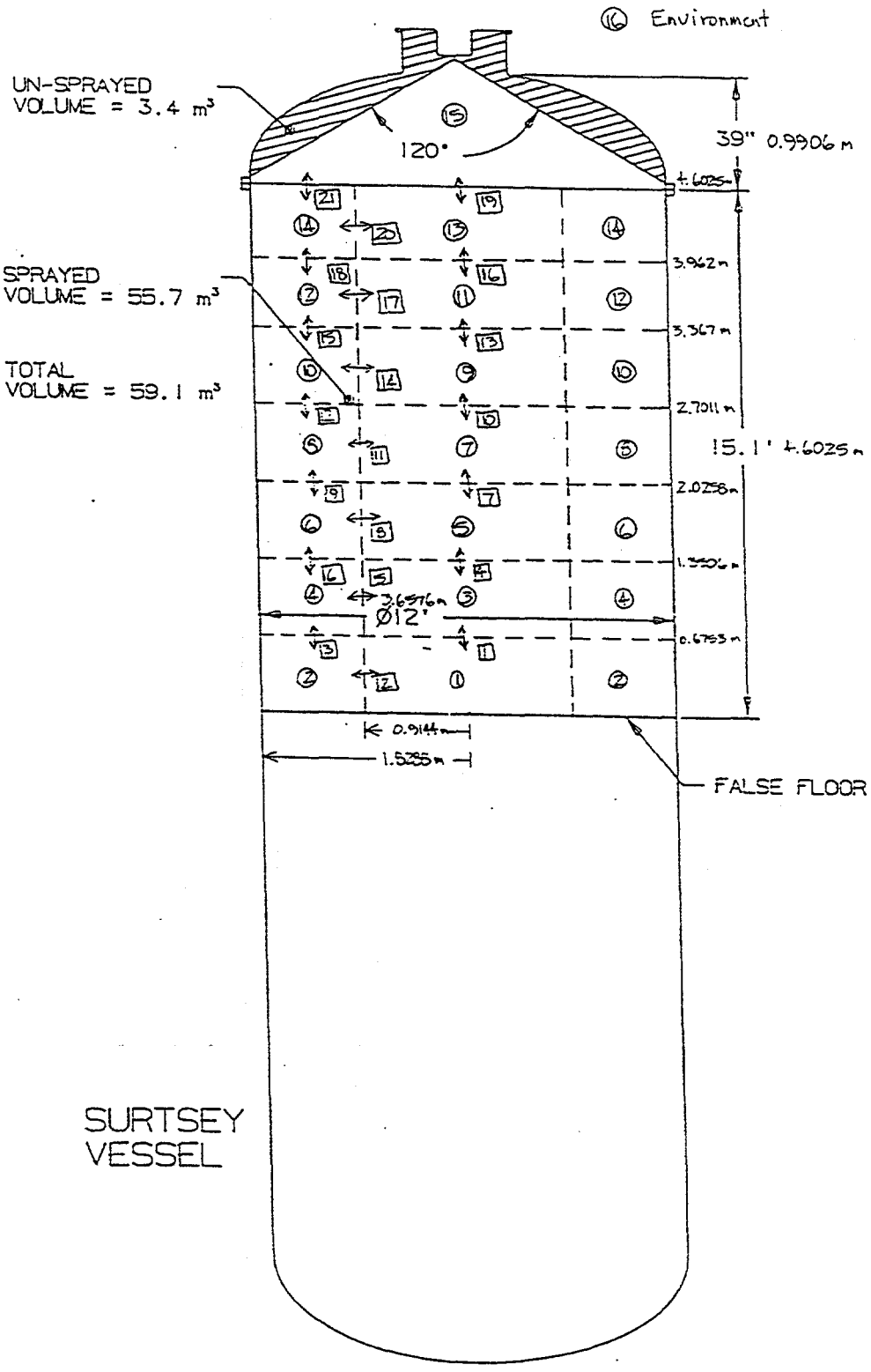

Figure 3.22. Alternate CONTAIN 16-cell nodalization for the Surtsey facility. Horizontal cross-sectional areas of the outer cells are 3 times larger than those of the inner cells, as opposed to being equal for all other nodalizations.

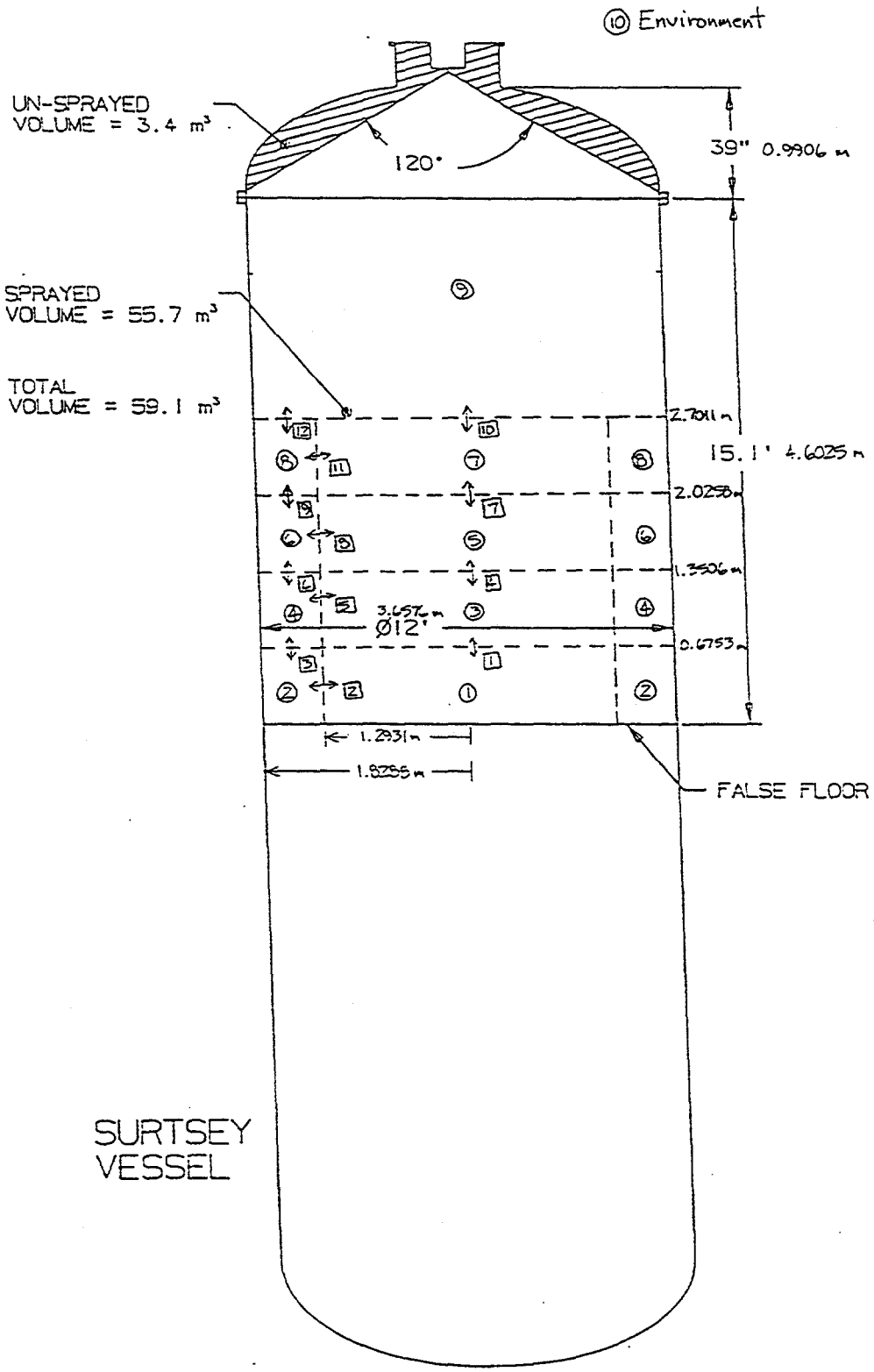

Figure 3.23. CONTAIN 10-cell nodalization for the Surtsey facility.

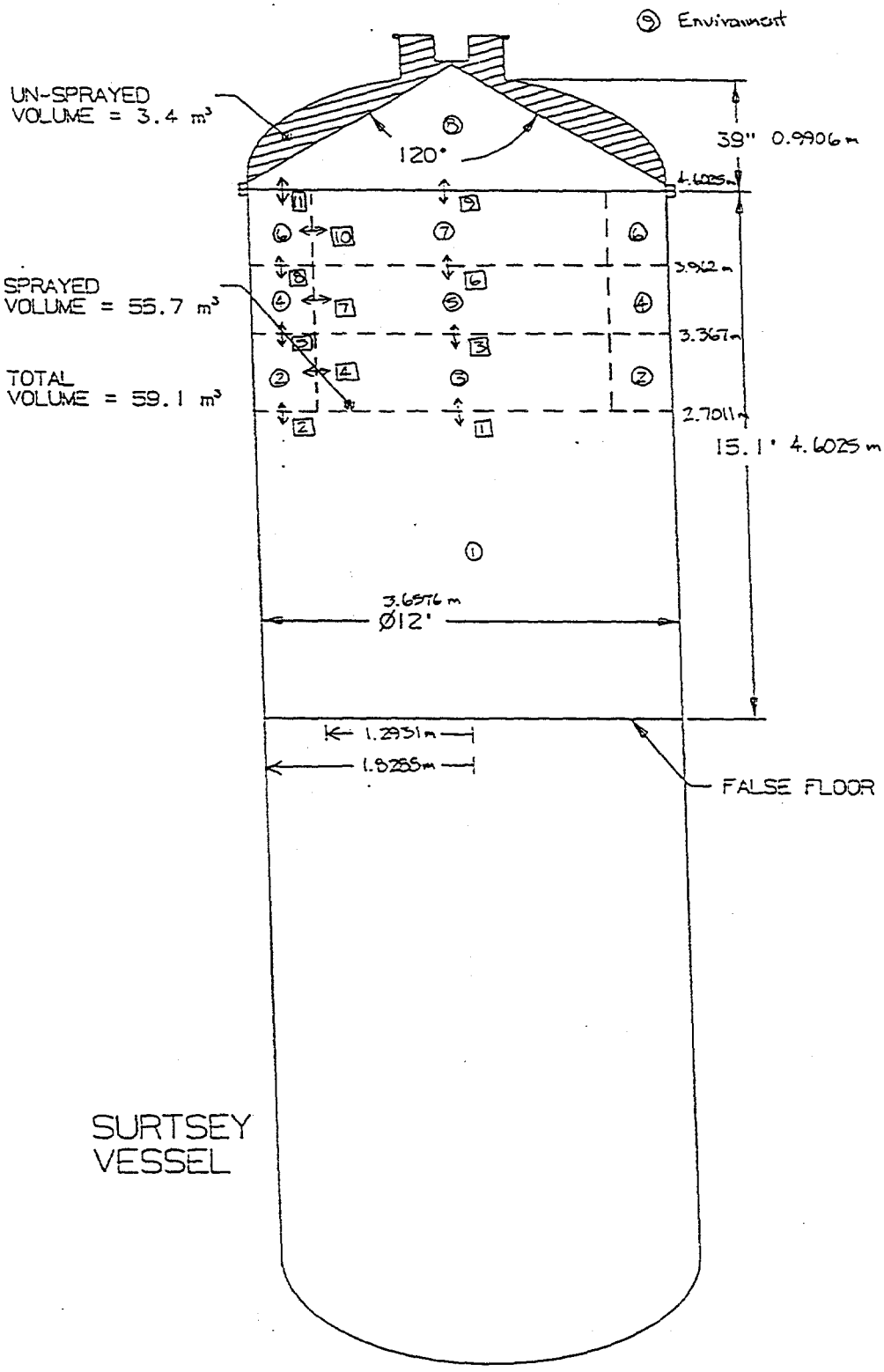

Figure 3.24. CONTAIN 9-cell nodalization for the Surtsey facility.

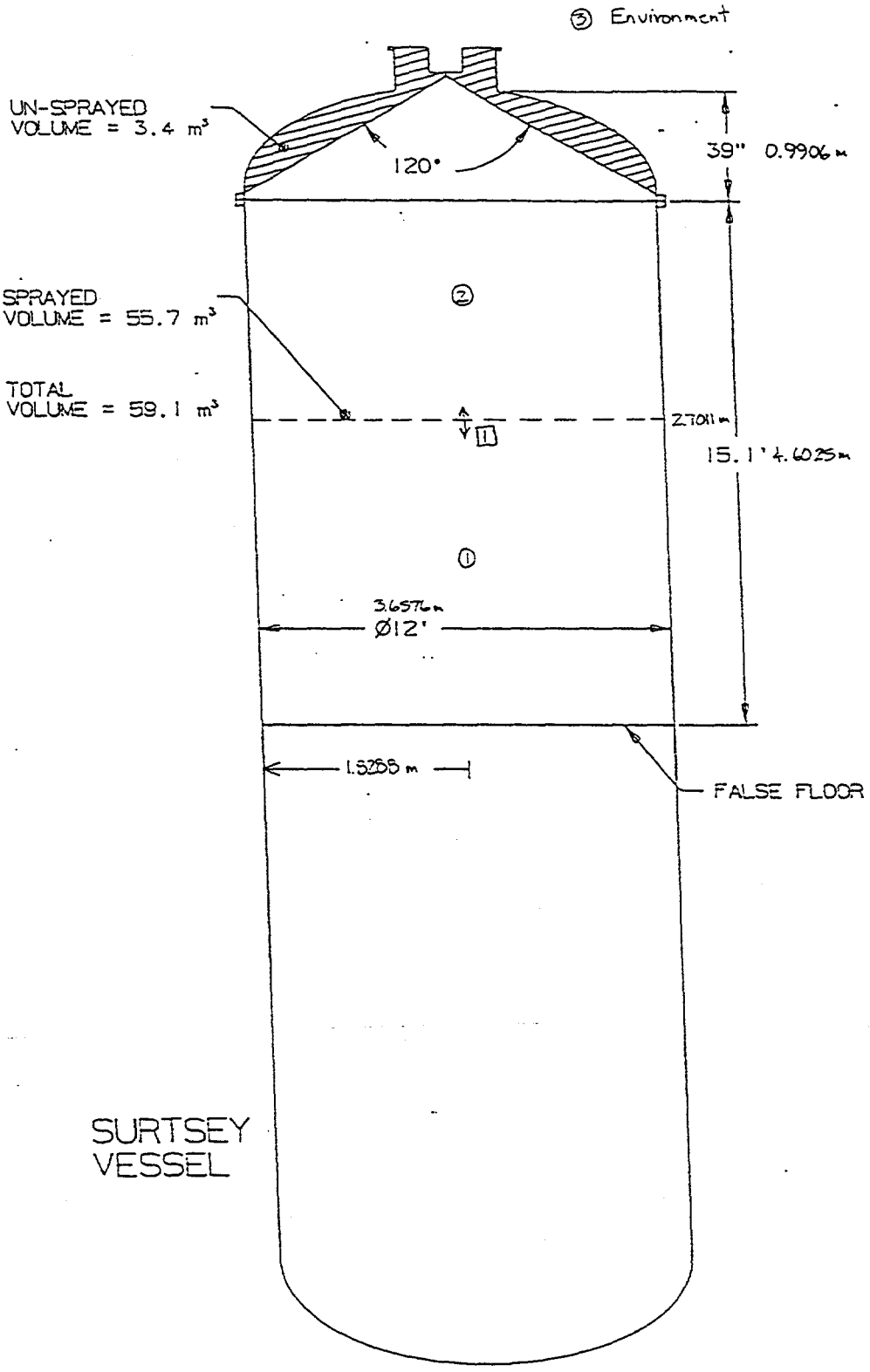

Figure 3.25. CONTAIN 3-cell nodalization for the Surtsey facility

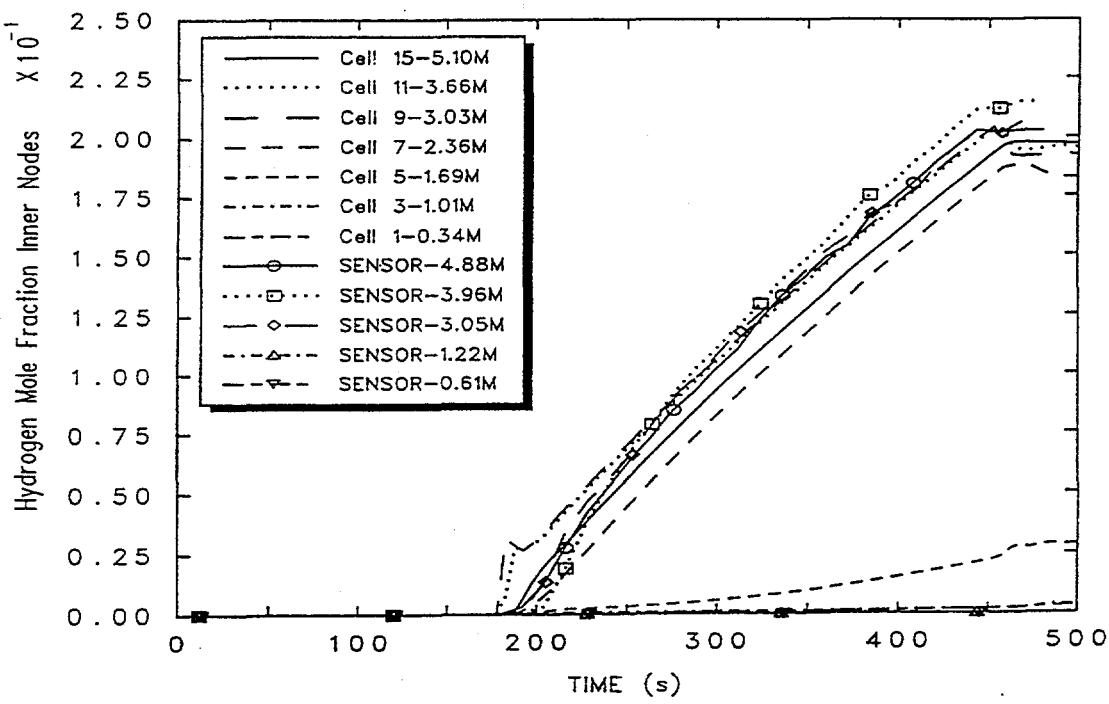

Figure 3.26. Comparison between the predicted hydrogen distribution for the inner cells for Surtsey test ST-3 using the 16-cell nodalization and the old gravitational head formulation and the experimental data[Blan95].

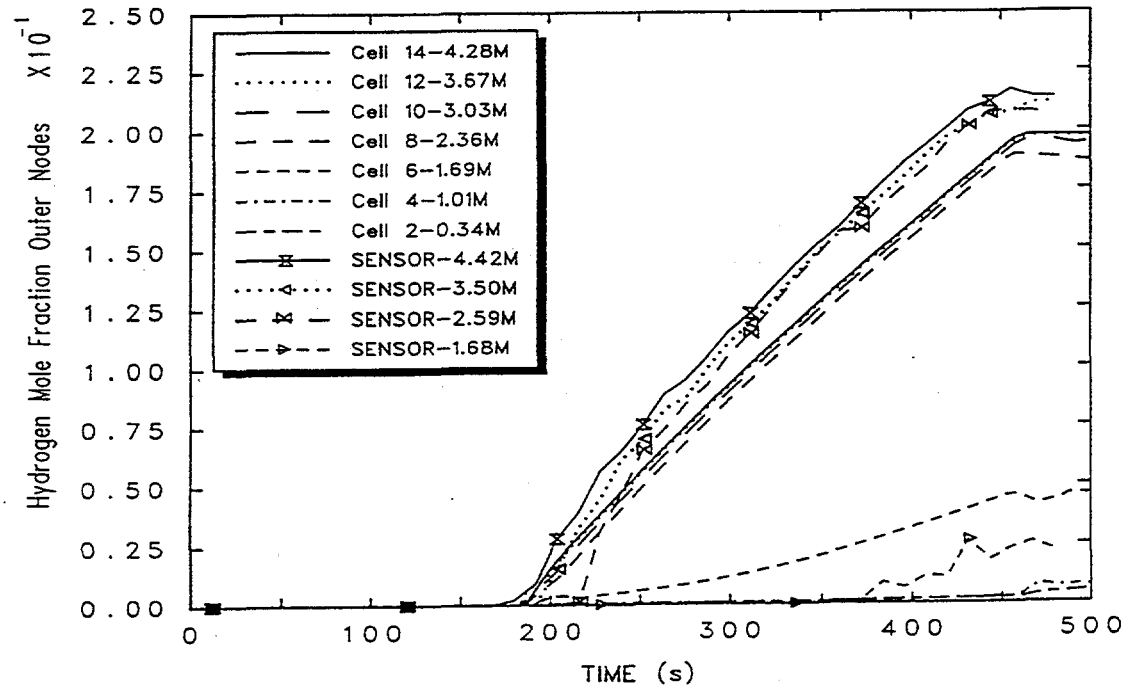

Figure 3.27. Comparison between the predicted hydrogen distribution for the outer cells for Surtsey test ST-3 using the 16-cell nodalization and the old gravitational head formulation and the experimental data[Blan95].

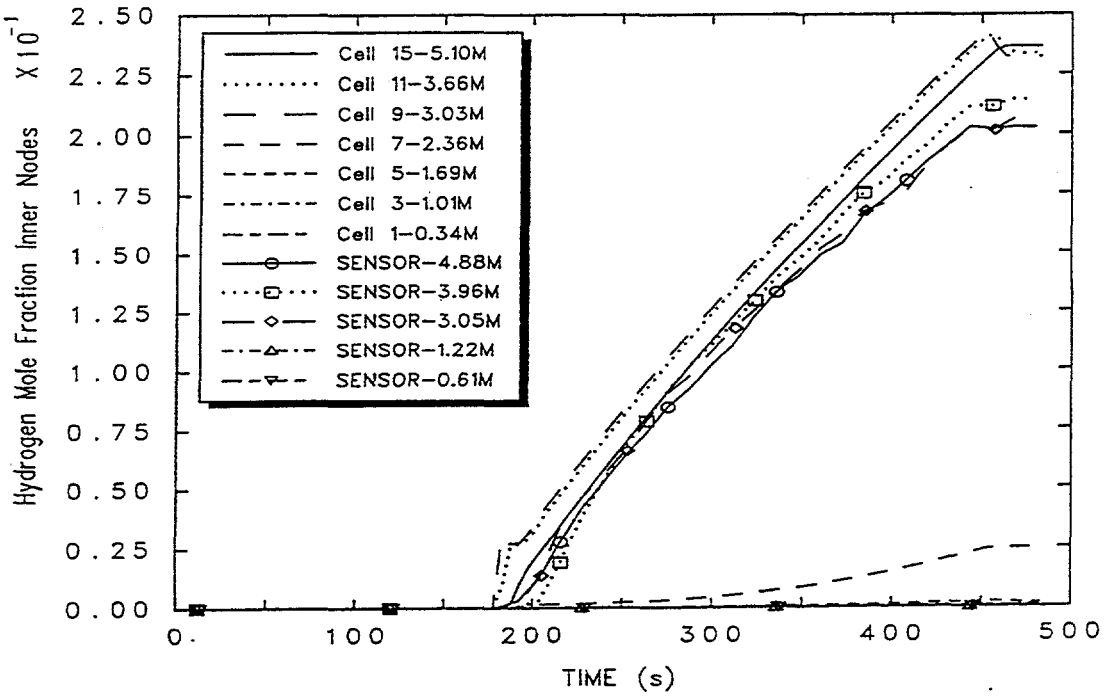

Figure 3.28. Comparison between the predicted hydrogen distribution for the inner cells for Surtsey test ST-3 using the 16-cell nodalization and the hybrid formulation and the experimental data[Blan95].

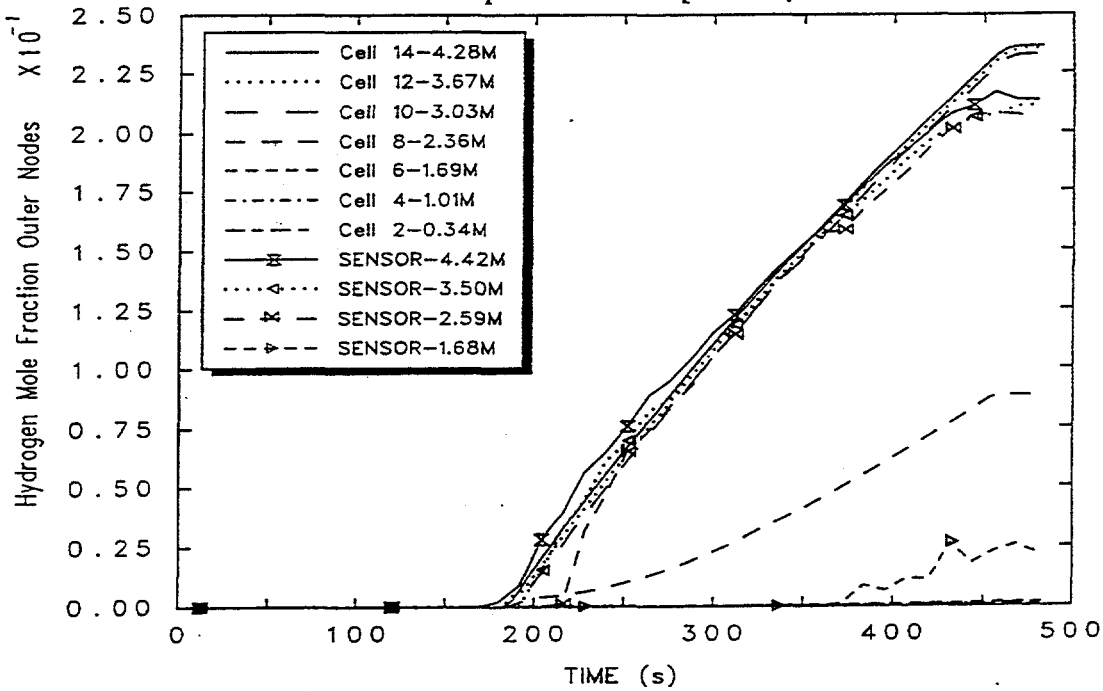

Figure 3.29. Comparison between the predicted hydrogen distribution for the outer cells for Surtsey test ST-3 using the 16-cell nodalization and the hybrid formulation and the experimental data[Blan95].

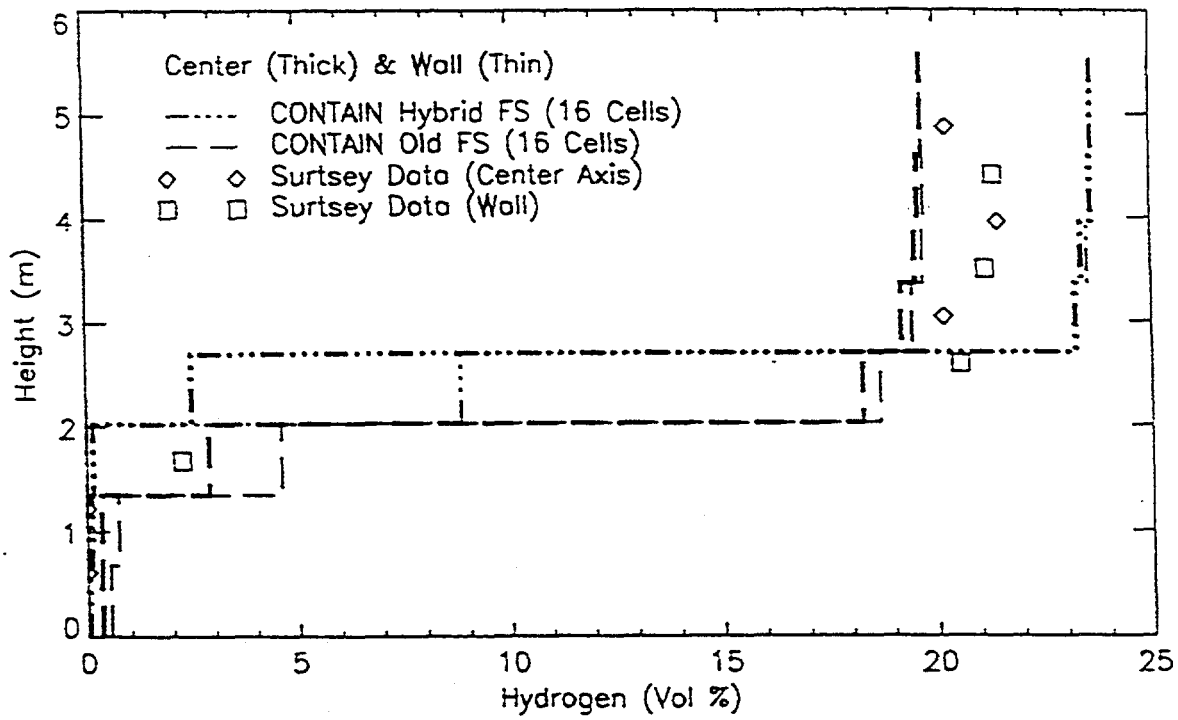

Figure 3.30. Comparison between the predicted hydrogen distribution for Surtsey test ST-3 using the 16-cell nodalization and the hydrogen microsensor measurements[Blan95].

solvers at a time of 500 seconds, which was 33 seconds after the end of hydrogen injection. The predicted vertical profiles are plotted in a step-wise manner to represent the fact that in a control volume formulation, the hydrogen concentration is assumed well-mixed within each cell and discontinuous across cell boundaries. Hydrogen concentrations are shown for the inner cells (thick lines) and outer cells (thin lines). The experimental data are plotted at the elevation of the hydrogen microsensors and show the output from the hydrogen sensors along the wall separately from those in the center of the facility. In general, however, the hydrogen above the source was fairly well-mixed. The old formulation predicted the hydrogen concentrations in the cell layer just below the source, consisting of cells 7 and 8, to be nearly the same as in the cells above the source. Some hydrogen was present even in the next layer of cells. This is to be expected from the fact that the stability criterion analogous to Equation (2-14) for the old formulation cannot be satisfied. Mixing below the source was not as pronounced with the hybrid formulation. This resulted in higher hydrogen concentrations in the region above the source, compared to the old formulation. Even though the results for both formulations are reasonably similar, a cursory comparison between the

predictions and the data indicates that the old formulation agrees slightly better with the data than the hybrid formulation. This conclusion is based on the consideration that the hydrogen microsensor measurements were probably about 10% high. This adjustment would yield a better comparison between the old formulation and the data in the region above the source. In addition, the old formulation predicted that the hydrogen concentrations just below the source were approximately the same as for locations above the source. It also predicted the hydrogen concentration reasonably well at the 1.69 m level and lower. However, as shown below by the other nodalizations, the somewhat better agreement with the data obtained with the old formulation in this case is quite sensitive to nodalization.

The somewhat better agreement obtained with the old formulation in the 16-cell nodalization is not only sensitive to nodalization but fortuitous in the sense that the cause of the mixing below the source in the test, momentum convection, is not modeled in CONTAIN. The predicted mixing below the source with the old solver is therefore due to numerical effects. This behavior is consistent with the general expectation, from the other comparisons given in this report, that the old formulation tends to overpredict the rate and extent of mixing below the source.

Although CONTAIN does not model momentum convection, the 16-cell calculation illustrates that the agreement between the hybrid formulation and experiment for a marginally unstable stratification is still reasonable with regard to peak hydrogen concentrations, even though the degree of penetration of the hydrogen below the injection point was not predicted well. Furthermore, as shown below the hybrid solver results are not sensitive to nodalization.

Results from the alternate 16-cell nodalization shown in Figure 3.22 are given for the old formulation in Figures 3.31 and 3.32 and for the hybrid formulation in Figures 3.33 and 3.34. The results for the old and hybrid formulations from the alternate 16-cell nodalization are similar to those obtained from the 16-cell nodalization shown in Figure 3.21. Therefore, the predicted results are relatively insensitive to variations in horizontal cross-sectional flow area, at least for variations within a factor of 3.

Results from the 10-cell nodalization shown in Figure 3.23 are given for the old formulation in Figures 3.35 and 3.36 and for the hybrid formulation in Figures 3.37 and 3.38. The concentration profiles at 500 seconds are also plotted in Figure 3.39. For both formulations, the cell layer just below the source, consisting of cells 7 and 8, has substantially less hydrogen than the cells above the source. In contrast, the results for the old formulation from the 16-cell nodalization shows that cells 7 and 8 have nearly the same concentration of hydrogen as those above the source. The similar results from the two solvers in this case may be attributed to the single cell used for the entire region at and above the source level. Apparently, the tendency of the old formulation to overpredict the rate

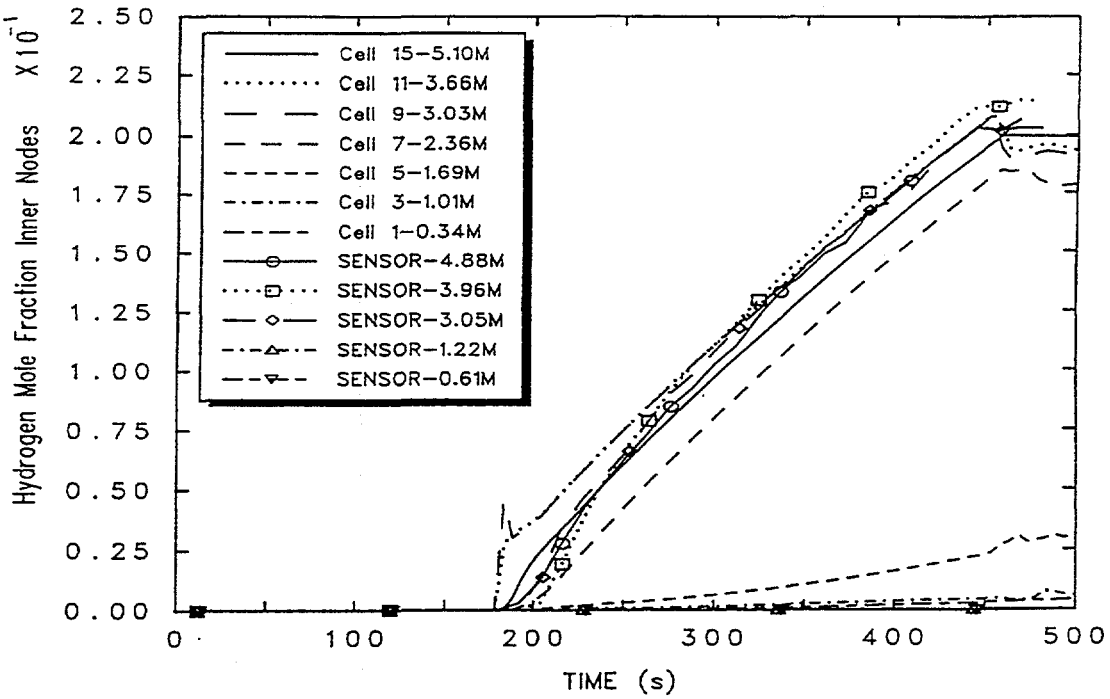

Figure 3.31. Comparison between the predicted hydrogen distribution for the inner cells for Surtsey test ST-3 using the alternate 16-cell nodalization and the old gravitational head formulation and the experimental data[Blan95].

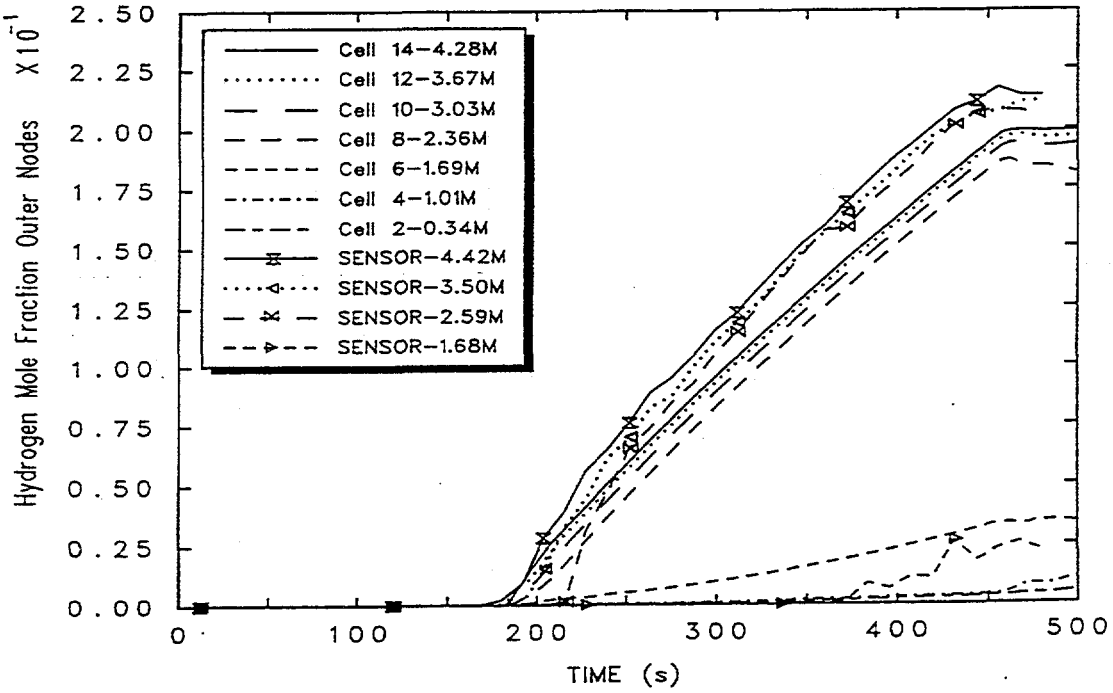

Figure 3.32. Comparison between the predicted hydrogen distribution for the outer cells for Surtsey test ST-3 using the alternate 16-cell nodalization and the old gravitational head formulation and the experimental data[Blan95].

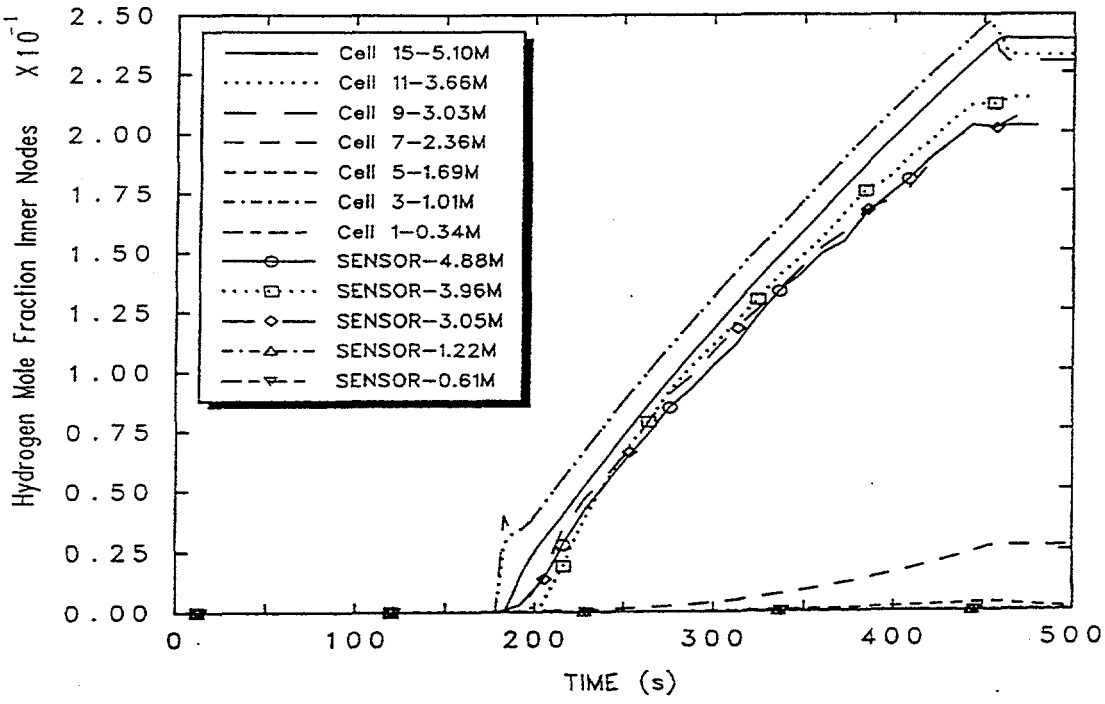

Figure 3.33. Comparison between the predicted hydrogen distribution for the inner cells for Surtsey test ST-3 using the alternate 16-cell nodalization and the hybrid formulation and the experimental data[Blan95].

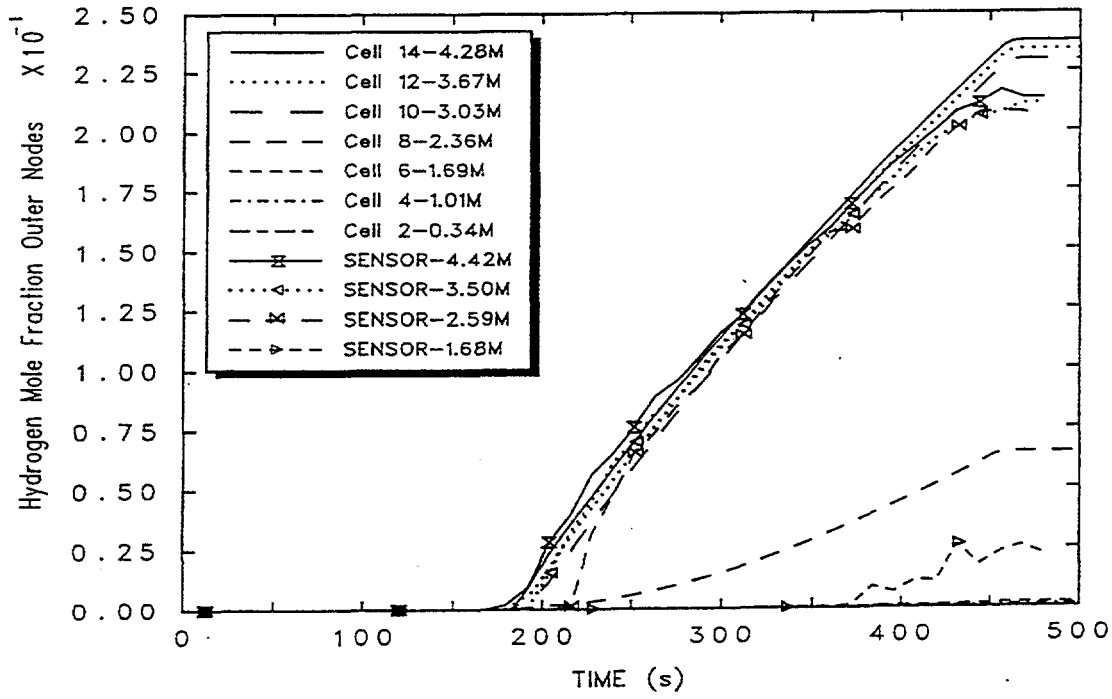

Figure 3.34. Comparison between the predicted hydrogen distribution for the outer cells for Surtsey test ST-3 using the alternate 16-cell nodalization and the hybrid formulation and the experimental data[Blan95].

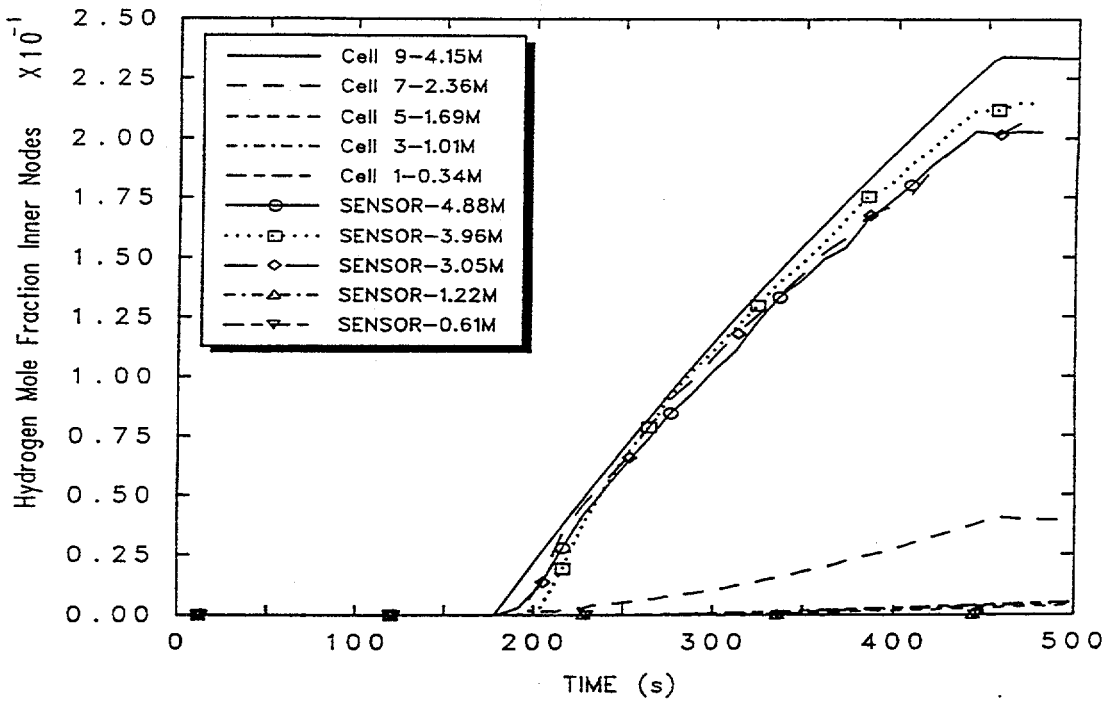

Figure 3.35. Comparison between the predicted hydrogen distribution for the inner cells for Surtsey test ST-3 using the 10-cell nodalization and the old gravitational head formulation and the experimental data[Blan95].

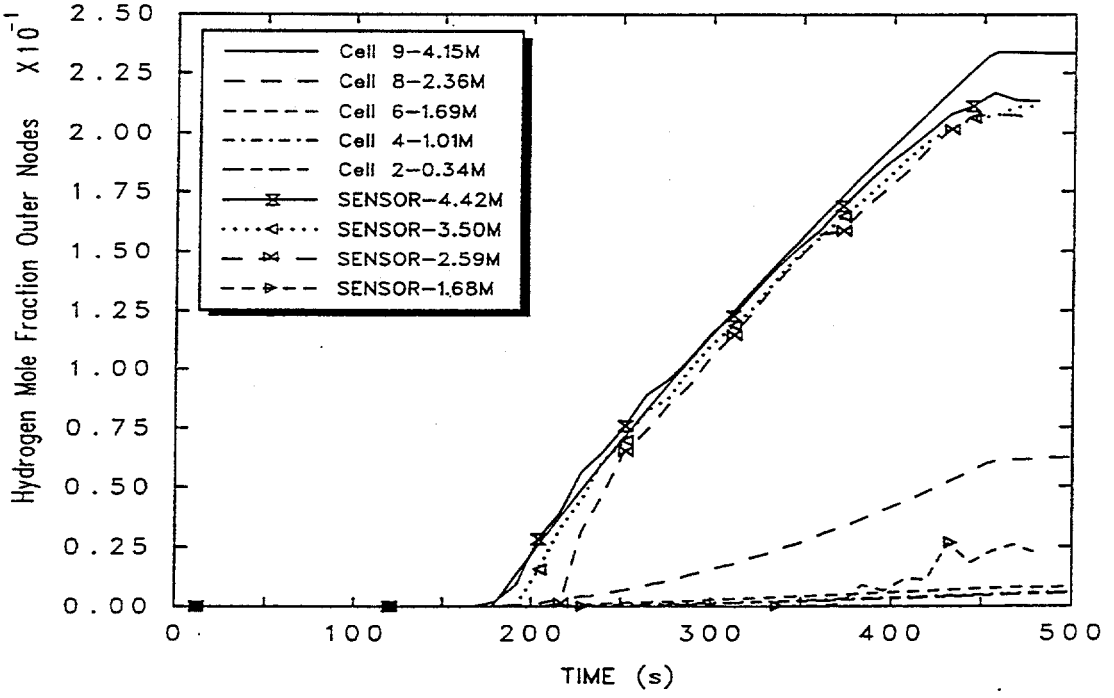

Figure 3.36. Comparison between the predicted hydrogen distribution for the outer cells for Surtsey test ST-3 using the 10-cell nodalization and the old gravitational head formulation and the experimental data[Blan95].

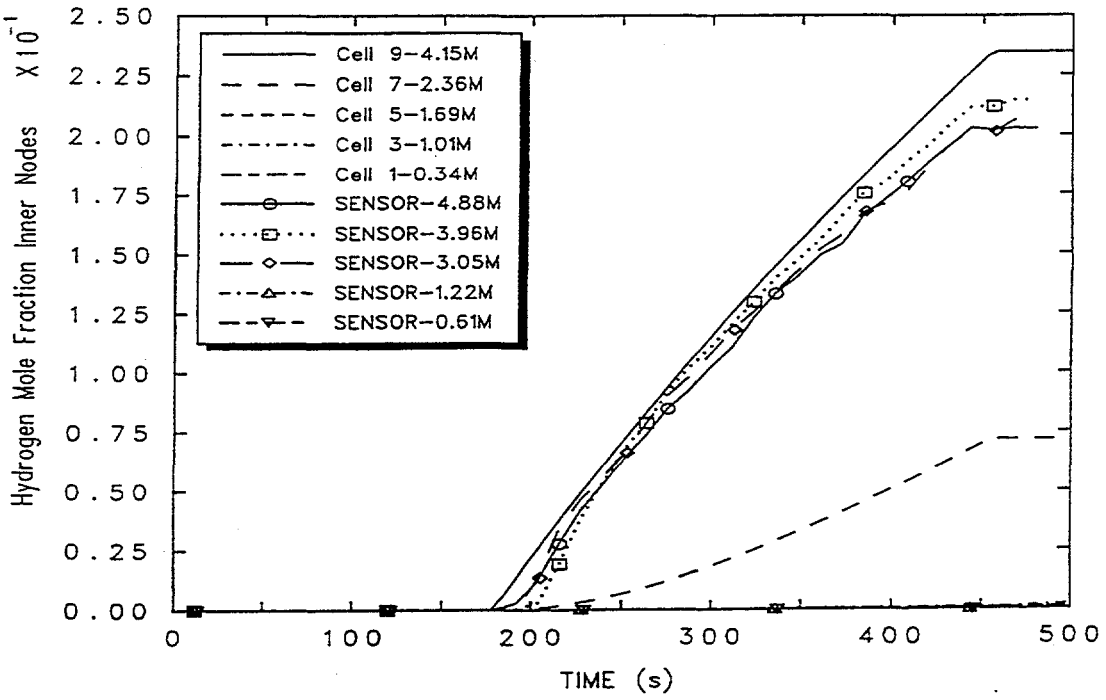

Figure 3.37. Comparison between the predicted hydrogen distribution for the inner cells for Surtsey test ST-3 using the 10-cell nodalization and the hybrid formulation and the experimental data[Blan95].

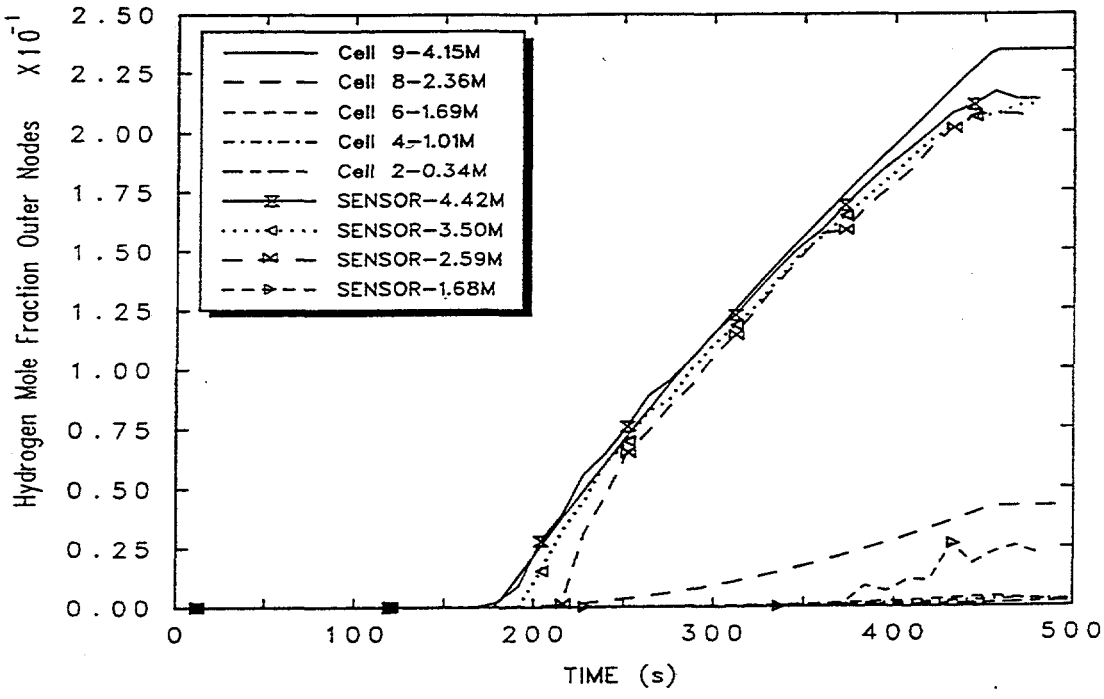

Figure 3.38. Comparison between the predicted hydrogen distribution for the outer cells for Surtsey test ST-3 using the 10-cell nodalization and the hybrid formulation and the experimental data[Blan95].

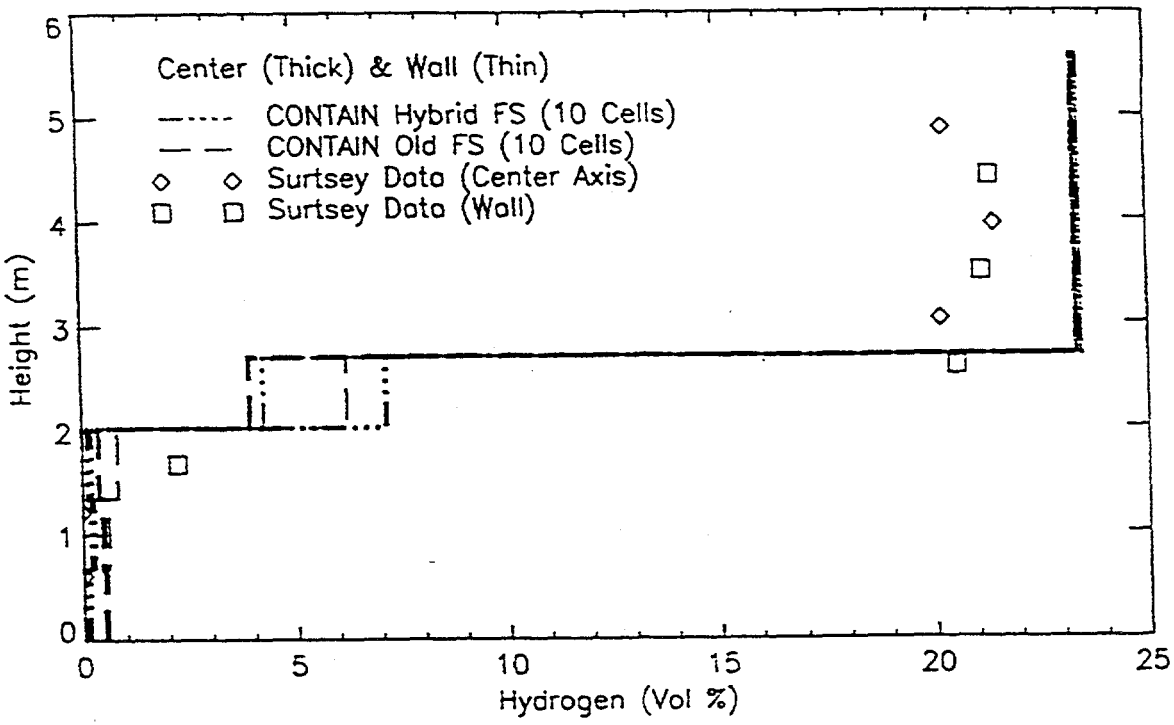

Figure 3.39. Comparison between the predicted hydrogen distribution for Surtsey test ST-3 using the 10-cell nodalization and the hydrogen microsensor measurements[Blan95].

and extent of mixing below the source is inhibited when recirculating flow at and above the source level is not explicitly modeled. This observation is consistent with Equation (2-14), which shows that the stability limit at the source level is determined by the horizontal entrainment flow rate W into the source cell. In the 10-cell nodalization and 3-cell nodalization, this entrainment flow is not modeled.

Results from the 9-cell nodalization shown in Figure 3.24 are given for the old formulation in Figures 3.40 and 3.41 and for the hybrid formulation in Figures 3.42 and 3.43. The concentration profiles are given in Figure 3.44. The results from the old formulation show the hydrogen concentration is nearly well-mixed throughout the entire facility, in gross disagreement with experiment, whereas the hybrid solver predicts concentrations very similar to those obtained with the other nodalizations studied here. Given that the old formulation gives reasonable agreement with the data with the other nodalizations, it is tempting to consider this poor prediction as an isolated case. But closer inspection shows that it is not. This nodalization is simply one that emphasizes the problem of overmixing with

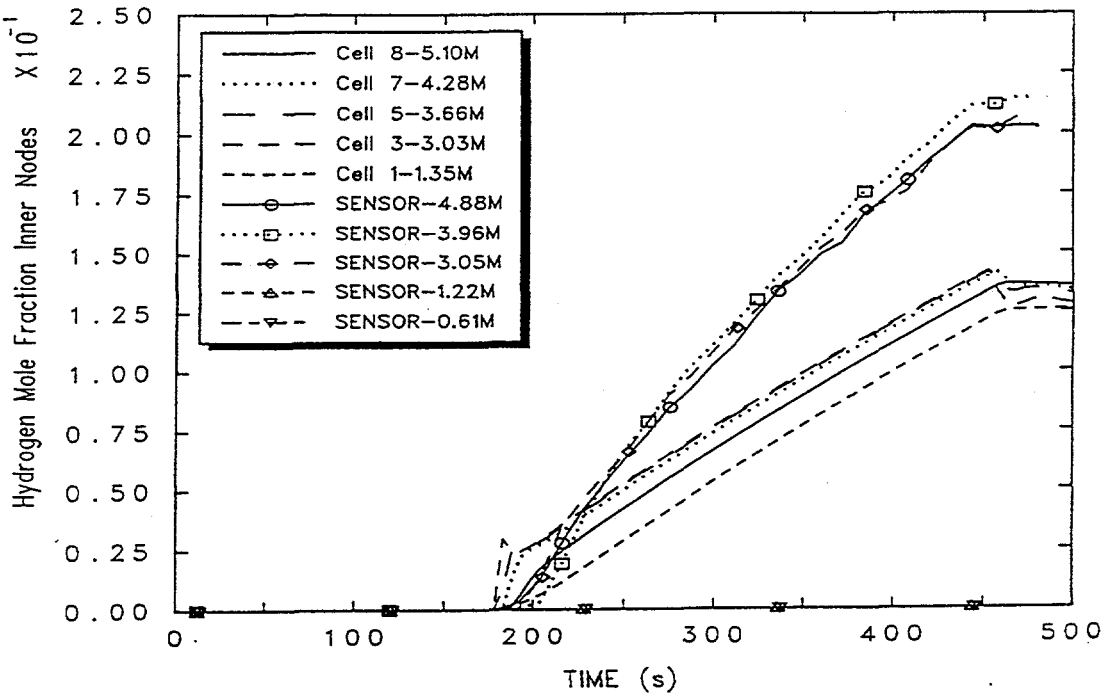

Figure 3.40. Comparison between the predicted hydrogen distribution for the inner cells for Surtsey test ST-3 using the 9-cell nodalization and the old gravitational head formulation and the experimental data[Blan95].

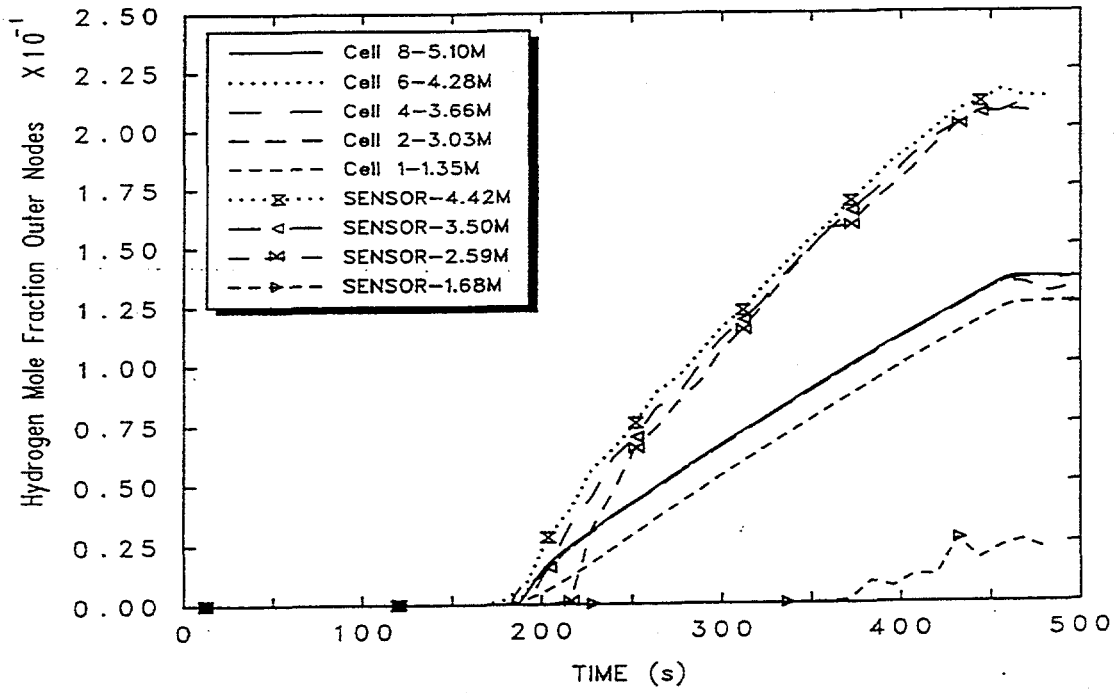

Figure 3.41. Comparison between the predicted hydrogen distribution for the outer cells for Surtsey test ST-3 using the 9-cell nodalization and the old gravitational head formulation and the experimental data[Blan95].

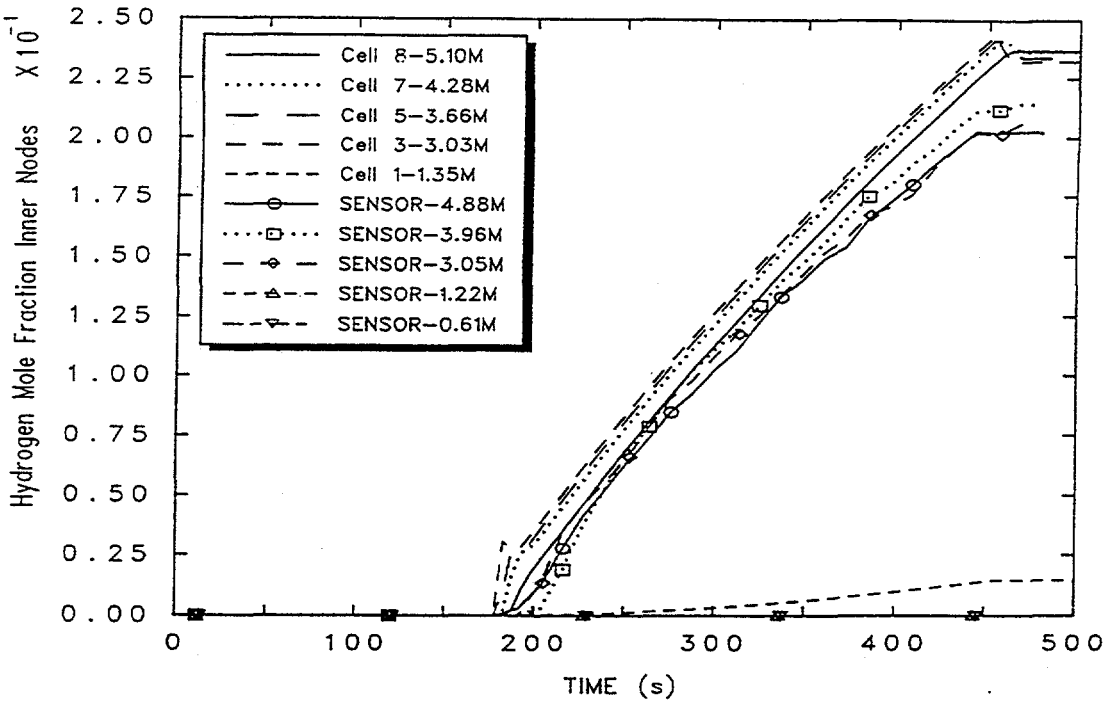

Figure 3.42. Comparison between the predicted hydrogen distribution for the inner cells for Surtsey test ST-3 using the 9-cell nodalization and the hybrid formulation and the experimental data[Blan95].

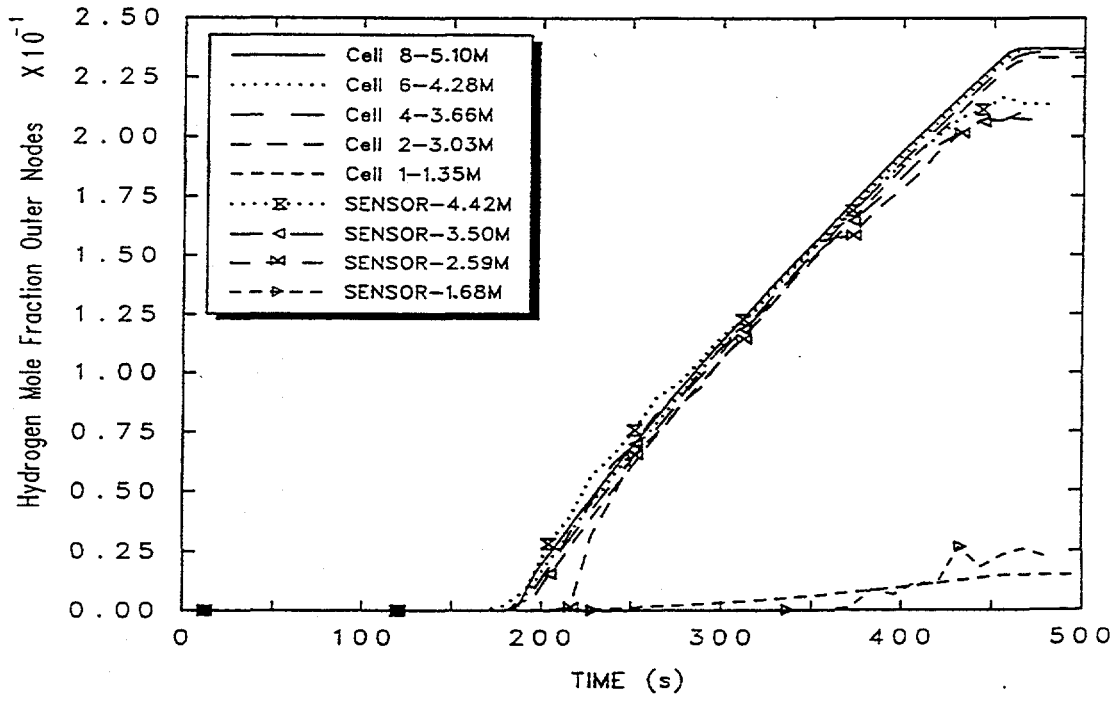

Figure 3.43. Comparison between the predicted hydrogen distribution for the outer cells for Surtsey test ST-3 using the 9-cell nodalization and the hybrid formulation and the experimental data[Blan95].

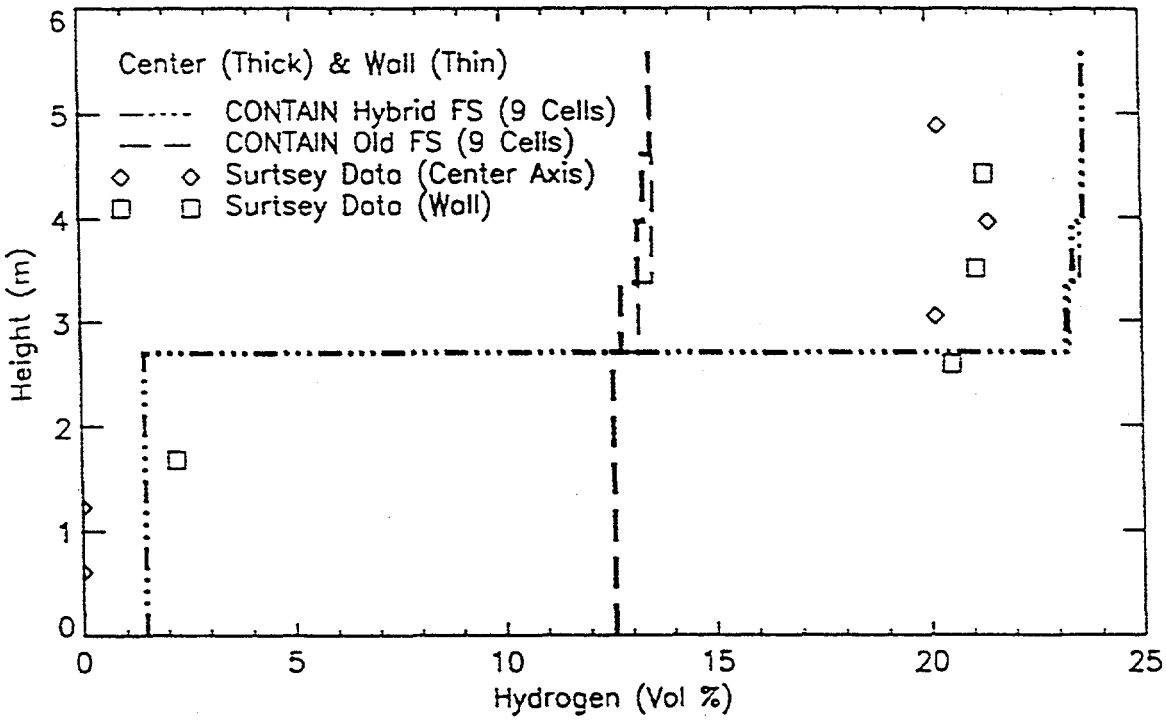

Figure 3.44. Comparison between the predicted hydrogen distribution for Surtsey test ST-3 using the 9-cell nodalization and the hydrogen microsensor measurements[Blan95].

the old formulation. In the other nodalizations that explicitly model recirculating flow at and above the source level, the concentrations in the cell layer immediately below the source are nearly the same as those above the source. The same is true for the present nodalization. The overmixing is simply more obvious in the present case because only one cell is used below the source.

Results from the 3-cell nodalization shown in Figure 3.25 are given for the old formulation in Figures 3.45 and 3.46 and for the hybrid formulation in Figures 3.47 and 3.48. The concentration profiles are plotted in Figure 3.49. The results for both formulations are nearly identical and are in reasonable agreement with the data. This nodalization lacks the capability of modeling recirculating flows at all. The fact that similar results for the dome concentrations were obtained from the 10-cell nodalization confirms the absence of recirculating flows with the latter. The old formulation is obviously very sensitive to nodalization. This formulation promotes mixing with the cell layer immediately below the source when recirculating flows at and above the source level are explicitly modeled, even when stable conditions should be present. As a result of this nonphysical mixing, the concentrations in the

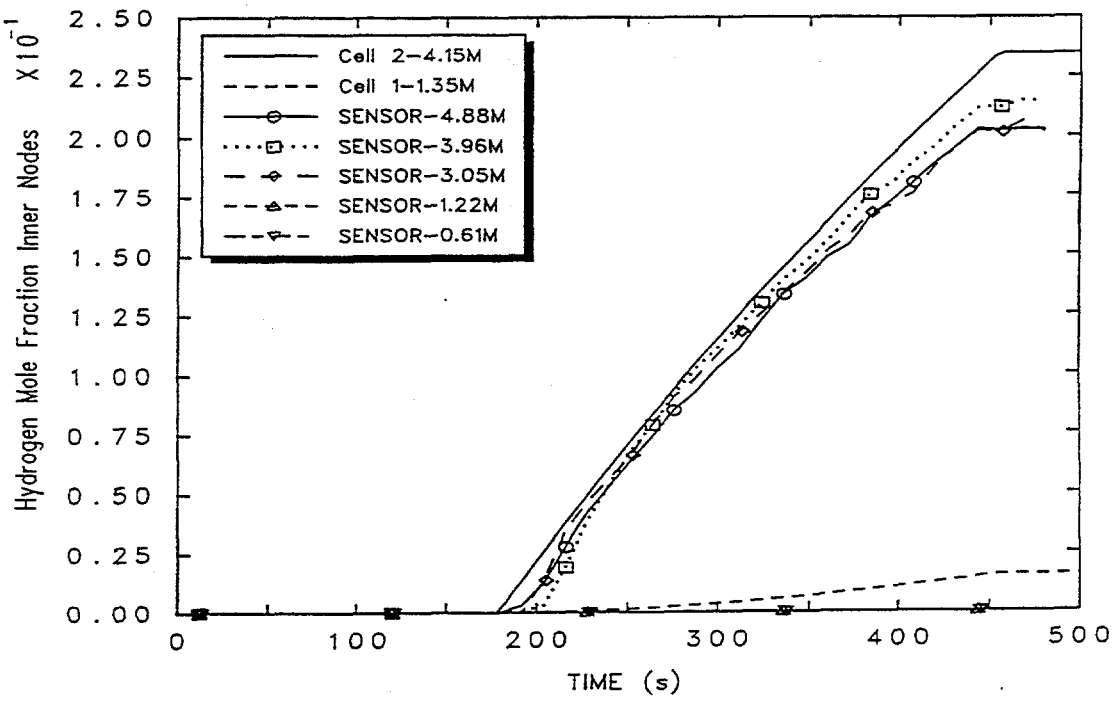

Figure 3.45. Comparison between the predicted hydrogen distribution for the inner cells for Surtsey test ST-3 using the 3-cell nodalization and the old gravitational head formulation and the experimental data[Blan95].

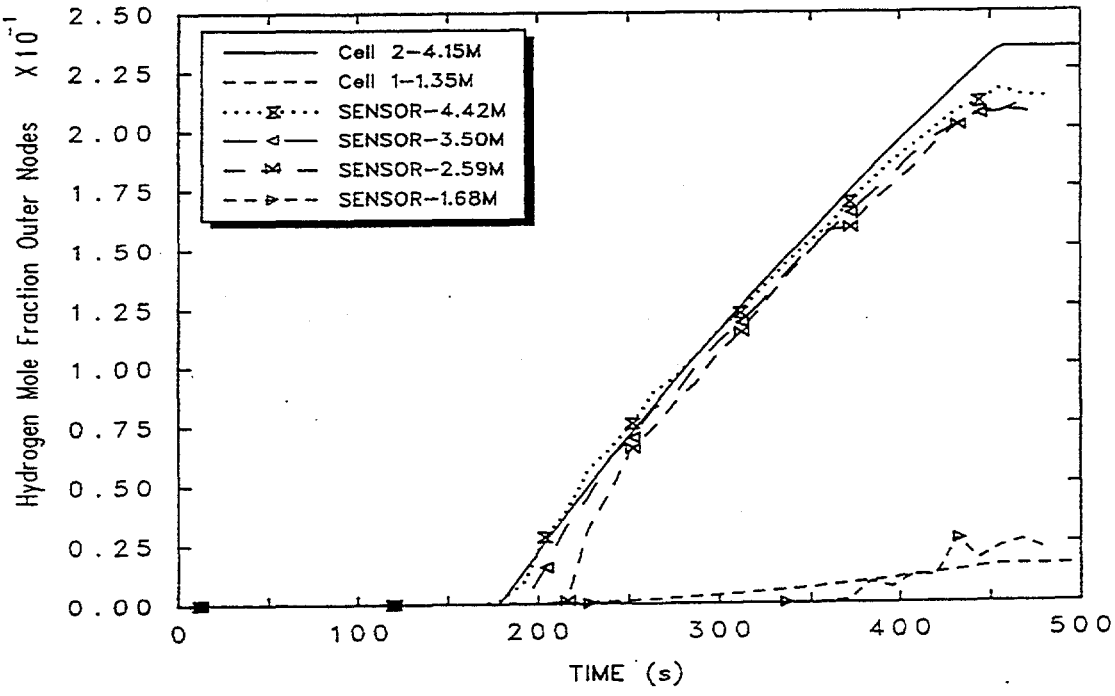

Figure 3.46. Comparison between the predicted hydrogen distribution for the outer cells for Surtsey test ST-3 using the 3-cell nodalization and the old gravitational head formulation and the experimental data[Blan95].

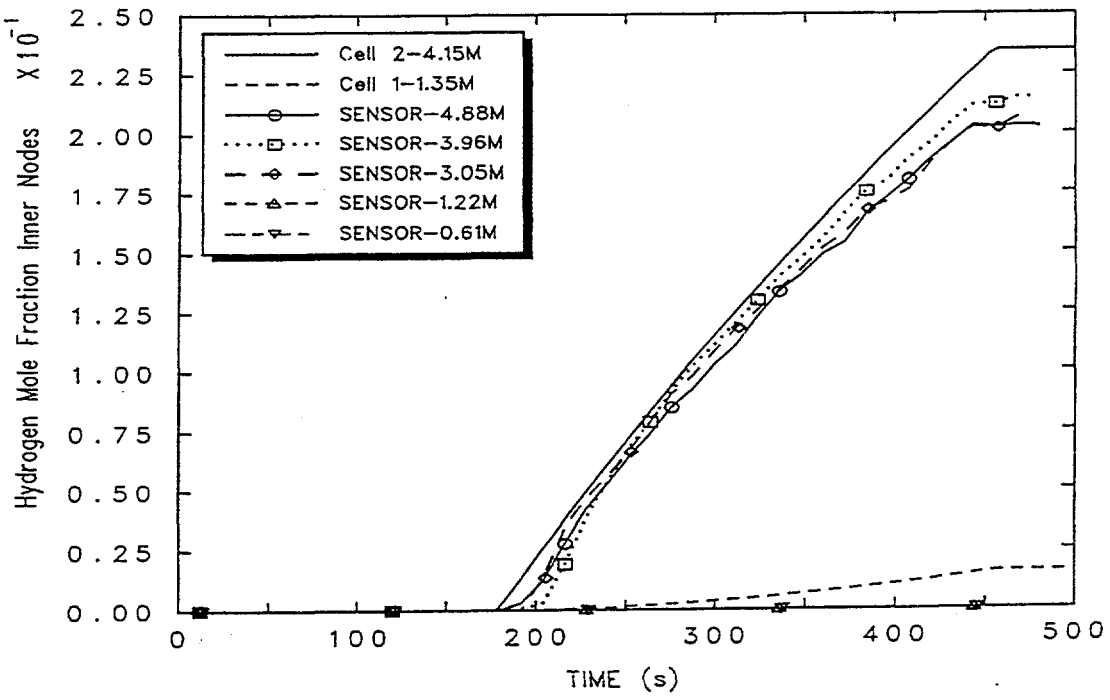

Figure 3.47. Comparison between the predicted hydrogen distribution for the inner cells for Surtsey test ST-3 using the 3-cell nodalization and the hybrid formulation and the experimental data[Blan95].

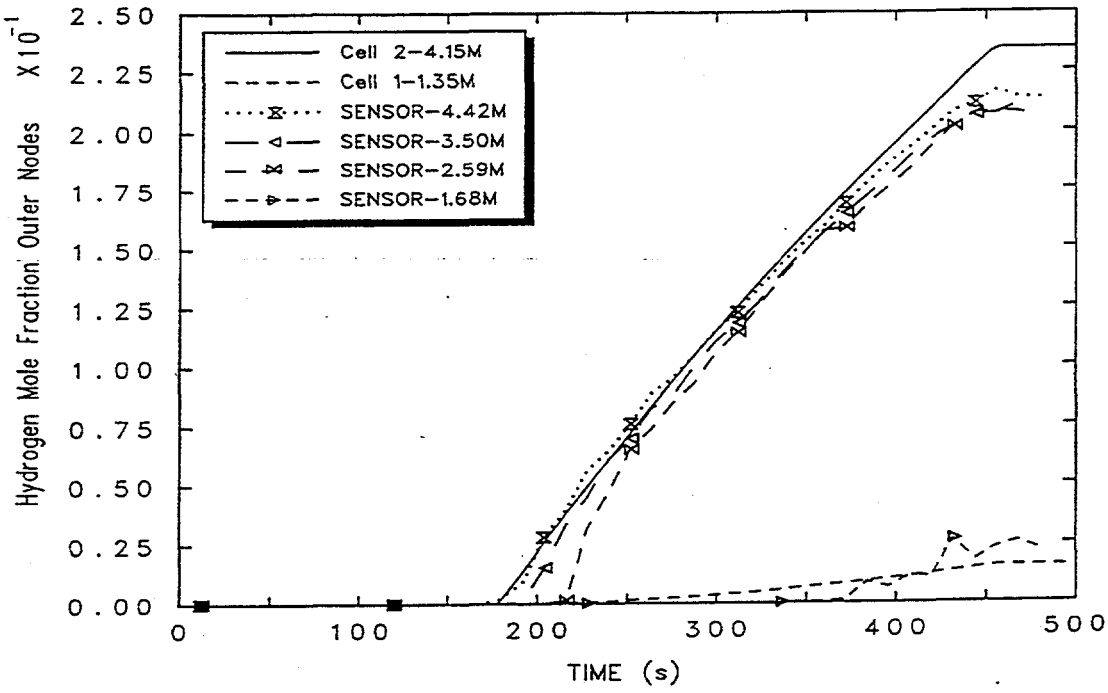

Figure 3.48. Comparison between the predicted hydrogen distribution for the outer cells for Surtsey test ST-3 using the 3-cell nodalization and the hybrid formulation and the experimental data[Blan95].

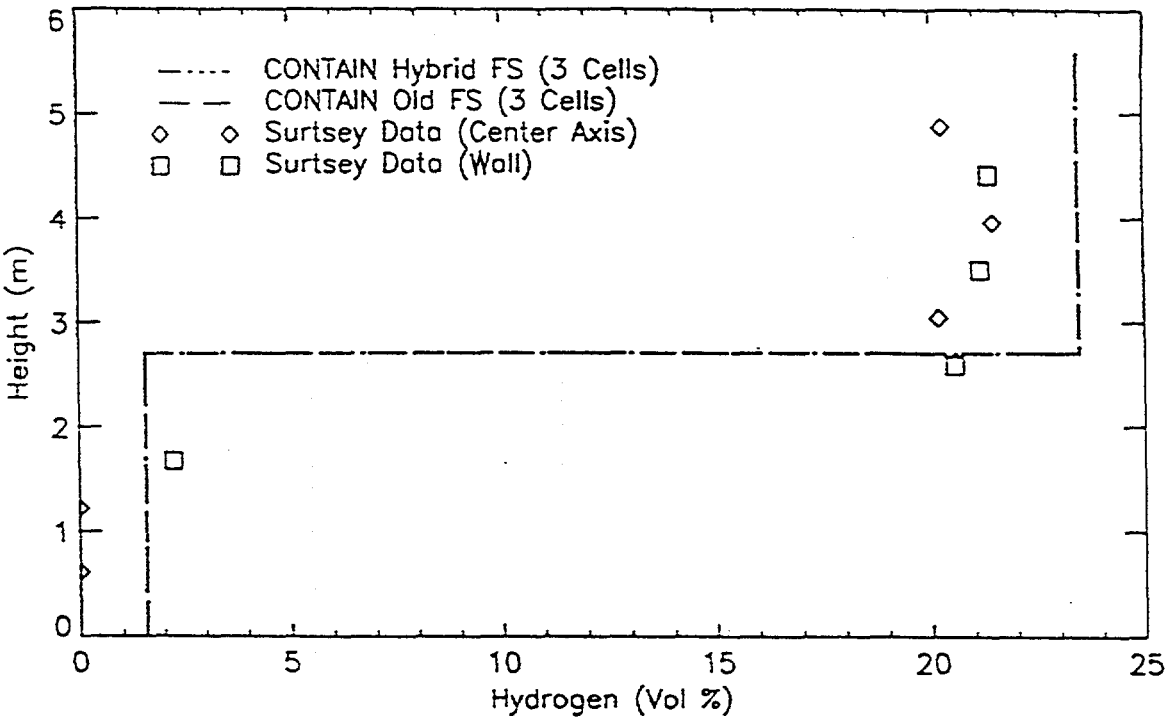

Figure 3.49. Comparison between the predicted hydrogen distribution for Surtsey test ST-3 using the 3-cell nodalization and the hydrogen microsensor measurements[Blan95].

cell layer immediately below the source can be nearly the same as in the cells above the source. In the limiting case that only one cell layer exists below the source, the nonphysical mixing may result in well-mixed conditions throughout the vessel. The largest nonphysical mixing occurs in the cell layer immediately below the source. As the number of cell layers below increases, the most pronounced effects of the nonphysical mixing are confined to a smaller and smaller volume. However, nonphysical mixing still occurs to some extent in all of the layers below.

3.3. The HDR E11.2 Experiment (ISP-29)

The HDR E11.2 experiment was the subject of the ISP-29 International Standard Problem[Karw92], a containment thermal-hydraulic code comparison exercise. ISP-29 had a large number of participants using a number of control volume codes, and included a submittal, using CONTAIN, from Sandia National Laboratories. This standard problem is of particular interest because it gave a convincing demonstration of the fact that the participating control volume codes, including CONTAIN, showed an inability in general to capture the degree of stratification that was observed in the experiment. The CONTAIN versions used in this exercise pre-dated the hybrid solver modification and as expected gave results qualitatively similar to the "old" solver results presented below.

One purpose of the present work is to assess the degree to which the hybrid solver improves on the results of the old solver. It should be clear from the NUPEC M-8-1 results above that the hybrid solver predicts the behavior of stable, fully developed stratifications, as defined in Section 2.4, fairly well. However, the stratifications in the E11.2 experiment do not seem to fit into this category. Although the stratifications were presumably stable against the momentum convection of the applied sources, the stratified layers had at times considerably more diffuse boundaries than generally expected with a stable, fully developed stratification, and conditions above the injection point were not always well-mixed. At certain times, the boundaries between stratified layers were also observed to move and/or destabilize with the application of a new source or sink. Thus, the E11.2 experiment is a good test case involving the general behavior of buoyancy-dominated stratifications.

The HDR de-commissioned-reactor facility has been the subject of a number of containment tests and has been described in a number of publications. Therefore the details of the facility will not be given except as necessary for the reader to understand the results presented below. A schematic of the facility is given in Figure 3.50. It should be noted that the containment pressure boundary in the upper containment is a steel shell, located inside of and separated by a substantial gap from an outer concrete shell that serves as a missile shield.

The E11.2 experiment utilized a number of sources at different levels: (1) a preheat steam source injected at the upper, mid-elevation "break" location indicated in Figure 3.50, (2) a mid-elevation steam and light-gas (hydrogen/helium) source, also at this break location, (3) a low-elevation steam source, at the lower break location indicated in Figure 3.50, and (4) an external spray of water directed on the outside of the steel dome of the containment. The timing of these sources was approximately sequential and is given in detail in Table 3.1. The dynamics of the stratifications formed during the experiment were extremely complicated. However, the behavior of stratifications observed in the experiment can be summarized as follows: (1) During the preheat period a stratified

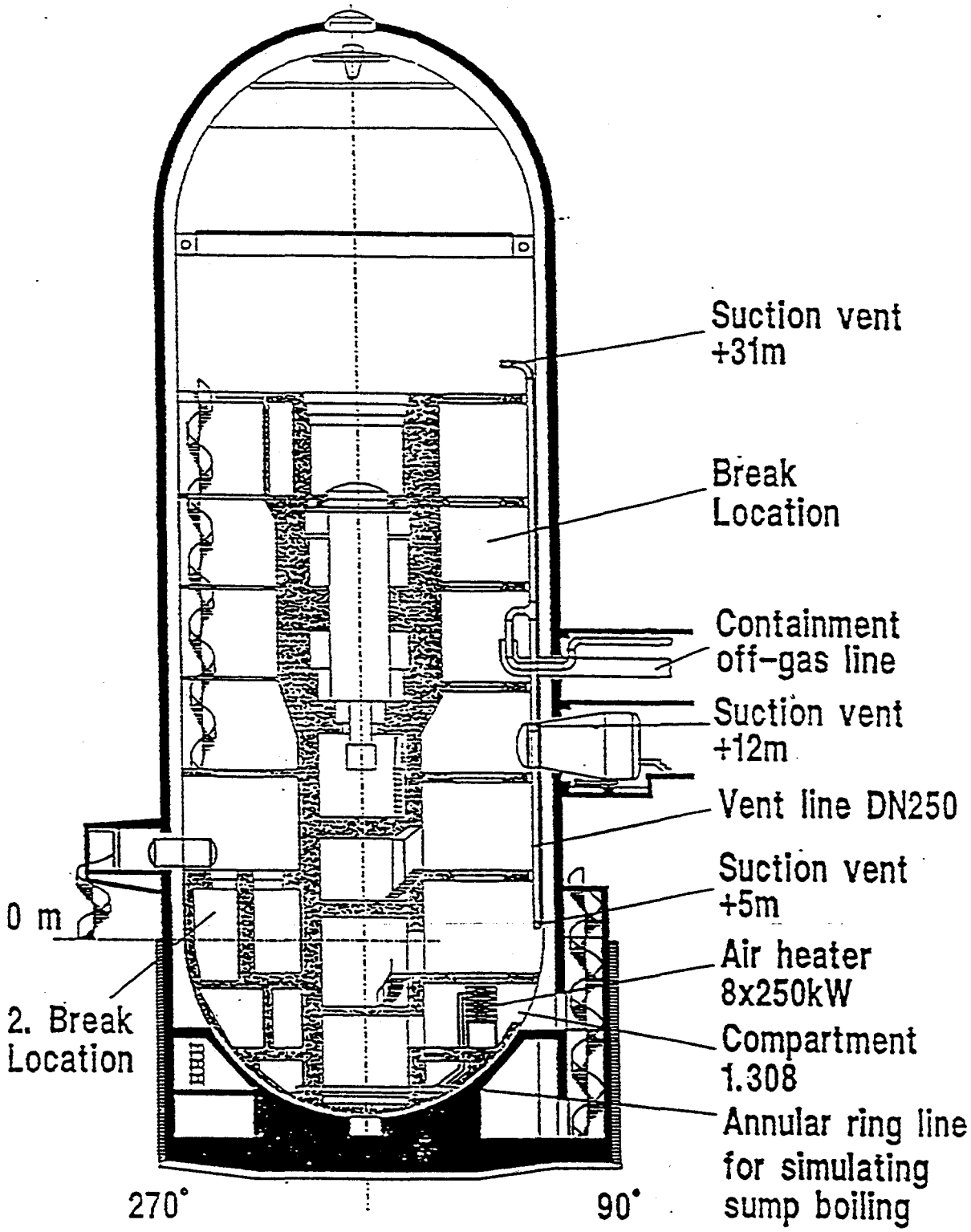

Figure 3.50. Schematic of the HDR facility, with the source locations in the E11.2 experiment[Karw92].

Table 3.1. Chronology of Operational Events of Experiment E11.2

Period	Time, minutes	Description
1. Heatup	0.0	Start small LOCA and upper external steam (R1805)
	693.8	End LOCA and reduce external steam
2. Gas injection	739.4	Start of light-gas injection (R1805)
	750.0	End of upper external steam
	772.3	End of gas injection
3. Lower steam	772.9	Start of lower external steam (R1405)
	958.8	End of lower external steam
4. Outer spray	975.0	Start of outer spray on dome
	1203.0	End of spray period and start of cooldown
5. Cooldown	1445.0	End of cooldown period

steam layer formed in the upper containment with a diffuse lower boundary located below the injection point. (2) The mid-elevation injection of light gas resulted in a light-gas layer with a higher degree of stratification than the preheat steam layer. (3) The low-elevation steam source resulted in plumes that presumably rose up under the light-gas layer, to a neutral buoyancy point just below the layer. Because other sources had been shut off at this point, this steam pressurized the lower containment, resulting in upward movement of the lower boundary of the light-gas layer. (4) The application of water sprays on the outside of the steel dome resulted first in the concentration of light gas in the dome, because of the condensation of steam on the interior of the dome, and then resulted in a gradual downward movement of the lower boundary of the light-gas layer.

While the HDR E11.2 experiment is interesting with regard to the observed stratification behavior, it should be noted that considerable difficulty[Karw92,Wenz91] was encountered by the HDR project in characterizing the experiment sufficiently well for code comparison purposes. The main problems were of two types: (1) The HDR project did not initially characterize a major heat sink in the experiment, namely, the chilled water lines routed into the containment to regulate the temperature of the instrumentation in the experiment. The heat losses from the containment to these instrument cooling lines were estimated by the project through a post-experiment analysis. They were of order 1 MW with an estimated uncertainty of ± 0.3 MW. (2) The steam mass injection rates in the

experiment were initially incorrectly specified because of calibration errors in the metering orifices used. A post-experiment recalibration determined the steam injection rate to be 62% of that originally specified. The revised rate was calculated to be approximately 2.1 kg/sec during the preheat period and the low-elevation steam injection period with known uncertainties of order +8% and -6%[Wenz91].

The analysis began with a modified 14-cell deck, based on the deck used in the original ISP-29 submittal. The results from this deck are discussed in Section 3.3.1. This modified deck shows a tendency to give excessively stable stratification during the preheat period when the hybrid solver is used. This behavior is related to the onset of stability associated with nearly free plume behavior. This stability was predicted in the case of the NUPEC M-8-1 experiment and lead to good agreement with experiment. It is interesting, in the case of the E11.2 experiment, that the onset of stability during the preheat lead to poorer agreement. As discussed in Section 2.4, when stability is achieved, the flow behavior changes from a buoyancy-driven loop flow behavior to plume-like. The poorer agreement found with plume-like behavior is consistent with the apparent intent of the experimenters[Vale89] to induce loop-flow behavior, rather than plume-like behavior, in the upper containment. While interesting, such loop-flow behavior depends heavily on the peculiarities of the HDR containment; namely, the existence of two long and essentially independent flow channels adjacent to the reactor pressure vessel (RPV), connecting substantial volumes above and below the RPV region. Thus, it is not clear that this loop-flow behavior is particularly relevant to the gas flow behavior in other containments.

The difficulty with the onset of stability lead to a re-evaluation of the 14-cell deck, as discussed in Section 3.3.2. This re-evaluation lead to a 15-cell deck, the results from which are discussed in Section 3.3.3. Sensitivity calculations based on the 15-cell deck are discussed in Section 3.3.4.

3.3.1. Calculations with the 14-cell Deck

Preliminary calculations for the E11.2 experiment for this report were done with the original 14-cell CONTAIN deck used in the Sandia National Laboratories submittal that was published in the ISP-29 report[Karw92]. Figure 3.51 shows the nodalization used in this deck. Figure 3.52 indicates the regions of the facility assigned to each of the interior cells. The reader will note that the nodalization looks somewhat different from the previously presented Surtsey ST-3 and NUPEC M-8-1 decks, which were designed from the start to deal with stratification. Despite the relatively simple nodalization, the ISP-29 submittal deck was selected as a documented starting point.[3] The

[3] A 47-cell deck was also developed at Sandia National Laboratories and used in the design phase of the E11.2 experiment[Vale89]. However, because of time constraints, the 47-cell

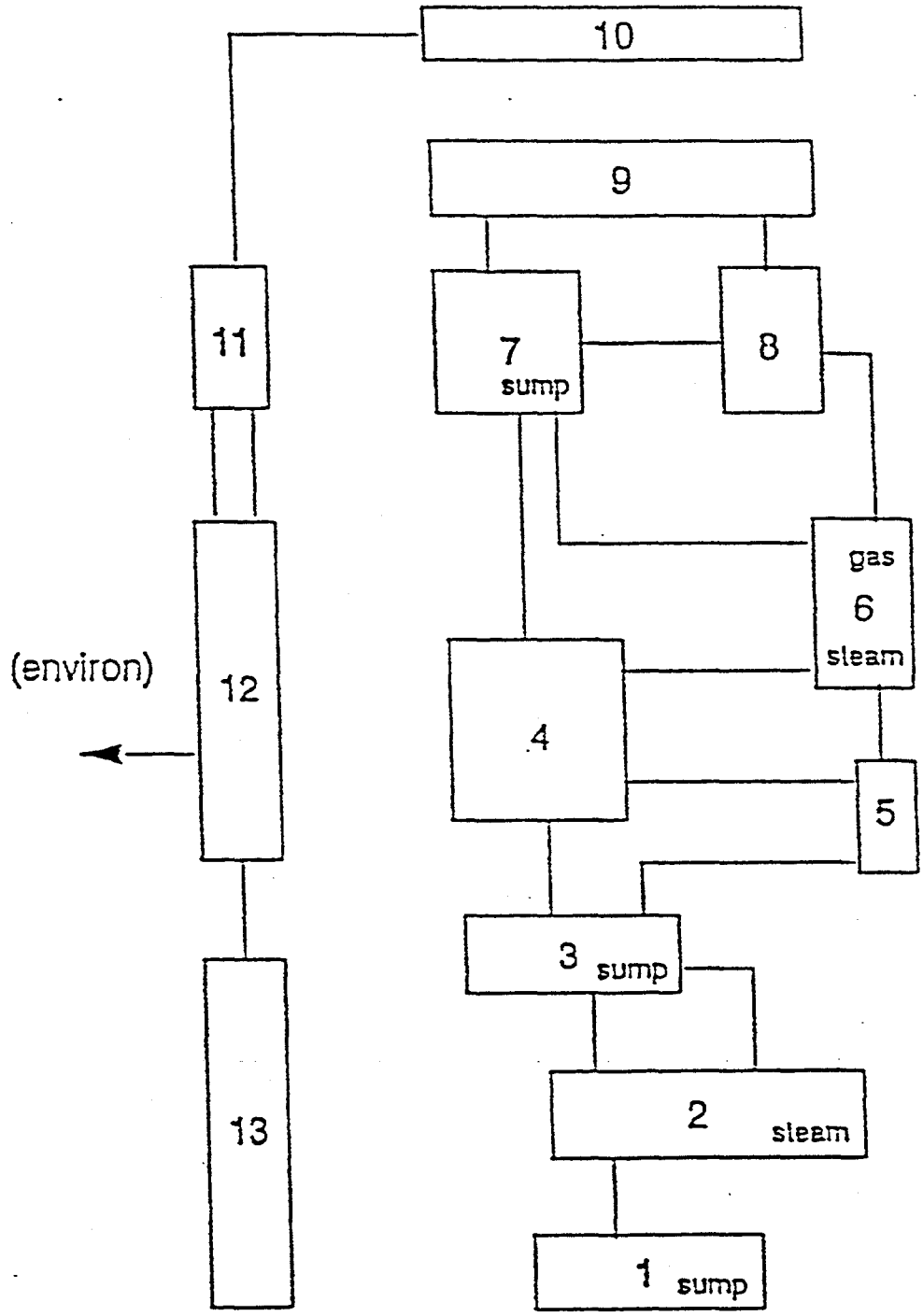

Figure 3.51. Schematic of the HDR 14-cell deck.

---

deck was not used for the ISP-29 submittal.

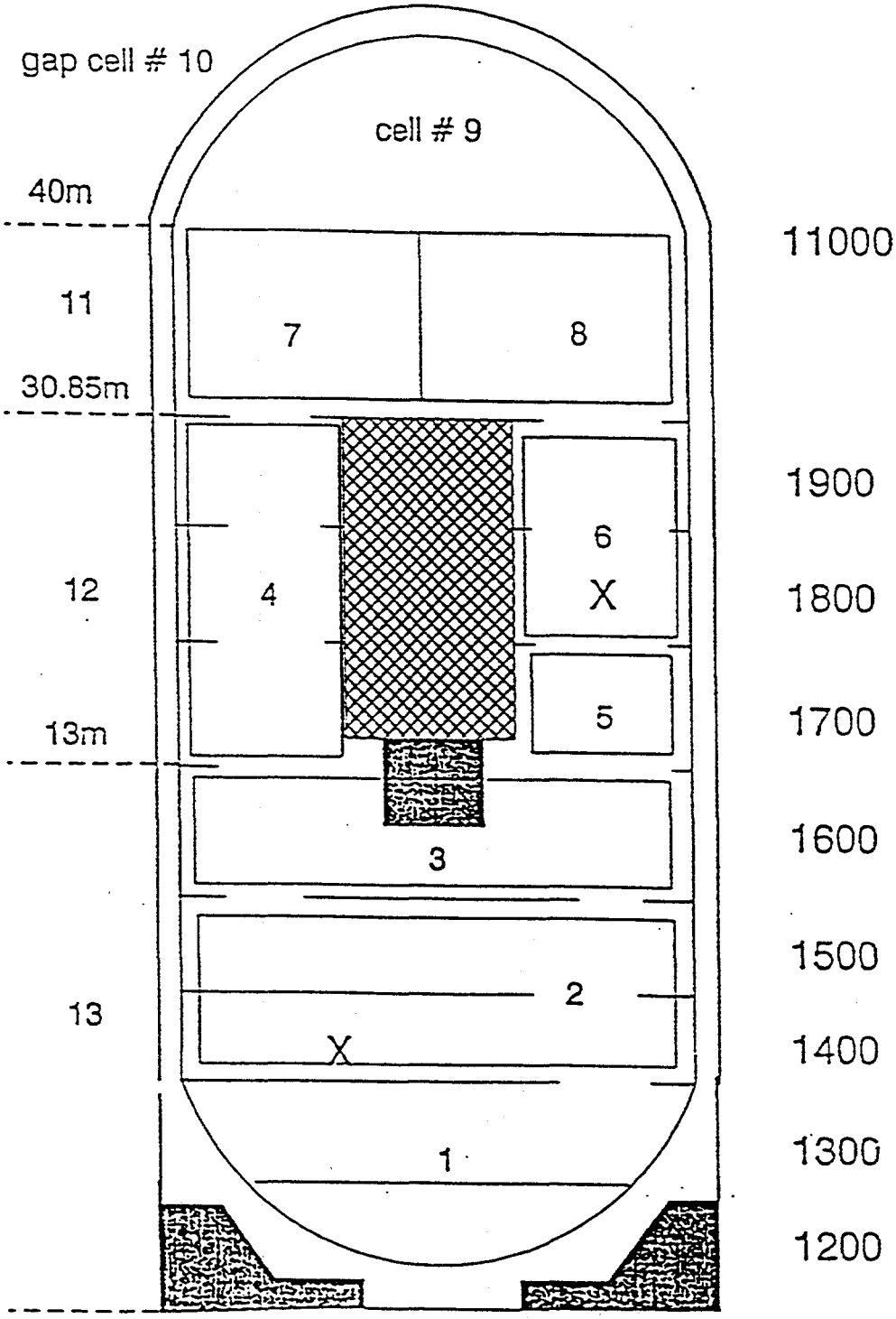

Figure 3.52. Layout of the HDR 14-cell deck.

philosophy was to start with this deck and to modify it to the extent necessary to remedy problems as they became apparent.

The preliminary runs and deck inspection uncovered three problems with the original submittal deck. The problems and how they were addressed are as follows: (1) A pool was inadvertently omitted in cell 3. This pool should have been present to intercept draindown of condensate from the upper containment, and then to allow the condensate to overflow to the sump in cell 1. This omission caused a substantial amount of water, which potentially could be a substantial sink, to be lost from the problem, and therefore a pool in cell 3 was defined in the input. (2) In CONTAIN 1.2, the pool area is now defined according to the cell cross-sectional area, not the lower cell basemat area. Thus, the cell cross-sectional areas were redefined so that the old pool areas (though only nominal) were recovered. (3) In the original 14-cell deck, parallel flow paths with elevation offsets are used to promote mixing between cells 2 and 3 and between cells 11 and 12. This mixing is to some extent unphysical and therefore was modified, as discussed below. It should be noted that this last modification with regard to mixing has significant effects on the predicted pressure and on the predicted stability of the stratifications in the upper containment with the hybrid solver.

The offset parallel flow paths in the 14-cell deck were originally used because the nodalization otherwise would not allow gas circulation between cells 2 and 3 during the low-elevation steam source or between cells 11 and 12. The difficulty with the offsets is that circulation is present when any density difference exists between the two cells, and this circulation is unphysical when the difference corresponds to a stable stratification.

For example, during the preheat period, the source elevation lies well above cell 3 and one would expect any steam working itself down to the level of cell 3 to be reasonably stable against further mixing with cell 2. The two cells therefore should not mix. However, during the low-elevation steam source introduced later into cell 2, it is reasonable to expect the buoyant steam source to mix the region above the source elevation, up to the point of neutral buoyancy. This point for the low-elevation steam source appears to have been approximately the lower boundary of the light-gas layer lying above cell 3. Thus, mixing between cells 2 and 3 should occur during the latter source. The input was therefore changed so that mixing between cells 2 and 3 through parallel paths is present only during the low-elevation steam source, and a fixed mixing rate of 16 kg/s was chosen to give a substantial amount of mixing. (Note that a more sophisticated plume model for the mixing rate is discussed in one of the sensitivity calculations presented below in conjunction with the 15-cell deck.)

In addition to this change in the mixing between cells 2 and 3, the mixing between the gap cells 11 and 12 through parallel paths was eliminated. Such mixing could be important because the containment steel shell is uninsulated above the operating deck and insulated below, at least according

to the original experiment specification. Any mixing between the above-deck and below-deck gap regions would allow gas that is heated by conduction through the shell above the operating deck to communicate with the substantial heat sinks (i.e., the concrete missile shield) below the deck. The problem is that one would expect the colder gas in the lower gap regions to be stable against the convective mixing in the dome region. From the experimental data, the gas below 25 m appears to have been decoupled from the convective mixing in the dome[Wolf95], during the preheat. Since the elevation of cell 12 is somewhat lower, at 22.4 m, the mixing between cell 11 and cell 12 was eliminated. However, it should be noted that the gap nodalization is not optimum with regard to mixing in the gap, since cell 12 spans 3 containment levels and straddles the mixed and unmixed regions.

One further problem with the 14-cell deck is related to a previous code limitation regarding the treatment of the wetting of the outer steel dome by sprays, which were initiated at 975 minutes. At the time of the ISP-29 submittal, this dome wetting could not be modeled through existing models, and therefore a simple model was implemented through a code modification. While these sprays now can be modeled (and are modeled in the 15-cell deck discussed below), the necessary input was not added to the 14-cell deck. Thus, the present 14-cell calculations will be compared to experiment only up to spray initiation.

The modifications discussed above were implemented and the modified deck was rerun. The results for the pressure for the modified 14-cell deck are given in Figure 3.53 for both the old and hybrid solvers. The measured pressure is also shown. The end of the preheat period occurs at 694 minutes and coincides with the first sharp drop in pressure seen in this figure. It should be noted that the predicted peak pressure with the old solver no longer has the excellent agreement with experiment found with the original ISP-29 submittal[Karw92].

The elimination of unphysical mixing through parallel paths between cells 2 and 3 and between cells 11 and 12 is believed to be responsible for the fact that the predicted peak pressure for the old solver now lies about 20 kPa above that found in the experiment. As discussed below, during the preheat the predicted steam concentration with the old solver tends to be localized in the upper containment, above cell 2. Eliminating the unphysical mixing between cells 2 and 3 thus would reduce the steam and the steam condensation occurring in cell 2. As discussed above, eliminating the unphysical mixing between cells 11 and 12 eliminates convective mixing between cell 11, which is heated by conduction through the containment shell, and cell 12, which has substantial heat sinks corresponding to the concrete missile-shield. The unphysical mixing would thus tend to decrease the pressure. In Figure 3.53, we note that the peak pressure predicted with the hybrid solver is considerably higher than that predicted with the old solver and that found in the experiment. The discussion of this result is deferred until Section 3.3.3, since the same is true of the 15-cell deck, although the overprediction

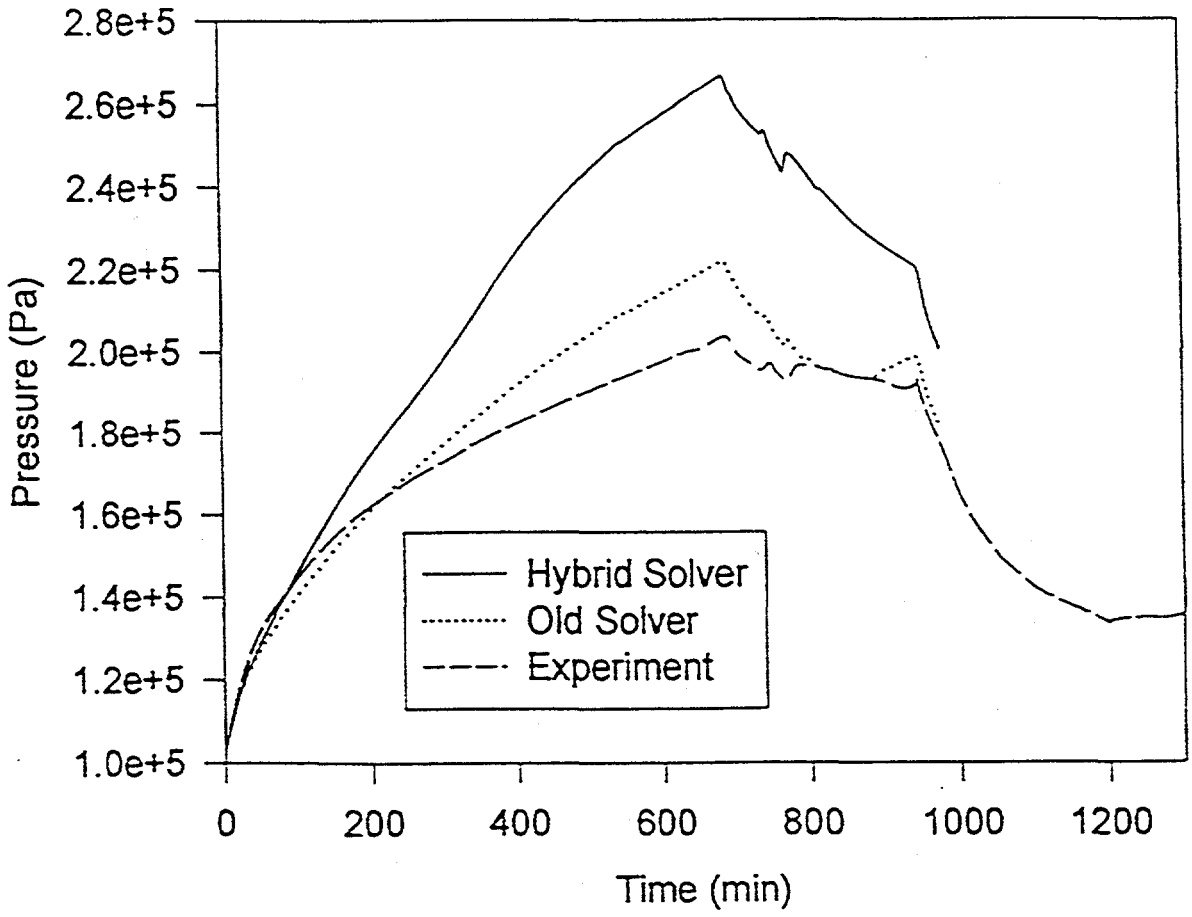

Figure 3.53. Gas pressures obtained with the modified 14-cell deck and the old and hybrid flow formulations, compared to experiment[Karw92].

in pressure is not as great.

The predicted temperature distributions are given in Figures 3.54 and 3.55 for the old and hybrid solvers, respectively, and the steam distributions are given in Figures 3.56 and 3.57, respectively. (The 80° azimuth corresponds to the side of the containment, also referred to as the "staircase" side, on which the mid-elevation sources were introduced; the 280° azimuth corresponds to the side of the containment containing the "spiral" stairway.) The preheat steam was injected at an elevation of approximately 23 m, in cell 6. The above figures show that the predicted region of high temperatures and steam concentrations extends much lower in the containment with the old solver than with the hybrid solver.

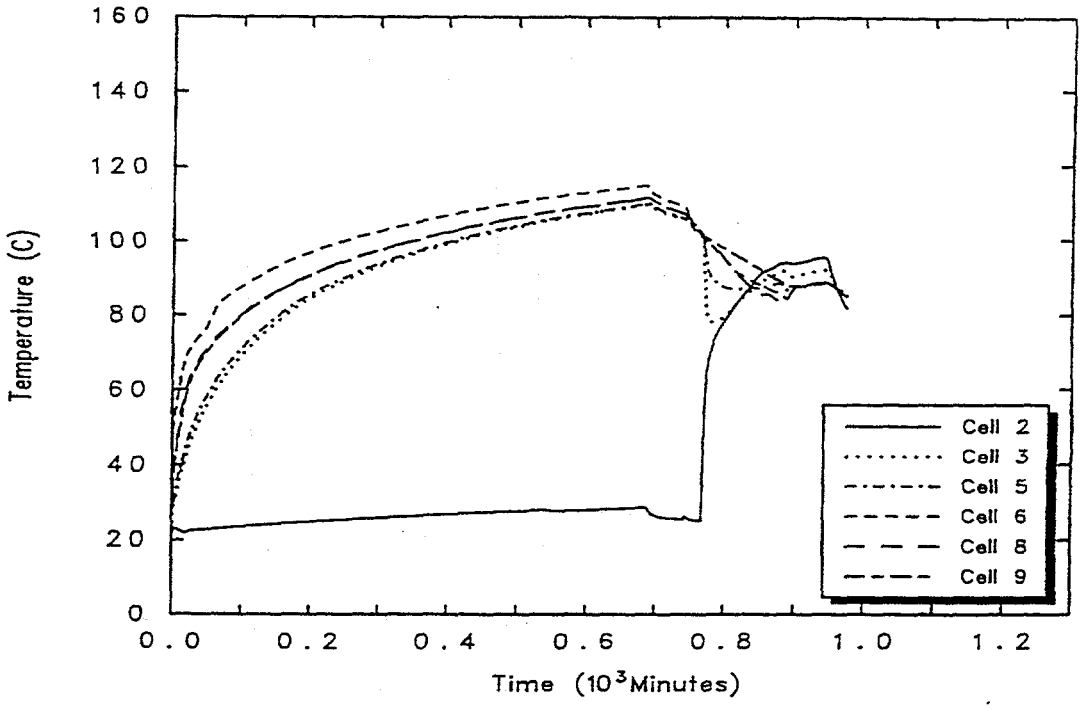

Figure 3.54. Gas temperatures obtained with the old gravitational head formulation and the modified 14-cell deck (80° azimuth).

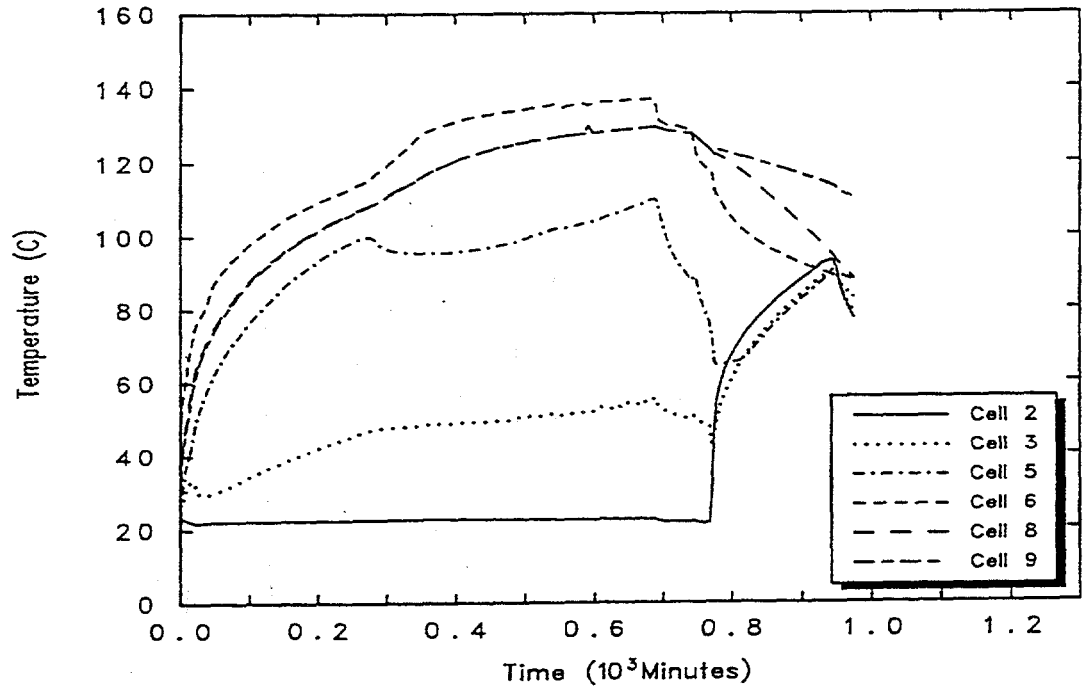

Figure 3.55. Gas temperatures obtained with the hybrid formulation and the modified 14-cell deck (80° azimuth).

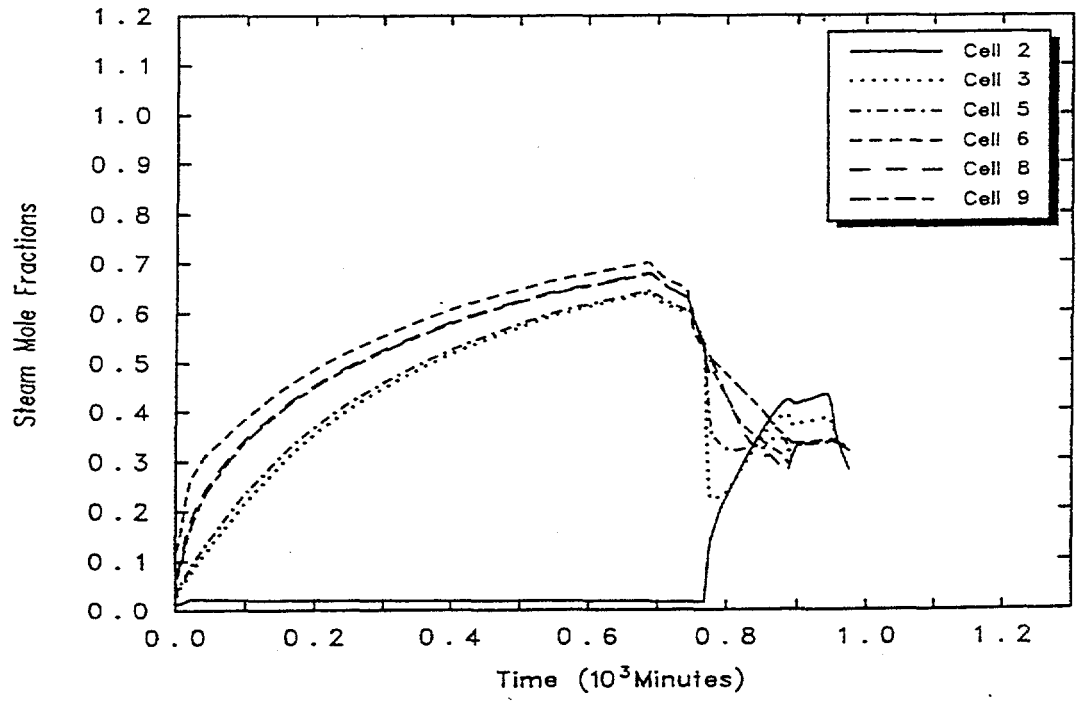

Figure 3.56. Steam mole fractions obtained with the old gravitational head formulation and the modified 14-cell deck (80° azimuth).

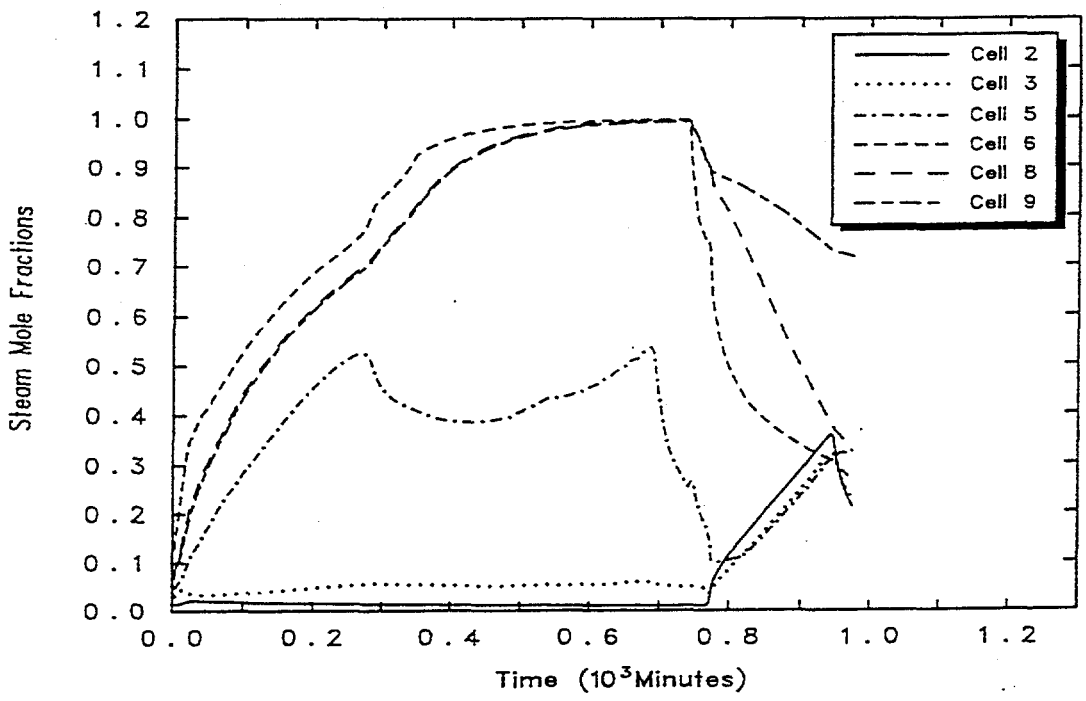

Figure 3.57. Steam mole fractions obtained with the hybrid formulation and the modified 14-cell deck (80° azimuth).

In the experiment light-gas injection began at 740 minutes at the mid-elevation location. The predicted light gas distributions are shown in Figures 3.58 and 3.59. The light gas distribution clearly extends to lower elevations with the old solver than with the hybrid solver.

Returning to Figures 3.55 and 3.57, we note that an abrupt change in behavior occurs in the predicted temperatures and steam concentrations in the hybrid solver calculation at 290 minutes, and thereafter the stratification becomes more severe, with concentrations of steam in the dome approaching unity. As we discuss in Section 3.3.3, such steam concentrations are inconsistent with the peak dome steam concentrations of approximately 70% - 80% found in the experiment. The abrupt change is related to the threshold at which the *de facto* or control volume stability condition (i.e., the analog of Equation (2-14) for the irregular geometry of the 14-cell deck) begins to be satisfied.[4] As discussed in Section 2.4, this threshold is related to the crossover between buoyancy-driven loop-flow behavior and stable behavior. Prior to the onset of stability, loop-flow behavior involving cells 4, 5, 6, 7, 8, and 9 is present, with cell 4 forming the downward-side of the loop, and cells 5 and 6 forming the upward side. When stability is present, the gas below the source cell (cell 6) is excluded from participation in the entrainment flow occurring at the source level and above. In the case of the 14-cell deck, the onset of stability creates an severe stratification with high concentrations of steam in cells 6, 7, 8, and 9. Note that cell 4 is excluded from participation because its center of volume is located below that of cell 6.

One should contrast this late onset of stability in E11.2 to the behavior in the NUPEC M-8-1 and Surtsey ST-3 comparisons, in which *de facto* stability is predicted and established relatively early in the calculation. In the M-8-1 comparison, this stability is necessary for good agreement with experiment, since without it the stratification would look more like the old solver results. In the ST-3 comparison, *de facto* stability is similarly predicted and is consistent with the fact that the mechanism in that experiment leading to marginally unstable conditions, momentum convection, is not modeled in the code.

The considerable difference in *de facto* stability in these calculations and that for E11.2 is related to the peculiar geometry of the latter experiment. This geometry consists of two long, essentially independent flow channels (formed by cell 4 and by cells 5 and 6) alongside the RPV. In addition, the mid-elevation sources were injected into the containment at the midpoint of one of these channels. This geometry is reflected in the deck by the fact that the paths for entrainment flow into the source

[4]It should be noted that this stability is marginal. Prior calculations with the hybrid solver indicated that the onset of stability could be delayed throughout the entire preheat period by making minor changes that reduce the stability of the stratification.

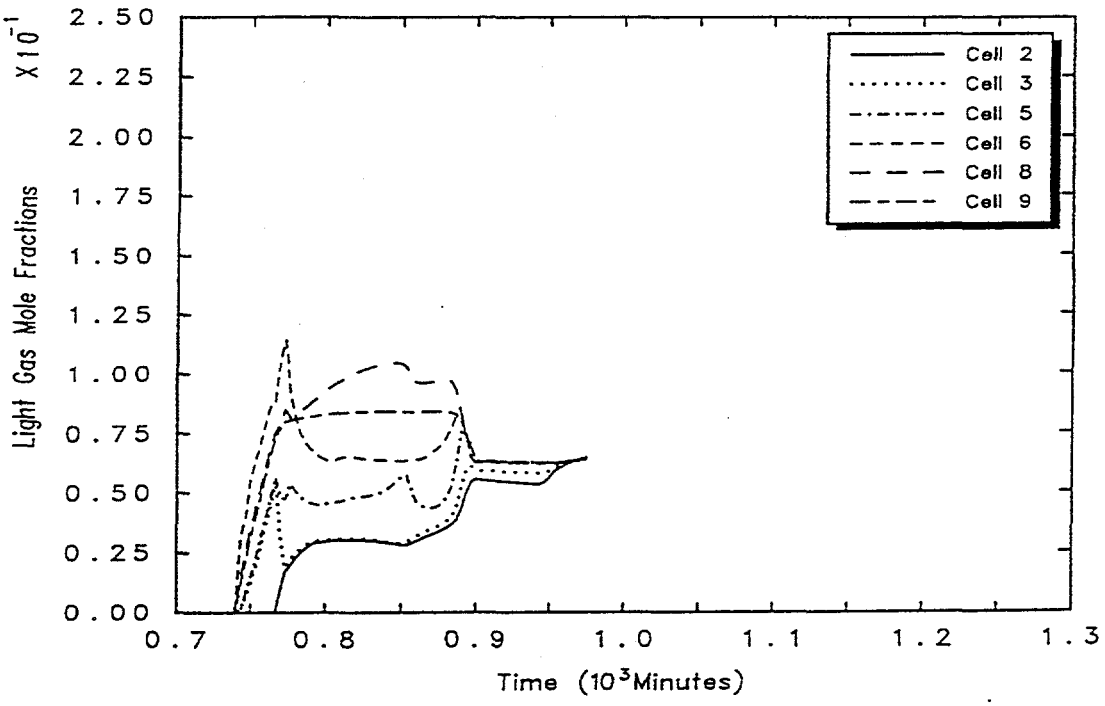

Figure 3.58. Light gas mole fractions obtained with the old gravitational head formulation and the modified 14-cell deck (80° azimuth).

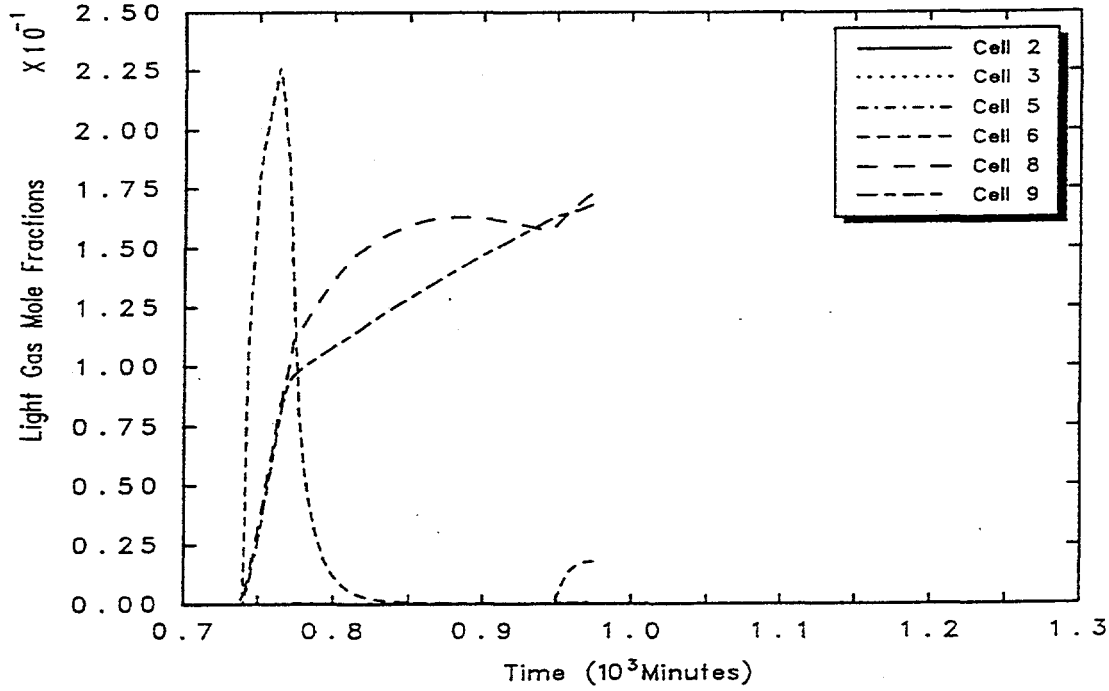

Figure 3.59. Light gas mole fractions obtained with the hybrid formulation and the modified 14-cell deck (80° azimuth).

cell at the source cell level and above are highly restricted: the flow area between cell 7 and cell 6 is only 0.42 m^2 and that between cell 4 and cell 6 is only 0.56 m^2. Consequently much of the entrainment flow may be forced to occur by way of the cell 5, the cell below 6, resulting in a "loop-flow" condition. In contrast, in the M-8-1 and ST-3 experiments, the source cell was an open volume, and the entrainment flow areas at the source level and above were unrestricted. Consequently, one would expect stable plume-like behavior to be predicted.

3.3.2. Development of the 15-cell HDR Base Case Deck

As discussed above, the onset of stability during the preheat period in the hybrid solver calculation with the modified 14-cell deck considerably worsened the agreement with experiment. This discovery lead to a re-evaluation of the modified 14-cell deck. The key question in this re-evaluation was the nature of the stratifications generated by the mid-elevation sources. To address this question we give in Table 3.2 the Froude numbers and ratio $\Delta H / D_0$ of the total rise height to jet diameter for the sources in the experiment. The Froude number and height-to-diameter ratio determine the stability of a stratification with respect to momentum convection, for a stratification created by a free vertical buoyant jet in a semi-infinite volume, with a ceiling but without confining walls. The stability category, determined from the Froude number and height-to-diameter ratio, according to the Peterson correlation given in Reference Pete94, is also given in Table 3.2 for each source. The stability categories indicate that the sources were at most marginally unstable when treated as free jets.

The actual nature of the stratifications that occurred in E11.2 with respect to the mid-elevation sources is difficult to characterize, because of the complicated geometry involved. The mid-elevation sources were not free jets but impinged directly from horizontal pipes against the vertical wall of an elevator shaft, at an elevation of approximately 23 m. The effect of the wall impingement, presumably, was to dissipate the momentum of the high velocity jets and enhance mixing with the surrounding gases. The access panels to this shaft, in turn, were open to allow the shaft to communicate with the neighboring stairwell, located at the 80° sector of the containment and previously referred to as the "staircase." The shaft/staircase in turn formed one of two main channels connecting the regions above and below the RPV. Thus, there were three sets of vertical boundaries of relevance to a discussion of entrainment flows: (1) the elevator shaft walls, (2) the shaft/staircase channel boundaries, and (3) the containment shell, or pressure boundary. Clearly, because of this complicated geometry, the exact nature of the mixing of the mid-elevation sources cannot be determined without detailed experimental measurements or computational fluid dynamics calculations, neither of which is available. However, because Table 3.2 indicates the sources were at most marginally unstable as free jets, and because of the dissipative and entrainment enhancement effects of wall impingement, it is likely that the mid-elevation sources were in fact stable against momentum convection effects, on the scale of the rise height. Note that this stability rules out recirculatory flow

Table 3.2. Free-jet stability, based on momentum convection effects, for various sources in the E11.2 experiment

Source Type	Froude Number† $=\rho_a U_0^2/[g(\rho_a-\rho_0)D]$	ΔH/D	Free Jet Stability††
Upper external steam (Preheat)	1.8×10^6	355	Marginally stable
Upper external steam (Reduced)	6.2×10^5	355	Marginally stable
Light gas	4.6×10^5	729	Stable
Lower steam	1.5×10^6	342 (estimated)	Marginally stable

†Based on estimates given in Reference Wolf96.

††Based on the Peterson correlation for stability, as given in Reference Pete94.

within the dome driven by momentum convection, but given sufficient mixing within the channel, buoyancy-driven loop flow involving the two main channels alongside the RPV is still possible.

It is obvious that the original 14-cell deck of Figure 3.51 is poorly suited to capturing vertical gradients in temperature and composition in the upper regions of the facility. For the purposes of capturing vertical density variations, it would clearly be desirable to use cells of consistent height and elevation at each given level of the containment, as was done with the NUPEC and Surtsey decks. It is also generally desirable to choose horizontal cell boundaries to coincide with source injection elevations, to be able to capture any fully developed stratifications that might arise in the problem. However, because of the diffuse nature and time-dependent position, in some cases, of the stratified layer interfaces in the E11.2 experiment, the benefit of the above nodalization guidelines was not obvious. Thus, the basic cell divisions and elevations used in the original deck were retained.

The following changes, made to the modified 14-cell deck to obtain the 15-cell deck, attempt to improve the deck with regard to the treatment of stratifications. The old cell 4 was split into an upper and lower part. Also, the buoyancy heads resulting from the mid-elevation sources were also increased through the adjustment of flow path elevations. In addition, the distribution of heat removal from the containment through the instrument cooling lines was also revised. Finally, input for modeling of the external dome sprays was added to the deck. The details of these changes are as follows:

1. Partitioning of the Old Cell 4 into an Upper and Lower Level. This change was motivated by the observation that the old cell 4, which spanned three containment levels, was too tall to capture stratification in the middle of containment. This was indicated by the fact that after the onset of stability in the 14-cell hybrid solver calculation, steam circulation began to be excluded from the old cell 4 (note that results for this cell are not explicitly presented in Figures 3.55 and 3.57). One reason for this exclusion apparently is that the center of volume of the old cell 4 was about 5 meters below that of cell 6. Since flow paths are attached effectively at cell centers with respect to the gravitational head calculations in the modified 14-cell deck, the denser gas in cell 4 would have to move uphill into cell 6 in order for circulation to occur through cell 4. In reality, a small flow path was present between the regions represented by cells 4 and 6 at the level of cell 6, and that would have allowed the upper part of cell 4 to included in the steam circulation even if the lower half was excluded. Thus, the old cell 4 was divided into an upper part (new cell 4) with vertical span similar to cell 6 and a lower part (new cell 14) with a vertical span similar to cell 5. The resulting 15-cell nodalization is given in Figure 3.60.

2. Refinement of the Instrument Cooling Line Heat Removal Modeling. As discussed in Reference Karw92, the heat removal from the containment through the chilled water lines used for instrument cooling during the E11.2 experiment had major uncertainties. The magnitude and distribution of this cooling effect could significantly affect the behavior of stratifications and also could be of some importance with respect to the pressure.

The recommended total heat removal rate through the instrumentation cooling lines [Karw92] was used in both the 14-cell deck and 15-cell deck. However, an inconsistency was apparent in the original 14-cell deck with respect to the spatial distribution of this heat removal rate, or cooling power, at late time. The problem was that the distribution of the cooling power was a fixed one and favored cooling in the dome (82.3 % of the heat removal was assigned in cells 7, 8, and 9). This distribution may be reasonable for the preheat period, during which the temperatures and steam concentrations in the dome were high and substantial steam was present throughout the upper part of the facility. However, after the preheat period, a stable light-gas layer formed in the upper part of the facility, and the temperatures and steam concentrations substantially decreased there, while substantial ones developed in the lower part of the facility as a consequence of the low-elevation steam source in cell 2. A redistribution of the cooling power presumably should accompany this change in conditions. Note that a large amount of cooling power in the dome would tend to destabilize the upper-containment steam layer and enhance mixing during the preheat, which seems desirable in view of the excessive stability found in the 14-cell deck during the preheat. However, such a distribution is not reasonable after the preheat and would tend to cause a premature

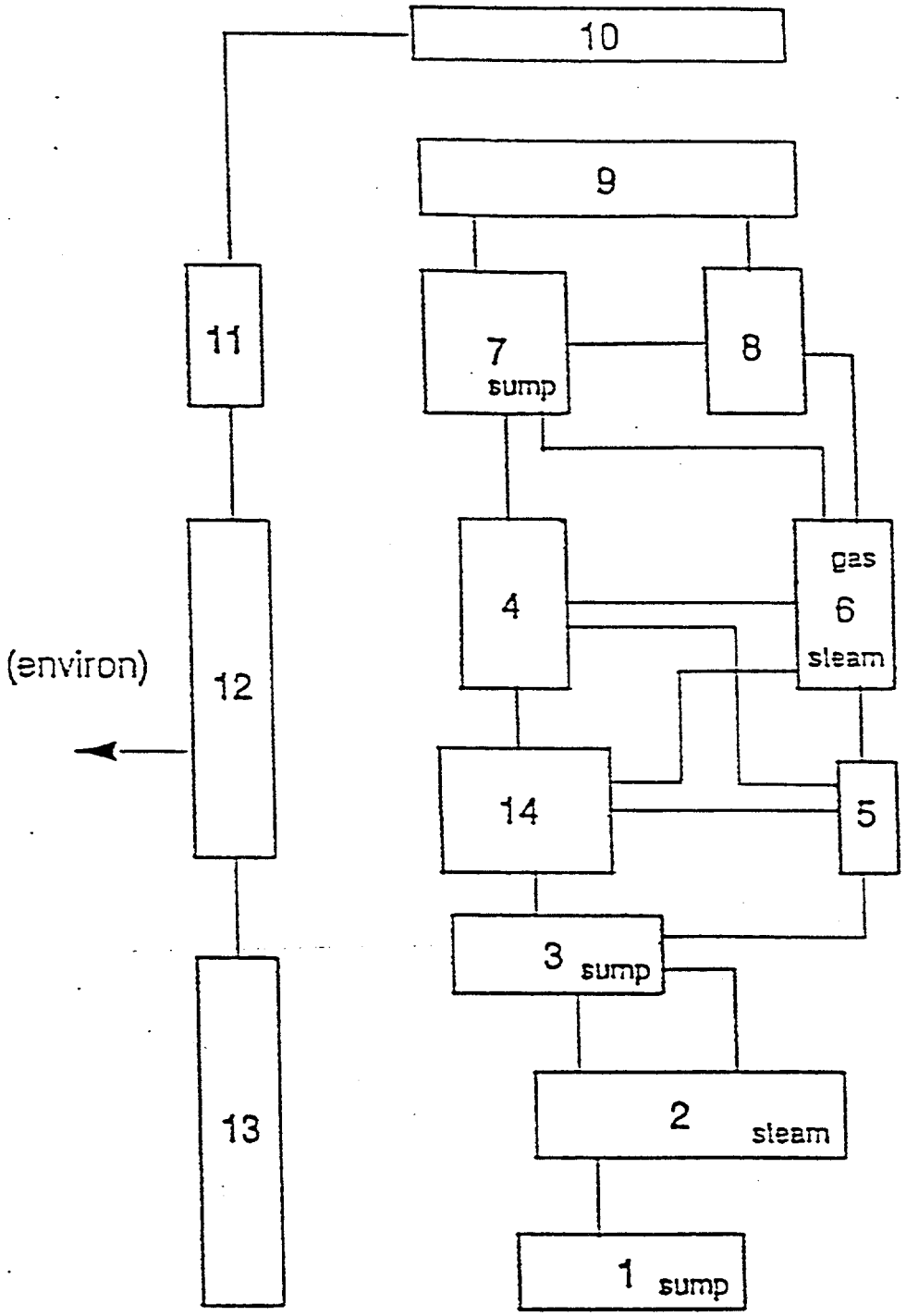

Figure 3.60. Schematic of the HDR 15-cell deck.

inversion of the light-gas layer at late time. Thus, an attempt was made to define the cooling power distribution in a realistic manner.

The approach taken to define the cooling power distribution for the 15-cell deck uses the cell weighting factors w_n given in Table 3.3. These are simply proportional to the number of cooled gas samplers found in each CONTAIN cell, as determined from facility drawings, since the distribution of samplers was the only readily available measure of the cooling power distribution. Since the heat extraction was likely to be dominated by steam condensation on the cooling lines, the fraction f_n of the total cooling power allocated to each cell *n* was also weighted by the steam partial pressure $P_{v,n}$ in the cell:

$$f_n = \frac{P_{v,n} w_n}{\sum_i P_{v,i} w_i} \qquad (3\text{-}1)$$

Because there is no way to specify such a steam-dependent distribution through input, this cooling power distribution was introduced through code modifications. It should be noted that the sum of the w_n weight factors for the dome (cells 7, 8, and 9) is only 20%, and as a consequence the cooling of the dome should be reduced significantly, compared to the treatment in the 14-cell deck. This change presumably has the effect of stabilizing the stratifications in the upper part of the facility during the preheat as well as at later times.

3. Addition of the Dome Sprays. In the experiment cooling water sprays were directed onto the outside of the steel dome beginning at 975 minutes. As discussed above, at the time the 14-cell deck was created, the effect of these sprays had to be modeled through code modifications. With CONTAIN 1.2, the effect of these sprays can now be modeled through the FILMFLOW film tracking model. The necessary FILMFLOW input was therefore added to the deck.

4. Adjustment of Buoyancy Heads from the Mid-elevation Sources. With the three changes discussed above in place, but without further adjustments, the 15-cell deck would still exhibit the same type of stability during the preheat that is observed with the 14-cell deck. Since this stability was not observed experimentally, the buoyancy heads from the mid-elevation sources were increased to remove the onset of stability, as discussed below.

If stability is marginal, then the resulting behavior could be sensitive to the gravitational head modeling of the source. The buoyancy head developed on the driving side of the loop (i.e.,

Table 3.3. Instrument cooling weighting factors, by internal cell, for the HDR 15-cell deck

Cell Number, n	Weight Factor, w_n
1	0.100
2	0.240
3	0.160
4	0.140
5	0.020
6	0.080
7	0.084
8	0.035
9	0.081
14	0.060

cell 6) is the most difficult to model, as this presumably depends on the mixing length of the injected gas, defined here as the length for the gas composition to become essentially uniform across the upward-flow channel cross-section. Clearly, if the mixing length were quite long, the injected gas would rise like a plume or jet in the channel, possibly creating some counter-current flow in the channel but having minimal effects on loop flow outside the upward-flow channel. Time constraints have prevented a careful study of gravitational heads resulting from the mixing of buoyant gas injected into the middle of vertical channel. For purposes of discussion, it is reasonable to assume that the mixing length approximately determines the point above which the fully-mixed gas density should be used in the gravitational head and below which the ambient gas density should be used.

Within this assumed relation between the mixing length and gravitational head, the well-mixed assumption made in CONTAIN is equivalent to assuming a fully-mixed elevation equal to the cell-center elevation, within the default donor- and cell-center-based hybrid solver modeling of gravitational heads in the 14-cell deck. In addition, the mixing length is equal to the difference between the cell-center elevation and the injection elevation of the source. The

mid-elevation source cell, cell 6, has a cell-center elevation at 25.3 m. The mid-elevation sources on the other hand, were injected at approximately 23 m, which is approximately the bottom of the cell. Thus, within the approximate relation between the mixing length and gravitational head described above, the mixing length was approximately 2 m. Depending on the actual mixing length, the buoyancy head may thus be either underestimated or overestimated by the well-mixed assumption.

Because of the lack of a mixing model for the complicated HDR geometry, we examined the experimental data to try to estimate an appropriate mixing length. Ideally, the data should be comprehensive enough to show the extent of mixing. Unfortunately, the available data[Karw92,Wolf95] are inconclusive. The instrumentation locations within the elevator shaft are the most likely to correspond to positions within the plume. Of these, only the 26.5 m and 30.6 m locations are relevant to mixing in the upflow channel. The slightly decreasing temperatures with elevation at these locations during the preheat are consistent with the presence of a fully-mixed condition at the lower elevation, but the steam concentrations suggest that the 26.5 m location was intermittently inside and outside of the plume. In addition, the relatively high steam concentrations (>90%) measured at the 30.6 m location are not understood, since jet entrainment calculations indicate that the steam concentrations in the preheat steam jet should approach the ambient values after the jet propagates only a few meters. With respect to the light gas sources, an apparent malfunction of the hydrogen concentration measurement device at 30.6 m prevented an evaluation of the mixing. Thus, no conclusions can be drawn from the data about what the mixing lengths actually were.

In the absence of information about the mixing lengths, in the 15-cell base case we chose to increase the buoyancy head of the mid-elevation sources by effectively decreasing, by 3 m, the elevation at which the sources were assumed to become fully mixed. The 3 m value was chosen as roughly the uncertainty in flow path elevations as a result of the 6 to 12 m cell heights in the deck. Note that, in one sensitivity calculation below, we increase the fully-mixed elevation by 1.5 m relative to the base case, and show this has little effect. This adjustment of the buoyancy head could have been accomplished by subdividing cell 6 and the new cell 4, which still span two containment levels, into an upper and lower half and using the lower half of cell 6 as the source cell. However, it was simpler to adjust flow path elevations to accomplish the same thing with respect to the gravitational head. Quite clearly, if a model for the mixing length were available and the length was not strongly time-dependent, we could adjust the buoyancy head to what the model predicts.

This change to increase the buoyancy head was accomplished by specifying the attachment points of flow paths to cells 4 and 6 to be 3 meters above or below cell center, depending on

whether the path is connected to a cell above or below, respectively. Through the RESOLVHD keyword, the respective cell 4 or cell 6 gas densities were in addition specified to be used in the gravitational head calculation over the 6 meter vertical span now present between the flow path ends for the upward- and downward-connected paths.

3.3.3. The 15-cell Base Case Results

The pressures predicted in the 15-cell base case with the old and hybrid solvers are compared to experiment in Figure 3.61. The dome temperatures are similarly shown in Figure 3.62. The results for the pressures are similar to that predicted with the modified 14-cell deck, which are shown in Figure 3.53. As these figures show, the pressures calculated with the hybrid solver are much too high compared to experiment, although the pressures predicted 15-cell deck are significantly less than those predicted with the 14-cell deck. With either deck the results with the old solver are in better agreement with experiment.

Overprediction of the pressures in the E11.2 experiment is a well-documented[Karw92] and unfortunately unresolved problem associated with calculations that give good agreement with the degree of stratification in the experiment. As we discuss below, good agreement with the degree of stratification is obtained with the hybrid solver. The problem is that calculations predicting the degree of stratification observed in the experiment often overpredict the pressure.

This problem suggests a correlation between higher predicted pressures and higher predicted degree of stratification, which can be explained in terms of the distribution of heat sinks in the containment. As one would expect, the important heat sinks in HDR with respect to pressure are the internal concrete heat sinks, and the effectiveness of these heat sinks in a region of high steam concentration is limited by the concrete thermal conductivity, except perhaps during the initial transients. An unusual feature of HDR is that most of the internal concrete in HDR is located below the dome, in cells 4 and 6 and below. Thus, the amount of heat sink area in contact with steam with a low degree of stratification, as well as the effectiveness of the heat sinks in reducing the pressure, could be considerably greater than that with a high degree.

This correlation between pressure and degree of stratification is consistent with code sensitivity calculations reported in conjunction with ISP-29[Karw92], in which flow to the lower regions of the facility was artificially restricted by the use of reduced flow areas or large flow loss coefficients. In particular, in GOTHIC sensitivity calculations, when flow areas were sufficiently restricted to produce pure steam conditions in the dome, high peak pressures of approximately 2.55×10^5 Pa were obtained. This is consistent with the peak pressure of 2.67×10^5 Pa shown in Figure 3.53.

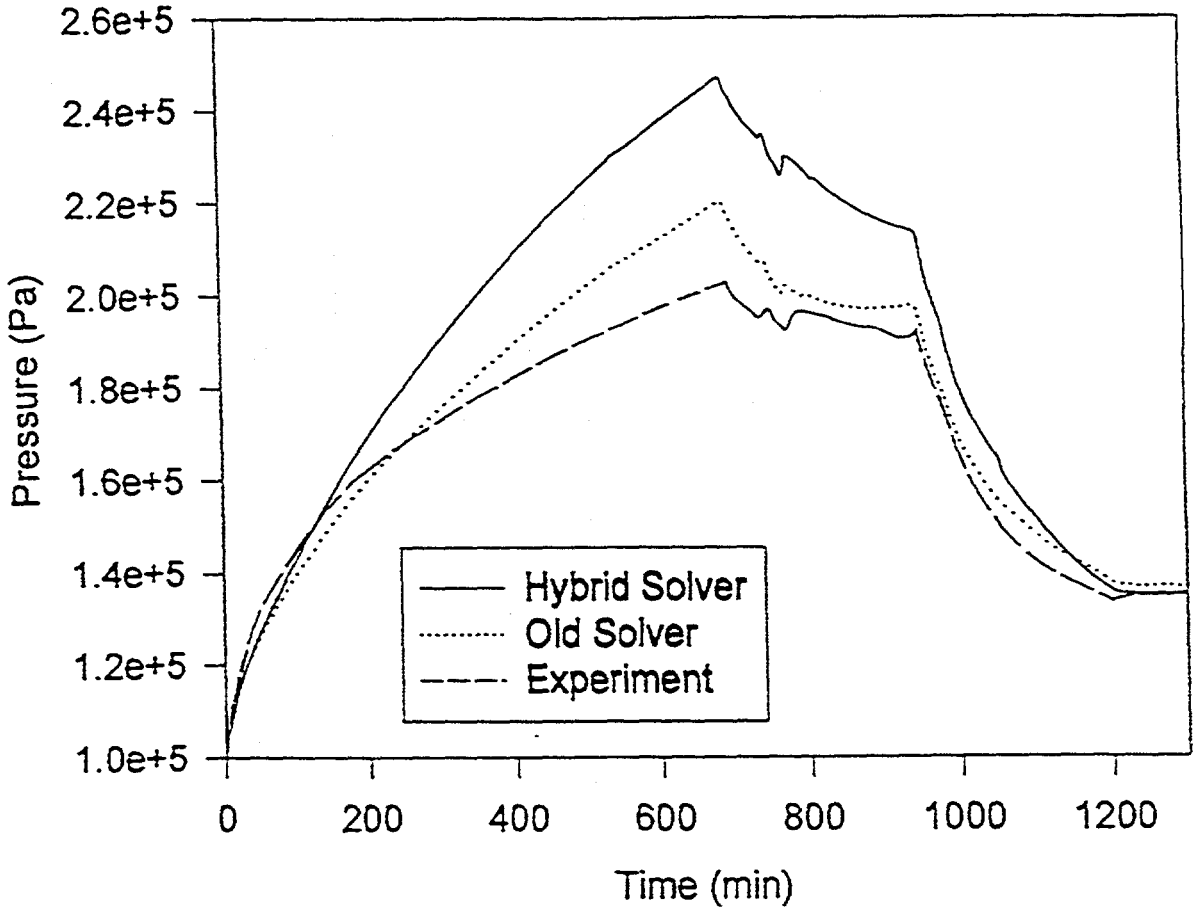

Figure 3.61. Gas pressures obtained in the 15-cell base case with the old and hybrid gravitational head formulations, compared to experiment[Karw92].

This difficulty suggests that modeling inconsistencies are still present, the likely ones being that either the specified steam and/or enthalpy injection rate is still too high or heat sinks and/or heat transfer rates in the problem are not characterized correctly. In view of the problems with experiment calibration discussed in Section 3.3, the specified steam injection rates are still suspect. We have deduced the reduction in steam injection rate required to bring the pressure predicted by the hybrid solver in Figure 3.61 during the preheat into agreement with experiment. This requires only a 20% reduction, compared to the uncertainty of order 10% in the source rate from known causes. Other authors[Royl96] have postulated that the insulation adjacent to the containment shell below the operating deck has failed and that heat transfer to the shell and concrete areas adjacent to the shell are much more effective than expected from the original experiment specification. This postulate

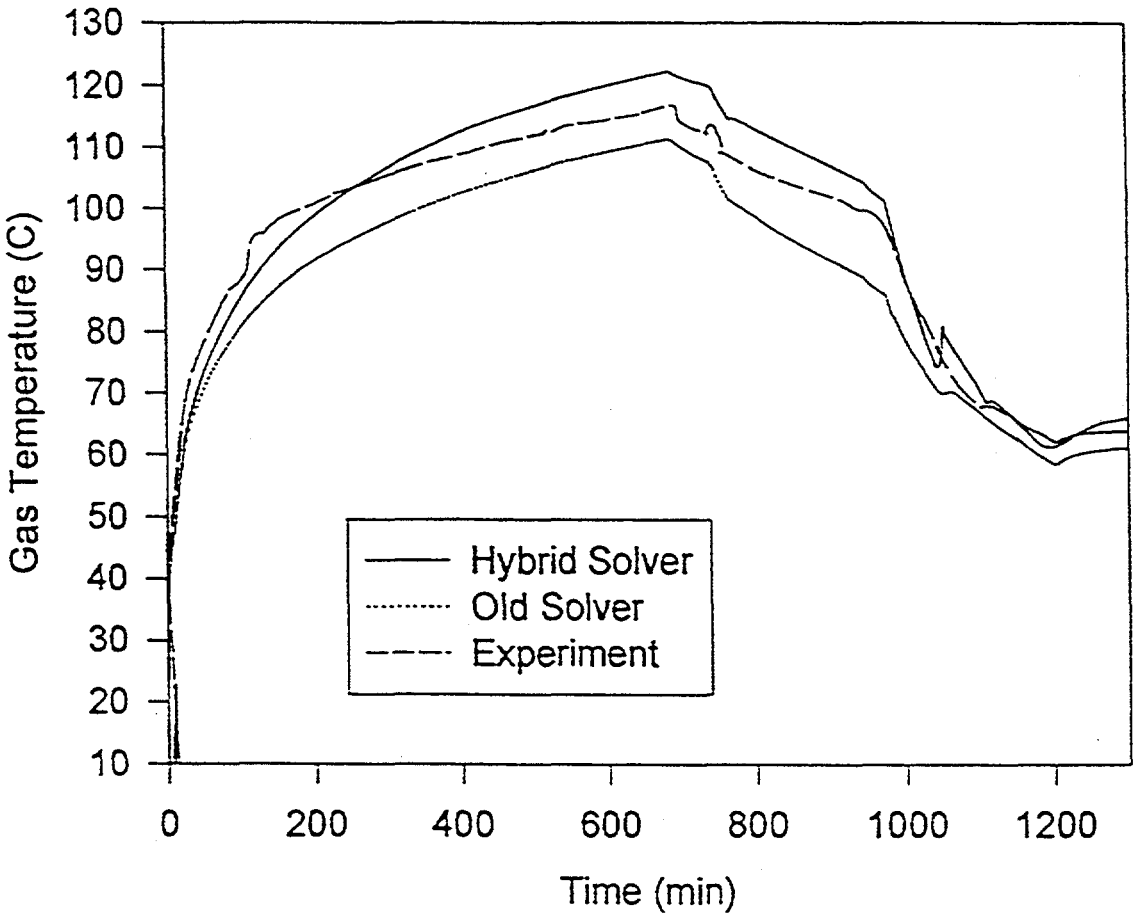

Figure 3.62. Gas temperatures obtained in the dome (cell 9) in the 15-cell base case with the old and hybrid gravitational head formulations, compared to experiment[Karw92].

allowed these authors to substantially improve the agreement with respect to pressure in computational fluid dynamics calculations of E11.2, in which highly stratified conditions were predicted. The lack of an adequate characterization of this insulation failure, however, has prevented an investigation of its impact in the present report. The above considerations do not resolve the problem with the pressure, and time constraints prevented further investigation. Thus, we will restrict any further discussion of this matter to the possible impact of the pressure overprediction on the stratification predictions, which are of primarily interest in this report.

The temperatures obtained with the 15 cell deck are plotted in Figures 3.63 and 3.64 and Figures 3.65

and 3.66 for the old and hybrid solvers, respectively. Figures 3.63 and 3.65 give results appropriate to the 80° azimuth of the HDR facility and Figures 3.64 and 3.66 give results appropriate to the 280° azimuth. Note that the mid-elevation sources were placed at an azimuth of approximately 80°, corresponding to cell 6. The corresponding figures for the steam distributions are shown in Figures 3.67 - 3.70. We see that the results with old solver show approximately the same steam distribution as shown in Figure 3.56 for the 14-cell deck. The minor differences observed after the preheat are presumably due to the changes in the cooling power distribution. The results with the hybrid solver show less severe stratification in the preheat period than shown in Figure 3.57 for the 14-cell deck. In particular, the excessively stable behavior shown in Figure 3.57 is absent from Figure 3.69.

The predicted steam concentration profiles are given in Figures 3.71 and 3.72, along with the experimental results, at the end of the preheat. We see that the hybrid solver profiles are in good agreement with experiment with respect to the lower boundaries of the steam layer, whereas those for the old solver extend too low into the facility. The predicted maximum steam concentration is too high, as one might expect from the fact that the predicted pressures are higher than observed and the predicted containment temperatures in Figure 3.62 are in relatively good agreement. In addition, the predicted steam concentration with the hybrid solver changes too abruptly with elevation in contrast to the more gradual change with elevation seen in the experiment. This may indicate an inadequate nodalization, for the following reasons: when loop flow occurs during the preheat with the present deck, the steam concentration in cell 14 should be high because the downward flow on the 280° azimuth (spiral stairway) side of containment must penetrate down to cell 14 for the gas to be able to return easily to the opposite side of the containment. This scenario is reasonable if the return paths are in fact located at the center of cell 14. However, if openings near the top of cell 14 in reality allow the flow to return along the ceiling without penetrating to cell center, then the buoyant steam will take those paths, and the steam concentration at lower elevations could be reduced considerably. In addition to reducing the steam concentration at lower elevations, such paths would reduce the buoyancy head required to sustain the loop flow, and mitigate the stability problem found with preliminary versions of the 15-cell deck.

The light gas molar fractions from the 15 cell deck are plotted in Figures 3.73 and 3.74 and Figures 3.75 and 3.76 for the old and hybrid solvers, respectively. Figures 3.73 and 3.75 give the results at 80° azimuth, and Figures 3.74 and 3.76 give the 280° results. Note that the peak concentration occurs in the mid-elevation source cell (cell 6) and that the concentrations in the new cell 4, on the opposite side of containment but at the same level as cell 6, are considerably less than in cell 6. Thus, mixing of the light gas between the two sides of the containment is not as complete as that of the preheat steam. A comparison with the experimental results[Karw92] corresponding to cell 6 (26.5 m elevation at 80° azimuth) shows a measured peak concentration of 16.5% compared to the peak of 17.5% in Figure 3.75. Similarly for cell 4 (26.5 m elevation at 280° azimuth) the measured peak

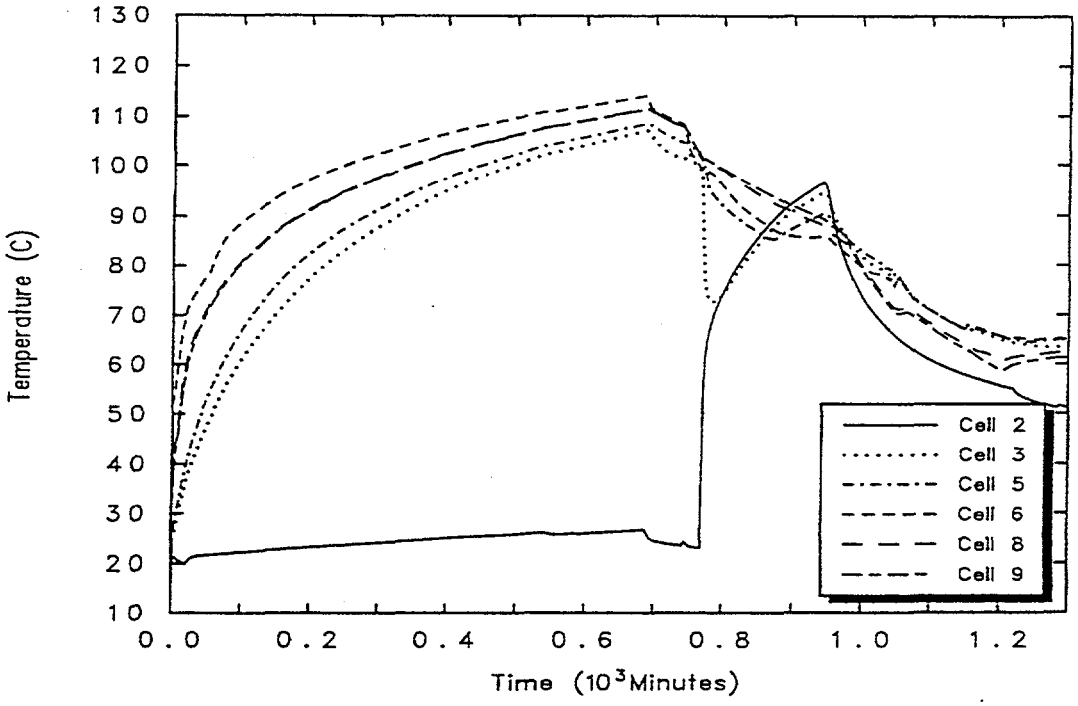

Figure 3.63. Gas temperatures obtained in the 15-cell base case with the old gravitational head formulation (80 azimuth).

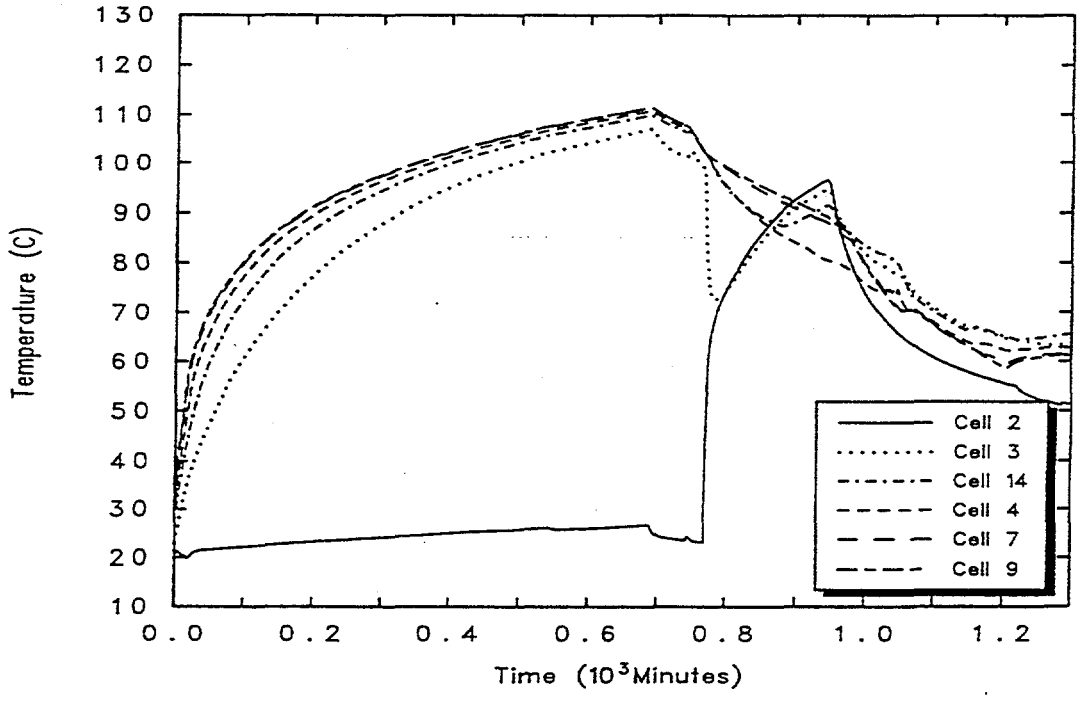

Figure 3.64. Gas temperatures obtained in the 15-cell base case with the old gravitational head formulation (280 azimuth).

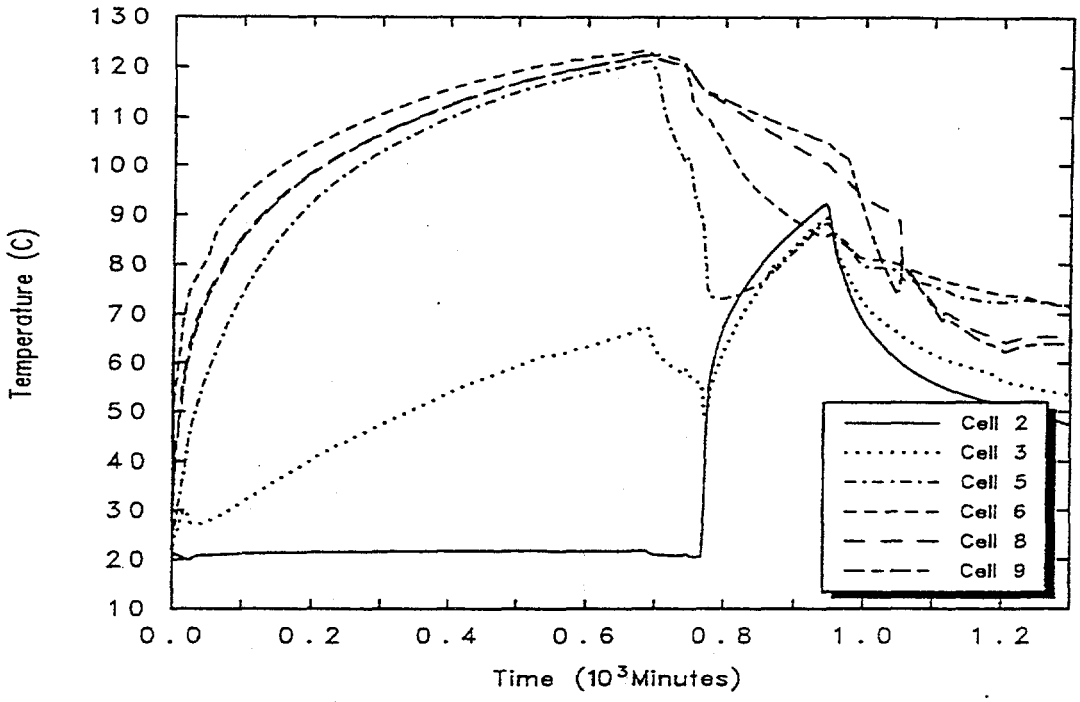

Figure 3.65. Gas temperatures obtained in the 15-cell base case with the hybrid formulation (80 azimuth).

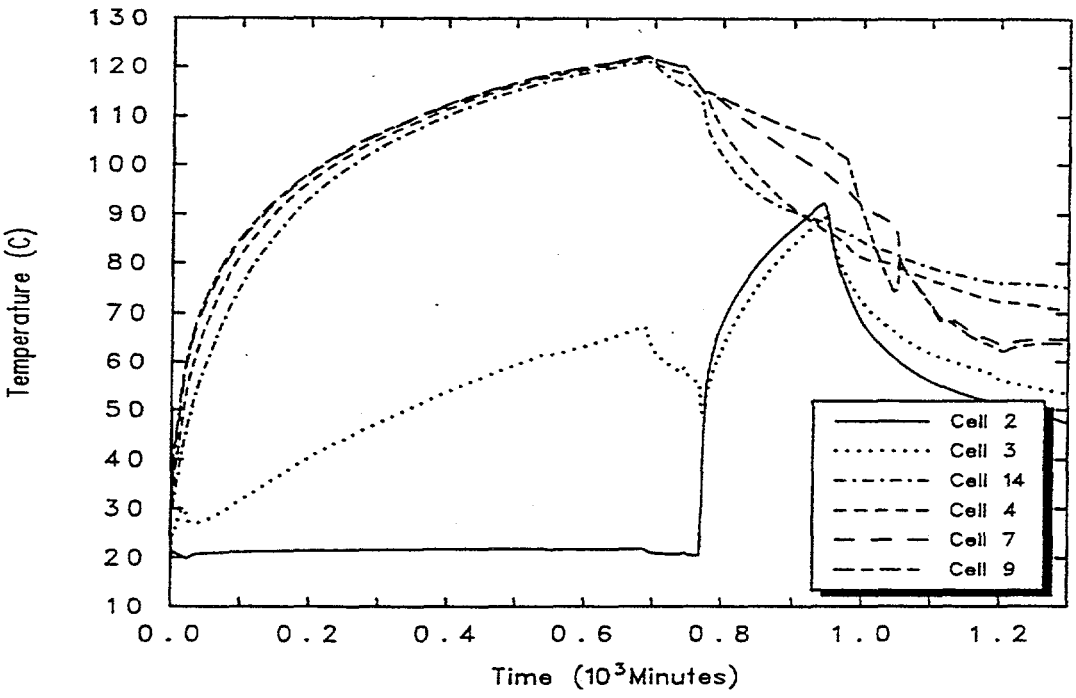

Figure 3.66. Gas temperatures obtained in the 15-cell base case with the hybrid formulation (280 azimuth).

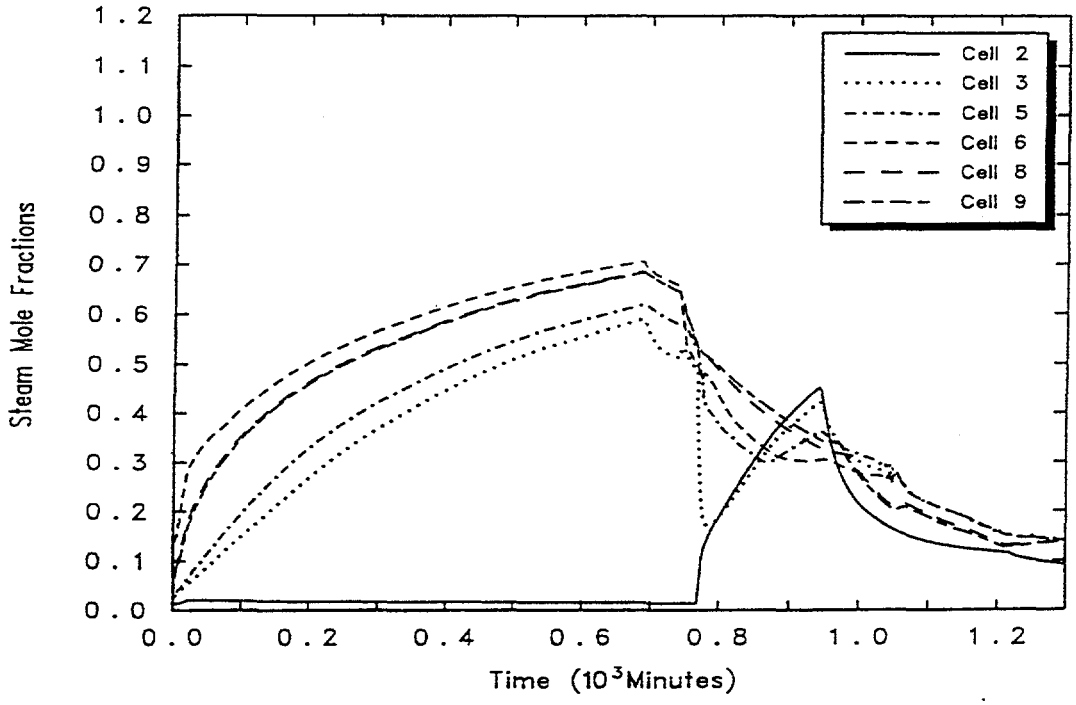

Figure 3.67. Steam mole fractions obtained in the 15-cell base case with the old gravitational head formulation (80 azimuth).

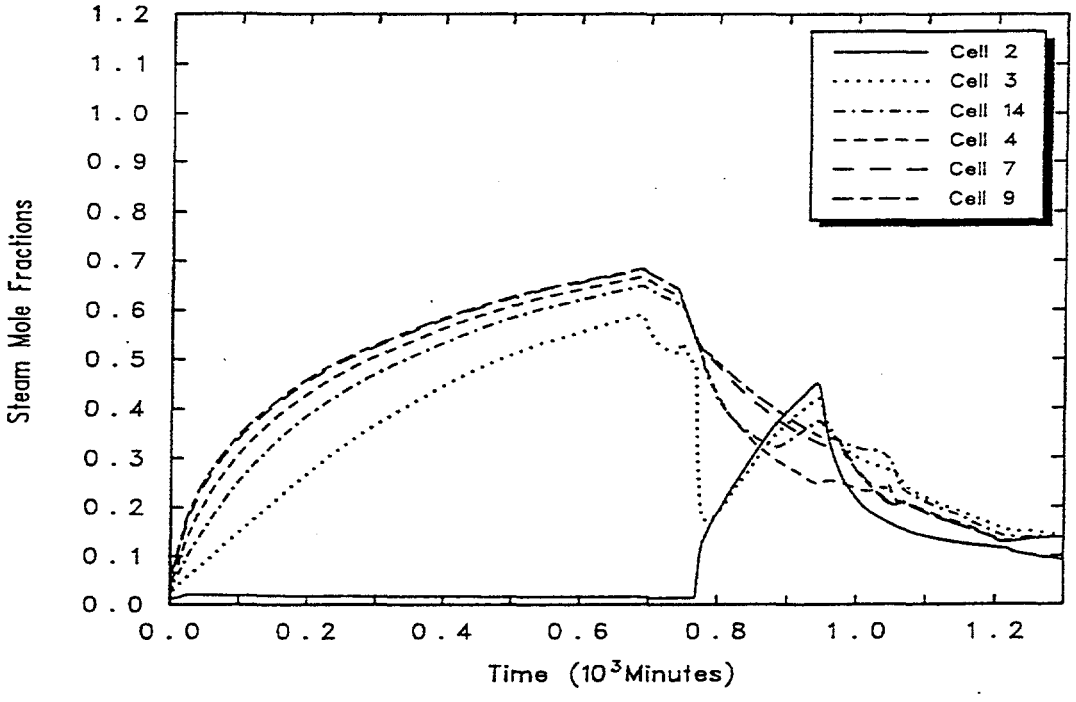

Figure 3.68. Steam mole fractions obtained in the 15-cell base case with the old gravitational head formulation (280 azimuth).

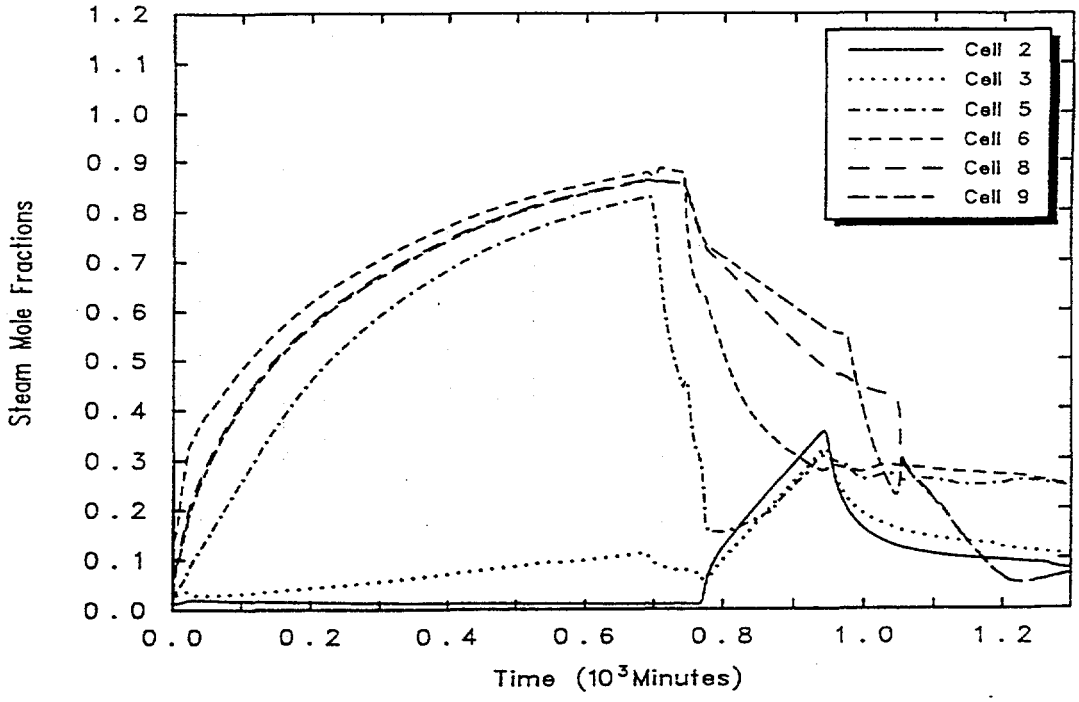

Figure 3.69. Steam mole fractions obtained in the 15-cell base case with the hybrid formulation (80 azimuth).

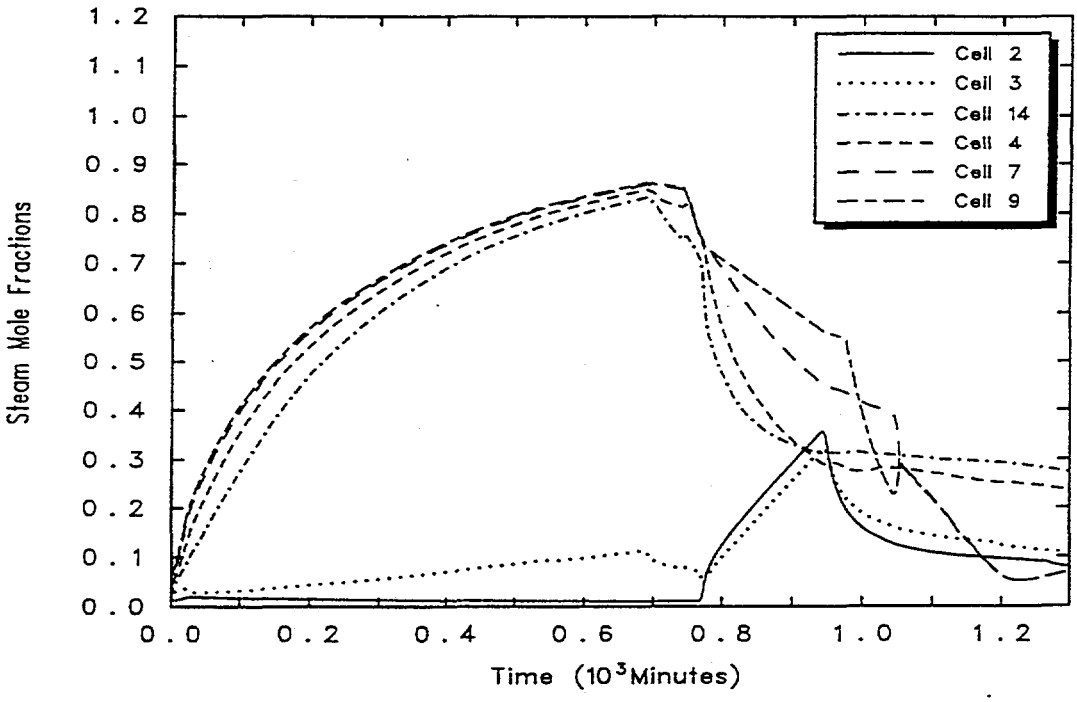

Figure 3.70. Steam mole fractions obtained in the 15-cell base case with the hybrid formulation (280 azimuth).

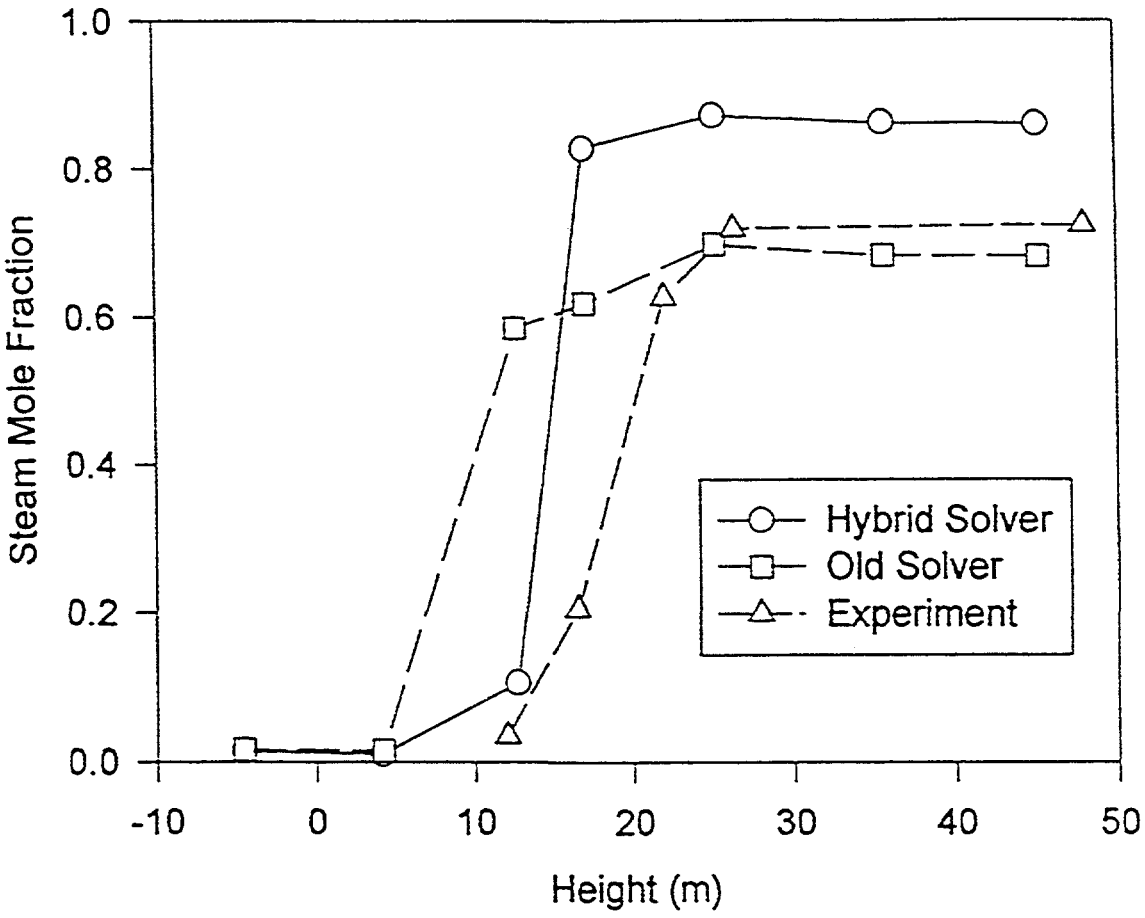

Figure 3.71. Steam mole fraction profiles predicted in the containment at 690 minutes in the 15-cell base case (80 azimuth), compared to experiment[Karw92].

is 12% compared to the peak of 7.5% in Figure 3.76. The cell 6 value would presumably be in considerably worse agreement with experiment and the cell 4 value in considerably better agreement with experiment if the predicted steam concentrations were in better agreement with experiment and the predicted degree of stratification of the light-gas were not changed. Note that the continued increase of the cell 9, or dome, concentrations after the end of the light gas injection at 772 minutes is due to the continuing low-elevation steam source in cell 2, which has the effect of displacing the light-gas layer upward. The sudden rise in the dome concentration at 975 minutes is due to the application of water sprays on the outside of the steel dome, which accelerates the internal steam condensation and increases the light-gas concentration. This is followed by a sudden decrease of the predicted dome concentration at 1050 minutes. This decrease is apparently due to rapid mixing of

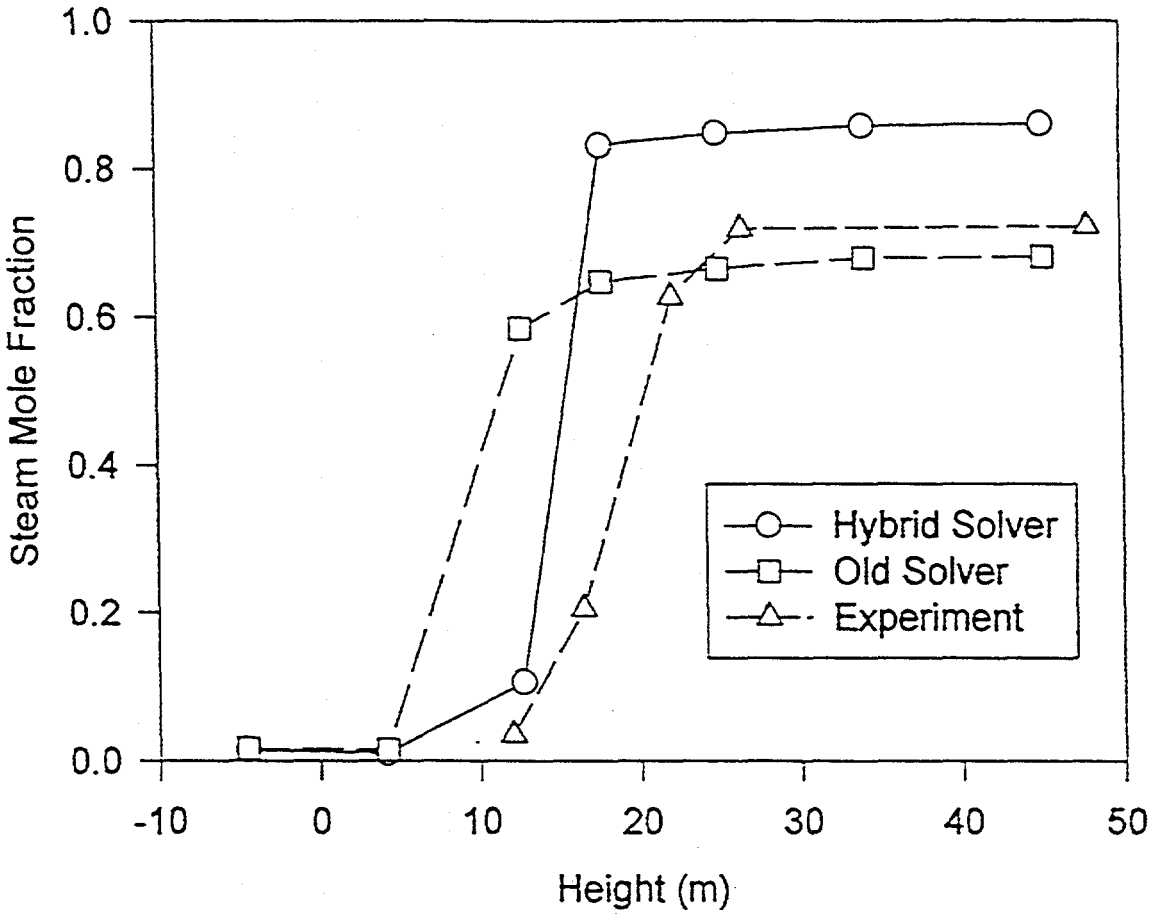

Figure 3.72. Steam mole fraction profiles predicted in the containment at 690 minutes in the 15-cell base case (280 azimuth), compared to experiment[Karw92].

the light gas in cells 7, 8, and 9 from a gas density inversion, which is an unstable situation in which a denser gas is found to overlie a lighter gas.

The light-gas profiles at 800 minutes, or 60 minutes after the start of injection, are presented and compared to experiment in Figures 3.77 and 3.78. The choice of this comparison time was influenced by the presence of an anomaly in the data at 30.6 m and 80° azimuth, prior to this point. As with the steam concentrations, there is good agreement with experiment with respect to the predicted lower boundaries of the light-gas layer with the hybrid solver. However, the predicted light-gas concentrations in the dome are too low. Figures 3.79 and 3.80 show the respective profiles at 1000

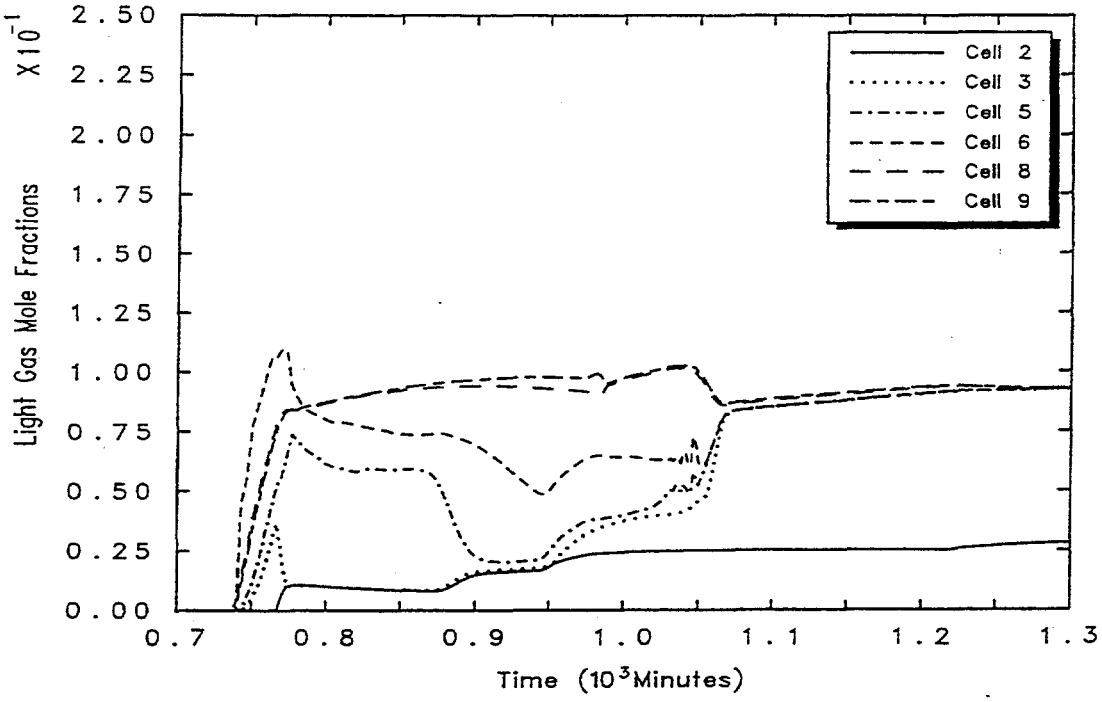

Figure 3.73. Light gas mole fractions obtained in the 15-cell base case with the old gravitational head formulation (80 azimuth).

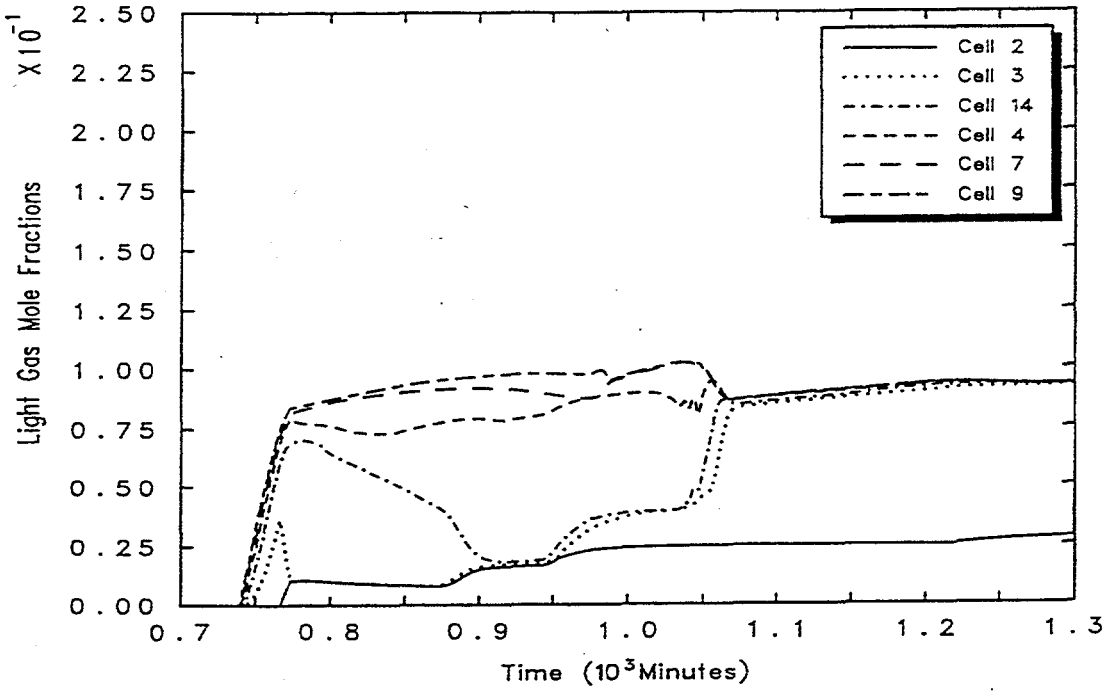

Figure 3.74. Light gas mole fractions obtained in the 15-cell base case with the old gravitational head formulation (280 azimuth).

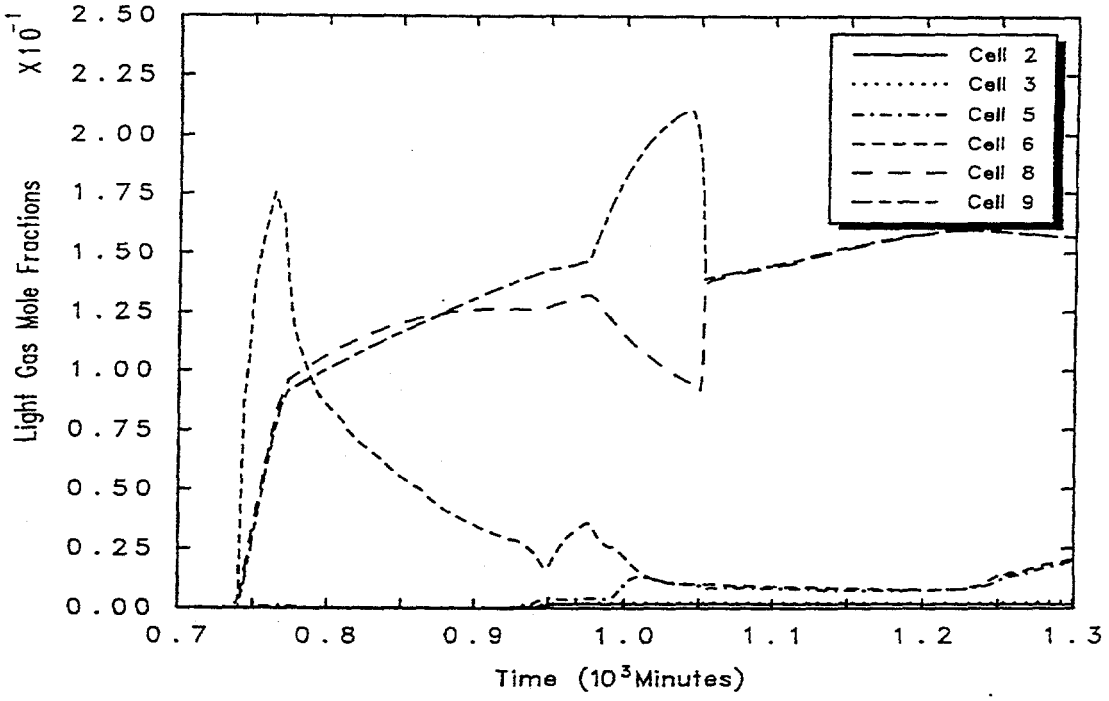

Figure 3.75. Light gas mole fractions obtained in the 15-cell base case with the hybrid formulation (80 azimuth).

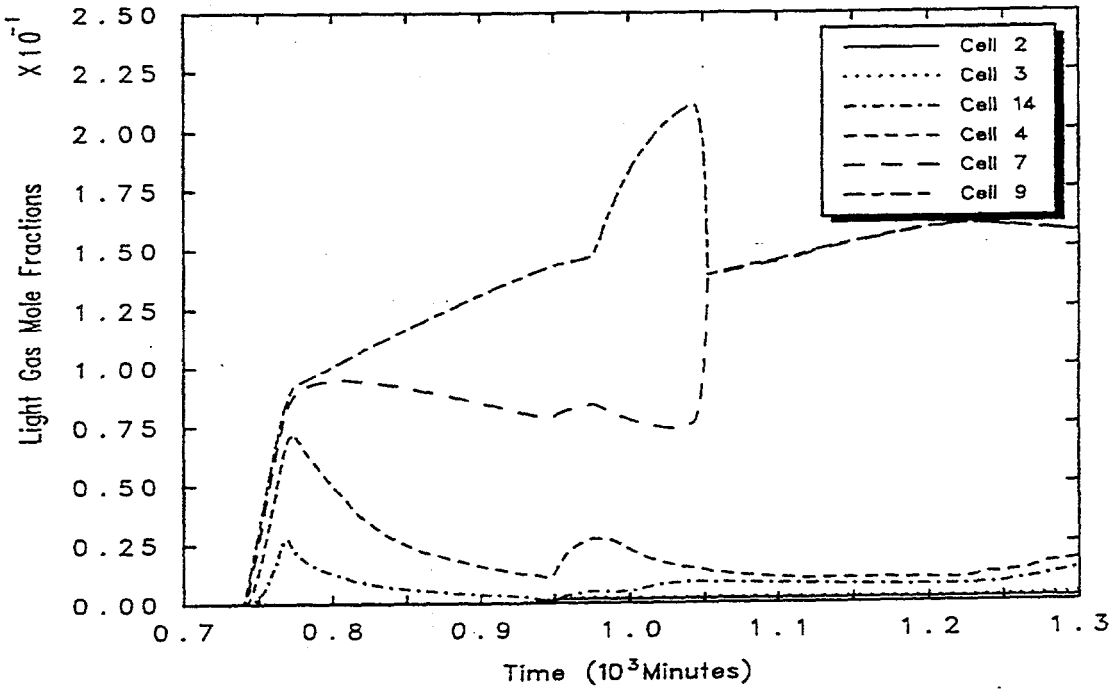

Figure 3.76. Light gas mole fractions obtained in the 15-cell base case with the hybrid formulation (280 azimuth).

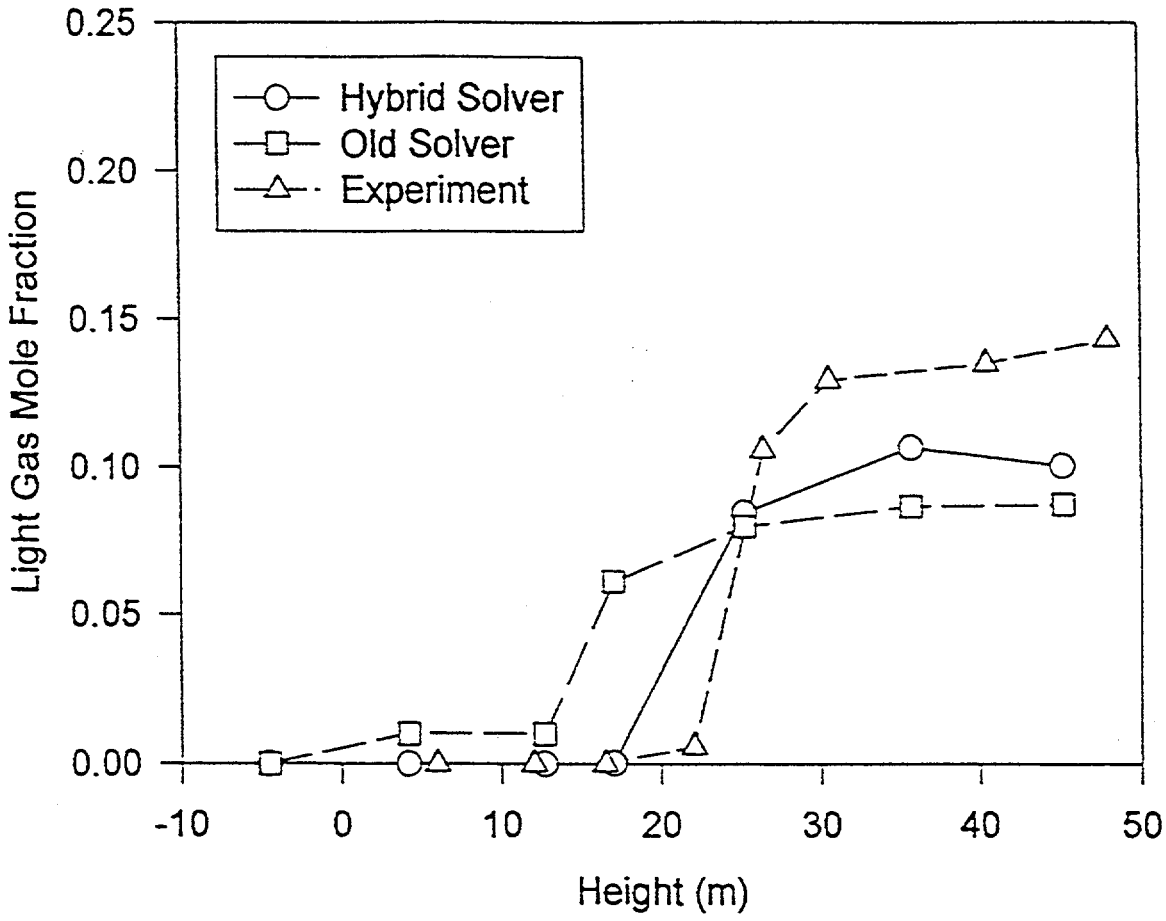

Figure 3.77. Light gas concentration profiles predicted in the containment at 800 minutes in the 15-cell base case (80 azimuth), compared to experiment[Karw92].

minutes, which is close to the time of peak dome concentration. Reasonable agreement with experiment is present at this time with the hybrid solver. Note that there is little evidence of the horizontal skewing of the concentrations in the lower dome region, represented by cells 7 and 8, that is shown in these figures and in Figures 3.75 and 3.76. This skewing is believed to be due in part to the fact that the elevation of cell 7 is lower than that of cell 8 by about a meter. It is not clear to what extent the skewing is an artifact of this elevation difference. However, it is obvious that with sharp interfaces between stratified layers, slight differences in elevation could create large concentration gradients in a horizontal direction that are unphysical. Thus, prudence dictates that the elevations for cells representing a given level in a containment be kept uniform.

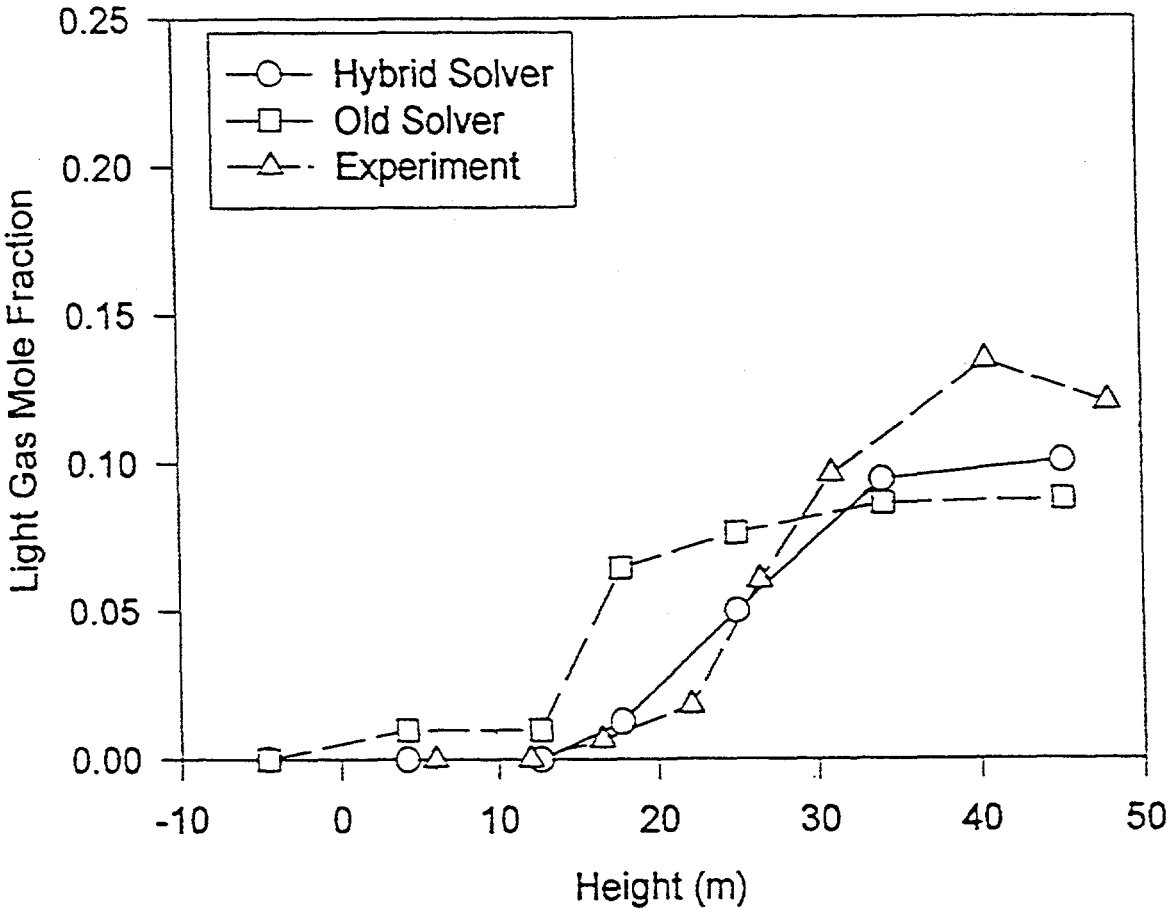

Figure 3.78. Light gas concentration profiles predicted in the containment at 800 minutes in the 15-cell base case (280 azimuth), compared to experiment[Karw92].

Figure 3.81 shows the predicted and measured dome light-gas concentrations as a function of time. We see that the agreement between the hybrid solver predictions and the experiment gets dramatically better as the discrepancy shown in Figure 3.61 between the predicted pressure and experiment gets smaller, presumably because of continued steam condensation in the dome. Dramatically improving agreement in the dome concentration with time is found up to the time of the density inversion with the hybrid solver. Figure 3.82 shows the predicted and measured light-gas concentrations as a function of time in the lower containment, at an elevation of 12 m. The agreement in this case with the hybrid solver is clearly very good, up to the time of dome spray activation (975 minutes).

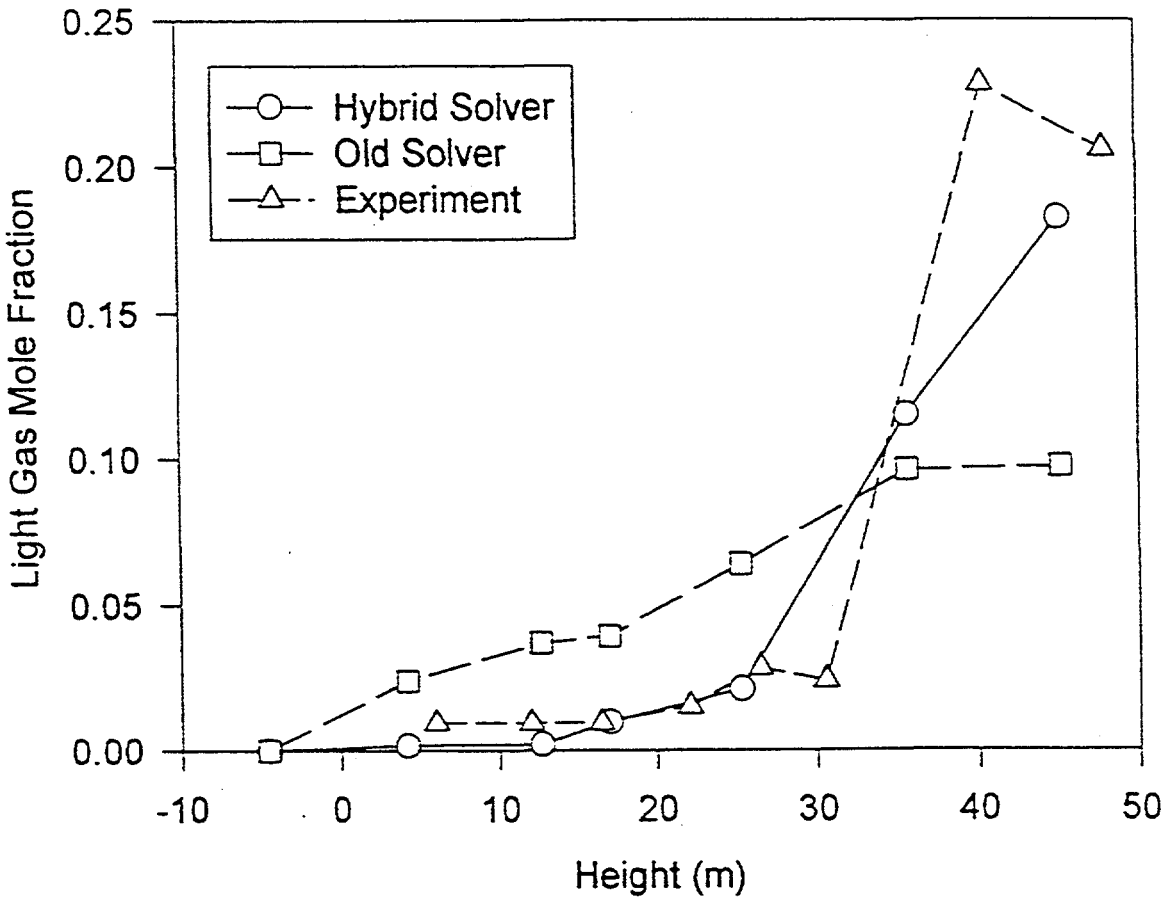

Figure 3.79. Light gas concentration profiles predicted in the containment at 1000 minutes in the 15-cell base case (80 azimuth), compared to experiment[Karw92].

As seen in Figure 3.81, a gradual decrease of the light-gas concentration was observed in the upper dome in the experiment, starting approximately at 1050 minutes, the time when CONTAIN predicts a density inversion. This decrease is associated in the experiment with a gradual downward motion of the lower boundary of the light-gas layer, with a velocity of approximately 2 mm/sec. At this point the light-gas layer was presumably well-mixed from the natural convection processes resulting from the external sprays. However, this natural convection by itself was presumably not able to penetrate the somewhat denser, warmer, steam-rich gas below it. Based on the observed downward motion of the light gas as a function of time, the variation in concentration at the bottom of the light-gas layer during its downward motion occurred over a distance of about 1 m. For typical gas diffusivities, a

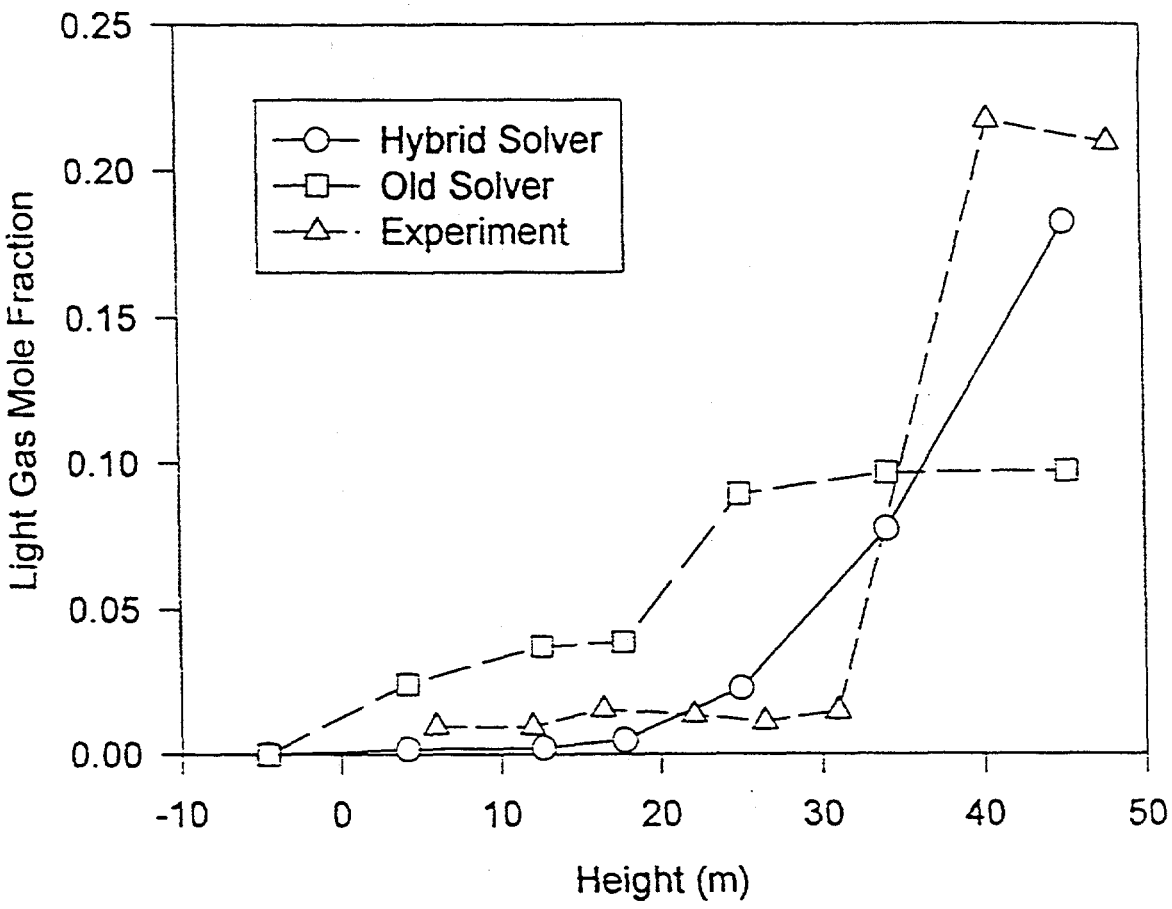

Figure 3.80. Light gas concentration profiles predicted in the containment at 1000 minutes in the 15-cell base case (280 azimuth), compared to experiment[Karw92].

velocity of 2 mm/sec is much too large to explain from molecular diffusion alone, for concentrations varying over 1 m, but may be consistent with a coupled convection/diffusion process. In this process the light gas from the light-gas layer diffuses into the gas below, and steam diffuses upward from the steam-rich layer below. For sufficiently small density differences between the light-gas layer and the steam-rich layer, such molecular diffusion may be sufficient to create a boundary layer in the steam-rich layer that is buoyant relative to that layer and a boundary layer in the light-gas layer that is denser than the light-gas layer. Such boundary layers would be unstable, and the resulting convective mixing could enhance the mixing rate of the light-gas layer into the gas below.

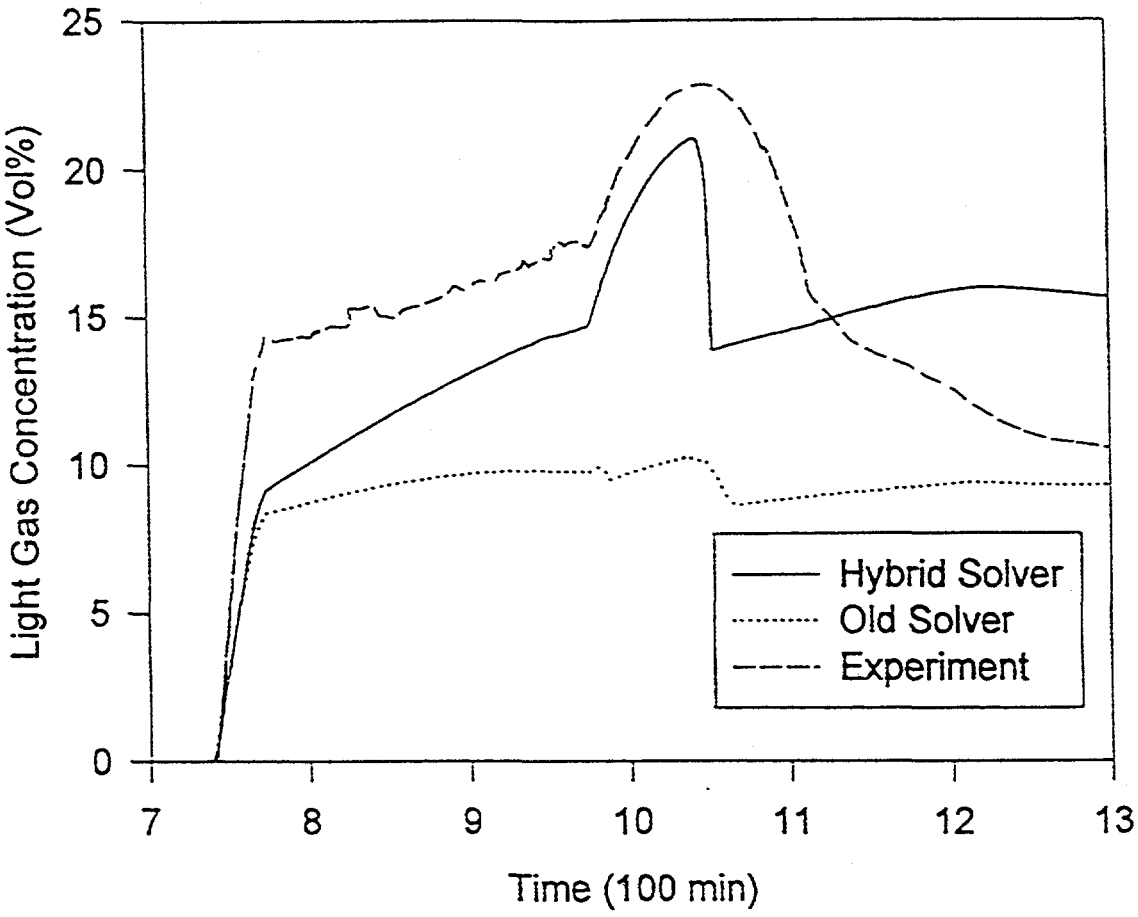

Figure 3.81. Comparison of the predicted light gas concentrations in the dome (cell=9) in the 15- cell base case with the experimental measurements[Karw92].

It should be noted CONTAIN cannot model this process since it makes no allowance for the presence of a gas-gas interface within a control volume and, although gas-gas interfaces may exist between control volumes, the code does not model boundary layer processes such as conduction or molecular diffusion across such interfaces. Thus, modeling the slow downward propagation of the lower boundary of the light-gas layer, as observed in the experiment, is well outside of the scope of the code.

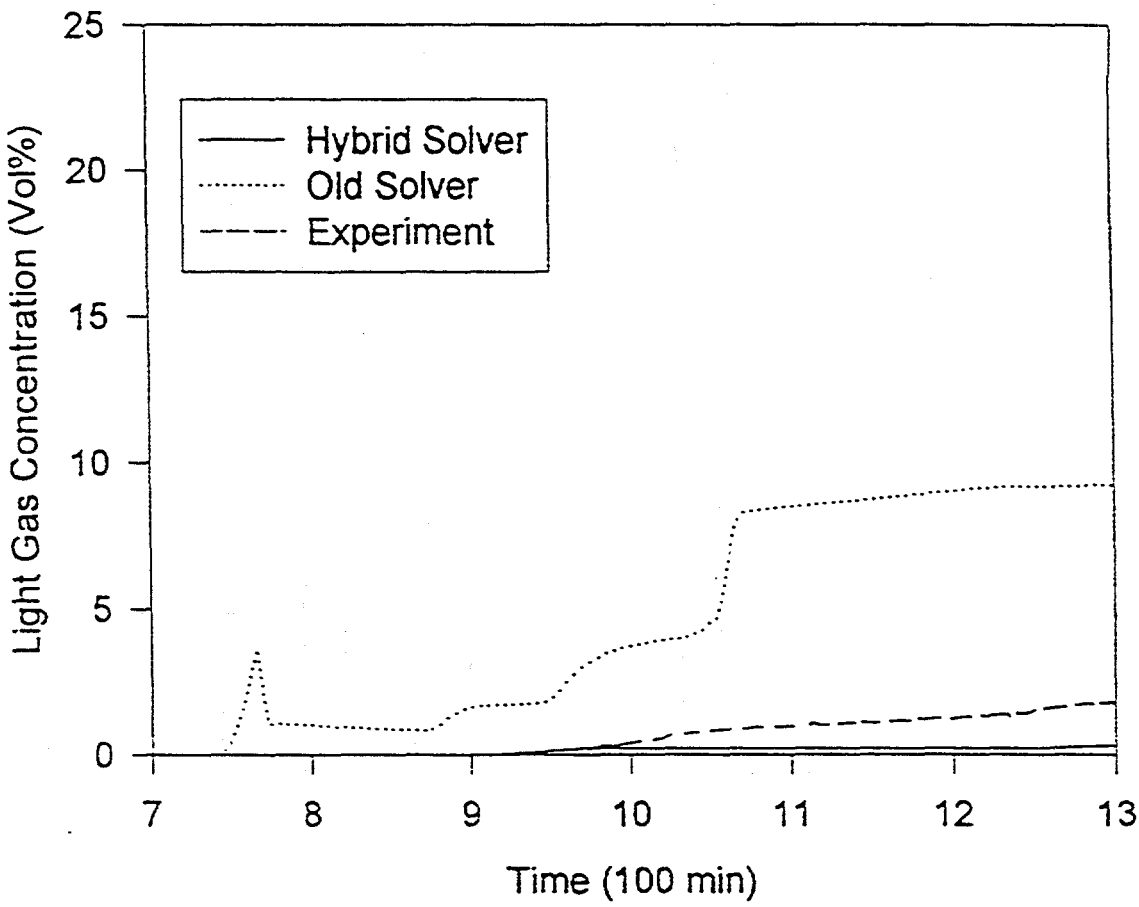

Figure 3.82. Comparison of the predicted light gas concentrations in the lower containment (cell=3) in the 15-cell base case with the experimental measurements[Karw92].

3.3.4. Sensitivity Calculations with the Hybrid Formulation

In addition to the 15-cell base case results discussed above, three additional cases were run with the hybrid formulation and 15-cell deck to check on the sensitivity of the base case calculation to modeling uncertainties. The primary purpose of these sensitivity cases was to explore the effect of the uncertainties on the stability of the stratifications.

The first case explores the sensitivity to the flow loss coefficients used. The value of one used for all flow paths in the base case was chosen as a nominal value. It is expected that the stability of a

stratification will be affected by the loss coefficient, since this determines the pressure drop across a flow junction, and it is the pressure drop caused by the entrainment flow into the source cell that determines the *de facto* stability of a stratification (see Equation (2-14)). While a loss coefficient of 1 is less than a typical orifice loss coefficient and is probably on the low side, the principal concern regarding the hybrid solver appears to be whether excessive stability is possible. Thus, in the sensitivity calculation the loss coefficients for all flow paths were further reduced by ½, to 0.5.

The second case provides a check on the mixing assumptions for the low-elevation steam source introduced into cell 2. This should have created convection patterns much like a plume, although the plume rise was presumably complicated by the presence of ceilings. In the base case, the convective mixing above the low-elevation steam source is not modeled explicitly through nodalization, since this would have required many more cells than currently used. Instead, a fixed mixing rate of 16 kg/s is used between cells 2 and 3 when the low-elevation steam source is present. This rate was chosen to mix those two cells reasonably well, but this treatment ignores the fact that the steam from the low-elevation source would probably penetrate higher into the facility than cell 3, presumably as far up as the lower boundary of the light-gas layer. The plume from the low-elevation steam source presumably penetrated asymmetrically into the two sides of the containment, depending on the gas density and access areas on the two sides. Ignoring this penetration would make the gas under the light-gas layer too dense and could possibly alter the structure of the stratification. In order to check on the sensitivity to the penetration of this steam, plume correlations were implemented into the code.

The third case is a check on the sensitivity to the buoyancy head generated by the mid-elevation sources. In the base case, flow path connections at the level of cells 4 and 6 were moved 3 m relative to those in the 14 cell deck, to eliminate the onset of stability that was observed in the results of a preliminary 15-cell deck, much as with the 14-cell deck. These flow path connections were moved back 1.5 m in this sensitivity case.

3.3.4.1. Results for Sensitivity Case 1: Reduced Flow Coefficients. In Sensitivity Case 1, the flow loss coefficients in the 15-cell deck were changed from a nominal value of 1 for all flow paths to 0.5, a relatively low value, and the calculation with the hybrid solver was rerun. The results for the pressure, as with the other sensitivity cases, are almost identical to the base case and therefore will not be presented. The same is true of the steam concentrations during preheat. However, minor changes in the light gas concentrations, shown in Figures 3.83 and 3.84, occurred. Note that the peak light-gas concentration in cell 6 is reduced somewhat but other changes are minor.

3.3.4.2. Implementation and Results for Sensitivity Case 2: Plume Mixing Model. Sensitivity Case 2 explores the effect of allowing the steam from the low-elevation source in cell 2 to mix with cell 3 and the region above cell 3, according to plume correlations. In order to calculate how high the

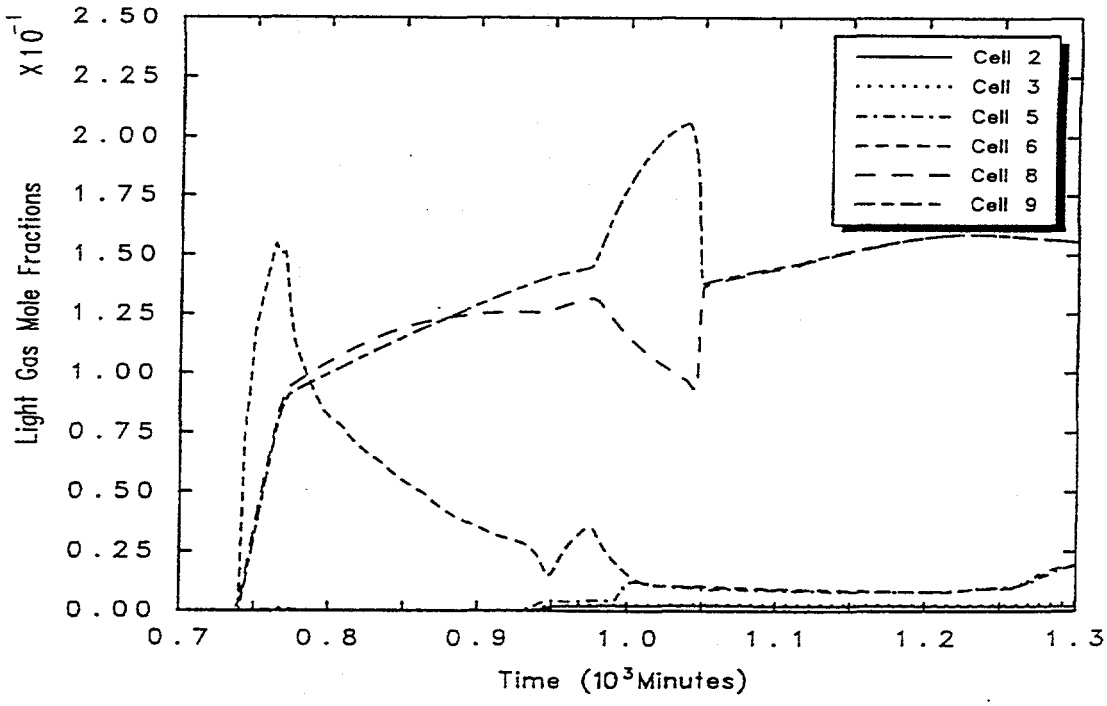

Figure 3.83. Light gas mole fractions obtained in sensitivity case 1 (80 azimuth).

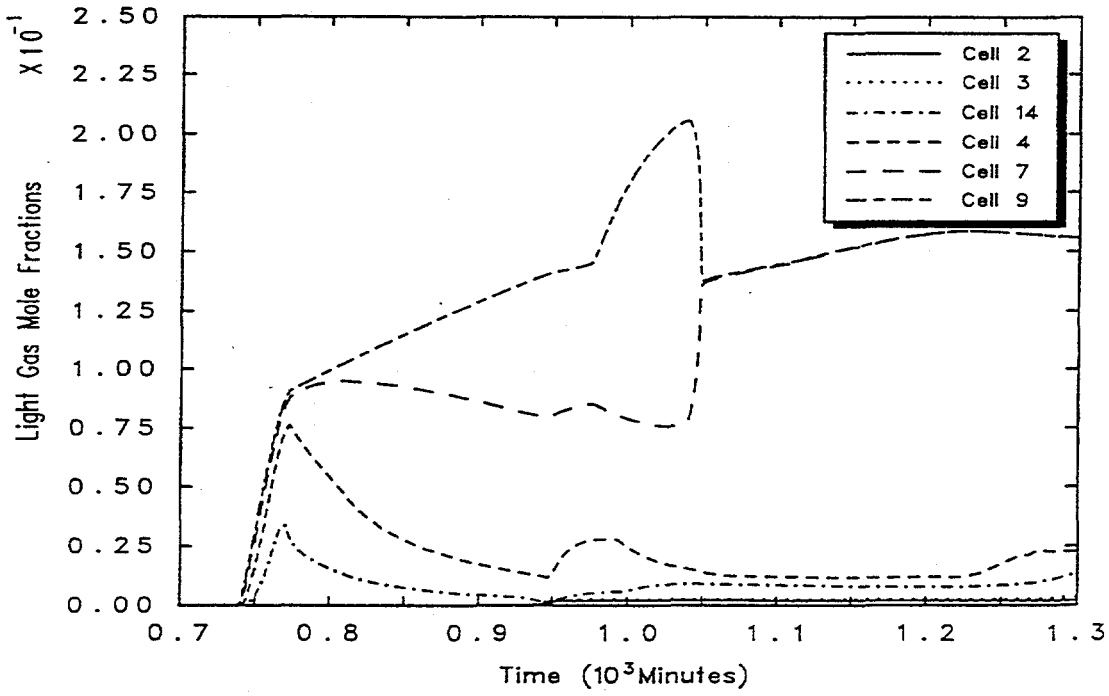

Figure 3.84. Light gas mole fractions obtained in sensitivity case 1 (280 azimuth).

steam plume rises, the degree of mixing of the surrounding gases into the plume must be known. Once that is known, the average density of the gases in the plume can be calculated at the top of each level in the containment, to determine whether the plume will continue to rise into the next level. Given that an opening to the next level exists, the plume is assumed to rise until the gas density in the plume is greater than or equal to the density in the next level.

Because plume correlations are not built into CONTAIN, this sensitivity case required code modifications to implement the plume mixing model. The basic equation used for plume rise is Equation (2.12). In the plume mixing model, Equation (2.12) is applied within each cell to calculate the evolution of the plume over the rise height of the cell and obtain the volumetric flow Q at the top of the cell. Given an initial volumetric flow Q_0 and density ρ_0, Equation (2.12) can be solved for z_0:

$$z_0 = \left(\frac{Q_0}{0.15} \right)^{0.6} B^{-0.2} \qquad (3\text{-}2)$$

where z_0 is the reference elevation for the plume. In the case in which the plume has already evolved over one or more cells below, we consider whether the volumetric flow Q', which is analogous to Q but calculated at the top of the cell below, is low enough so that the plume of area A' and density ρ' at that point will "fit" through the opening of area A between the cell below and the current cell. For any Q_0 the asymptotic initial diameter of the plume is $D_0 = 0.22\ z_0$ and the plume area is $A_0 = \pi D_0^2/4$. If we assume $Q_0 = Q'$ and $\rho_0 = \rho'$ and the opening A is larger than twice the resulting A_0, then Q' is used as the Q_0 for the current cell and none of the plume material is assumed retained in the cell below. Note that the factor of two is assumed to allow for the countercurrent flow that must replace entrained gas carried upward by the plume. If the opening is not sufficiently large, then Q_0 should be reduced. For the present purposes of doing a sensitivity calculation, we make the simple assumption that the reduction is governed by plume scaling. Using the definition of B in Equation (2-12), one can deduce that Q_0 scales as $Q_0 \sim (\rho_a - \rho_0)^{1/2} z_0^{5/2}$, where ρ_a is the ambient gas density of the current cell. Using the matching condition $Q_0 = Q'$ when $A = 2A'$ and assuming that z_0 scales as square root of the area for smaller areas, we obtain

$$Q_0 = \left(\frac{A}{2A'} \right)^{1.25} Q' \qquad (3\text{-}3)$$

In this case the volumetric flow that is not accepted by the cell above is assumed to be retained in the cell below.

One further complication is that in HDR, the plume rising to the top of cell 3 can split and go to either the 80° azimuth or 280° azimuth side of the containment. If the split is not area-limited, how this split occurs is not clear and may depend on the extent to which the buoyant layer at the top of a cell is able to float along the ceiling to access the openings. For simplicity, we assume that the split, if not area-limited, is also governed by plume scaling, i.e., proportional to $A^{1.25} (\rho_a-\rho')^{0.5}$. The plume rise process is assumed to go on until the point of neutral buoyancy is achieved, or $\rho_a \leq \rho'$. Given the source rate and the various Q's, the source distribution amongst the various cells and the entrainment flow conveyed from cell to cell by the plume can be calculated.

The results obtained for the pressure in this sensitivity case are almost identical to that of the base case and therefore will not be presented. The results for the steam concentrations in this sensitivity case are given in Figures 3.85 and 3.86, and those for the light-gas concentrations are given in Figures 3.87 and 3.88. From the former, we see that in comparison to Figures 3.69 and 3.70, more of the lower steam source, which was on from 773 to 959 minutes, is conveyed to cells above cell 3 (i.e., to cells 4, 5, 6, and 14). In addition, the relative amounts of steam in cells 2 and 3 have changed. The reason for the latter is that in the base case, the steam is first mixed completely in cell 2 and then allowed to flow out, whereas with the plume model the steam is first conveyed to the destination cells, and then conveyed back to cell 2 by countercurrent flow. In comparing Figures 3.87 and 3.88 with Figures 3.75 and 3.76, we see that the light gas in the sensitivity case, in contrast to the base case, appears to have been well-mixed among the cells which support the plume at around 950 minutes. However, shortly after termination of the low-elevation steam source, the overall change in distribution appears to be minor.

3.3.4.3. Results for Sensitivity Case 3: Buoyancy Heads. This case checks the sensitivity to buoyancy heads generated by the mid-elevation sources by moving flow path connections to cells 4 and 6 by 1.5 m to decrease the head from the base case. The results for pressures, steam concentrations, and light-gas concentrations are almost identical to those from the base case. Since the principal concern regarding buoyancy heads, besides stability, is the overprediction of the head for the light-gas source in the base case, the light-gas concentrations from this case are explicitly presented in Figures 3.89 and 3.90 for comparison to Figures 3.75 and 3.76. We see that the results are quite similar.

3.3.4.4. Comparison of Dome Light Gas Concentrations. Figure 3.91 compares the predicted dome light-gas concentrations from the base case and the sensitivity cases with experiment. It is clear that the predictions are relatively insensitive to the parameter variations considered, and that in all cases dramatically improving agreement with the measured concentration occurs with time, until the time of the predicted density inversion.

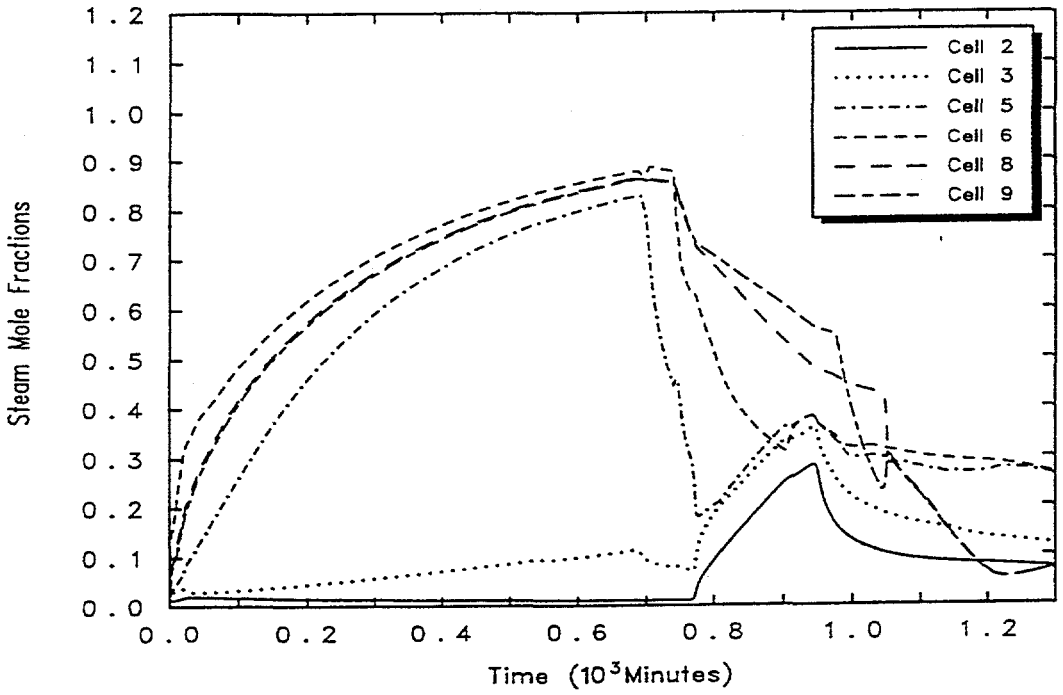

Figure 3.85. Steam mole fractions obtained in sensitivity case 2 (80 azimuth).

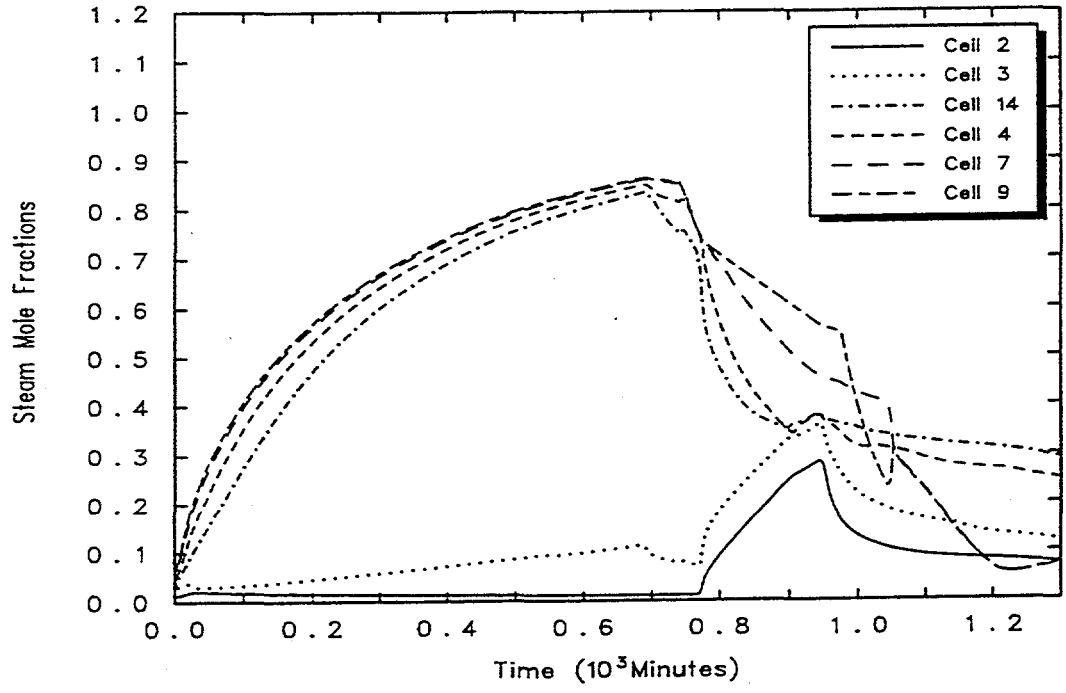

Figure 3.86. Steam mole fractions obtained in sensitivity case 2 (280 azimuth).

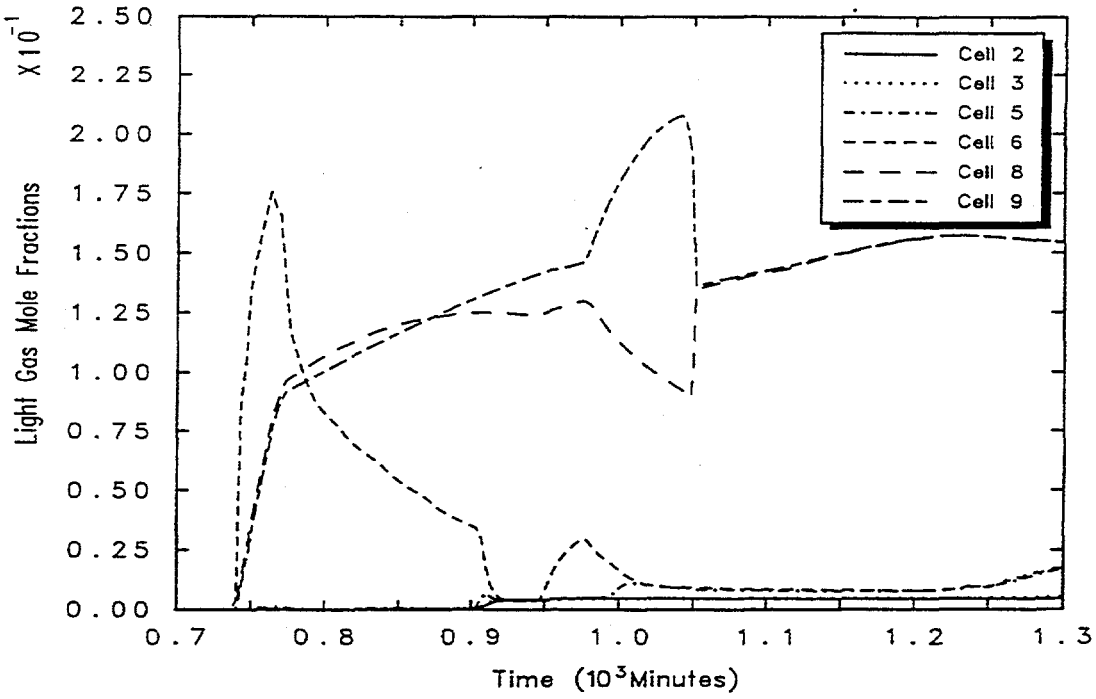

Figure 3.87. Light gas mole fractions obtained in sensitivity case 2 (80 azimuth).

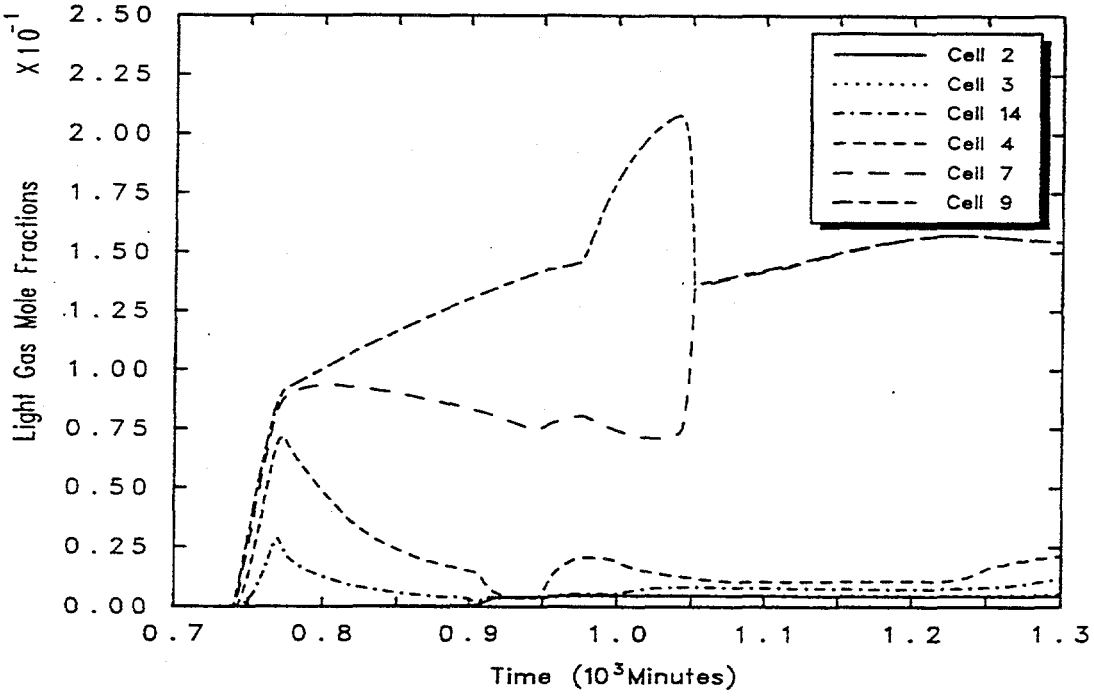

Figure 3.88. Light gas mole fractions obtained in sensitivity case 2 (280 azimuth).

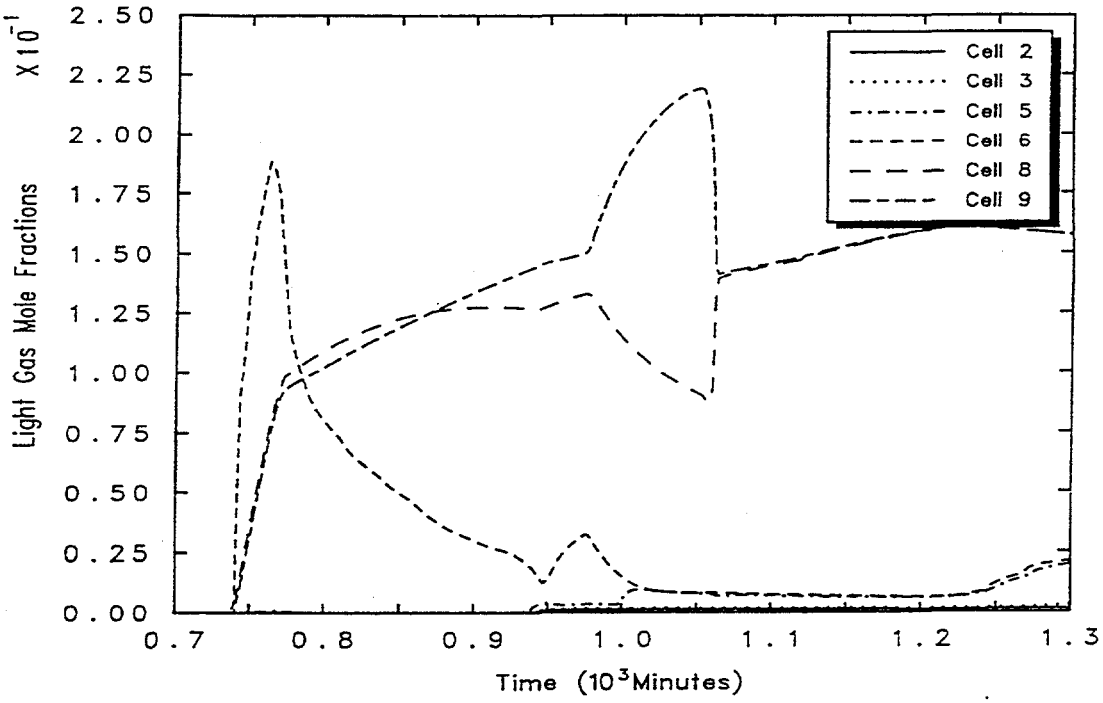

Figure 3.89. Light gas mole fractions obtained in sensitivity case 3 (80 azimuth).

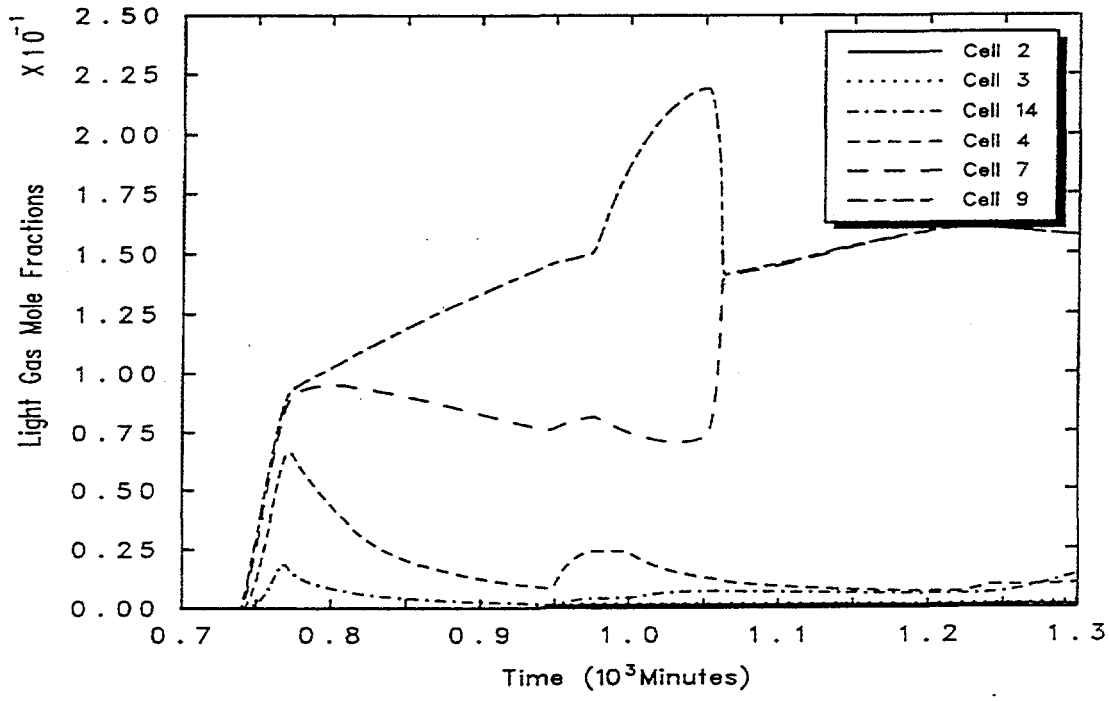

Figure 3.90. Light gas mole fractions obtained in sensitivity case 3 (280 azimuth).

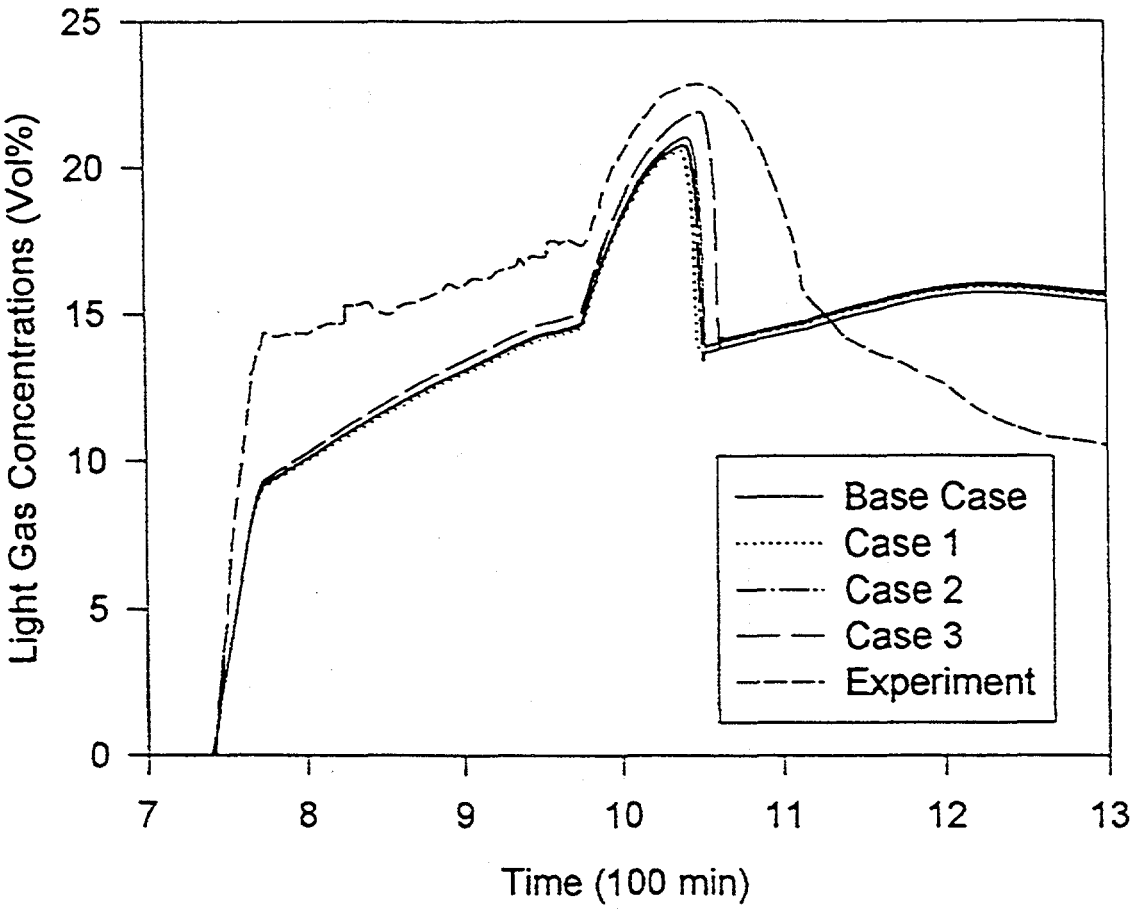

Figure 3.91. Comparison of the predicted light gas concentrations in the dome (cell=9) from all 15-cell calculations, with the experimental measurements.

4. User Guidance

The hybrid formulation of gravitational heads offers significant improvements in the treatment of stable stratifications formed by the injection of buoyant gas at an elevated location within a plant. A stability criterion, Equation (2-14), can be derived within the hybrid formulation. This criterion is almost always satisfied for a buoyant source injected into an open volume. On the other hand, the analogous criterion for the old formulation can never be satisfied. The old formulation consequently predicts that the region immediately below the injection point will mix significantly with the region above the injection. Thus, general statements about the tendency of control volume codes to overmix stratifications do not apply to the hybrid formulation. In situations with nearly well-mixed conditions, the hybrid solver should predict nearly the same results as the old formulation. Since there is almost no additional computational overhead associated with the hybrid formulation, it should be used in all cases.

One should keep in mind the fact that there are inherent limitations to control volume code. A major limitation is that momentum convection is ignored within a control volume. Thus, instability with respect to momentum convection, as discussed in References Pete94 and Hiha95, is not considered, and the hybrid solver should not be applied to stratifications that are unstable in that respect. With respect to stratifications that are stable against momentum convection, two classes of behavior may be expected, based on whether the stability criterion given in Equation (2-14) is satisfied or not: the stable behavior obtained when it is satisfied and buoyancy-dominated loop-flow behavior. The latter may be viewed as unstable counterpart of stable behavior in highly compartmentalized or channeled geometries. Although Equation (2-14) is almost always satisfied for a source injected into an open volume, strong compartmentalization or channeling effects may affect the stability of the resulting stratification. An example is the HDR E11.2 experiment, which had two essentially independent flow channels connecting the dome region with the lower containment. The mid-elevation sources injected at the midpoint of one of these channels induced loop-flow behavior, which caused the sources to mix lower in the containment than expected from a stable condition.

In many containment scenarios, stable behavior is expected after the initial blowdown. However, independent verification of the stability regime should be carried out. For nearly free jets or confined vertical jets in a cylindrical geometry, the user may use the guidelines of References Pete94 and Hiha95. This requires knowing the Froude number, the rise height and diameter of the jet, and the cylindrical wall diameter. For more general types of injection geometries no simple guidelines can be given. Experimental input or computational fluid dynamics calculations may be required to determine the stability regime.

Another modeling limitation is related to lack of a general model for the entrainment or mixing of a

buoyant jet or plume: CONTAIN 1.2 simply uses a well-mixed assumption for the injected gas in place of a general model. As discussed in Section 2.4, if the stratification is stable, as in the NUPEC M-8-1 experiment, the details of this mixing do not appear to be important for the fully developed stratification formed after the initial transient. However, for transient but stable conditions or for unstable conditions, the details of the mixing could be important in determining the flows and gas distribution. Again, experimental input or computational fluid dynamics calculations may be required to determine the mixing behavior in all but the simplest of geometries. One further modeling limitation is the lack of a coupled convective/molecular-diffusion model for the motion of gas-gas interfaces, as observed, for example, at late time in the HDR E11.2 experiment.

An important matter of user guidance has became apparent from general experience with the hybrid solver, although it has not been mentioned thusfar. This is related to the fact that a donor-based formulation is prone to introducing large "integration" errors in the gravitational head when flows occur from short cells to tall cells with significantly different gas densities. In such cases, within a donor formulation, the density of the short cell is used to calculate the gravitational head for the first half node of the tall cell. The use of this density may not be appropriate if the flow from the short cell is assumed to mix rapidly with the inventory of the tall cell, and in addition, the error is compounded by the large vertical span of a tall cell. Consequently, the calculated gravitational head may be in considerable error in this case. We refer to this below as the "half-node" problem within a donor formulation. It should be noted that gravitational heads will also be in error in an average-density treatment in this case, but typically will be only about half as large. Figure 4.1 shows two examples of a nodalization with a potential "half-node" problem, in this case representing a thermal siphon connected to a large reservoir cell in two different ways. The hot leg of the thermal siphon heats the reservoir gas in each case so that the gas density in the hot leg is less than that in the reservoir. The parts of the recirculating flow loop marked "underpredicts" and "overpredicts" lead to underprediction and overprediction, respectively, of the gravitational head driving the flow, assuming that the gas from the hot leg mixes rapidly with the reservoir. To minimize this problem, one can use cells of approximately the same height where needed and/or invoke flow path options to refine the gravitational head definition.

The flow path option approach is particularly desirable for environment cells, which should not be subdivided because the cell conditions are essentially fixed. In Figure 4.1, the "half-node" problem with respect to the tall reservoir, or environment, cell can be minimized by specifying the elevations of the flow paths at the inlet and outlet of the thermal siphon and using the RESOLVHD keyword. This will result in the use of the reservoir cell gas density to calculate the gravitational head within the reservoir cell.

Guidelines for nodalization are straightforward when using the hybrid flow solver: (1) At each

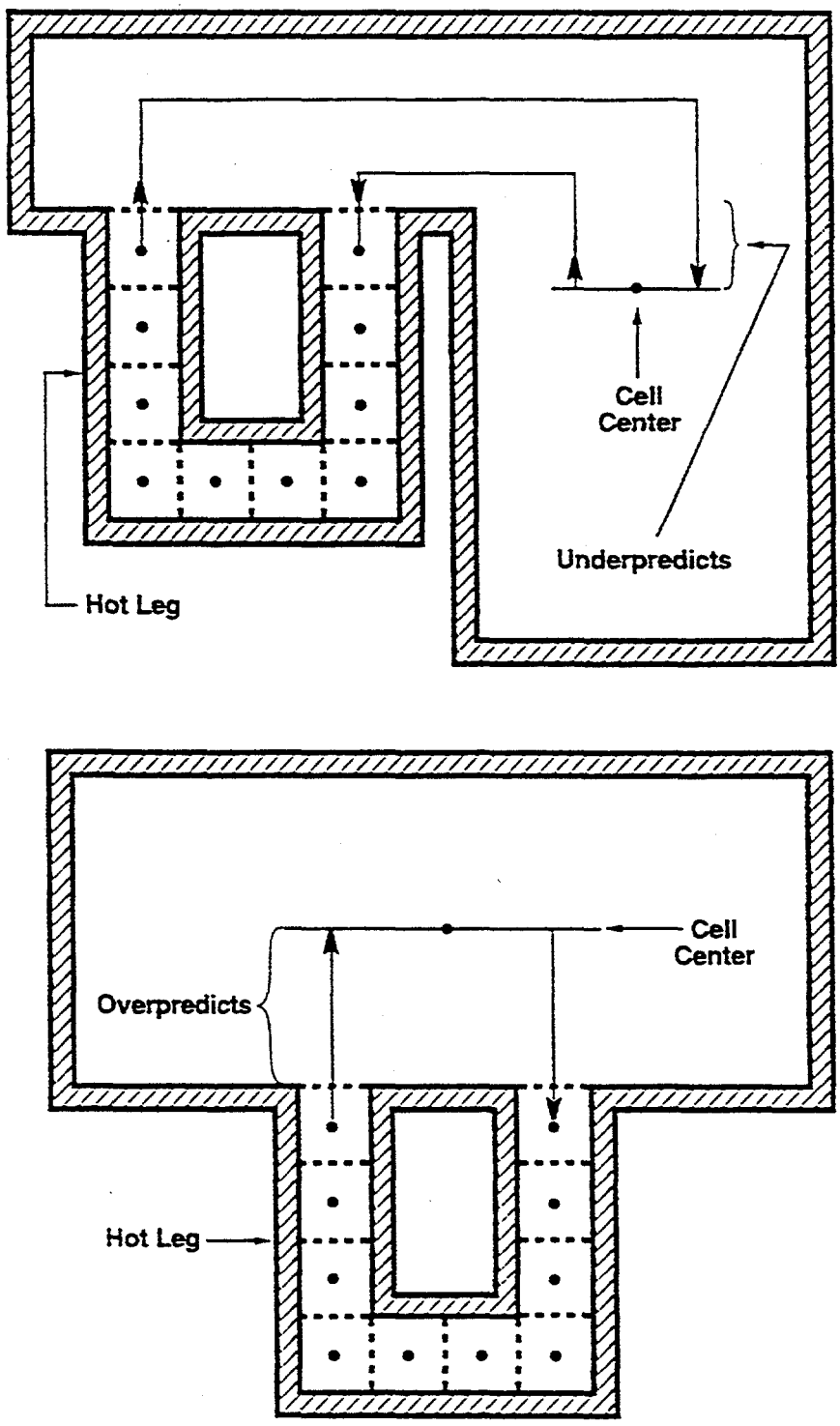

Figure 4.1. Two thermal siphon nodalizations which underpredict and overpredict the thermal siphon flow, respectively, within a donor approximation.

elevation for which a horizontal interface is present between cells, the interfaces should span the containment cross section. This should help capture the essentially one-dimensional nature of most stratifications of interest in a containment. (2) The same cell elevations should be used for all cells representing the same containment level. Slightly staggered elevations, for example, to represent minor differences in the centers of volume of the cells at a given level, should be avoided. As observed in the HDR analysis, slight elevation offsets may result large horizontal gas composition gradients resulting from the fact that buoyant gas will tend to accumulate in the uppermost of the cells at the same basic level. (3) Horizontal cell interfaces should be placed, if possible, at each location at which one would expect a stratified layer boundary to form (e.g., at each possible injection elevation). (4) A large variation in cell heights, except that caused solely by the presence of environment cells, should be avoided. As discussed above, a donor-based formulation like the hybrid formulation is particularly sensitive to gravitational head "integration" error when flows occur from a short cell to a tall cell. (5) Flow path options, as discussed above, should be used to refine gravitational head definitions for environment cells and in other situations as needed. (6) The vertical height of an environment cell should be comparable to the total height of the internal cells in the problem. The nodalizations from these guidelines should be similar to the NUPEC M-8-1 and Surtsey ST-3 nodalizations used to assess the hybrid solver.

5. Assessment Summary and Conclusions

The hybrid formulation of gravitational heads has been developed for the CONTAIN code to specifically address the demonstrated tendency of control volume codes to overmix stable stratifications formed by buoyant sources. The old CONTAIN formulation by default calculated the gravitational head between cells on the assumption that flow paths are connected to cell centers and the flow path density is the average of the cell densities connected by the flow path. While giving the proper behavior in a well-mixed asymptotic limit and exhibiting stability properly for certain configurations, this formulation was shown to be unstable in the important case in which a stratification is being created by injection of buoyant gas. The hybrid formulation, however, was shown to be consistent with the momentum equation, to correctly treat the stability of stratifications, within the inherent limitations of a control volume formulation, and to give the correct approach to the well-mixed asymptotic limit. Prior work to assess the hybrid flow solver was summarized in the Introduction. In the present assessment, code comparisons to three experiments exhibiting substantial stratification (NUPEC M-8-1[OECD94], Surtsey ST-3[Blan95], and the HDR E11.2[Karw92]) were presented to further demonstrate the capabilities and limitations of the hybrid formulation.

Other limitations of the CONTAIN code besides the treatment of stable stratifications could enter into the discrepancy between the code predictions and experiments. The ones of interest here were therefore discussed and include the lack of modeling of momentum convection within a control volume, the lack of a proper plume or jet entrainment model, and the lack of modeling of thermal conduction or molecular diffusion across gas-gas interfaces. Whenever relevant, the impact of each of these deficiencies on the present code comparisons with experiment was discussed in detail.

A *de facto* condition, i.e., one obtained within the usual assumptions of a control volume code, was derived for the stability of a stratification being formed by buoyant gas injection, within the hybrid formulation. In contrast, such a condition for the old formulation could not be satisfied. This condition seemed to correlate well with the stability, or lack thereof, that was predicted with the two formulations in the present assessment. It was argued that with the hybrid solver *de facto* stability is almost assured for buoyant sources injected into an open volume, with ample entrainment flow areas. However, it was also shown that good agreement in the HDR comparison could not be obtained when the stratification formed by the mid-elevation sources was predicted to be stable. In contrast, good agreement in the NUPEC M-8-1 comparison depended on this stability being present.

It was also discussed that the hybrid solver is more useful than one might expect from the lack of an appropriate entrainment model, because of the fact that for stable, fully developed stratifications, the lack of such a model is not important. Such stratifications are created by buoyant gas injection, under the stable conditions necessary for generating one-dimensional behavior. After the stratified layer has

worked its way down to the injection elevation, such layers then become essentially well-mixed. When the time to form such a stratification is short compared to the time scale of interest, good agreement between calculation and experiment may be expected because the resulting stratification is insensitive to the actual entrainment rates.

The NUPEC M-8-1 experiment provided a classic example of a fully developed stratification. The time required to attain fully developed conditions was apparently short. Good agreement between the predicted degree of stratification and the experiment was obtained with the hybrid formulation, in contrast to the old formulation, despite the fact that a plume entrainment model was not used in the comparison.

The Surtsey ST-3 experiment used a high velocity hydrogen jet that resulted in a marginally unstable stratification, as a consequence of the momentum convection carried by the jet. It therefore provided an opportunity to assess the hybrid formulation in such a regime. This experiment was also nearly isothermal and therefore provided an opportunity to conduct nodalization studies with five different nodalizations, without the complexities of modifying heat sinks. The observed stratification was somewhat unstable, with mixing observed below the injection elevation. The best agreement with the observed stratification was provided by the old formulation for the most detailed nodalization. However, this agreement was clearly fortuitous because momentum convection, the mechanism causing the mixing below the source, is not modeled in CONTAIN. The worst agreement was also provided by the old formulation, with a nodalization resulting in essentially well-mixed conditions. In comparison, the hybrid formulation performed robustly, with a consistent degree of stratification predicted for all the nodalizations. In addition, the hybrid solver gave good agreement with the dome hydrogen concentrations for all nodalizations despite the fact that the stratifications were predicted to be stable and the degree of penetration of the hydrogen below the injection point was not predicted well.

The HDR E11.2 experiment exhibited the most complex stratification behavior of the three experiments. In preliminary calculations with the 14-cell deck, it was found that the stratification formed during the preheat period could not be described as having *de facto* stability, as did the first two experiments. The agreement with experiment in fact worsened considerably in a calculation in which stability was obtained during the preheat. Instead, the preheat source appeared to have unstable, buoyancy-driven loop flow behavior, which drove the buoyant gas into the dome, down below the injection elevation on the other side of the containment, and back up under the injection location. It should be noted that this unstable loop flow behavior is not generally expected of stratifications in a containment and was the result of the peculiar HDR upper containment geometry. This geometry consists of two long, essentially independent flow channels alongside the RPV, connecting substantial volumes above and below the RPV. The upper containment sources were

injected at the midpoint of one of these channels to promote loop flow. In such a situation, a detailed entrainment or mixing model is required to calculate the buoyancy head from the source, since this head determines the amount of loop flow that occurs. Such a model was not available for the complex geometry involved. In addition, while the experimental data indicated that the mid-elevation sources could have been reasonably well-mixed at or just above the source elevation, the mixing could not be adequately characterized by the data available. Therefore, in the base case, the mid-elevation sources were assumed to be fully mixed at approximately the source elevation. Three sensitivity calculations, including one in which the fully mixed elevation was varied, were also done with the hybrid solver. In the second sensitivity calculation, a modeling limitation was addressed: the effect of implementing plume entrainment correlations for use with the low-elevation steam source was explored. In the third, sensitivity to flow loss coefficients was explored.

Neither formulation appeared to predict the pressure well during the preheat period, with both predicting pressures that were too high. The hybrid formulation produced much worse agreement with respect to pressure than the old formulation, but much better agreement with respect to the degree of stratification. The hybrid solver sensitivity calculations all produced essentially the same pressures as the hybrid solver base case. The difficulty in getting agreement with experiment with regard to both the pressures and the degree of stratification is not unique to the present assessment. This problem was also reported by other participants in ISP-29 in Reference Karw92 and remains unresolved.

Good agreement on the location of the lower boundaries of the stratified layers was found in the hybrid base case and all three sensitivity calculations, up to the time of decreasing light-gas concentrations in the dome in the external spray period. As expected, poor agreement was found with the old formulation. Predictions of the light-gas concentration in the dome were poor and too low initially in all cases, in spite of good agreement with respect to the location of the layer boundaries with the hybrid formulation. This was to be expected from fact that in the hybrid cases, the predicted steam concentrations in the dome were too high. As shown in Figure 3.91, in all of the hybrid cases, the agreement in the concentration increased dramatically as the steam condensed out with time, up the time of decreasing light gas concentrations in the dome.

The modeling limitation that was most obvious in the present comparisons appeared to be the lack of modeling of coupled convection/molecular-diffusion across gas-gas interfaces. This was conjectured to be origin of the slow, late-time downward motion of the lower boundary of the light-gas layer in the experiment, which was responsible for the slowly decreasing concentrations observed in Figure 3.91, beginning at 1050 minutes. In contrast to this behavior, the hybrid cases all predicted an density inversion at about this time, which lead to sudden mixing involving only the dome.

An important matter of user guidance has become apparent through the general use of CONTAIN 1.2. This is related to the fact that donor formulation that is effectively used most of the time in the hybrid formulation may generate buoyancy heads over multiple cell layers that are less accurate than the old formulation. Either more or less than the appropriate buoyancy may be generated. The problem is accentuated when flow occurs from a short cell to relatively tall cell, such as an environment cell, and the two cells have significantly different gas densities. Within a donor formulation and default flow path options, the density of the short cell is used for the first half-node of the tall cell. However, if the flow is assumed to mix quickly with the tall cell, then it would be more appropriate to use the density of the tall cell for this half-node. This "half-node" problem, however, can be reduced through increased nodalization or through use of flow path modeling options. The user may, for example, adjust flow path elevations and use the RESOLVHD option. User guidance is given in detail in Section 4 with respect to reducing buoyancy head errors and also in constructing nodalizations that are effective in capturing stratifications.

6. References

Blan95 Blanchat, T. and Stamps, D., "Deliberate Ignition of Hydrogen-Air-Steam Mixtures under Conditions of Rapidly Condensing Steam," SAND94-3101C, Sandia National Laboratories, Albuquerque, NM, January 1995.

Blev84 Blevins, R. D., Applied Fluid Dynamics Handbook, Van Nostrand Reinhold, New York, 1984.

Boya95 Boyack, B. E., Corradini, M. L., Denning, R. S., Khatib-Rahbar, M., Loyalka, S. K., and Smith, P. N., "CONTAIN Independent Peer Review," LA-12866, UC-000, Los Alamos National Laboratory, Los Alamos, NM, January 1995.

Hiha95 Hihara, E. and P. F. Peterson, "Mixing in Thermally Stratified Fluid Volumes by Buoyant Jets," Proceedings of the ASME/JSME Thermal Engineering Conference, Vol. 1, ASME, 1995.

Karw92 Karwat, H., "Distribution of Hydrogen within the HDR-Containment under Severe Accident Conditions -Final Comparison Report-," OECD Standard Problem OECD-CSNI-ISP 29, August 1992.

Mura96 Murata, K. K. et al., "CONTAIN 1.2 Code Manual, for Revision 1.21" Sandia National Laboratories, Albuquerque, NM, to be published.

OECD94 "Final Comparison Report on ISP-35 NUPEC's Hydrogen Mixing and Distribution Test (Test M-7-1)," NEA/CSNI/R(94)29, Organization for Economic Co-Operation and Development (OECD), December 1994.

Pete94 Peterson, P. F., "Scaling and Analysis of Mixing in Large Stratified Volumes," International Journal of Heat and Mass Transfer, Vol. 37, Suppl. 1, pp. 97-106, 1994.

Royl96 Royl, P., et al., "Analysis of Mitigating Measures during Steam/Hydrogen Distributions in Nuclear Reactor Containments with the 3D Field Code GASFLOW," OECD/NEA CSNI Workshop on the Implementation of Hydrogen Mitigation Techniques, Winnipeg, Manitoba, Canada, May 13-15, 1996.

Stam95 Stamps, D., "CONTAIN Assessment of the NUPEC Mixing Experiments," SAND94-2880, Sandia National Laboratories, Albuquerque, NM, August 1995.

Till95 Tills, J. L., et al. , "User Guidance on the CONTAIN Code for Advanced Light Water Reactors," Sandia National Laboratories, Albuquerque, NM, to be published.

Vale89 Valencia, L., and L. Wolf, "Preliminary Design Report, Hydrogen Distribution Experiments E11.1 - E11.5," PHDR Working Report 10.003/89, Kernforschungszentrum Karlsruhe, FRG, 1989.

Wenz91 Wenzel, H.-H., et al., "Quality Considerations of Major Direct and Indirect Measured Quantities During the Experiments of Test-Group E11," PHDR Working Report 10.025/91, Kernforschungszentrum Karlsruhe, FRG, 1991.

APPENDIX A

DERIVATION OF THE CONTAIN MOMENTUM EQUATION

The CONTAIN momentum equation is intended to describe relatively low speed flows. It is derived here to sufficient accuracy to define the mass flow rate to lowest order in the Mach number M, which entails including terms up to $O(M^2)$ in the momentum equation. Such terms include the kinetic energy terms in the flow.

A convenient starting point for the derivation is Equation (3.3-2) of Reference Bir60 for the time derivative of the kinetic energy per unit volume. This equation follows with no further approximation from the Navier-Stokes equations. The form of this equation is appropriate for the flow paths in CONTAIN, which are assumed not to have mass sources or sinks or to involve external work. Flow paths in CONTAIN are also considered to be adiabatic. (Mass and energy sources and sinks are considered to occur in the mass and energy control volumes, or cells, but not the momentum control volumes, or flow paths.)

This starting equation can be rearranged slightly to read as follows:

$$\frac{1}{2}\frac{\partial}{\partial t}(\rho v^2) = -\frac{1}{2}\nabla\cdot(\rho v^2 \mathbf{v}) - \mathbf{v}\cdot\nabla P - \nabla\cdot(\tau\cdot\mathbf{v}) + \tau:\nabla\mathbf{v} + \rho(\mathbf{v}\cdot\mathbf{g}) \qquad \text{(A-1)}$$

where ρ is the density, $\mathbf{v}$ is the velocity, P is the pressure, τ is the stress tensor, and $\mathbf{g}$ is the acceleration due to gravity.

This equation can be integrated over the momentum control volume of Figure A-1, between points 1 and 2 along a streamline, with the usual simplifying assumption that variations in quantities such as the velocity occur along the streamline but not transverse to it. In addition, it is assumed that mass accumulation $\partial\rho/\partial t$ at each point along the streamline is zero; i.e., the flow rate instantaneously reaches steady state. Thus, the mass flow rate W is assumed to be spatially invariant, although it may be time-dependent. One consequence of the latter assumption is that mass flowing into the momentum control volume is instantaneously balanced by mass outflow; consequently, as far as the mass and energy control volumes are concerned, the momentum control volume inventory can be neglected.

The various terms in Equation (A-1) are treated as follows. The volume integral of the left hand side of Equation (A-1) is approximated by:

$$\frac{1}{2}\int\frac{\partial}{\partial t}(\rho v^2)dV = \frac{1}{2}\frac{\partial}{\partial t}\left(W\int_1^2 v\,d\ell\right) = \frac{LW}{\rho_f A}\frac{\partial}{\partial t}W \qquad \text{(A-1)}$$

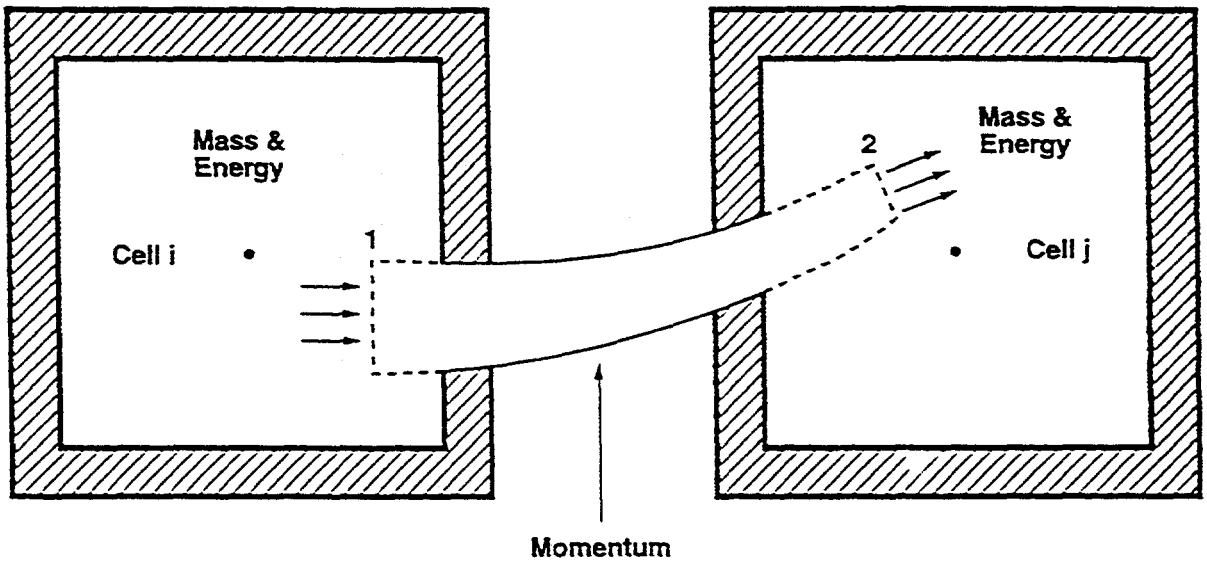

Figure A.1. Schematic of a CONTAIN momentum control volume, or flow path, between two mass and energy control volumes, or cells.

where ℓ is the distance along the streamline, L is an effective inertial length, A is a representative flow area, and ρ_f is the effective flow path density defined below. These latter variables are assumed not to change with time.

The first term on the right hand side of Equation (A-1) represents the rate of accumulation of kinetic energy through flow and is approximated by:

$$-\frac{1}{2}\int \nabla\bullet(v^2\mathbf{v})dV=\frac{1}{2}W(v_1^2-v_2^2) \qquad \text{(A-3)}$$

The second term on the right represents the rate of work done by pressure effects, including that converted to internal energy, and is approximated by:

$$-\int \mathbf{v}\bullet\nabla P\, dV=-W\int_1^2 \frac{1}{\rho}dP=\frac{W}{\rho_f}(P_1-P_2) \qquad \text{(A-4)}$$

where ρ_f is the effective density in the flow path, which by the mean-value theorem should be the density at some point within the path. The approximations used for this effective density are discussed in Section 2.

The third term on the right represents the rate of work done by viscous forces. It can be converted to a surface integral that is customarily neglected (see Reference Bir60, p. 214). The fourth term on the right is the conventional flow loss term as discussed in Reference Bir60, p.215:

$$-\int \tau:\mathbf{v}dV=-C_{FC}Wv_p^2 \qquad \text{(A-5)}$$

where v_p is the flow velocity at a representative point in the flow path, taken here to be the point at which the effective density occurs. The loss coefficient C_{FC} is conveniently referenced to this point. The last term on the right represents the rate of work done by gravity and can be expressed as

$$\int \rho\mathbf{v}\bullet\mathbf{g}dV=gW(H_1-H_2) \qquad \text{(A-6)}$$

where H_1 and H_2 are the elevations of the two ends of the control volume.

Thus, one obtains the equation:

$$\frac{L}{A}\frac{\partial}{\partial t}W = P_1 - P_2 + \frac{1}{2}\rho_f v_1^2 - \frac{1}{2}\rho_f v_2^2 + g\rho_f(H_1 - H_2) - C_{FC}\frac{W|W|}{\rho_f A^2} \qquad \text{(A-7)}$$

provided the representative area A (hitherto unspecified) is assumed to correspond to the point at which the effective density occurs.

The following observations are made: the points 1 and 2 do not necessarily correspond to the gas center of volume location at which the gas thermodynamic conditions in the mass and energy control volumes (i.e., cells) are calculated. In order to extrapolate conditions from the gas center of volume to the momentum control volume interfaces it is assumed that the stagnation pressure $P^* = P + \rho v^2/2 + O(M^4)$ in the mass and energy control volume, adjusted for the gravitational head in that control volume, matches the stagnation pressure in the flow at the momentum control volume interface. Note that, for simplicity, we have neglected the possible submergence of points 1 and 2 below the surface of the pool that may be present in the mass and energy control volumes. This matching procedure is correct for two important limiting cases: (1) the case in which the composition and "flow" in the downstream cell are dominated by the influx from a single flow path, in which case the matching condition is just the lossless Bernoulli condition to $O(M^4)$, and (2) the case in which a small jet is directed into a relatively large stagnant volume with an arbitrary composition. This matching procedure clearly does not properly treat situations such as jet pumps, for which the proper consideration of vector nature of the influx momentum is important.

Since $P_1^* = P_1 + \rho_1 v_1^2/2 + O(M^4)$ and $\rho_1 = \rho_f + O(M^2) + O(g\rho\Delta H/P)$, and so forth, where ΔH is a characteristic height, one obtains the CONTAIN momentum equation to the necessary accuracy as:

$$\frac{L}{A}\frac{\partial}{\partial t}W = P_i^* - P_j^* + \Delta P_{g,ij} - C_{FC}\frac{W|W|}{\rho_f A^2} + O(M^4) \qquad \text{(A-8)}$$

where the gravitational head is defined as

$$\Delta P_{g,ij} = \rho_i g(H_i - H_1) + \rho_f g(H_1 - H_2) + \rho_j g(H_2 - H_j)$$

where *i* refers to the cell with interface 1, and *j* refers to the cell with interface 2, ρ_i the gas density of cell *i*, H_i is the elevation of the gas center of volume of cell *i*, and so forth.

It should be noted that CONTAIN calculates stagnation properties, and not the gas stream properties,

in the equation-of-state calculation for each cell, and these stagnation properties are used in the momentum equation. Thus, it is not strictly correct to say that the kinetic energy is neglected in the mass and energy control volumes. Rather, the effects of kinetic energy are taken into account to the extent possible through a scalar formulation based on stagnation properties. In one-dimensional flow, without converging streams, there is no ambiguity about the vectorial nature or sign of the momentum convection associated with this kinetic energy. Thus, in this case CONTAIN should give the same results as a code, such as RELAP, that explicitly takes momentum convection into account, at least for low Mach numbers.

Since the CONTAIN equation-of-state calculation actually yields stagnation properties, calculated quantities such as the gas temperature are not strictly correct to use in calculating other processes such as heat transfer to structures. However, since the differences between a gas stream temperature and stagnation temperature are of $O(M^2)$, the error involved should be negligible under typical containment conditions.

REFERENCES

Bird60 Bird, R. B., W. E. Stewart, and E. N. Lightfoot, Transport Phenomena, John Wiley and Sons, New York, 1960.

EXTERNAL DISTRIBUTION:

U.S. Nuclear Regulatory Commission (8)
Division of Reactor System Safety
Office of Nuclear Regulatory Research
ATTN: C. Ader, T-10K-8
A. Drozd
C. G. Gingrich, NLN-344
R. Lee, T-10K-8
J. Monninger, OWFN 8-D
A. Notafrancesco (20 cys)
A. Rubin, T-10K-8
T. Spies, T-10F-12

U.S. Nuclear Regulatory Commission (3)
Office of ACRS
ATTN: M. D. Houston, T-2E-26
T. Kress, T-2E-26
I. Catton
Washington, D.C. 20555-0001

U.S. Department of Energy (2)
Albuquerque Operations Office
Post Office Box 5400
ATTN: C. E. Garcia, Director
For: C. B. Quinn
R. L. Holton
Albuquerque, NM 87185

U.S. Department of Energy
Office of Nuclear Safety Coordination
ATTN: R. W. Barber
Washington, D.C. 20545

U.S. Department of Energy
Idaho Operations Office
850 Energy Drive
ATTN: S. W. Sorrell
Idaho Falls, ID 83401

U.S. Department of Energy
Scientific and Technical Information Center
Post Office Box 62
Oak Ridge, TN 37831

Argonne National Laboratory
9700 South Cass Avenue
ATTN: B. Spencer
Argonne, IL 60439

Battelle Columbus Laboratory (2)
505 King Avenue
ATTN: R. Denning
J. Gieseke
Columbus, OH 43201

Battelle Pacific Northwest Laboratory
Post Office Box 999
ATTN: M. Freshley
Richland, WA 99352

Ebasco Services Incorporated
Applied Physics Department
Two World Trade Center
Attn: J. J. Shin
New York, NY 10048

EG&G Idaho
Post Office Box 1625/MS2508
ATTN: D. L. Knudson
Idaho Falls, ID 83415

Electric Power Research Institute (2)
3412 Hillview Avenue
ATTN: A. Michaels
M. Murillo
Palo Alto, CA 94303

Energy Research, Inc. (2)
Post Office Box 2034
ATTN: H. Esmali
M. Khatib-Rahbar
Rockville, MD 20852

Fauske & Associates, Inc. (2)
16W070 West 83rd Street
ATTN: R. Henry
M. G. Plys
Burr Ridge, IL 60952

General Electric Company
Advanced Boiling Water Reactor Program
175 Curtner Avenue
ATTN: W. Holtzclaw
San Jose, CA 95125

Knolls Atomic Power Laboratory
Post Office Box 1072
ATTN: J. M°Mullan
Schenectady, NY 12301

Levy & Associates
3880 South Bascom Avenue, Suite #112
ATTN: S. Levy
San Jose, CA 95124

Los Alamos National Laboratory
Post Office Box 1663
ATTN: B. Boyack, K-551
Los Alamos, NM 87545

Massachusetts Institute of Technology
ATTN: M. Golay
Cambridge, MA 02139

Oak Ridge National Laboratory (3)
Post Office Box 2009
ATTN: S. A. Hodge
C. Hyman
K. Smith, MS-8057
Oak Ridge, TN 37831-8057

Pennsylvania Power & Light Company
Two North Ninth Street
ATTN: T. S. Yih
Allentown, PA 18101

Purdue University
Heat Transfer Laboratory
School of Mechanical Engineering
ATTN: R. Viskanta
West Lafayette, IN 47907-1209

Purdue University
School of Nuclear Engineering
ATTN: M. Ishii
West Lafayette, IN 47907

Rennselaer Polytechnic Institute
Department of Nuclear Engineering &
Engineering Sciences
Tibbits Avenue, NES Building
ATTN: M. Podowski
Troy, NY 12180-3590

Science Applications International Corp.
2109 Air Park Road, S.E.
ATTN: D. R. Bradley
Albuquerque, NM 87106

Stone & Webster Engineering
Post Office B ox 2325
ATTN: J. Metcalf, MS245-2
Boston, MA 02107

Texas A&M University
Department of Nuclear Engineering
ATTN: Y. A. Hassan
College Station, TX 77843

Jack Tills & Associates
Post Office Box 549
ATTN: J. Tills
Sandia Park NM 87047

University of California
Department of Chemical and
Nuclear Engineering
ATTN: T. Theofanous
Santa Barbara, CA 93106

University of Evansville (5 cys)
Department of Mechanical and
Civil Engineering
ATTN: D. Stamps
Evansville, IN 47722

University of Maryland
Department of Nuclear Engineering
ATTN: Professor K. Almenas
College Park, MD 20742

University of Missouri
Nuclear Engineering Department
ATTN: S. K. Loyalka
Columbia, MO 65211

University of New Mexico
Department of Chemistry and
Nuclear Engineering
ATTN: F. E. Haskin
Albuquerque, NM 87131

University of Wisconsin
Department of Nuclear Engineering
153 Engineering Research Building
1500 Johnson Drive
ATTN: M. L. Corradini
Madison, WI 53706

Westinghouse Bettis Atomic Laboratory
Post Office Box 79
ATTN: J. W. Wolfe, ZAP 34N
West Mifflin, PA 15122

Westinghouse Savannah River (3)
Woodside Executive Park
1359 Silver Bluff Road
ATTN: K. O'Kula
Aiken, SC 29808-0001

FOREIGN DISTRIBUTION:

IAEA
Division of Nuclear Reactor Safety
Wagranerstrasse 5
Post Office Box 100
A/1400 Vienna
ATTN: M. Jankowski
AUSTRIA

Belgonucleaire SA
Rue du Champ de Mars 25
ATTN: H. Bairiot
B-1050 Brussels
BELGIUM

Director, Research, Science Education CEC
Rue de la Loi 2000
1049 Brussels
ATTN: W. Balz
BELGIUM

Commission on the Use of Atomic Energy for
Peaceful Purposes - 69 Shipchenski
Prokhod Boulevard, 1574, Sofia
ATTN: Y. Yanev
BULGARIA

AECL CANDU
Sheridan Park Research Community
2251 Speakman Avenue
ATTN: V. J. Nath
Mississauga, Ontario L5K 1B2
CANADA

AECL Research
Chalk River Research Laboratories
ATTN: B. H. McDonald
Chalk River, Ontario KOJ 1JO
CANADA

AECL Research
Whitshell Laboratories
ATTN: S. R. Mulpuru
Pinawa, Manitoba R0E 1L0
CANADA

Ontario Hydro
700 University Avenue
ATTN: O. Akalin
Toronto, Ontario M5G 1X6
CANADA

Nuclear Research Institute
250 68 Rez
ATTN: J. Kujal
CZECH REPUBLIC

State Office for Nuclear Safety
Slezska 9
ATTN: J. Stuller
120 00 Prague 2
CZECH REPUBLIC

RISO National Laboratory
Department of Energy Technology
Post Office Box 49
DK-4000 Roskilde
ATTN: P. B. Fynbo
DENMARK

Finnish Center Radiation & Nuclear Safety
Department of Nuclear Safety
Post Office Box 268
SF-00101 Helsinki
ATTN: J. V. Sandberg
FINLAND

Tech Research Centre of Finland (VTT)
Nuclear Engineering Laboratory (YDI)
PL 169
00181 Helsinki
ATTN: L. Mattila
FINLAND

Cadarache Center for Nuclear Studies (3)
F-13108 Sait Paul-Lez-Durance Cedex
ATTN: M. Schwartz
F. Serre
A. Meyer-Heine
FRANCE

Inst. de Protection et de Surete Nucleaire
CEN/FAR-B.P. No. 6
F-92265, Fontenay-aux-Roses
ATTN: J. Bardelay
Cedex, FRANCE

Battelle Institute e. V.
Am Romerhof 35
D-6000 Frankfurt am Main 90
ATTN: D. T. Kanzleiter
GERMANY

Gesellschaft fur Reaktorsicherheit (3 cys)
Forschungsgelande
8046 Garching
ATTN: K. Trambauer
G. Weber
M. Sonnenkalb
GERMANY

Gesellschaft fur Reaktorsicherheit mbH
Postfach 101650
Glockengasse 2
D-5000 Koln 1
ATTN: J. Langhans
GERMANY

Ruhr-University of Bochum
Department of Nuclear & New Energy System
ATTN: U. Brockmeier
GERMANY

University of Stuttgart
IKE
Pfaffenwaldring 31
ATTN: U. Bieder
D-7000 Stuttgart 80
GERMANY

Technische Universitat Munchen
Forschungsgelande
8046 Garching
ATTN: Professor Dr. I. H. Karwat
GERMANY

Forschungszentrum Karlsruhe (3 cys)
Post Office Box 3640
ATTN: V. Scholtyssek
75 Karlsruhe
GERMANY

Research Centre Rossendorf, Inc.
Forschungszentrum Rossendorf
Postfach 19
ATTN: Dr. H. Funke
DO-8051 Dresden
GERMANY

Institute for Electric Power Research
Division of Nuclear & Power Engineering
Post Office Box 233
ATTN: Z. Techy
H-1368 Budapest
HUNGARY

Hungarian Atomic Energy Commission
H-1374 Budapest, Post Office Box 565
ATTN: S. Elo
Budapest
HUNGARY

CEC Joint Research Center (3)
I-21020 Ispra (Varese)
ATTN: P. Fasoli-Stella
A. Markovina
R. Ricchena
ITALY

Nucleare e della Protezione Sanitaria
(DISP) (ENEA)
Ente Nazionale Energie Alternative
Viale Regina Margherita, 125
Cassella Postale M. 2358
ATTN: G. Petrangeli
1-00144 Roma A.D.
ITALY

ENEL-CRTN
Via Monfalcone 15
ATTN: E. Borioli
20132 Milan
ITALY

Toshiba Corporation
Nuclear Safety Engineering Section
8, Shinsugita-Cho, Isogo-Ku
Yokohama 235
ATTN: M. Naito
JAPAN

Power Reactor Nuclear Fuel Development
Corporation (PNC)
9-13, 1-Chome
ATTN: H. Hiroi
Minato-Ku, Tokyo
JAPAN

Nuclear Power Engineering Center
Fujitakanko Building
17-1, 3-Chome, Toranomon, Minato-Ku
ATTN: Kenji Takumi
Tokyo, 105
JAPAN

Japan Atomic Energy Research Institute (2)
Tokai-mura
Naku-gun
ATTN: K. Soda
J. Sugimoto
Ibaraki-ken, 319-11
JAPAN

POSTECH
Department of Mechanical Engineering
Post Office Box 125
Kyungbuk 790-600
ATTN: M. H. Kim
KOREA

Korea Atomic Energy Research Institute
150 Dukjin-dong, Yoosung-gu
ATTN: Hee-Dong Kim
Taejon 305-353
KOREA

Korea Institute of Nuclear Safety
Safety Review and Assessment Division
Post Office Box 16, Daeduk-Danji
ATTN: J. J. Lee
Taejon, 305-353
KOREA

VATESI
Gediminis Prospect 36
ATTN: P. Vaisnys
Vilnius
LITHUANIA

Com. Nacional de Seguridad Nucl. Salvag
Colonia Narvarte Delegation B. Juarez
ATTN: Dr. Abrtshsm #779
C.P. 03020
MEXICO

Atomic Energy Council
67, Lane 144 Keelung Road
Section 4, Taipei, Taiwan
ATTN: S. J. Shieh
REPUBLIC OF CHINA

Institute of Nuclear Energy Research
Post Office Box 3
Lungtan, Taiwan 325
ATTN: S. I. Chang
REPUBLIC OF CHINA

Nuclear Safety Institute
Russian Research Center KI
1 Kurchatov Square
ATTN: V. Asmolov
123182 Moscow
RUSSIA

Russian Academy of Sciences
Nuclear Safety Institute
52, B. Tulskaya
ATTN: V. F. Strizhov
113191 Moscow
RUSSIA

Nuclear Regulatory Authority, Slovak Republic
Post Office Box 24
820 07 Bratislava 27
ATTN: J. Misak
SLOVAK REPUBLIC

Jozef Stefan Institute
Jamova 39
ATTN: B. Mavko
61111 Ljubljana
SLOVENIA

Catedra de Tecnologia Nuclear
E.T.S. Ingenieros Industriales
Universidad Politecnica
Jose Gutierrez Abascal, 2
28006-Madrid
ATTN: L. Herranz
SPAIN

Consejo de Seguridad Nuckan
SOR Angela de la Cruz No. 3
ATTN: J. Bagues
28056 Madrid
SPAIN

Consejo de Seguridad Nuclear
Justo Dorado 11
ATTN: J. E. deCarlos
28040 Madrid
SPAIN

E.T.S. Ingenieros Industriales
Jost Gutierrez Abascal, 2
ATTN: A. Alonso
28006 Madrid
SPAIN

Royal Institute of Technology
Nuclear Power Safety
S-100 44 Stockholm
ATTN: B. R. Sehgal
SWEDEN

Swedish Nuclear Power Inspectorate
S-106 58 Stockholm
ATTN: W. Frid
SWEDEN

Studsvik Nuclear
S-611 82, Nykoping
ATTN: K. O. Johansson
SWEDEN

Swiss Federal Nuclear Safety Inspectorate
CH-5303 Wurenlingen
ATTN: S. Chakraborty
SWITZERLAND

Paul Scherrer Institute
ATTN: P. Hosemann
CH-5232 Villigen, PSI
SWITZERLAND

Institute of Nuclear Energy Research
Post Office Box 3
ATTN: Sen-I Chang
Lung-Tan
TAIWAN 325

Netherlands Energy Research
Foundation (ECN) (2)
Postbus 1
1755 ZG Petten
ATTN: K. J. Brinkman
P. M. Stoop
THE NETHERLANDS

N. V. Kema
Post Office Box 9035
ATTN: P. Kloeg
6800 ET Arnhem
THE NETHERLANDS

AEA Culham Laboratory (2)
Abingdon
Oxfordshire, OX14-3DB
ATTN: B. D. Turland
D. F. Fletcher
UNITED KINGDOM

AEA Winfrith (3)
Dorchester
Dorset DT2 8DH
ATTN: S. Kinnersley
P. N. Smith
B. Bowsher
UNITED KINGDOM

Nuclear Electric
Berkeley Nuclear Laboratory, Berkeley
ATTN: C. Chapman
Gloucestershire GL 13 9PB
UNITED KINGDOM

CEGB, Booths Hall
Chelford Road, Knutsford
Cheshire WA16 8QG
ATTN: N. E. Buttery
UNITED KINGDOM

AERE Harwell
Didcot
ATTN: A. L. Nichols
Oxfordshire OX11 ORA
UNITED KINGDOM

UKAEA, Risely Nuclear Laboratories (2)
Risley, Warrington
ATTN: A. T. D. Butland
I. H. Dunbar
Cheshire WA3-4NE
UNITED KINGDOM

INTERNAL DISTRIBUTION:

MS0619 Review & Approval Desk (12630),
For: DOE/OSTI (2 cys)
MS0736 N. R. Ortiz (6400)
MS0739 K. D. Bergeron (6421) (5)
MS0739 R. K. Cole, Jr. (6421)

MS0739 R. O. Gauntt (6421)
MS0739 R. G. Gido (6421)
MS0739 R. O. Griffith (6421)
MS0739 K. K. Murata (6421) (30 cys)
MS0739 S. B. Rodriguez (6421)
MS0739 D. C. Williams (6421)
MS0742 J. E. Kelly (6414)
MS0744 D. A. Powers (6404)
MS0747 A. L. Camp (6412)
MS0748 F. E. Harper (6413)
MS0899 Tech Library (4414) (5 cys)
MS1137 M. D. Allen (6422)
MS1137 T. K. Blanchat (6422)
MS1137 M. M. Pilch (6422)
MS1139 K. O. Reil (6423)
MS9018 Central Technical Files (8523-2)